THE CRYOGENIC DARK MATTER SEARCH: FIRST 5-TOWER DATA AND IMPROVED UNDERSTANDING OF IONIZATION COLLECTION

by

CATHERINE NOEL BAILEY

Submitted in partial fulfillment of the requirements

for the degree Doctor of Philosophy

Dissertation Advisor: Professor Daniel S. Akerib

Department of Physics

CASE WESTERN RESERVE UNIVERSITY

January 2010

CASE WESTERN RESERVE UNIVERSITY

SCHOOL OF GRADUATE STUDIES

We hereby approve the thesis/dissertation of

Catherine Bailey

candidate for the PhD degree *.

(signed) Daniel S. Akerib
(chair of the committee)

Brett Ellman

Tom Shutt

Harsh Mathur

(date) 14 July 2009

*We also certify that written approval has been obtained for any proprietary material contained therein.

Copyright ©2009 by Catherine Noel Bailey

All rights reserved

To my Family

and

To Nick

Contents

Contents **i**

List of Tables **v**

List of Figures **vi**

Preface **xxii**

Acknowledgements **xxv**

1 Dark Matter and Detection **1**
1.1 Introduction . . . 1
1.2 Evidence for Dark Matter . . . 2
1.2.1 Galaxies . . . 3
1.2.2 Galaxy Clusters . . . 5
1.2.3 Cosmic Microwave Background Radiation . . . 7
1.2.4 Large Scale Structure Formation . . . 10
1.2.5 Big Bang Nucleosynthesis . . . 11
1.3 Dark Matter Candidates . . . 14
1.3.1 MACHOs . . . 15
1.3.2 Neutrinos . . . 15
1.3.3 Axions . . . 15
1.3.4 Weakly Interacting Massive Particles . . . 17
1.4 Dark Matter Detection . . . 19
1.4.1 Cryogenic Solid State Detectors . . . 23
1.4.2 Liquid Noble Detectors . . . 24
1.4.3 Super Heated Detectors . . . 25
1.4.4 Annual Modulation . . . 26

2 The Cryogenic Dark Matter Search **29**
2.1 Introduction . . . 29
2.2 ZIP Detectors . . . 29
2.3 Phonon Measurement . . . 32
2.3.1 Phonon Generation and Propagation . . . 32

2.3.2 Phonon Collection . . . 34
2.4 Ionization Measurement . . . 38
2.5 Ionization Yield Discrimination . . . 39
2.6 Charge Trapping . . . 41
2.6.1 Surface Trapping, Dead Layers, and Phonon Timing Discrimination . . . 42
2.6.2 Bulk Trapping and Neutralization . . . 46

3 CDMS-II Experimental Setup in the Soudan Underground Laboratory 50
3.1 Introduction . . . 50
3.2 Location - Soudan Underground Laboratory . . . 50
3.3 Cryogenics . . . 51
3.4 Shielding . . . 52
3.5 Cold Hardware . . . 54
3.5.1 Detector Housing . . . 56
3.5.2 Tower . . . 56
3.5.3 Side Coax . . . 57
3.5.4 SQUET . . . 58
3.5.5 Stripline . . . 59
3.6 Warm Electronics . . . 59
3.7 DAQ and Data Handling . . . 61

4 5-Tower Run 62
4.1 Introduction . . . 62
4.2 Detector Testing and Selection . . . 62
4.3 Soudan Preparation . . . 65
4.4 Detector Tuning . . . 67
4.5 Operations . . . 74
4.6 Real-Time Data Quality . . . 78
4.6.1 Noise . . . 78
4.6.2 Diagnostic Plots . . . 79
4.6.3 DAQ Monitoring . . . 81
4.6.4 KS Tests . . . 82
4.6.5 PipeDisplay . . . 83
4.6.6 Neutralization . . . 84

5 5-Tower Analysis and Results 86
5.1 Introduction . . . 86
5.2 Blinding . . . 86
5.2.1 Blinding Method . . . 86
5.2.2 Blinding Cut . . . 89
5.2.3 Blinding Implementation . . . 90
5.3 Data Quality Cuts . . . 91
5.3.1 Detectors Problems . . . 91
5.3.2 Detector Pathologies . . . 92

5.3.3 Stable Tuning . . . 93
5.3.4 Stable Performance . . . 94
5.3.5 Neutralization . . . 95
5.4 Science Cuts . . . 101
5.4.1 Veto . . . 101
5.4.2 Thresholds . . . 101
5.4.3 Event Multiplicity . . . 104
5.4.4 Fiducial Volume . . . 105
5.4.5 Ionization Yield . . . 106
5.4.6 Phonon Timing . . . 108
5.5 Analysis Exposure . . . 109
5.6 Background Estimate . . . 111
5.6.1 Nuclear Recoil Background Events . . . 111
5.6.2 Surface Events . . . 112
5.7 Unblinding . . . 113
5.8 Results . . . 114

6 Neutralization 118
6.1 Introduction . . . 118
6.2 Neutralization Methods . . . 119
6.2.1 LED Neutralization . . . 119
6.2.2 Strong Source Neutralization . . . 120
6.3 Assessing Neutralization . . . 122
6.3.1 Pulse Shapes . . . 122
6.3.2 Voltage Monitoring . . . 123
6.3.3 Low Yield Events . . . 124
6.4 Optimizing running conditions . . . 130
6.4.1 LED Optimization . . . 130
6.4.2 Strong Source Optimization . . . 134
6.4.3 Neutralization Effectiveness . . . 137
6.5 Maintaining Neutralization . . . 137
6.6 External Influences on Neutralization . . . 140
6.6.1 Temperature . . . 141
6.6.2 Event Rate . . . 145
6.6.3 Charge Bias . . . 145
6.7 1 inch Detector Neutralization . . . 146
6.8 Neutralization Model . . . 148

7 Design Studies toward Improving Surface Event Rejection 162
7.1 Introduction . . . 162
7.2 Interleaved ZIP . . . 163
7.3 Phonon and Ionization Side Yield Discrimination Asymmetry . . . 166
7.3.1 Hydrogenated Amorphous Silicon . . . 168
7.3.2 Ion Implantation . . . 179
7.4 Other Phenomena Observed During Device Testing . . . 183
7.4.1 Dead Layer Electric Field Dependence . . . 184

7.4.2 Electric Field Dependent Ionization Collection 184
7.4.3 Position Dependent Charge Collection 190
7.4.4 Charge Instability after Changing Charge Bias 195
7.4.5 N- vs. P-type Germanium 200
7.5 SuperCDMS Detector Design 203

8 Conclusion **208**

A LED Neutralization Details **212**
A.1 Introduction 212
A.2 LEDs 212
A.3 LED Circuit 213
A.4 Non-working LEDs 216

B Soudan LED Tests **218**
B.1 Introduction 218
B.2 Run 127 LED tests 218

C Neutralization Methods **221**
C.1 Introduction 221
C.2 Soudan Neutralization Methods 221
C.2.1 Strong Source Bake 221
C.2.2 LED bake 222
C.2.3 LED flash 223
C.3 Test Facility Neutralization Methods 224

D Five-Tower Run Neutralization Summary **227**
D.1 Introduction 227
D.2 Run 123 227
D.3 Run 124 228
D.4 Run 125 229
D.5 Run 126 229
D.6 Run 127 230
D.7 Run 128 230
D.8 Run 129 231

E Soudan Neutralization Procedure **232**

F Test Facility Neutralization Procedure **234**

G Calculating the Detector Dead Layer **236**
G.1 Introduction 236
G.2 Procedure 236

Bibliography **240**

List of Tables

4.1 Table of Soudan Detectors. 64

5.1 Phonon recoil energy thresholds (in keV) for the Run 123 and 124 analysis. Germanium detectors are in bold. 103
5.2 The 15 germanium and 6 silicon Run 123 detectors included in the analysis. Germanium detectors are bold. 110
5.3 The 7 germanium and 2 silicon Run 124 detectors included in the analysis. Germanium detectors are bold. 110
5.4 The predicted number of single-scatter events failing the phonon timing cut along with the observed number in parentheses. Germanium detectors are bold. 114

6.1 Detectors used to study loss of ionization collection along with important properties. 149

7.1 Si detectors used to study the effects of hydrogen passivating the amorphous silicon blocking layer along with important properties. 171
7.2 Soudan Run 123 detectors along with the germanium crystal boule identification and doping type. 202

B.1 Individual LED bakes taken during the Soudan 5-tower study 219
B.2 Detectors used during the Soudan 5-tower study 219
B.3 LED on times used for each bake (note that the LED pulse step size is 10 μA) 220
B.4 Maximum mixing chamber and Tower 5 temperature during each LED bake . 220

G.1 G3D -3 V data dead layer based on the 60 keV gamma-rays for each ^{241}Am source, measured at the 63% level of the dead layer distribution. 239

List of Figures

1.1 Pie chart representing the present composition of the universe, as inferred from current cosmological measurements. Courtesy of NASA / WMAP Science Team. 2

1.2 Rotation curves of 6 spiral galaxies. The dotted, dashed, and dash-dotted lines are the contributions of gas, galaxy disk, and dark matter. From [1]. 4

1.3 A Hubble Space Telescope image of the Abell 2218 galaxy cluster showing prominent arcs of distant objects due to strong gravitational lensing. Courtesy of Space Telescope Science Institute. 6

1.4 (a) Optical (from the Hubble Space Telescope) and (b) x-ray (from the Chandra X-ray Observatory) images of the Bullet cluster. The green and white curves are mass contours from weak lensing data. Notice how the mass contours do not coincide with the x-ray distribution. From [2]. 7

1.5 A full sky map of the Cosmic Microwave Background, from the WMAP 5 yr data set, that shows the μK temperature fluctuations. Courtesy of NASA / WMAP Science Team. 8

1.6 The CMB temperature power spectrum with data points from the WMAP 5 yr data along with Acbar, Boomerang, and CBI. The curve indicates the prediction of the best-fit ΛCDM cosmology. From [3]. 9

1.7 The CMB E-mode polarization power spectrum with data points from the WMAP 5 yr data along with Boomerang, CAPMAP, CBI, DASI, and QUAD. The curve indicates the prediction of the best-fit ΛCDM cosmology. From [3]. 9

1.8 Map of the galaxy distribution as a function of redshift, as projected from the 2dF Galaxy Redshift Survey, showing the universe's current large scale structure. From [4]. 11

1.9 Evolution of light element abundances during Big Bang Nucleosynthesis as a function of time (or temperature). From [5]. 12

1.10 Figure summarizing primordial light element abundances. Bands show predictions of the primordial abundances of ^{4}He, D, ^{3}He, and ^{7}Li as functions of the baryon-to-photon ratio, η. The small yellow boxes indicate 2σ observational constraints based upon statistical errors while the larger blue boxes incorporate systematic errors. The vertical bands represent the CMB and combined BBN results on η (and therefore Ω_b). From [6]. 13

1.11 Figure showing axion mass ranges excluded by various astronomical and laboratory constraints (light rectangles) as well as those ranges that will be probed by current and upcoming experiments (dark rectangles). The vertical arrow indicates the axion mass range with cosmologically-interesting relic densities. From [6]. 16
1.12 Figure of the WIMP comoving number density as a function of time (or temperature) in the early universe. The solid curve corresponds to the equilibrium abundance while the dashed curves represent forming the WIMP relic abundance (and how that varies with annihilation cross section). From [7]. 19
1.13 (a) The nuclear form factors as a function of energy for silicon (solid line), germanium (dashed line), and xenon (dash dotted line) targets. From [8]. (b) The integrated WIMP interaction rate as a function of threshold energy for silicon (solid line), germanium (dashed line), and xenon (dash dotted line) targets and assuming a WIMP with a mass of 100 GeV and interaction cross section of $10^{-42}\,\mathrm{cm}^2$. From [9]. 22
1.14 Images of three different types of particle interactions in the COUPP bubble chamber: (A) cosmic ray event, (B) neutron multiple-scatter event, and (C) neutron single-scatter event. From [10]. 26
1.15 The annual modulation signal observed in the DAMA/NaI and DAMA/LIBRA experiments. These plots show the residual rates for low energy single-scatter events in the 2-4, 2-5, and 2-5 keV energy intervals. The time scale begins on January 1st and the solid lines correspond to cosine functional with a period of one year and phase of 152.5 days. From [11]. 28

2.1 Photo of a CDMS-II Z-sensitive Ionization and Phonon (ZIP) detectors with the phonon side showing. Each detector is 3 inch in diameter and 1 cm thick. A single germanium (silicon) detector has a mass of ∼250 g (∼100 g). 30
2.2 Schematic of the CDMS-II ZIP detector configuration with 4 phonon sensors on the "top" face and 2 ionization electrodes on the "bottom" face. 31
2.3 Illustration of the aluminum metal grid covering the detector's ionization and phonon face. 31
2.4 Cartoon of a Quasiparticle-assisted Electrothermal-feedback Transition-edge sensor (QET) showing the quasiparticle production and diffusion. Phonons break Cooper pairs in aluminum fins creating quasiparticles that diffuse through the aluminum. Quasiparticles that reach the tungsten enter a region with lower bandgap (top diagram), get trapped, and create the phonon signal. 35
2.5 Plot of resistance as a function of temperature for a superconducting Transition-Edge Sensor (TES) showing the bias point and how a small temperature change causes a large change in resistance. 36

2.6 Schematic of the CDMS-II ZIP detector configuration. *Bottom right:* detector ionization face depicting the inner and outer electrodes. *Bottom left:* detector phonon face illustrating the large-scale photolithographic patterning, naming scheme of the four sensor quadrants (A-D), and the x-y reference coordinate system. *Top left:* close-up of one of the 37 "dies" making up each of the phonon sensors. Each die consists of 28 individual Quasiparticle-assisted Electrothermal-feedback Transition-edge sensors (QETs). *Top right:* a single QET consisting of a 1 μm wide by 250 μm long tungsten Transition-Edge Sensor (TES) connected to 8 aluminum collection fins. 37
2.7 Diagram of germanium energy bands and levels. From [12]. 38
2.8 Schematic of the CDMS charge amplifier. From [13]. 39
2.9 Absolute ionization collection of 60 keV photons as a function of applied electric field for 1 cm thick (a) germanium and (b) silicon devices. This shows that full ionization collection is achieved in germanium (silicon) devices by $\sim$200 mV/cm ($<$2 V/cm), well below current operational bias voltages. Additionally (a) shows the agreement between the observed (circles) and predicted (curve) phonon amplitude based on phonon recoil and Luke phonon production. From [12, 14]. 40
2.10 Density plots showing ionization yield as a function of phonon recoil energy. The dashed curves represent the $\pm 2\sigma$ electron recoil (upper) and nuclear recoil (lower) bands as defined by calibration data. (a) Density plot of electron and nuclear recoil events from a ^{252}Cf neutron calibration source. (b) Density plot of electron recoil events from a ^{133}Ba gamma calibration source. After removing the neutron source the nuclear recoil band is clear of any events. This illustrates the ionization yield electron recoil rejection power of $>10^4$. 41
2.11 Cartoon depicting events occurring in the ZIP detector bulk (left) and surface (right). Electron (e^-) and hole (h^+) charge carriers from the bulk event are fully collected while some from the surface event may be lost in the adjacent electrode. The metal at the surface also causes high-frequency phonons (red curve) to quickly decay to low-frequency ballistic phonons (orange curve). From [15]. 42
2.12 Illustration of the geometric effect of the charge carrier cloud which reduces ionization collection near the detector surface. The dashed curve shows how the carrier cloud moves away from the surface with time and the subsequent reduction in the dead layer depth (bottom). From [16]. 43
2.13 This plot shows the same density plot of ionization yield as a function of phonon recoil energy for electron recoil events from a ^{133}Ba gamma calibration source as Figure 2.10b. Additionally this plot shows electron recoil surface events (green points representing single events) that have reduced ionization yield. 44
2.14 Comparison of the leading edges of the primary phonon pulse from 60 keV bulk (blue) and surface (red) electron recoil events. 45

2.15 Raw ionization and phonon pulses illustrating the phonon delay and risetime parameters. Channel A (blue), the largest and fastest phonon pulse, is the primary phonon channel and the channel where the event occurred. The blue vertical dashed lines represent phonon delay, the difference between the ionization and primary phonon pulse start times. The red vertical dashed lines represent phonon risetime, the difference between the 10% and 40% points on the primary phonon pulse rising edge. 46
2.16 Ionization yield as a function of the phonon timing parameter showing the ZIP detector electron recoil discrimination power. Plotted here is calibration data from one of the Soudan germanium detectors. Red dots are bulk electron recoils and black crosses are surface electron recoils from ^{133}Ba calibration data while blue circles are nuclear recoils from ^{252}Cf calibration data. The vertical dashed line indicates the minimum value of the phonon timing parameter allowed for candidate dark matter events and the box shows the approximate signal region combining both ionization yield and phonon timing discrimination. From [17]. 47
2.17 Ionization collection as a function of time for 60 keV ^{241}Am events taken at a test facility. This shows reduced ionization collection after a period of time as the detector becomes "de-neutralized" due to bulk trapping. 48
2.18 Like Figure 2.17 the plot shows ionization collection as a function of time for 60 keV ^{241}Am events taken at a test facility. Neutralization occurred during the periods of time showing no events. Notice how, despite losing full ionization collection prior to neutralization, after neutralization full ionization collection is regained. 49

3.1 Photos of the headframe at the Soudan Underground Mine taken in (a) winter and (b) summer. 51
3.2 Schematic of the CDMS experimental setup at the Soudan site. 52
3.3 Schematic of the active and passive shielding surrounding the icebox at the Soudan site. This drawing shows the refrigerator (right), icebox (middle), and electronics e-stem (left). From closest to the detector volume the icebox is surrounded by a layer of polyethylene, ancient lead, ordinary lead, polyethylene, and finally the active muon veto. From [18]. 53
3.4 Schematic of a tower assembly in the innermost icebox can along with the cold hardware discussed in this section. Note that the icebox shown in this drawing is the one previously used at the Stanford Underground Facility (SUF). The major different between the icebox at the Stanford and Soudan sites is that the Soudan icebox can hold seven Towers and does not have inner lead or polyethylene (not shown) shields. Courtesy of Dennis Seitz. 55
3.5 (a) Photo of a tower. Picture and annotations courtesy of Dennis Seitz. (b) Photo of an assembled "tower" with the tower and detector stack along with the side coaxes connecting the two. 57
3.6 (a) Photo of a side coax. (b) Photo of a SQUET with the separate FET (left) and SQUID (right) cards connected by a copper and kapton "fly-over" cable. Picture and annotations courtesy of Dennis Seitz. 58
3.7 Photo of a stripline. Picture and annotations courtesy of Dennis Seitz. 59

4.1 The inner ionization channel noise spectrum from T3Z5 taken with the cryocooler on (top, solid) and off (bottom, dashed). Notice the improvement in noise performance when the cryocooler is turned off. This was one indication that led to replacing the hard cryocooler couplings with annealed copper braids. From [15]. 66
4.2 Photo of the annealed copper braids forming the flexible coupling between the cryocooler drive head and the E-stem. 66
4.3 600 mK can (a) with oxide (b) and clean after scrubbing. 67
4.4 Photo of the final Soudan 5-tower installation showing the 4K lid. 68
4.5 Screen capture of the LabView SQUID tuning program with results after tuning the SQUID of channel A on T4Z1. The large bottom left window shows the V-Φ modulation curve, while the large top left window represents the SQUID responsivity as a function of lock point. Although this SQUID has a resonance (left side of modulation curve), the SQUID operates far from it (as indicated by the vertical lines in the bottom left window). The numbers on the top right and smaller windows show the results of SQUID checks that ensure proper configuration. For example, this SQUID is tuned to a bandwidth of $\sim$370 kHz. 69
4.6 Screen capture of the LabView TES tuning program with results after tuning T3Z4. The plots in the top row allow the graphical creation of data selection cuts that are then applied to the data before creating the plots in the bottom row. The plots shown here represent a well tuned detector. Notice how the risetime and delay distributions of the four phonon sensors (the two bottom left windows) are balanced with each other. Also notice the middle two plots in the top row. These are the phonon delay ("delay") and partition ("box") plots which provide approximate event position reconstruction. 71
4.7 An example of the bump sometimes seen in the SQUID bandwidth near the roll-off frequency. 72
4.8 An example of how changing the TES bias current affects the noise spectrum for a detector showing large excess noise (the large bump near the roll-off) under specific bias conditions. Notice how increasing the TES bias current decreased the excess noise. This is dramatically seen by comparing the amplitude of the yellow (lowest TES bias current) and green (highest TES bias current) traces near their roll-off frequencies. 73
4.9 An example of a detector's phonon noise spectrum where one of the channels, channel C (green), went superconducting due to its bias point being too close to the superconducting transition. Phonon channels that are biased in their superconducting transition (like the blue, magenta, and yellow traces) have a noise spectrum that is relatively flat at low frequencies and then decreases at a roll-off frequency ($\sim$100 kHz for germanium). The fact that the green trace shows elevated noise and no flat spectrum at low frequencies indicates that the TES is superconducting. 74

4.10 Examples of how the phonon noise spectrum is affected by a 15 mK difference in temperature from (a) T3Z5 channel D and (b) T5Z6 channel B. Notice how, in (a), the blue trace has a slightly lower amplitude and higher roll-off frequency than the magenta trace. This indicates a higher TES resistance caused by to the increased temperature. The same trend can be seen in (b) when comparing the magenta trace with the blue and green traces. 75
4.11 Schematic of the Soudan 5-tower detector orientation in the icebox and towers. The two calibration source tubes are located at the northeast and southwest ends of the icebox. Courtesy of Kyle Sundqvist. 77
4.12 An example of the automatically generated noise spectrum for the inner ionization channel of T3Z5. The two traces shown here are from two different runs to give an illustration of what would generate a warning message based on this technique. 79
4.13 An example of the real time diagnostic plots showing (a) phonon and ionization channel and (b) trigger information. These graphical interfaces allow quick checks on detector performance. For example, by looking at the plots in (a) one can identify phonon and ionization channels that are not working properly. The bottom panel in (b) shows trigger rate as a function of time and illustrates rate changes that could cause an adjustment to a detector's trigger threshold (Section 4.6.3). 80
4.14 An example of the PipeDisplay webpage showing raw traces for each detector and veto panel. 84

5.1 (a) Delay plot for T3Z2 highlighting neutrons (green) and low-yield events (black, with blue and red indicating phonon and ionization face selections). (b) Phonon partition plot for T3Z2 illustrating the bad detector region at the right. Black points show inner ionization electrode events, blue outer ionization electrode events, and magenta events shared between the two electrodes. The right half of this detector is excluded from the WIMP search analysis. 93
5.2 Phonon delay (left) and partition plot (right) for T5Z1 illustrating the distortion in channel D (top right). 94
5.3 Both of these plots show ionization yield as a function of time for T2Z5 during the Run 119 data set with the candidate event that exhibited poor neutralization. (a) Shows WIMP search data only. The blue crosses are single events, black crosses are 7-10 keV events passing all cuts except phonon timing, the red cross is an event above the phonon analysis threshold passing all cuts except phonon timing, and the red cross with a circle around it is the candidate event. From [19]. (b) Shows WIMP search data (black) along with barium data (green) for comparison with well neutralized data as a function of time. 96
5.4 Illustrations of the neutralization stability analyses using the fraction of low yield events. In both of these plots points in red are tagged as poorly neutralized and the horizontal dashed magenta line is the mean fraction of low yield events. (a) This plot shows the fraction of low yield events computed for each Run 123 and 124 barium data set as a function of time. (b) Plotted here is the fraction of low yield events for a single barium data set in 100,000 event bins. From [20]. 97

5.5 Plots showing the results of applying the "Run 119" neutralization cut to the T2Z5 data. Red points are tagged as being poorly neutralized. The candidate event was in the red data set in the middle of June. (a) Like Figure 5.4a, this plot shows the fraction of low yield events computed for each Run 119 WIMP search data set as a function of time. (b) Plotted here is another way of looking at the same data. This shows the probability of a data set having the observed number of low yield events based on the expected number. 98
5.6 Plots comparing the different methods of looking at data from the neutralization analysis. In all of the plots the red points were tagged as poorly neutralized based on the method used in the Run 123 and 124 neutralization cut. (a) Like Figures 5.4a and 5.5a, this plot shows the fraction of low yield events computed for each WIMP search data set as a function of time. (b) Like Figure 5.5b, this is another way of looking at the same data. This shows the probability of a data set having the observed number of low yield events based on the expected number. (c) A histogram of the fraction of low yield events for all of the WIMP search data sets. This does not take statistical variations into account. 100
5.7 An energy deposition histogram of 1 million Run 123 events for one of the top veto panels along with the cut position. The dashed green vertical line is the 50 pC mark were the threshold was previously set for an old version of this cut and the red dashed is were it is now set for the Run 123 analysis. From [21]. . 102
5.8 (a) T1Z2's noise blob in phonon and ionization energy from the random triggered events in the Run 123 data along with the gaussian fit to the Q_{inner} noise blob that was used in the ionization threshold cut. From [22]. (b) The ionization energy resolution for Tower 1 as a function of time during Run 123. From [23]. 103
5.9 The mean of the phonon energy noise blob for Tower 1 as a function of time during Run 123. Note how the mean varies with time, especially for Z4. This caused many single-scatter events to appear as multiple-scatters during periods of high noise in the initial singles cut. From [23]. 105
5.10 A slice of the phonon position manifold, phonon partition radius vs. delay radius, for T1Z5. The colors indicate values of the primary phonon risetime value. The star is a timing outlier event and the black circles show this event's nearest neighbors used during the position correction. This illustrates an example of mixing high (red and yellow) and low (blue) radius events during correction. From [24]. 107
5.11 Both of these plots show ionization yield as a function of phonon recoil along with the calculated electron (red) and nuclear (blue) recoil bands for the germanium detector T1Z5. The dashed points represent the center of the electron and nuclear recoil bands while the solid lines denote the 2σ bands. (a) Black points are events from ^{133}Ba gamma calibration data sets. (b) Black points are events from ^{252}Cf neutron calibration data sets. From [25]. 108

5.12 Phonon delay as a function of risetime for T1Z5 neutron (green) and surface (red) events. The acceptance region for bulk nuclear recoil events is defined to the upper right of the blue dashed line and between the black dashed lines. Surface events that pass the timing cut are represented by the circled red dots. From [26]. 109
5.13 The efficiency of the R123 and 124 (a) germanium and (b) silicon WIMP search analysis as a function of phonon recoil energy. Curves represent the total efficiency after the subset of cuts described in the caption were applied to the data. From [17] and [27]. 110
5.14 Ionization yield as a function of phonon recoil energy for the Run 123 and 124 germanium WIMP search data. These plots focus on the nuclear recoil band region. Events in the top plot pass all cuts except ionization yield and phonon timing while events in the bottom plot include all cuts. From [17]. 114
5.15 90% confidence level upper limits on the spin-independent WIMP-nucleon scattering cross section as a function of WIMP mass for CDMS-II germanium (black) and silicon (gray) data showing the results of the Soudan 2-tower reanalysis (dot-dash), the 5-tower analysis (dash), and the combination of the two (solid). Courtesy of Jeff Filippini, from [28]. 115
5.16 Like Figure 5.15, this shows the 90% confidence level upper limits on the spin-independent WIMP-nucleon scattering cross section as a function of WIMP mass. The curves represent the results from the combined CDMS Soudan data (solid black, germanium, and gray, silicon), XENON10 (red dashes, red dots indicate the effect of the newest scintillation yield measurements on the XENON10 result), ZEPLIN III (magenta crosses), WARP (green triangles), and EDELWEISS (blue squares) while the shadded regions indicate parameter ranges expected from the DAMA/LIBRA modulation result and supersymmetric models. Courtesy of Jeff Filippini, from [28]. 116
5.17 90% confidence level upper limits on the spin-dependent (a) WIMP-neutron and (b) WIMP-proton scattering cross section as functions of WIMP mass. The curves represent the results from the combined CDMS Soudan data (solid black, germanium, and gray, silicon), XENON10 (red dashes), Super-Kamiokande (blue triangles), KIMS (green crosses), and COUPP (blue circles) while the shadded regions indicate parameter ranges expected from the DAMA/LIBRA modulation result and supersymmetric models. Courtesy of Jeff Filippini, from [28]. 117

6.1 Close-up photo of LED mounted in CDMS ZIP detector housing. Picture and annotations courtesy of Dennis Seitz. 119
6.2 Plot showing a figure-of-merit of good neutralization (fraction of low yield events) for Ge Boule B detector Z28 (T5Z4) for barium calibration data sets taken at the beginning of Run 128. Each point represents a single data set and the vertical blue lines represent when strong source neutralization occurred. Note how the fraction of low yield events is high (indicates poor neutralization) after each strong source bake and then becomes low (indicates good neutralization) due to LED neutralization. 121

6.3 Oscilloscope trace showing voltage as a function of time for a charge pulse due to a LED flash (black) and the FEB front panel voltage monitor trace showing the voltage through the LED (red). 123
6.4 Histograms of charge (a) and ionization yield (c) and 2-D scatter plots of charge (b) and ionization yield (d) as a function of detector y-position comparing the neutralization states of two barium calibration data sets, one (blue) taken prior to any neutralization and the other (red) after an initial LED bake. 125
6.5 2-D scatter plots of ionization yield defined using only q-outer energy vs. ionization yield defined using only q-inner energy. (a) The black events make up the event population known as the "funnel" and the blue events to the left of the red (q-outer events) make up the event population known as the "ear". (b) Compares the neutralization states of two barium calibration data sets, one (blue) taken prior to any neutralization and the other (red) after an initial LED bake. Notice how the "funnel" and "ear" event populations shift between the blue and red data sets. 126
6.6 Like Figure 6.2, these plots show the fraction of low yield events as a function of time. These plots are for Si detector Z15 (T3Z3) barium calibration data sets taken at the beginning of Run 127. Each point represents a single data set and the vertical blue lines represent when LED neutralization occurred. (a) uses the fraction of low yield event definition of 0 <ionization yield <0.8. (b) uses the fraction of low yield event definition of 0 <ionization yield <0.2. Note how the fraction of low yield events decreases after fewer LED bakes using the low yield definition in (b). While this does not indicate good neutralization, it shows that the LED neutralization is beginning to work and affect the detector's ionization collection. 128
6.7 Like Figure 6.2, this plot shows the fraction of low yield events as a function of time. This plot is for Ge detector Z28 (T5Z4) barium calibration data sets taken throughout the Soudan 5-tower Runs 123 through 128. Each point represents a single data set and the vertical blue lines represent the division between each of the runs. Despite a few outlier data sets, the fraction of low yield events, and neutralization, remained fairly constant throughout. 129
6.8 Like Figure 6.2, this plot shows the fraction of low yield events as a function of time. This plot is for Si detector Z13 (T3Z1). Each point is a single data set and the vertical blue lines represent times strong source neutralization occurred. Notice that the fraction of low yield events was very high during the fifth data set. This correlates with a change in T3Z1 phonon channel A state. 130
6.9 Like Figure 6.2, this plot shows the fraction of low yield events as a function of time. This plot is for Ge detector Z26 (T5Z2). Each point is a single data set and the vertical blue lines represent times strong source neutralization occurred. Notice that the fraction of low yield events suddenly decreased after the sixth data set. This correlates with a change in T5Z2 charge bias. 131

6.10 Like Figure 6.2, this plot shows the fraction of low yield events as a function of time. This plot is for Ge detector Z28 (T5Z4). Each point is a single data set. Notice that the fraction of low yield events was very high in May and again in August. The high fraction of low yield events in May was due to bad neutralization at the beginning of the run, prior to any LED or strong source bakes, while in August was due to zero charge events caused by helium films. . 132
6.11 Like Figure 6.2, this plot shows the fraction of low yield events as a function of time. This plot is for Ge detector Z23 (T4Z5) barium calibration data sets taken during the LED tests at the beginning of Run 127. Each point represents a single data set and the vertical blue lines represent when LED neutralization (using T4Z5 LED) occurred. Note how the fraction of low yield events began dramatically decreasing, showing effective neutralization, after the third LED bake. 133
6.12 Like Figure 6.2, these plots show the fraction of low yield events as a function of time. (a) This plot is for Ge detector Z22 (T4Z4) barium calibration data sets taken during the LED tests at the beginning of Run 127. (b) This plot is for Ge detector Z24 (T4Z6) barium calibration data sets taken during the LED tests at the beginning of Run 127. Each point represents a single data set and the vertical blue lines represent when LED neutralization (using T4Z5 LED) occurred. Note how the fraction of low yield events began dramatically decreasing, showing effective neutralization, after the third LED bake for Z22 (T4Z4, adjacent to Z23's LED) but not Z24 (T4Z6, opposite from Z23's LED). 135
6.13 Diagram showing the possible LED reflection pattern allowing for neutralization of both the detector it is mounted on as well as the adjacent detector. Courtesy of Dennis Seitz. 136
6.14 Like Figure 6.2, this plot shows the fraction of low yield events as a function of time. This plot is for Si detector Z15 (T3Z3) barium calibration data sets taken at the beginning of Run 128. Each point represents a single data set and the vertical blue lines represent when strong source neutralization occurred. Note how the fraction of low yield events did not indicate good neutralization after the first strong source bake that occurred during the cooldown. 136
6.15 (a) Plot of several weeks of Run 123 WIMP search data ionization yield as a function time from the beginning of the data set for Z28 (T5Z5). The black points are individual events and the red points show the ionization yield mean and one standard deviation error bars for 1 hr time bins. Note how the ionization yield is stable with time. From [29]. (b) Plot showing the fraction of low yield events for Ge detector Z20 (T4Z2) for 2 months of Run 127 WIMP search data. Each point represents a 1 hr time bin measured from the beginning of the data set. Note how the fraction of low yield events remains stable with time. . . . 139
6.16 Plot showing the fraction of low yield events for Ge detector Z28 (T5Z4) for a long Run 127 barium calibration data set. Each point represents a 100,000 event bin. Note how the fraction of low yield events remains stable throughout the entire data set. 140

6.17 (a) Prediction for the concentration of ionized impurities as a function of temperature. (b) Prediction for partial charge collection as a function of temperature. From [30]. 142
6.18 Like Figure 6.2, these plots show the fraction of low yield events as a function of time. Plots for Ge detector Z14 (T3Z2) (a) and Si detector Z15 (T3Z3) (b) barium calibration data sets taken at the beginning of Run 124, 126, 127, and 129 after cooling down from approximately 10 K, 40 K, 70 K, and room temperature (respectively) and before any neutralization occurred. Each point represents a single data set and the vertical blue lines represent the temperature excursions. Note how, for both the Ge and Si detector, the fraction of low yield events changes the most between points 2 and 4 (after warming to approximately 40 K). Also note how the Si detector loses all ionization collection (seen by a fraction of low yield events equal to 1) while the Ge detector maintains some ionization collection. 144
6.19 Plots of test facility data showing the 60 keV ^{241}Am line ionization collection as a function of time for -3 V charge bias (a) and -0.5 V charge bias (b). Note how the 60 keV events lose full ionization collection after less time for the -0.5 V data than the -3 V data. 146
6.20 Plots of test facility data of p-type G3D showing how the 60 keV ^{241}Am line changes as a function of time in ionization energy (a), total phonon energy (b), and phonon recoil energy (c). The primary charge carrier for events from sources over phonon sensors A (cyan) and C (magenta) were electrons while the primary charge carrier for events from sources over phonon sensors B (blue) and D (green) were holes. 150
6.21 Similar to Figure 6.20, except for n-type G28B, showing ionization energy (a), total phonon energy (b), and phonon recoil energy (c). Unlike Figure 6.20, the primary charge carrier for events from sources over phonon sensors A (cyan) and C (magenta) were holes while the primary charge carrier for events from sources over phonon sensors B (blue) and D (green) were electrons. 151
6.22 Semiconductor band gap diagram for Schottky contacts between metal and a n-type crystal (left) and a p-type crystal (right). Notice how the band gap bends, near the metal-semiconductor interface, in different directions for n-type and p-type materials. This "band bending" creates a depletion zone near the contact for electrons (n-type) or holes (p-type). For CDMS detectors this could mean electrons get "trapped" at the contact in n-type crystals while holes get "trapped" at the contact in p-type crystals. From [31]. 152
6.23 Plots of test facility data of n-type G2E showing how the 60 keV ^{241}Am line changes as a function of time in ionization energy (a), total phonon energy (b), and phonon recoil energy (c). The primary charge carrier for events from sources over phonon sensors A (cyan) and C (magenta) were holes while the primary charge carrier for events from sources over phonon sensors B (blue) and D (green) were electrons. 153

6.24 Similar to Figure 6.23, this shows n-type G2E ionization energy (a), total phonon energy (b), and phonon recoil energy (c). Unlike Figure 6.23, the primary charge carrier for events from sources over phonon sensors A (cyan) and C (magenta) were electrons while the primary charge carrier for events from sources over phonon sensors B (blue) and D (green) were holes. 154
6.25 Plots of test facility data of p-type G3D showing how the 60 keV ^{241}Am line changes as a function of time in ionization energy (a), total phonon energy (b), and phonon recoil energy (c). The primary charge carrier for events from sources over phonon sensors A (cyan) and C (magenta) were electrons while the primary charge carrier for events from sources over phonon sensors B (blue) and D (green) were holes. 155
6.26 Similar to Figure 6.25, this shows p-type G3D ionization energy (a), total phonon energy (b), and phonon recoil energy (c). Unlike Figure 6.25, the primary charge carrier for events from sources over phonon sensors A (cyan) and C (magenta) were holes while the primary charge carrier for events from sources over phonon sensors B (blue) and D (green) were electrons. 156
6.27 Plots of test facility data showing delay plot blobs forming voids with no events at the end of long data sets which had no explicit neutralization or grounding and where holes were the dominant charge carriers. (Note that the primary charge carrier for events from sources over phonon sensors A, B, and C were holes while the primary charge carrier for events from sources over phonon sensors B and D were electrons.) (a) Delay plot blobs at the beginning of the run. (b) Delay plot blobs at the end of the run. 158
6.28 Plots of test facility data of p-type G3D showing how the 60 keV ^{241}Am line changes as a function of time in ionization energy (a), total phonon energy (b), and phonon recoil energy (c) overnight. The primary charge carrier for all events were holes. (Events from the source over phonon channel A are cyan, channel B are blue, channel C are magenta, and channel D are green) 159
6.29 Similar to Figure 6.28, this shows p-type G3D ionization energy (a), total phonon energy (b), and phonon recoil energy (c) overnight. Unlike Figure 6.28, the primary charge carrier for all events were electrons. (Events from the source over phonon channel A are cyan, channel B are blue, channel C are magenta, and channel D are green) 160

7.1 Calculated electric field distribution for the interleaved ZIP electrode configuration. (a) 2-dimensional cross-section. From [32]. (b) 3-dimensional view. Courtesy of B. Cabrera. 163
7.2 Schematic of the interleaved ZIP detector. 164
7.3 (a) Design layout for one of the phonon channels. (b) Close-up of one of the 1246 QETs that make up one of the phonon sensors. Eight Al collection fins are connected to the 1 μm wide W TES. 165

7.4 (a) Ionization signal from the ionization electrode on the top detector face (Q_{top}) plotted again the electrode on the bottom detector face (Q_{bottom}) for data with internal ^{241}Am sources and no analysis cuts. Bulk events lie along the line down the middle of the plot with equal charge collection in both electrodes while surface events lie along the edges of this plot having ionization collection in only one of the two electrodes. (b) Histogram of a depth dependent position parameter based on ionization collection (the difference between the energy in Q_{top} and Q_{bottom} normalized by the sum of the two) for 60 keV events in (a). Surface events on the top detector face occur at 1 and on the bottom detector face occur at -1. Bulk events lie in the peak around 0. 166
7.5 Plots showing ionization energy as a function of phonon recoil energy for bulk events from (a) a ^{60}Co calibration source producing only gamma events and (b) a ^{252}Cf calibration source producing both electron and nuclear recoil events. Red nuclear recoil events are clearly identified in the band with reduced ionization collection. From [32]. 167
7.6 Histogram of the uncalibrated phonon energy collected in one of the four phonon sensors, sensor BC, of 60 keV surface events (as selected based on ionization energy), divided into events occurring near the top (magenta) or bottom (cyan) surface. The bimodal nature of these distributions can be understood to come from events occurring near the phonon sensor plotted (higher peak) versus those off sensor. In addition, since there were two collimated internal sources, one on sensor BC and one off sensor, the events in these peaks can be correlated with which source they came from. An interesting feature is that the higher energy peak of the top events does not match the top peak of the bottom events, indicating that the depth of the interaction in the crystal affects the phonon collection. 168
7.7 Plots showing ionization yield as a function of phonon recoil energy for calibration data on a Ge ZIP detector using an external ^{252}Cf and internal ^{109}Cd source. The ^{109}Cd source produces many β events which probe the detector surface layer creating the event population with low ionization yield between the upper electron recoil and lower nuclear recoil bands. (a) ^{109}Cd source (and surface events) on the ionization side (b) ^{109}Cd source (and surface events) on the phonon side. 169
7.8 Plot showing the fraction of low yield events for 14 keV x-rays from ^{241}Am sources on the ionization detector face (blue) and the phonon detector face (red) for negative and positive 1.5 V/cm electric fields. Notice how the discrepancy in the fraction of low yield events between ionization and phonon side events for negative electric field disappears under positive electric field. 172
7.9 Plot showing the calculated dead layer for the 1 inch germanium detector G3D (no hydrogen added to the amorphous silicon on either detector face) as a function of charge bias. The detector side the ^{241}Am source was located on corresponds to the side the events occur on. Source A (cyan) and C (magenta) were located on the ionization side while B (blue) and D (green) were located on the phonon side. 174

7.10 This is the same type of plot as Figure 7.9, only for the 1 inch germanium detector G2E (hydrogen added to the amorphous silicon on the ionization side detector face). Unlike Figure 7.9, source B (blue) and D (green) were located on the ionization side while A (cyan) and C (magenta) were located on the phonon side. 175
7.11 This is the same type of plot as Figure 7.9, only for the 1 cm germanium detector G28B (hydrogen added to the amorphous silicon on the phonon side detector face). Figure 7.9, source B (blue) and D (green) were located on the ionization side while A (cyan) and C (magenta) were located on the phonon side. 175
7.12 This is the same type of plot as Figure 7.9, showing the calculated dead layer as a function of electric field. This plot compares all three germanium detectors and demonstrates how G3D (no hydrogen in the amorphous silicon layer on either detector face) has the smallest dead layer for a given charge bias. To see how hydrogenating the ionization side (from 0% to 20%) amorphous silicon layer affects the detector dead layer, compare the charge side of G2E (red square) with G3D (black circle and blue open star) and compare the phonon side of G2E (magenta triangle) with G3D (cyan triangle). To see how hydrogenating the phonon side (from 0% to 8%) amorphous silicon layer affects the detector dead layer, compare the charge side of G28B (green diamond) with G3D (black circle and blue open star) and compare the phonon side of G28B (yellow triangle) with G3D (cyan triangle). To see how ion implantation affects the detector dead layer, compare G3D's non-implanted charge side (black circle and blue open star) with G3D's implanted charge side (black circle and blue closed star). To see how the applied electric field (charge bias) affects the detector dead layer, compare multiple biases of a single detector and single source side. The dead layer is inversely proportional to the applied electric field, to a certain point, and is then fairly independent of field. 176
7.13 This is the same plot as Figure 7.12, except that it has a smaller y-axis ranges. 177
7.14 (a) Plot showing a simulation of the iron ion concentration as a function of depth into the amorphous silicon and germanium substrate. (b) Plot showing a simulated distribution of dislocations created by a single iron ion. From [33]. 180
7.15 The internal collimated ^{241}Am source configuration for G3D during two test facility runs. (a) All sources were on the detector's ionization side. Two sources were over the detector half that had been iron ion implanted and two were over the control half. (b) Two sources were on the detector's ionization side and two on the phonon side. One source on each detector side was over the detector half that had been iron ion implanted and the other over the control half. . . 181
7.16 Plot showing the calculated dead layer for the 1 inch germanium detector G3D (no hydrogen added to the amorphous silicon on either detector face) as a function of charge bias. The detector side the ^{241}Am source was located on corresponds to the side the events occur on, that is, on the ionization side. Sources A (blue circle) and B (blue star) were located on the half with no iron ion implantation while C (black square) and D (black diamond) were located on the half with iron ion implantation. 182

7.17 Plot showing the raw collected ionization energy of 60 keV ^{241}Am events, with 1σ error bars, as a function of applied electric field for the 1 inch silicon detector S06C. Two sources were located on the ionization side (blue) while another two were located on the phonon side(red). 185
7.18 Plots showing the raw collected ionization energy of 60 keV ^{241}Am events, with 1σ error bars, as a function of applied charge bias for the 1 inch germanium detector G3D. (a) and (b) show the same data but have different y-axis ranges. The detector side the ^{241}Am source was located on corresponds to the side the events occur on. All of the sources were located on the ionization side. 186
7.19 Similar to Figure 7.18, except that this is for the 1 inch germanium detector G3D and source A (cyan) and C (magenta) were located on the ionization side while B (blue) and D (green) were located on the phonon side. 187
7.20 Similar to Figure 7.18, except that this is for the 1 inch germanium detector G2E and source B (blue) and D (green) were located on the ionization side while A (cyan) and C (magenta) were located on the phonon side. 188
7.21 Similar to Figure 7.18, except that this is for the 1 cm germanium detector G28B and source B (blue) and D (green) were located on the ionization side while A (cyan) and C (magenta) were located on the phonon side. 189
7.22 Histograms of the ^{241}Am 60 keV ionization energy in the inner charge electrode for 1 inch germanium detector G3D with (a) a -3 V charge bias and (b) a +3 V charge bias. The detector side the ^{241}Am source was located on corresponds to the side the events occur on. Source A (cyan) and C (magenta) were located on the ionization side while B (blue) and D (green) were located on the phonon side. 192
7.23 Similar to Figure 7.22, except for 1 inch germanium detector G2E. Again, (a) a -3 V charge bias and (b) a +3 V charge bias. Unlike Figure 7.22, source B (blue) and D (green) were located on the ionization side while A (cyan) and C (magenta) were located on the phonon side. 193
7.24 Similar to Figure 7.22, except for 1 cm germanium detector G28B. Again, (a) a -3 V charge bias and (b) a +3 V charge bias. Unlike Figure 7.22, source B (blue) and D (green) were located on the ionization side while A (cyan) and C (magenta) were located on the phonon side. 194
7.25 Plots of the ^{241}Am 60 keV ionization energy in the inner charge electrode as a function of time for 1 cm germanium detector G28B with (a) a -6 V charge bias and (b) a +6 V charge bias. 195
7.26 Similar to Figure 7.25, except for (a) a -3 V charge bias and (b) a +3 V charge bias. 196
7.27 Similar to Figure 7.25, except for 1 inch germanium detector G3D. Again, (a) a -6 V charge bias and (b) a +6 V charge bias. 196
7.28 Similar to Figure 7.25, except for 1 inch germanium detector G2E. Again, (a) a -6 V charge bias and (b) a +6 V charge bias. 197
7.29 Plots of the ^{241}Am 60 keV (a) ionization energy in the inner charge electrode, (b) total phonon energy, and (c) phonon recoil energy as a function of time for 1 cm germanium detector G28B with a -6 V charge bias. 198

7.30 Oscilloscope traces of the ionization channel baseline changing when stepping the applied charge bias from ground to (a) -6 V, (b) +6 V, (c) -3 V, and (d) +3 V. 199
7.31 Raw traces of 60 keV pulses from G28B data of phonon channels A, B, C, and D, inner and outer ionization electrodes (from top to bottom) taken with a -6 V applied charge bias. The pulses were taken (a) 3 seconds, (b) 7 seconds, (c) 13 seconds, and (d) 25 seconds after stepping the applied charge bias from ground to -6 V. 200
7.32 (a) Photo of two 1 inch detectors showing both the ionization and phonon detector faces. (b) Photo of a 1 inch detector, with phonon detector face up, after packaging. 204
7.33 (a) Drawing of the mask for the new QET design with the same amount of tungsten and greater aluminum coverage. (b) Photo of a single QET during fabrication. 205
7.34 (a) Schematic showing the new geometry for the four phonon sensors which allows for better radial event position reconstruction. (b) Photo of a 1 inch detector with this new phonon sensor geometry. 205
7.35 (a) Photo of the first SuperTower prior to installation in the Soudan icebox. (b) Photo of the Soudan icebox with three towers of CDMS-II detectors along with the new SuperTower. 206

A.1 Schematic of the LED drive circuit with the current source, stripline, and LED diode. 213
A.2 Schematic of the LED drive equivalent circuit showing the current source, stripline capacitance, and LED diode in parallel. 213
A.3 Illustration of a LED's current vs. voltage curve. The black and red curves represent profiles for different temperatures. As the LED emits photons and warms it changes between these two curves. 215
A.4 Oscilloscope trace showing voltage as a function of time for the FEB front panel voltage monitor trace showing the voltage through the LEDs (blue and red) and the charge pulse due to the LED pulses (yellow and green) for two non-working LEDs. 216
A.5 Oscilloscope trace showing voltage as a function of time for the FEB front panel voltage monitor trace showing the voltage through a LED (red) and the charge pulse due to the LED pulse (black) for a working LED with a pulse that was not sufficiently long to produce photons. 217

G.1 G3D -3 V residuals between the data and gaussian fit of the ^{241}Am 60 keV line. 237
G.2 Dead layer distribution for G3D -3 V charge bias data. This plot shows the partial ionization collection of 60 keV ^{241}Am gamma rays as a function of depth into the Germanium crystal. 238

Preface

This dissertation summarizes the work that I have done during the last six years as a graduate student at Case Western Reserve University. Since the CDMS collaboration is fairly large, made up of over 50 scientists and engineers from over a dozen institutions, all of the work discussed here was not completed by me alone. It takes the collaboration of many people to perform an experiment of this magnitude. To properly explain the experiment, and provide context for my focus, this dissertation describes not only my work, but also the contributions of many others. Here, in this preface, I outline how I spent the last six years, including some of the "service" tasks that didn't make it into the following story line but have taught me about the realities of experimental physics.

Case Western was one of two detector testing facilities during CDMS-II. When I joined the group individual detector testing for the final 3 towers (of CDMS-II) to be installed at the Soudan Underground Laboratory had finished. Rather than beginning with individual detector testing I jumped right into the "tower testing." My first experiences with a dilution refrigerator and CDMS detectors were while verifying the performance of Tower 3 and Tower 4 prior to their shipment to the Soudan site. During this testing I learned how the detectors work, techniques for tuning the SQUIDs and phonon channels, basic detector performance tests (such as characterizing the phonon channel superconducting transition temperatures and taking noise traces), how to take data, and quite a bit about what affects noise is a

low-noise environment.

Following the tower testing I studied individual R&D detector performance that influenced (and will yet affect) SuperCDMS detector designs. The first R&D detector that I evaluated was one of the two original interleaved ZIPs (iZIPs, see Section 7.2). While the particular iZIP that I studied was not fully functioning (only one out of the four phonon channels worked), I completed some of my first analysis projects using that data. Following the iZIP I began to test the new 1 inch detectors and focus on ionization collection in CDMS crystals. Using 1 inch silicon and germanium detectors I studied whether hydrogenating the amorphous silicon blocking layer improved the ionization yield discrimination of surface events (Section 7.3.1) and how iron ion implantation affects surface event rejection (Section 7.3.2).

During these tests my interest in detector neutralization increased. When studying poor ionization collection it is necessary to begin with good collection and therefore good neutralization. This was one of the motives for me to find a quantitative figure-of-merit to determine what "good" neutralization is (Section 6.3.3). In addition to determining when and how detectors achieve good neutralization (Chapter 6), I became interested in the physics behind neutralization (Sections 2.6.2 and 6.8) and what affects it (Section 6.6). I have worked closely with Kyle Sundqvist on neutralization and charge collection. I usually took a more empirical approach while Kyle created charge transport models and simulations.

At the test facility I was also involved in assisting with troubleshooting why the phonon sensors in the Soudan detectors were not superconducting during the first attempts at cooling down the 5-towers (Section 4.3). In order to determine if vibrations from the newly installed cryocooler could heat the phonon channels, we performed "thump tests" on our dilution refrigerator where we monitored the phonon channel resistance (to determine if they were superconducting) as we physically vibrated the cryostat (with a rubber mallet). Based on these tests the hard couplings between the cryocooler drive head and the E-stem were replaced with annealed copper braids to

minimize the vibrations reaching the detectors.

Besides my work at the Case Western test facility I took "shifts" on-site at the Soudan lab. At Soudan I participated with the cryogenic activities, 5-tower commissioning, and daily operational tasks. During my Soudan shifts I learned much about experimental physics. My first shift at the mine was in February 2005 (I remember this because it was the first of three consecutive Valentine's days that I spent in northern Minnesota!) when we were supposed to be cooling the 5-towers for the first time. However, during that trip we discovered that the primary impedance was blocked. Along with the "standard" cryogenic and operational activities, I participated in verifying the cryostat performance following the blockage removal, scrubbing the tower ears and icebox cans to remove oxidation and allow sufficient thermal conductivity to cool the detectors, and tuning the 120 SQUID and phonon channels.

My data analysis contributions ranged from studying R&D detectors to the Soudan 5-tower data. I already mentioned some of my test facility detector analysis. During the 5-tower data analysis I created the blinding cut to mask the WIMP search signal region (Section 5.2.2) and part of the neutralization cut (Section 5.3.5). In addition, I helped with many of the data quality studies and cuts.

Acknowledgements

Let me start by saying thank you to all of my family, friends, and colleagues. I cannot list everyone who has supported, encouraged, and helped me along my journey. Please accept my apologies for not mentioning everyone.

Next I would like to acknowledge everyone in the CDMS collaboration. I have been fortunate to work with such a great group of people, many of whom I have become great friends with. You have made my graduate experience a very special time and taught me so much. I will miss working with you all.

Dan Akerib, my thesis advisor, has provided me with support and encouragement from the time I stepped into the Rockefeller physics building at Case Western. From the time that I started working with him he seemed to know my strengths and helped me grow into the scientist I am today. Dan, I especially appreciate your confidence in me and your help in increasing my confidence in myself. Thank you for building my scientific speaking and writing skills. Finally, I think one of the things that truly helped me enjoy my graduate experience is your understanding that, hard as it is to believe, we have a life outside physics too.

As in most academic groups, our group at Case Western has changed during my time here, but it has always been a great source of support, growth, and fun! While I may not have taken advantage of this enough, Richard Schnee was always ready to help and guide me through any of my analysis questions. Mike Dragowsky and Adam Sirois taught me how to use the dilution refrigerator and CDMS detectors. We

had many fun afternoons in the shroud! I have had fun working and growing with all of my fellow CWRU lab mates – Laura Boon, Ken Clark, Meredith Danowski, Darren Grant, Raul Hennings-Yeomans, Ben Kreis, Patrick Phelps, Kristin Poinar, Ryan Sacks. Matt Whilden and Alex Hojem helped take over test facility operations from me during the last two years.

I am grateful to have gotten the chance to work closely with my Berkeley test facility colleagues. Nader Mirabolfathi for organizing the detector testing schedule and keeping our interests in mind. Bruno Serfass for helping with my data processing needs. Dennis Seitz for guiding me through the CDMS electronics and always helping me troubleshoot fridge, detector, and noise problems. Jeff Filippini for always taking my calls and answering my analysis and general science questions. Kyle Sundqvist for providing me with the focus for my dissertation and always helping me understand charge collection theory. I remember getting a call from you asking me if our fridge was cold and if I could look at some LED traces. That seemed to be when I started serious studies of detector neutralization and charge collection.

Jim Beaty, you make Soudan a great place to work, not only in the mine but enjoying the beauty of northern Minnesota. I greatly enjoyed hiking around Ely and canoeing through the Boundary Waters. Thanks for being there for all of us. Dan Bauer is someone else who gave me constant support and encouragement. Thanks for seeing my strengths. The project is lucky to have such a great project manager. Jodi Cooley-Sekula, its been a pleasure working with a fellow cheese-head. Matt Pyle, you always could answer my detector questions. Wolfgang Rau, thanks for helping me understand my data and connect it to physical phenomena.

I would like to thank all of my friends, especially Jeremy Heilman for helping me through grad school and adding some comedy in the lab, Tim Peshek and Sean Bryan for introducing me to intramural softball, and Ross Burton for our many lunch time conversations and for helping me maintain my sanity.

My family, especially my parents, have always supported and encouraged me

to pursue my dreams. Finally, but definitely not least, to Nick, for your constant understanding, support, encouragement, and love. I am grateful to have been on this journey with you beside me and I look forward to discovering where life takes us, together, from here.

The Cryogenic Dark Matter Search:

First 5-Tower Data and Improved Understanding of Ionization Collection

Abstract

by

CATHERINE NOEL BAILEY

The Cryogenic Dark Matter Search (CDMS) is searching for Weakly Interacting Massive Particles (WIMPs) with cryogenic particle detectors. These detectors have the ability to discriminate between nuclear recoil candidate and electron recoil background events by collecting both phonon and ionization energy from recoils in the detector crystals. The CDMS-II experiment has completed analysis of the first data runs with 30 semiconductor detectors at the Soudan Underground Laboratory, resulting in a world leading WIMP-nucleon spin-independent cross section limit for WIMP masses above $44\,\mathrm{GeV/c^2}$.

As CDMS aims to achieve greater WIMP sensitivity, it is necessary to increase the detector mass and discrimination between signal and background events. Incomplete ionization collection results in the largest background in the CDMS detectors as this causes electron recoil background interactions to appear as false candidate events. Two primary causes of incomplete ionization collection are surface and bulk trapping.

Recent work has been focused on reducing surface trapping through the modification of fabrication methods for future detectors. Analyzing data taken with test devices has shown that hydrogen passivation of the amorphous silicon blocking layer worsens surface trapping. Additional data has shown that the iron-ion implantation used to lower the critical temperature of the tungsten transition-edge sensors causes a degradation of the ionization collection. Using selective implantation on future detectors may improve ionization collection for events near the phonon side detector surface.

Bulk trapping is minimized by neutralizing ionized lattice impurities. Detector investigations at testing facilities and in situ at the experimental site have provided methods to optimize the neutralization process and monitor running conditions to maintain full ionization collection.

This work details my contribution to the 5-tower data taking, monitoring, and analysis effort as well as the SuperCDMS detector development with the focus on monitoring and improving ionization collection in the detectors.

Chapter 1

Dark Matter and Detection

1.1 Introduction

Natural human curiosity leads us to understand the world around us. Since the ancient Babylonians and Greeks, humans have studied the heavens to develop a cosmological model explaining how the universe works. From Ptolemy's earth centered and Copernicus' heliocentric model to Einstein's cosmological constant, human nature has pushed us to discover the origins, evolution, and make-up of the universe. During the last several decades experimental and observational evidence has increased our knowledge of the universe allowing the formation of the cosmological concordance model.

The current cosmological picture, called ΛCDM [7, 34, 35], has formed from the convergence of many independent investigations. According to this model the universe is expanding, has a spatially flat geometry, and consists of three types of matter: normal baryonic matter, dark matter, and dark energy (Figure 1.1). Normal baryonic matter makes up less than 5% of the universe's total energy density while dark matter and dark energy dominate. Dark, or vacuum, energy is a repulsive force that constitutes approximately 72% of the total energy density. The final 23% of the universe's energy density is made up of dark matter. What little is known about dark mat-

ter has been learned from its gravitational effects on baryonic matter (Section 1.2). While this prevailing cosmological model accepts the dark matter hypothesis, there is a class of alternative hypotheses (MOND [36] extensions to it, such as TeVeS [37]) which try to explain the astrophysical observations by modifying gravity on large scales. The discussion here will focus on particle dark matter and assume Newtonian gravity holds on all scales.

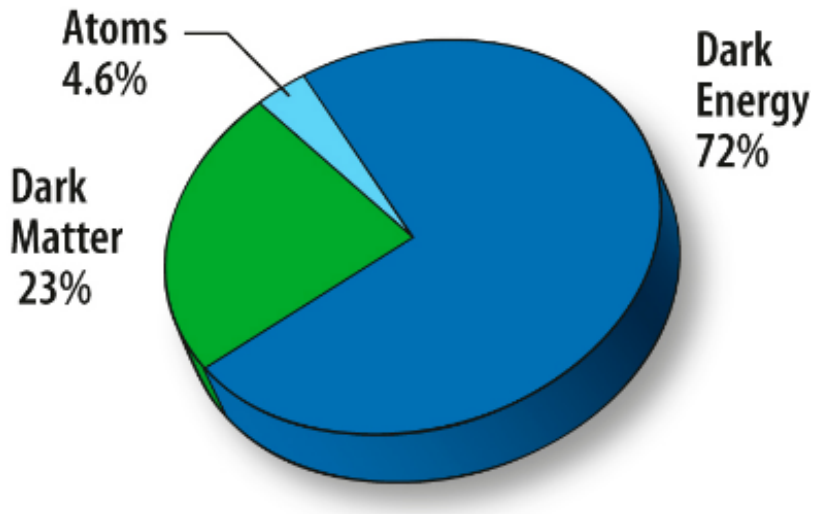

Figure 1.1: Pie chart representing the present composition of the universe, as inferred from current cosmological measurements. Courtesy of NASA / WMAP Science Team.

Since this dissertation describes a search for dark matter, this chapter discusses experimental evidence, leading particle candidates, and methods of detection.

1.2 Evidence for Dark Matter

Evidence for the existence of dark matter comes from many different and independent observations. Dark matter was first proposed in the 1930s as a solution to explain why galaxies in the Coma cluster were observed to move faster than expected [38, 39]. Since then evidence of dark matter's gravitational effects on individual galaxies, galaxy clusters, and large scale structure has combined to describe the amount ($\sim$23% total energy density of the universe), properties (non-baryonic and non-relativistic),

and distribution (halos around galaxies and clusters) of dark matter. This section reviews the evidence for dark matter.

1.2.1 Galaxies

Spiral Galaxy Rotation Curves

Some of the clearest, and most intuitive, evidence for the existence of dark matter comes from studying the rotational dynamics of spiral galaxies. Spiral galaxies, such as our own Milky Way Galaxy, have a central bulge surrounded by a rotating disk of stars and gas. Assuming circular orbits for stars and gas in the disk, Newtonian dynamics can be used to predict their rotational velocity. By equating the gravitational and centripetal forces:

$$F = \frac{GmM}{r^2} = \frac{mv^2}{r} \tag{1.1}$$

the velocity, as a function of radius, can be calculated:

$$v(r) = \sqrt{\frac{GM}{r}} \tag{1.2}$$

where G is the gravitational constant, m is the mass of the star or gas, v is the velocity of the star or gas, r is the radius (from the center of the galaxy) of the star or gas, and M is the total mass of the galaxy contained by an orbit of radius r. Therefore, if light traces the galaxy's matter distribution, velocities should decrease with radius as $\bar{\mathrm{r}}^{1/2}$.

Experimentally measuring the rotational velocities of stars and gas as a function of radius from the galactic center and comparing these measurements with the expectations discussed above shows that there is more matter in spiral galaxies than expected. Observations show flat velocity distributions out to large radii (Figure 1.2), [40, 1]. This is consistent with the visible spiral galaxy embedded in a large spherically-symmetric "dark matter halo."

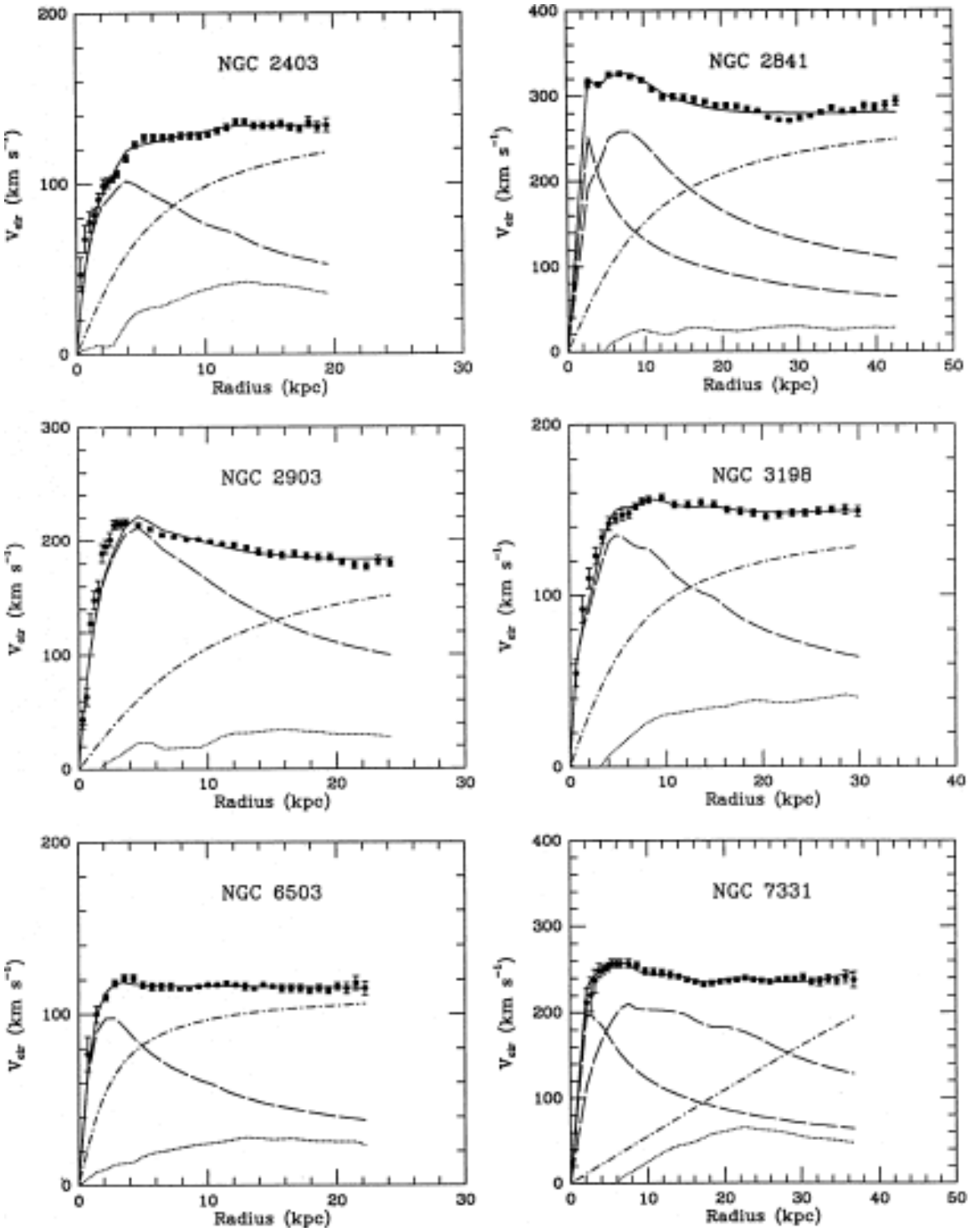

Figure 1.2: Rotation curves of 6 spiral galaxies. The dotted, dashed, and dash-dotted lines are the contributions of gas, galaxy disk, and dark matter. From [1].

Elliptical and Dwarf Galaxies

Elliptical and dwarf galaxies have more complicated structures than spiral galaxies. However the mass of elliptical and dwarf galaxies can be estimated through an analysis similar to what is used with spiral galaxies. In a gravitationally-relaxed system, one can use the virial theorem:

$$2 < T >= - < V > \tag{1.3}$$

to calculate the relationship between the velocity dispersion and mass:

$$< v^2 > \sim GM < \frac{1}{r} > \tag{1.4}$$

where T is the kinetic energy, V is the potential energy, G is the gravitational constant, v is the velocity of the star or gas, r is the radius (from the center of the galaxy) of the star or gas, and M is the total mass of the galaxy contained by an orbit of radius r. By measuring the velocity dispersion of stars and gas, the total mass of the object can be estimated. Comparing this mass estimate with those based on the mass-to-light ratio, dark matter is generally required to keep structures gravitationally bound.

1.2.2 Galaxy Clusters

As mentioned earlier, studying galaxy velocities in the Coma cluster [38, 39] was one of the first observations pointing to extra matter in the universe. This method is based on the same principle as that used for elliptical and dwarf galaxies (Section 1.2.1), assuming equilibrium and using the virial theorem to relate velocities and mass. When studying a cluster, the Doppler effect is used to measure line-of-sight velocities for individual galaxies. Based on these measurements, galaxy clusters are dominated by dark matter.

Another method of estimating the mass of a galaxy cluster is to measure the x-ray emitting gas in the intergalactic medium. Assuming hydrostatic equilibrium, the gas

temperature is related to the system's energy and therefore mass. This independent method of calculating cluster masses gives results consistent with other methods, such as cluster dynamics and gravitational lensing.

Gravitational lensing is a powerful method of determining cluster masses and mass distributions that is independent of equilibrium assumptions. Cluster masses are determined by their lensing effect on light from distant sources. According to general relativity, light passing a distance r away from a body of mass M will be deflected by an angle α:

$$\alpha = \frac{4GM}{c^2}\frac{1}{r} \tag{1.5}$$

where G is the gravitational constant and c is the speed of light. Studying distorted images of distant objects not only provides a mass estimate of the cluster, but can also be used to create a spatial map of the overdensity.

Figure 1.3: A Hubble Space Telescope image of the Abell 2218 galaxy cluster showing prominent arcs of distant objects due to strong gravitational lensing. Courtesy of Space Telescope Science Institute.

There are two types of gravitational lensing. Extremely dense galaxy clusters produce "strong lensing." In strong lensing there are multiple images of distant objects and the images are obviously distorted into arcs or rings (Figure 1.3). Less dense galaxy clusters cause "weak lensing." Weak lensing distorts distant objects, but this distortion is not obvious like in strong lensing, nor are multiple images created. Statistical correlations between numerous background objects are used to

determine the cluster mass and distribution. Both strong and weak gravitational lensing techniques estimate dark matter abundances consistent with the standard ΛCDM model.

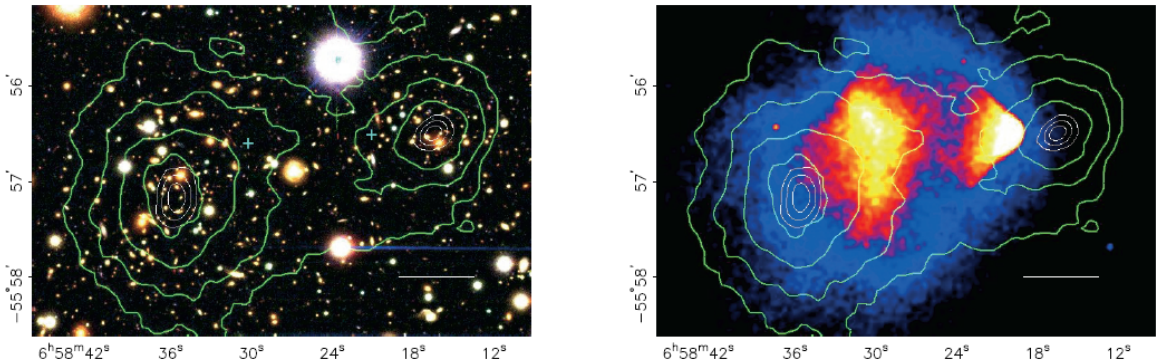

Figure 1.4: (a) Optical (from the Hubble Space Telescope) and (b) x-ray (from the Chandra X-ray Observatory) images of the Bullet cluster. The green and white curves are mass contours from weak lensing data. Notice how the mass contours do not coincide with the x-ray distribution. From [2].

Recent observations of the "Bullet cluster" have produced strong evidence for the existence of dark matter in galaxy clusters. The "Bullet cluster" is a pair of colliding galaxy clusters that has been observed in multiple wavelengths and whose mass distribution has been determined through gravitational lensing. Comparing the reconstructed mass distribution with visible and x-ray images shows a striking difference between the total matter (from weak lensing) and baryonic matter (from x-ray emission) distributions (Figure 1.4). This observation is consistent with the collisionless dark matter model where the dark matter halos of the original two clusters pass through each other unchanged while the hot gas distributions remained between the two structures due to interactions during the collision [41, 2].

1.2.3 Cosmic Microwave Background Radiation

The Cosmic Microwave Background (CMB) radiation is the oldest light in the universe that can be seen from Earth. The early universe was so hot that it was opaque due to the strong coupling between photons and baryons. Tiny density perturba-

tions, on the order of 10^{-5}, created potential wells. Since baryons and photons were strongly coupled, there was a competition between gravity and radiation pressure around these wells which caused "acoustic oscillations." These oscillations continued until the universe expanded and cooled sufficiently so that the photons were no longer coupled to baryons. This point is known as "last scattering." The acoustic oscillations created temperature fluctuations in the CMB (Figure 1.5) which were "frozen" at last scattering. Measuring the resulting CMB temperature power spectrum (Figure 1.6) gives information about the dark energy, dark matter, and baryonic matter densities in the universe. The relative amounts of dark and baryonic matter affect the amplitudes and positions of the power spectrum peaks because they have strong effects on the acoustic oscillations; baryons increase the oscillations while dark matter reduces them. This occurs because dark matter interacts gravitationally but would not have been coupled to the photons.

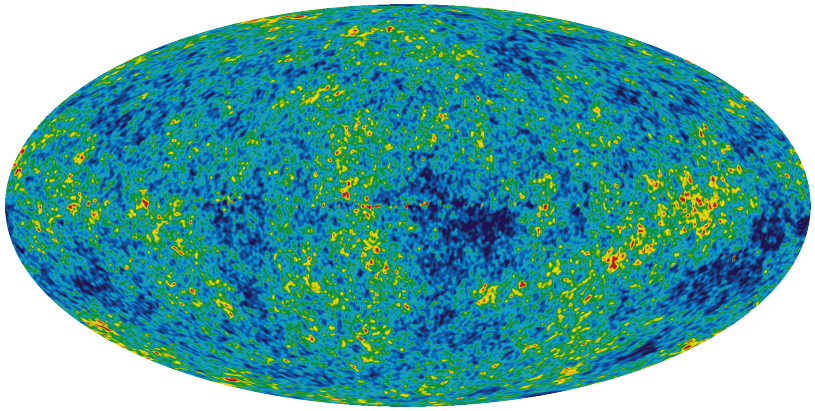

Figure 1.5: A full sky map of the Cosmic Microwave Background, from the WMAP 5 yr data set, that shows the μK temperature fluctuations. Courtesy of NASA / WMAP Science Team.

In addition to temperature fluctuations in the CMB, there are also polarization fluctuations (Figure 1.7). These fluctuations are at an even smaller scale ($\sim$0.1 μK as opposed to $\sim$10 μK), but polarization detections will discover the scale of inflationary gravitational waves and allow degeneracies between fundamental cosmological parameters to be broken.

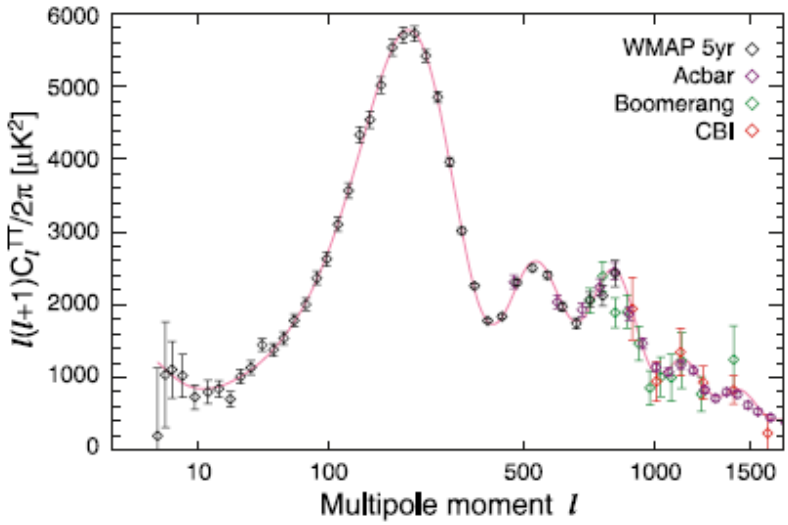

Figure 1.6: The CMB temperature power spectrum with data points from the WMAP 5 yr data along with Acbar, Boomerang, and CBI. The curve indicates the prediction of the best-fit ΛCDM cosmology. From [3].

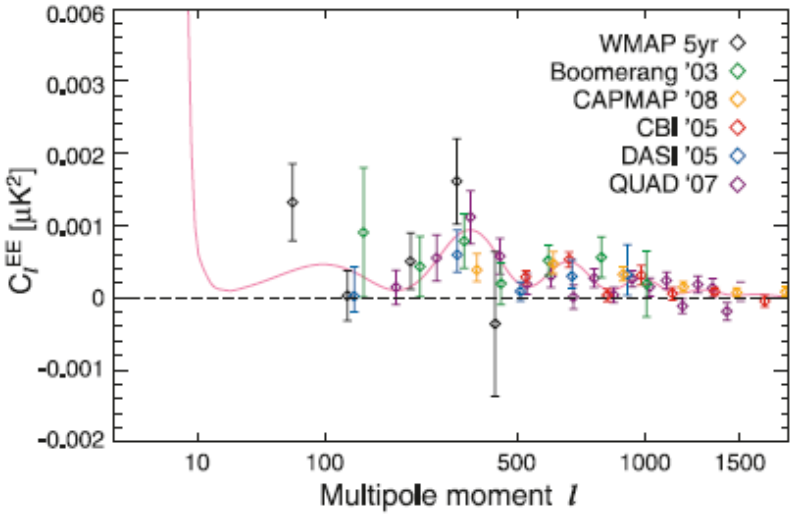

Figure 1.7: The CMB E-mode polarization power spectrum with data points from the WMAP 5 yr data along with Boomerang, CAPMAP, CBI, DASI, and QUAD. The curve indicates the prediction of the best-fit ΛCDM cosmology. From [3].

Current CMB data provides precision measurements of parameters in the modern cosmological model, $\Omega_b = 0.0456 \pm 0.0015$, $\Omega_\chi = 0.228 \pm 0.013$, and $\Omega_\Lambda = 0.726 \pm 0.015$ (where Ω_b is the baryonic energy density, Ω_χ is the dark matter energy density, and Ω_Λ is the dark energy density, where all are in units of critical density), [42]. These results not only show that dark matter makes up $\sim$23% of the energy density in the universe, but that most of it must be non-baryonic since Ω_b <5%.

1.2.4 Large Scale Structure Formation

Observations of large scale structure in the universe provides a means of learning about the amount and properties of dark matter.

One way to learn about dark matter through large scale structure is to compare the density perturbations seen today (i.e., at redshift much less than 1) with those seen in the CMB and estimate if there was sufficient time for gravitational collapse to produce the observed universe. Perturbations seen in the CMB, at redshift of $\sim$1000, are $\sim 10^{-5}$. For a matter dominated universe, where Ω_b=1, perturbations would grow with time (or redshift, z) as $\frac{1}{1+z}$. Based on this reasoning, the density perturbations today would be $\sim$0.01. However this value is smaller than the observed fluctuations in the universe today. Therefore this model does not allow enough time to produce the present universe.

This argument can also be used to estimate the amplitude of the CMB density perturbations based on the structure seen today. Assuming that galaxies and quasars form when the perturbations are >1, the fact that there are quasars at a redshift of 6 predict CMB temperature fluctuations of $\sim 10^{-3}$. However this is larger than the observed CMB temperature fluctuations of $\sim 10^{-5}$. Non-baryonic dark matter, on the other hand, allows the observed large scale structure to form from the initial perturbations measured in the CMB.

Comparing numerical simulations of structure growth with the observed large scale

structure (Figure 1.8) gives additional information about the dark matter properties. In particular these comparisons show that relativistic, or "hot," dark matter produces more structure than seen today while non-relativistic, or "cold," dark matter with an energy density ∼23% creates approximately the structure seen today.

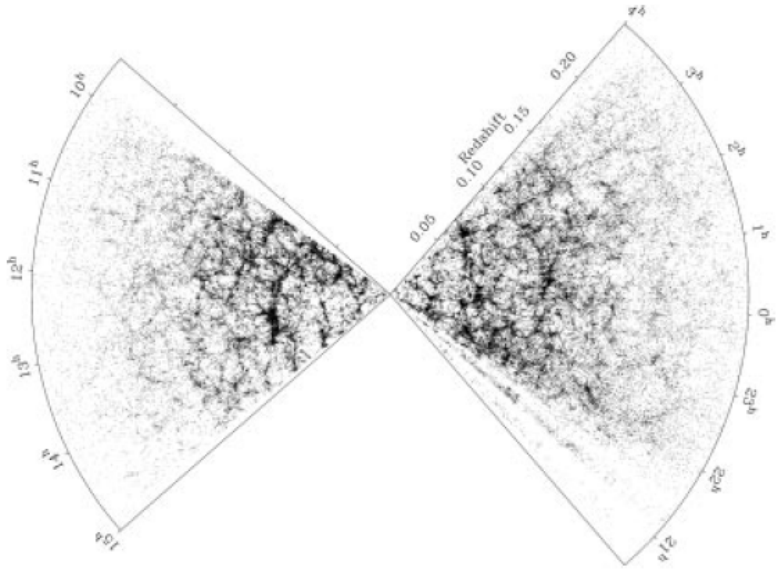

Figure 1.8: Map of the galaxy distribution as a function of redshift, as projected from the 2dF Galaxy Redshift Survey, showing the universe's current large scale structure. From [4].

1.2.5 Big Bang Nucleosynthesis

Studies of the abundances of light elements created in the first few minutes after the Big Bang (Figure 1.9) have produced robust constraints on the baryon density in the universe requiring the majority of dark matter to be non-baryonic.

Light element abundances are strongly coupled to initial conditions in the early universe, in particular to the baryon-to-photon ratio, η. The photon density controls the universe's expansion rate, and therefore sets the duration of nucleosynthesis, while the baryon density sets the rate of fusion into ^{4}He. The photon density is known from the CMB temperature while the baryon density is measured from primordial light element abundances.

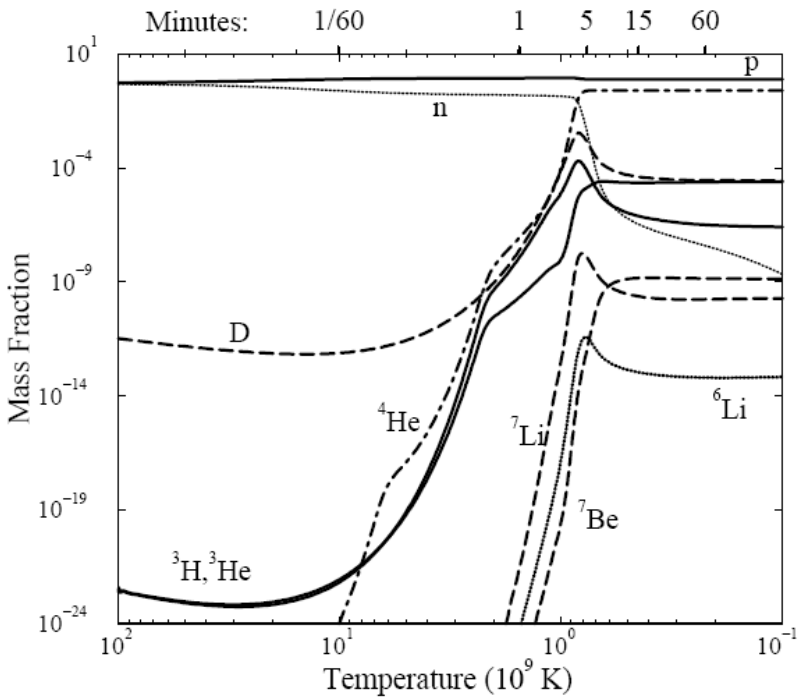

Figure 1.9: Evolution of light element abundances during Big Bang Nucleosynthesis as a function of time (or temperature). From [5].

One of the most powerful measurements of baryon density comes from observing the primordial deuterium abundance. These measurements are so powerful because deuterium is destroyed and not created after initial production, therefore producing a direct upper limit on η. Primordial deuterium abundances are measured in high-redshift intergalactic absorption systems illuminated by quasars and imply a current baryon density of $\Omega_b \sim 0.04$ [5, 43, 44].

Figure 1.10 summarizes Big Bang Nucleosynthesis predictions of light element abundances as a function of η along with primordial abundance measurements. Deuterium abundance measurements provide the strongest constraints on η and therefore Ω_b. The primordial abundances of other elements, in particular ^{4}He and lithium, have also been estimated based on astronomical observations.

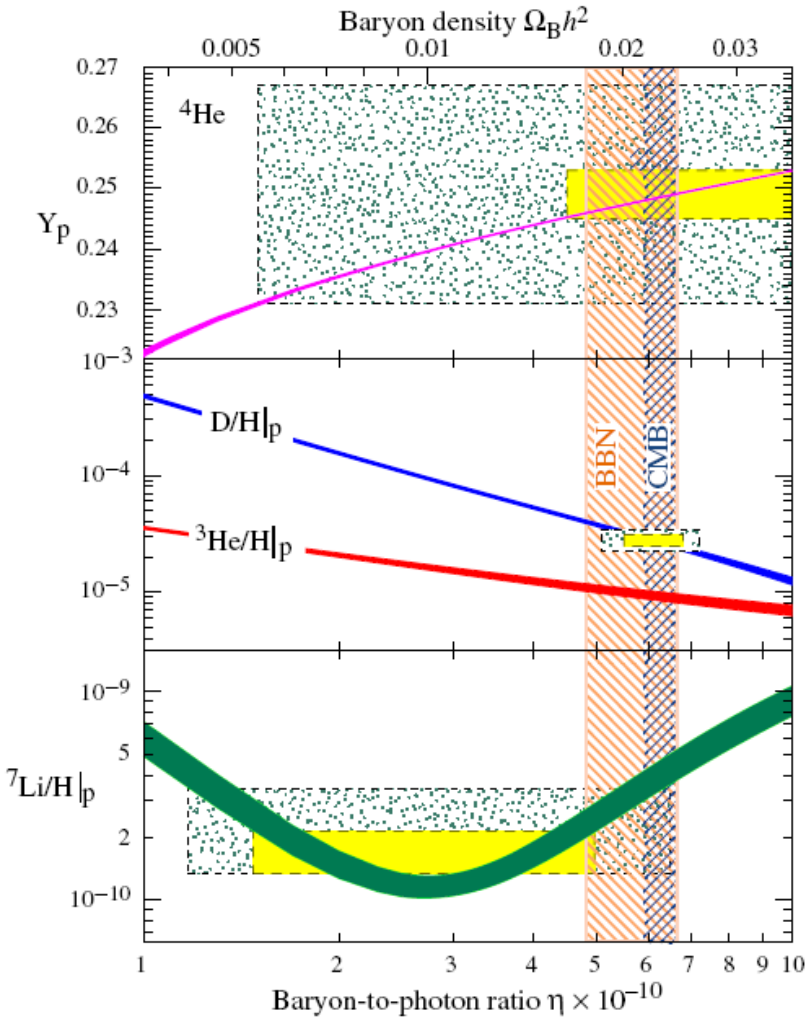

Figure 1.10: Figure summarizing primordial light element abundances. Bands show predictions of the primordial abundances of ^{4}He, D, ^{3}He, and ^{7}Li as functions of the baryon-to-photon ratio, η. The small yellow boxes indicate 2σ observational constraints based upon statistical errors while the larger blue boxes incorporate systematic errors. The vertical bands represent the CMB and combined BBN results on η (and therefore Ω_b). From [6].

1.3 Dark Matter Candidates

Observations from the many techniques described in Section 1.2 provides strong evidence for the existence of dark matter in the universe. Based on this evidence dark matter is expected to have the following properties:

- Non-baryonic: This is due to the discrepancy between Ω_b and Ω_χ from BBN (Section 1.2.5) and CMB (Section 1.2.3) measurements
- Cold or non-relativistic during structure formation: So that the large scale structure develops from the CMB initial conditions into what is seen today (Section 1.2.4)
- Non-interacting: The lack of electromagnetic signals from dark matter and the bullet cluster provide good examples of this (Section 1.2.2)
- Stable: Have a lifetime long compared the age of the universe

This section describes some of the dark matter candidates. While a single type of particle is often assumed to make up all the dark matter in the universe, the total dark matter density could be from a combination of sources. In fact the total luminous baryonic matter does not account for all the measured baryon energy density, so some fraction of dark matter could be baryonic. Also, while neutrinos cannot be the sole dark matter particle (Section 1.3.2), non-zero neutrino masses have been experimentally inferred and therefore they compose part of the dark matter. The total allowed neutrino energy density depends on the absolute neutrino mass, but cosmological constraints restrict neutrinos to make up only a few percent of the total non-baryonic dark matter component in the universe [6, 42].

1.3.1 MACHOs

One of the simplest candidates for dark matter is a Massive Astrophysical Compact Halo Object, or "MACHO." MACHOs are objects that not directly observed and made of ordinary, baryonic matter. These could be compact objects such as cold white dwarfs or black holes. Astronomical searches have found such object through microlensing, but not enough of them to make up all the dark matter. This result is consistent with CMB and BBN constraints on the allowed amount of baryonic dark matter.

1.3.2 Neutrinos

An experimentally verified dark matter candidate is the neutrino. Neutrinos are non-baryonic and have small masses. However, neutrinos are relativistic particles which large scale structure constrains to make up only a few percent of the total non-baryonic dark matter.

1.3.3 Axions

One possible candidate that could account for most of the total dark matter energy density is the axion. This particle arises in a model to solve the "strong CP problem." In the Standard Model of particle physics there is a term, Θ, in the quantum chromodynamics (QCD) Langrangian which, if non-zero, violates CP symmetry and produces a neutron electric dipole moment. Experimental limits on the neutron electric dipole moment force Θ to be extremely small ($\sim 10^{-10}$). To solve this non-observation, Peccei and Quinn's model introduces a new global symmetry [45] which conserves CP symmetry by a spontaneous symmetry breaking which generates a Goldstone boson, the axion, with a mass given by the coupling constant, f_a:

$$m_a \simeq 6\,\mu\,eV \frac{10^{12}\,GeV}{f_a} \tag{1.6}$$

Non-relativistic axions would be created in the early universe when the U(1) symmetry is broken at a temperature $T \sim f_a$. Axions would have a relic energy density of:

$$\Omega_a h^2 \sim (\frac{f_a}{10^{12}\,GeV})^{7/6} \tag{1.7}$$

where h is the current Hubble parameter, in units of 100 km/s/Mpc. An axion with a 10 μeV mass could constitute the universe's dark matter while lighter axions are cosmologically excluded.

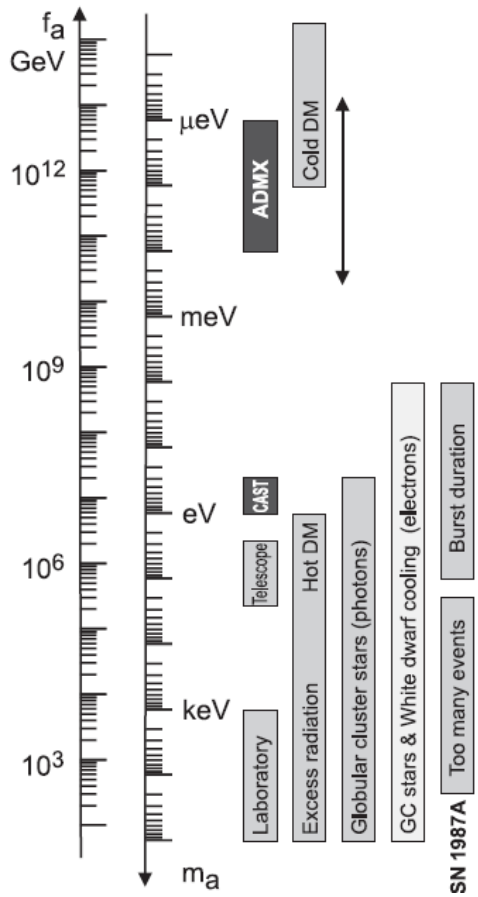

Figure 1.11: Figure showing axion mass ranges excluded by various astronomical and laboratory constraints (light rectangles) as well as those ranges that will be probed by current and upcoming experiments (dark rectangles). The vertical arrow indicates the axion mass range with cosmologically-interesting relic densities. From [6].

Astrophysical observations and laboratory experiments have placed constraints on the axion mass. Astrophysical constraints are placed on the axion mass based on effects they would have on cooling stars and supernovae. The most sensitive labora-

tory experiments, such as ADMX, are based on the Primakoff process, the conversion of axions to photons in a strong magnetic field. Measurements are made to detect these excess photons in resonant microwave cavities [46]. Figure 1.11 shows the approximate regions of excluded axion masses along with the cosmologically interesting mass region probed by the ADMX experiment.

1.3.4 Weakly Interacting Massive Particles

One of the most promising dark matter candidates, and the topic of this dissertation, is the weakly interacting massive particle, or "WIMP." The WIMP is a hypothetical particle, χ, with a mass between $10\,\mathrm{GeV} \lesssim \mathrm{M}_\chi \mathrm{c}^2 \lesssim 10\,\mathrm{TeV}$ and coupling strengths characteristic of weak interactions.

Considering a massive particle in thermal and chemical equilibrium in the early universe can put constraints on that particle's properties. In thermal and chemical equilibrium, the particle's equilibrium abundance is maintained through a balance of particle production and annihilation. As the universe expands and its temperature decreases (to $\mathrm{T} < \mathrm{M}_\chi$), particle production is suppressed. The equilibrium abundance can be described by the Grand Canonical distribution:

$$n_\chi^{(eq)} \simeq 4(\frac{M_\chi kT}{2\pi\hbar^2})^{3/2} e^{-\frac{M_\chi c^2}{kT}} \tag{1.8}$$

where $n_\chi^{(eq)}$ is the particle's equilibrium density, M_χ is the particle's mass, k is the Boltzmann constant, T is the universe's temperature, $\hbar$ is Planck's constant, and c is the speed of light. The particle falls out of equilibrium, producing a "relic" density, when the annihilation reaction falls below the expansion rate H.

The particle density time evolution is described by the Boltzmann equation:

$$\frac{dn_\chi}{dt} + 3Hn_\chi = - < \sigma_{\chi\chi} > [(n_\chi)^2 - (n_\chi^{(eq)})^2]^2 \tag{1.9}$$

where H is the Hubble constant today, n_χ is the particle number density, $\sigma_{\chi\chi}$ is the particle annihilation cross section, and $n_\chi^{(eq)}$ is the equilibrium number density. The

second term on the left is due to the universe's expansion while the terms in the brackets on the right-hand side are from the particle depletion due to annihilation (first term) and particle production (second term). This leads to an approximate solution for the WIMP relic density of:

$$\Omega_\chi h^2 \simeq \frac{(0.1\,pb)c}{< \sigma_{\chi\chi} v >} \tag{1.10}$$

where Ω_χ is the WIMP energy density, h is the current Hubble parameter, $\sigma_{\chi\chi}$ is the particle annihilation cross section, c is the speed of light, and v is the velocity. This argument shows that particles with larger annihilation cross section remain in equilibrium longer and experience more Boltzman suppression resulting in a lower relic density. Figure 1.12 shows a pictorial representation of the WIMP number density as a function of time (or temperature).

Following the reasoning above, if WIMPs make up the total dark energy density (as measured from the CMB and other experimental techniques), the relic density calculation implies an annihilation cross section on the order of the weak scale.

WIMP dark matter candidates naturally arise in extensions to the Standard Model. Supersymmetry solves the "heirarchy problem," why M_Z is much less than M_{Planck}, and how electroweak symmetry is broken in the Standard Model. In supersymmetric models every Standard Model particle has a "super" partner with similar mass and couplings. For these models to be consistent with experimental observations, in particular with the limits on proton decay, R-parity symmetry is introduced. A particle's R-parity can be expressed as:

$$R = (-1)^{3B+L+2s} \tag{1.11}$$

where B is the baryon number, L is the lepton number, and s is the particle spin. All Standard Model particles have R-parity = +1 while their supersymmetric partner have R-parity = -1. Conservation of R-parity requires the lightest supersymmetric particle (LSP) to be stable. In the Minimal Supersymmetric Standard Model

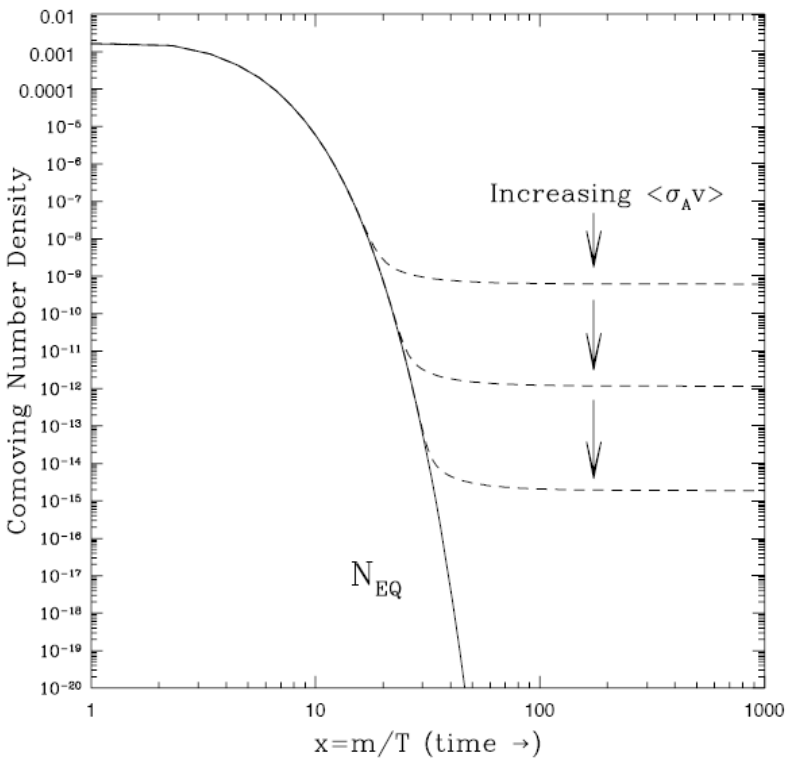

Figure 1.12: Figure of the WIMP comoving number density as a function of time (or temperature) in the early universe. The solid curve corresponds to the equilibrium abundance while the dashed curves represent forming the WIMP relic abundance (and how that varies with annihilation cross section). From [7].

(MSSM), the neutralino is likely the LSP and would be massive, stable, and weakly interacting, making it a good dark matter candidate.

1.4 Dark Matter Detection

While there are several dark matter candidates (as described in Section 1.3), the rest of this dissertation focuses on the detection of WIMPs. In the same way that multiple methods have been used to show the existence of dark matter (Section 1.2), there are many experimental techniques used to test the WIMP hypothesis. This section briefly describes three general classes of methods used to search for WIMP signatures:

- Direct Detection: searches for WIMP particle interactions directly with a terrestrial detector

- Indirect Detection: searches for non-WIMP particles produced from WIMPs
- Collider Production: creation of WIMP particles at accelerators

Particle accelerators have long been used to investigate particle phenomenology. Current colliders are beginning to characterize phenomena at the TeV scale. At these energies WIMPs could be produced.

Since WIMPs have small interaction cross sections they would not be detected in the collider particle detectors. However signatures of WIMPs could be detected by missing mass and momentum in reconstructed events.

Additionally, heavier supersymmetric particles may be created in the accelerators. These particles could decay to WIMPs and produce a distinctive signature of hard jets with missing transverse energy.

Indirect detection dark matter experiments search for WIMP annihilation products in high density regions of the universe. These annihilation products include photons, neutrinos, and antimatter. Just as there are multiple direct detection experiments and techniques, there are many indirect detection searches. While some of these searches have given hints of a dark matter signature, there has been no hard evidence yet.

Based on measurements of spiral galaxy rotation curves, it is inferred that these galaxies, such as our own Milky Way Galaxy, are embedded in large dark matter halos (Section 1.2.1). Using this information, one would expect dark matter particles to interact with detectors on Earth. Techniques developed to look for these interactions are called "direct detection" experiments.

WIMPs within the galactic halo travel at typical galactic velocities $v \simeq 230\,\mathrm{km/s}$ $\sim 10^{-3}\,\mathrm{c}$. Therefore, a WIMP with mass $M_\chi \sim 100\,\mathrm{GeV/c^2}$ will have kinetic energy $= \frac{M_\chi v^2}{2} \sim 50\,\mathrm{keV}$. A WIMP elastic scattering with a stationary target of mass m will cause the target to recoil with a mean kinetic energy (averaging over recoil angles)

of:

$$\frac{E_{recoil}}{E_\chi} = \frac{2\frac{m}{M_\chi}}{(1+\frac{m}{M_\chi})^2} \tag{1.12}$$

where E_{recoil} is the kinetic energy of the recoiling target and E_χ is the WIMP kinetic energy. An elastic collision between a 100 GeV/c^2 galactic WIMP and a germanium nucleus ($m_{Ge} \approx 67\,\mathrm{GeV/c^2}$) will cause the nucleus to recoil with a typical kinetic energy of ~25 keV. A similar elastic collision with an electron, instead of the nucleus, will make the electron recoil with a typical kinetic energy of <1 eV. This energy is below most detector thresholds. As will be discussed later, most direct detection experiments take advantage of this calculation by discriminating between electron and nuclear recoil events, where WIMP interactions would create detectable nuclear recoil events.

To develop experiments that are sensitive enough to detect WIMP interactions, the event rate needs to be estimated. The differential rate per unit mass of a particle with velocity v incident on a detector is:

$$dR = \frac{N_0}{A}\sigma_0 v dn \tag{1.13}$$

where N_0 is Avogadro's number, A is the atomic mass of the target nucleus, σ_0 the WIMP-nucleon scattering cross section assuming zero-momentum transfer, and n is the number density of incoming particles. Following the formalism in Lewin and Smith's review paper [47], the differential rate with energy is:

$$\frac{dR}{dE_R} = \frac{R_0}{rE_0}e^{-E_R/rE_0} \tag{1.14}$$

where E_R is the recoil energy, E_0 is the WIMP's incident kinetic energy, R_0 is the total event rate, and $r = \frac{4M_\chi m}{(M_\chi+m)^2}$ (where M_χ is the WIMP mass and m is the target mass). Combined with the nuclear form factor, which is <1 due to the nucleus' finite size and dependent on the nuclear radius and recoil energy, this equation is re-written as:

$$\frac{dR}{dE_R} = \frac{R_0}{rE_0}e^{-E_R/rE_0}F_2(q^2) \tag{1.15}$$

where F is the nuclear form factor and $q^2 = 2mE_R$ (where m is the target mass and E_R is the recoil energy). Figure 1.13a shows the nuclear form factor values as a function of recoil energy for silicon, germanium, and xenon targets while Figure 1.13b shows the expected integrated WIMP event rates (for a WIMP with a mass of 100 GeV and interaction cross section of $10^{-42}\,\mathrm{cm}^2$) as a function of an experiment's energy threshold for silicon, germanium, and xenon targets. This shows the dependence of the target nucleus and experimental threshold on the expected event rate, which is less than 0.01 events per kg per day.

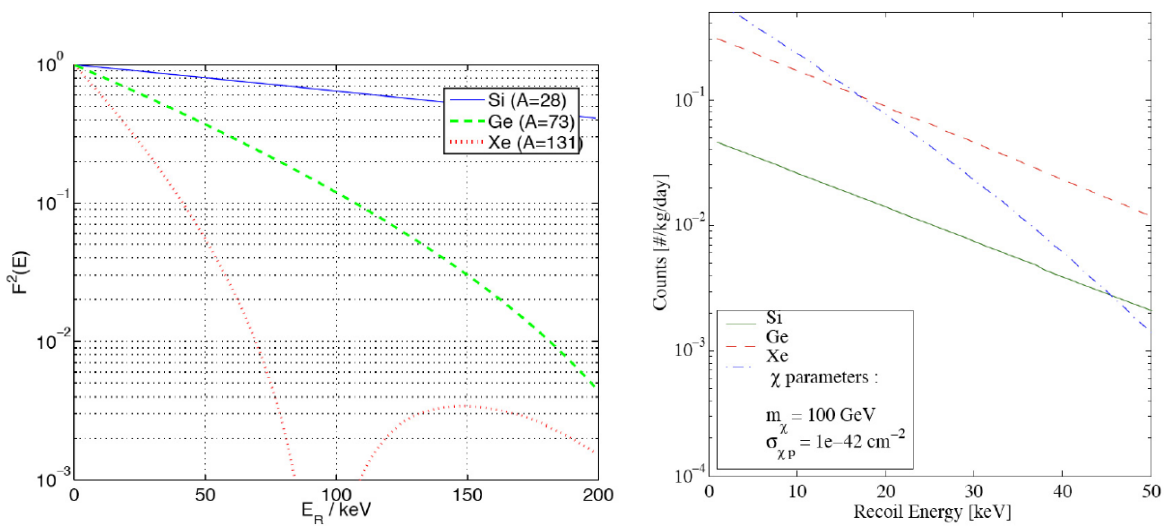

(a) (b)

Figure 1.13: (a) The nuclear form factors as a function of energy for silicon (solid line), germanium (dashed line), and xenon (dash dotted line) targets. From [8]. (b) The integrated WIMP interaction rate as a function of threshold energy for silicon (solid line), germanium (dashed line), and xenon (dash dotted line) targets and assuming a WIMP with a mass of 100 GeV and interaction cross section of $10^{-42}\,\mathrm{cm}^2$. From [9].

The spin-independent WIMP-nucleus cross section is:

$$\sigma_{SI} \simeq \frac{4M_\chi^2 m^2}{\pi(M_\chi + m)^2}[Zf_p + (A - Z)f_n]^2 \tag{1.16}$$

where M_χ is the WIMP mass, m is the target mass, Z is the target's atomic mass, A is the target's atomic number, and f_p (f_n) is the WIMP coupling to protons (neutrons). Most models predict $f_p \approx f_n$, therefore the WIMP-nucleus cross section, σ_{SI}, is

proportional to A^2. This can be seen in Figure 1.13b where heavier nuclei have larger event rates.

Direct detection experiments must overcome a number of challenges to detect WIMP dark matter. As discussed earlier, WIMPs are weakly interacting, have low recoil energies, and very low event rates. Additionally, the background rate is much higher than the expected WIMP rate. To overcome these challenges, direct detection experiments must be designed with low energy thresholds, large target masses, long term stability, and background control. To achieve background control, direct detection experiments must maintain radio-purity in and around their target mass and are located in underground sites to reduce the overall interaction rate, especially cosmic-ray induced nuclear recoils. Most direct detection experiments achieve discrimination between electron recoils, primarily due to backgrounds, and nuclear recoils by measuring two types of energy from an interaction: a combination of scintillation, ionization, and phonon energy. The sections below describe some of the techniques used by direct detection experiments to detect WIMP dark matter.

1.4.1 Cryogenic Solid State Detectors

One of the first techniques used for direct WIMP detection were cryogenic solid state detectors. Several experiments continue to use this method, including the Cryogenic Dark Matter Search (CDMS) which has set some of the strongest limits on the WIMP-nucleon cross sections and is the topic of this dissertation.

The CDMS [18] and EDELWEISS [48] experiments use very similar detection techniques. Both experiments use very pure germanium crystals (CDMS also uses some silicon crystals) as the target material for WIMP-nucleon interactions. Discrimination between electron and nuclear recoils occurs on an event-by-event basis by measuring both the phonon and ionization energy from an interaction. Since the ionization energy produced for a nuclear recoil is $\sim$3 times smaller than that generated

for an electron recoil with the same recoil energy, the ratio of ionization to phonon energy is a powerful discriminator. Additionally, CDMS is able to use phonon timing information to reject electron recoil surface events with poor ionization collection (Section 2.6.1).

In both the CDMS and EDELWEISS crystals, ionization energy is measured by drifting charge carriers through the crystal with an applied electric field. CDMS-II uses superconducting transition-edge sensors (TESs) to measure the phonon energy while EDELWEISS uses NTD thermistors.

The CRESST dark matter experiment [49] also uses cryogenic solid state detectors. CRESST measures phonon energy and scintillation light from interactions in $CaWO_4$ crystals. CRESST uses the ratio of scintillation to phonon energy, similar to the CDMS and EDELWEISS approach using the ratio of ionization to phonon energy, to discriminate between electron and nuclear recoils. The scintillation produced in nuclear recoils is quenched compared with electron recoils.

CRESST uses a superconducting tungsten thermometer on the $CaWO_4$ crystal to measure the phonon energy while a separate cryogenic silicon detector with a second tungsten thermometer is used to measure the scintillation light.

1.4.2 Liquid Noble Detectors

Over the past several years, dark matter detection techniques using liquified noble gases have been demonstrated and have started to set competitive limits on WIMP-nucleon cross sections. These experiments create detectors with large volumes of liquified xenon, argon, or neon. Interactions with this target material produce scintillation light that is measured with PMTs. Among the noble liquid experiments there are two general classes, dual- and single-phase experiments.

Dual-phase experiments include XENON [50], LUX, ZEPLIN [51], WARP [52], and ArDM [53]. These dual-phase experiments measure both the scintillation and

ionization produced during an interaction for event-by-event discrimination between electron and nuclear recoils. An interaction in the liquid produces "primary" scintillation light and charge carriers. An applied electric field drifts the charge carriers through the detector volume to a gas phase where they produce a "secondary" scintillation light signal which is proportional to the number of carriers. Nuclear recoils produce less charge carriers than electron recoils of the same recoil energy. Therefore dual-phase experiments are able to discriminate between these two types of interactions by comparing the amplitudes of the primary and secondary scintillation light signals. Additionally, measuring the time delay between the two light signals permits these dual-phase experiments to operate as Time Projection Chambers (or "TPCs") allowing event reconstruction important for creating a fiducial detector volume and taking advantage of the noble liquid self-shielding properties.

Single-phase experiments, including DEAP [54] and CLEAN [55], use the pulse shape of the primary scintillation signal to discriminate between electron and nuclear recoils. Noble liquids produce scintillation through the decay of excimers that can exist in a singlet or triplet state, where the two states have different time constants. Since nuclear recoils preferentially populate the singlet state, the relative amplitudes of the prompt and slow scintillation signals can be used to discriminate electron and nuclear recoils.

The use of liquified noble gases is exciting for a variety of reasons, including their relative ease in scaling, "high" boiling points, heavy nuclei, and self-shielding properties. Some of the greatest challenges for these experiments is reaching the necessary levels of radio-purity in the liquid and surrounding materials.

1.4.3 Super Heated Detectors

Another approach to detecting WIMP dark matter is to use a target material in a superheated metastable state. Particle interactions depositing sufficient energy cause

the target material to undergo a physical phase transition, creating bubbles. The distribution and number of bubbles allows an identification of the particle or interaction type (Figure 1.14). For example, long tracks of bubbles are created by minimum ionizing cosmic ray events while nuclear recoils create separate bubbles. Neutrons may create multiple bubbles in the target material, however a WIMP interaction would only create one.

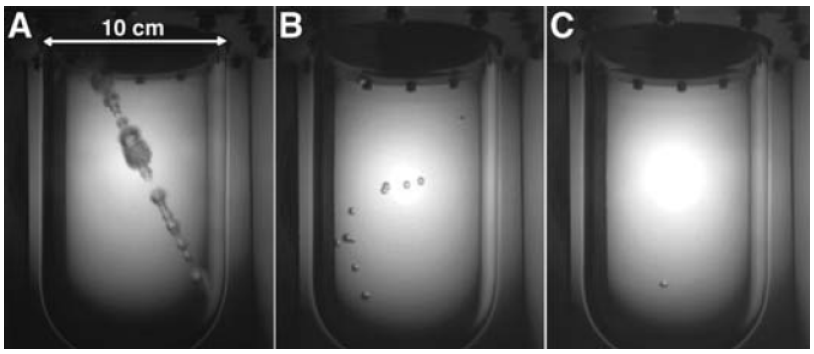

Figure 1.14: Images of three different types of particle interactions in the COUPP bubble chamber: (A) cosmic ray event, (B) neutron multiple-scatter event, and (C) neutron single-scatter event. From [10].

Changing the pressure or temperature of the target material changes the energy threshold required to cause the phase transition as well as the nucleation energy, allowing immunity to minimum ionizing particles. By taking data with multiple energy thresholds allows this type of experiment to distinguish WIMPs from a higher energy background spectrum and possibly even resolve the WIMP recoil spectrum.

The PICASSO [56] and SIMPLE [57] experiments use arrays of superheated droplets in fluorine-containing fluids while the COUPP experiment [10] uses a superheated CF_3I liquid operated as a bubble chamber.

1.4.4 Annual Modulation

The interaction rate of WIMP dark matter in terrestrial detectors is expected to vary during the year due to Earth's motion around the sun. This annual modulation

is expected to peak around June 2nd when the sum of the Earth and solar system velocities is maximum with respect to the galaxy.

The DAMA, and more recently the DAMA/LIBRA, collaboration has searched for this WIMP annual modulation signal using NaI(T1) scintillator crystals [58]. The DAMA/NaI and DAMA/LIBRA experiments do not discriminate between electron and nuclear recoil events, but statistically identify WIMPs based on their annual modulation. WIMPs should cause the rate of low-energy single-scatter counts to vary with a period of 1 yr while the rates of multiple-scatter and higher-energy background counts should remain constant.

The DAMA/NaI experiment began operation in 1996 and took approximately 7 yrs of data with $\sim$100 kg of target mass. More recently the DAMA/LIBRA experiment has taken over 3 yrs of data with $\sim$250 kg of target mass. The DAMA/LIBRA exposure was 0.53 ton yr. Adding the original DAMA/NaI data increased their total exposure to 0.82 ton yr.

Figure 1.15 shows the combined DAMA/NaI and DAMA/LIBRA residual rates for low energy single-scatter events. This data shows an annual modulation, with a confidence level greater than 8σ, consistent with that expected from WIMP interactions [11]. As expected, the annual modulation is only seen for low-energy single-scatter events.

Interpreting this annual modulation signal in the standard WIMP framework produces a conflict with all other direct detection techniques. Results from many experiments, using various techniques, have excluded the parameter space corresponding to the DAMA/LIBRA signal region under standard WIMP assumptions for both spin-dependent and spin-independent couplings.

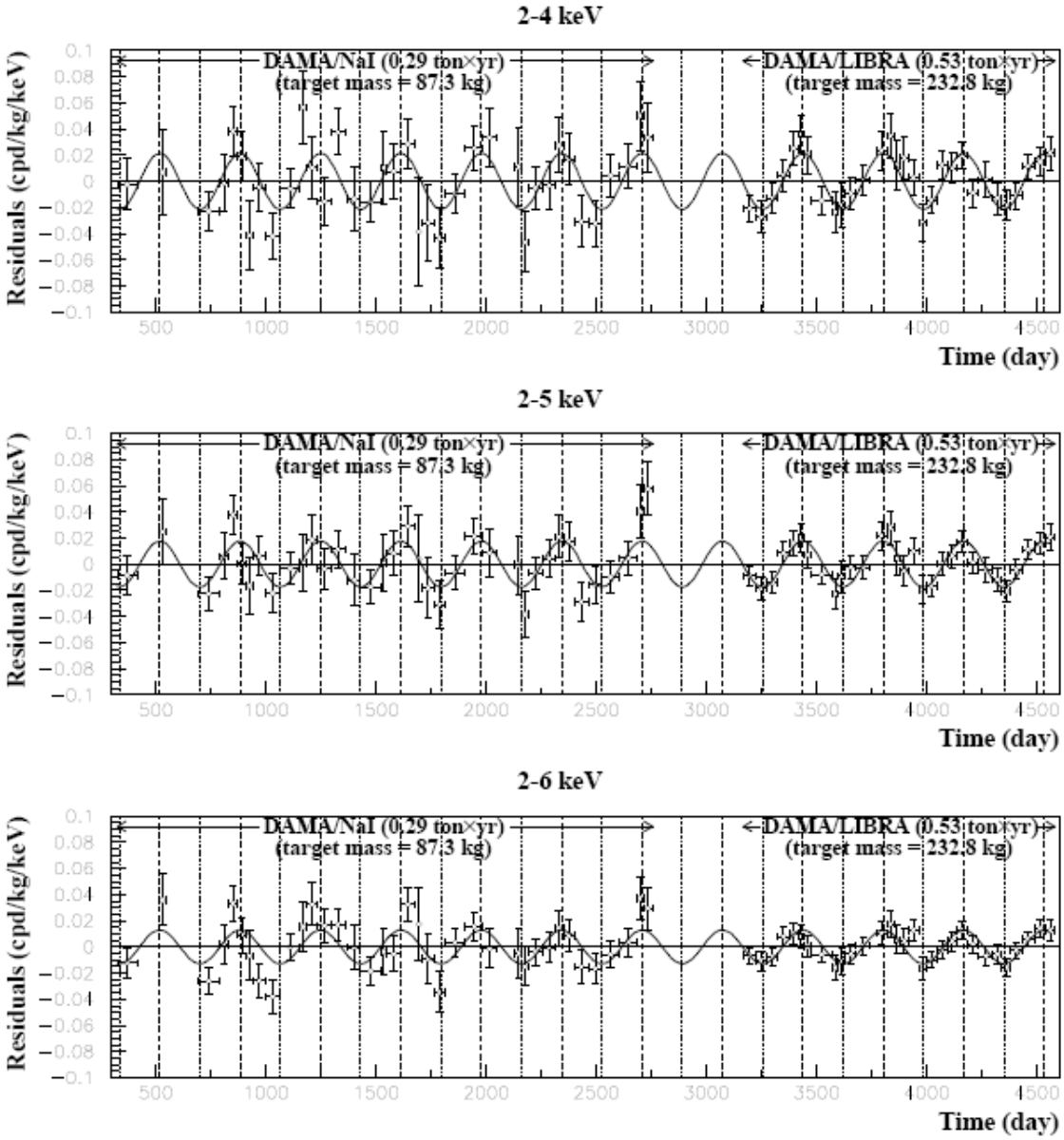

Figure 1.15: The annual modulation signal observed in the DAMA/NaI and DAMA/LIBRA experiments. These plots show the residual rates for low energy single-scatter events in the 2-4, 2-5, and 2-5 keV energy intervals. The time scale begins on January 1st and the solid lines correspond to cosine functional with a period of one year and phase of 152.5 days. From [11].

Chapter 2

The Cryogenic Dark Matter Search

2.1 Introduction

As discussed in Section 1.4, direct detection experiments must overcome a number of challenges when searching for WIMP dark matter particles. The Cryogenic Dark Matter Search (CDMS) uses Z-sensitive Ionization and Phonon (ZIP) detectors to measure both phonon and ionization energy. This dual measurement technique allows event-by-event discrimination between electron recoil background and nuclear recoil signal events. These ZIP detectors are also able to maintain event discrimination with low thresholds, on the order of 5 keV. This chapter reviews the CDMS ZIP detector, phonon and ionization measurements, and event discrimination methods.

2.2 ZIP Detectors

CDMS ZIP detectors (Figure 2.1) are cylindrical semiconductor crystals made from germanium (∼250 g each) or silicon (∼100 g each) that are 3 inches in diameter and 1 cm thick operated at ∼40 mK temperatures. Phonon and ionization channels are photolithographically patterned on the flat detector faces (Figure 2.2). The "top" detector face consists of four phonon sensors laid out in a quadrant pattern. Each

phonon sensor is made up of over 1000 tungsten transition-edge sensors (TESs) operated in parallel. Two concentric ionization electrodes are located on the "bottom" detector face. The inner ionization electrode ("Q_{inner}") covers ∼85% of the detector surface while an outer ionization electrode ("Q_{outer}") forms a 3 mm ring around "Q_{inner}" near the edge of the detector. Multiple phonon sensors allow event position reconstruction while the "Q_{outer}" electrode enables the rejection of high radius events occurring where ionization collection may be reduced due to electric field termination on side walls.

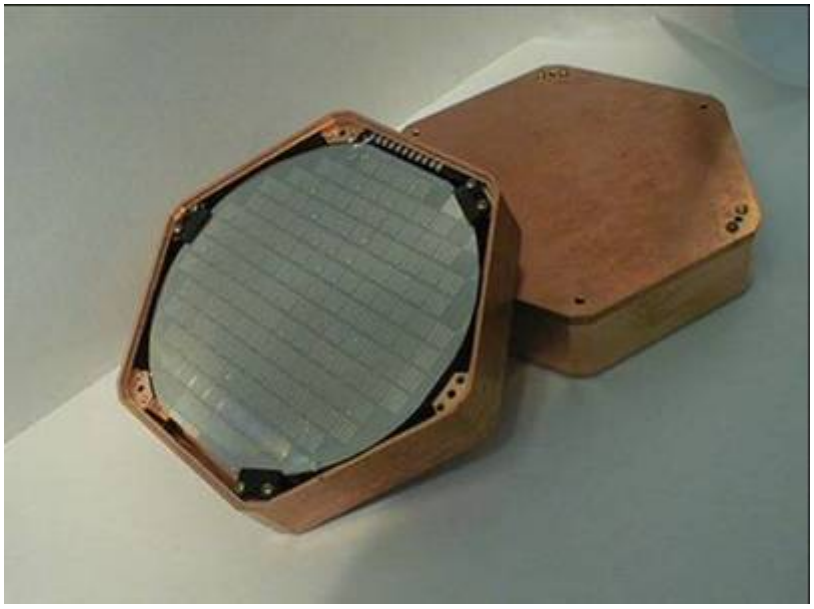

Figure 2.1: Photo of a CDMS-II Z-sensitive Ionization and Phonon (ZIP) detectors with the phonon side showing. Each detector is 3 inch in diameter and 1 cm thick. A single germanium (silicon) detector has a mass of ∼250 g (∼100 g).

A trilayer of materials, amorphous silicon, aluminum, and tungsten, is used to create both the phonon and ionization sensors. The amorphous silicon, aluminum, and tungsten layers are 40 nm (40 nm), 300 nm (20 nm), and 35 nm (20 nm) respectively for the phonon (ionization) detector face [59]. Amorphous silicon provides a blocking layer against charge carriers collected in the adjacent ionization electrode (see Section 2.6.1). On the ionization side the aluminum creates the electrodes while on the phonon side it has two purposes, part maintains the detector face at electrical

Figure 2.2: Schematic of the CDMS-II ZIP detector configuration with 4 phonon sensors on the "top" face and 2 ionization electrodes on the "bottom" face.

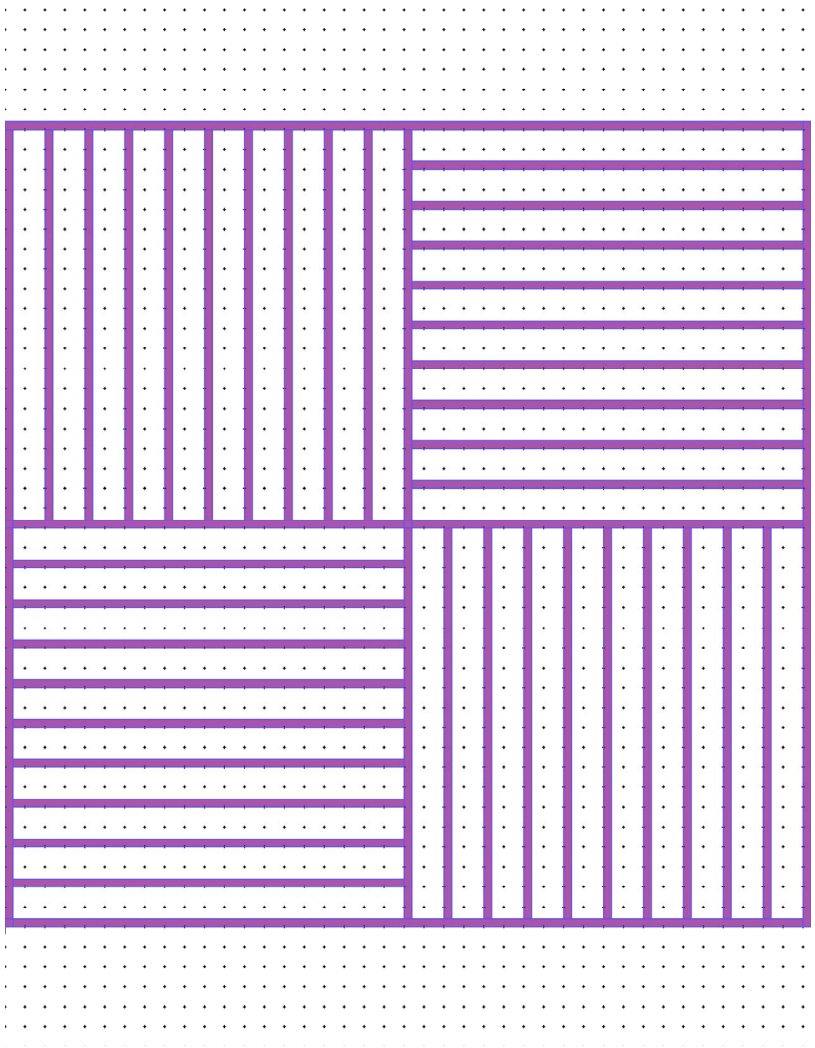

Figure 2.3: Illustration of the aluminum metal grid covering the detector's ionization and phonon face.

ground while additional aluminum acts as quasiparticle traps to increase the phonon collection area (see Section 2.3.2). On both the phonon and ionization detector faces the aluminum layer is patterned into a grid with 2 μm wide lines spaced 20 μm apart to fill roughly 20% surface area (Figure 2.3). This affects how $^{56}Fe^{+}$ ion implantation can cause damage to the detector crystal (Section 7.3.2). Briefly the partial aluminum coverage leaves about 80% exposed amorphous silicon. $^{56}Fe^{+}$ ions, used to tune the tungsten superconducting transition temperatures, are able to penetrate bare amorphous silicon surfaces causing potential damage to the underlying crystal. The tungsten is used to create the TESs on the phonon side.

While both germanium and silicon crystals are used in CDMS, they do not have the same cross sections for coherent WIMP-nucleon interactions due to different nuclear couplings. As discussed in Section 1.4, since the WIMP-nucleus cross section is proportional to A^2, WIMP targets with larger nuclear couplings are more sensitive to spin-independent WIMP interactions. This leads to an expected WIMP-nucleon interaction rate 5-7 times higher in germanium than silicon. Considering germanium and silicon have similar scattering rates per nucleon for neutrons, the rate of neutrons events is ~ 2 times greater in a silicon detector as opposed to germanium [60]. Therefore comparing nuclear recoil rates seen in germanium and silicon detectors can statistically differentiate a WIMP signal from potential neutron backgrounds.

2.3 Phonon Measurement

2.3.1 Phonon Generation and Propagation

Particle interactions in the detector create lattice vibrations, quantized as phonons. These phonons are measured before coming into thermal equilibrium in the ZIP detector. This phonon signal is made up of three main components, primary phonons created directly from the particle interaction, relaxation phonons produced by energy

stored in electron-hole pairs, and Luke phonons generated by electron and hole charge carriers drifting through the crystal.

Primary phonons are created at the Debye energy (∼10 THz in Ge and Si crystals). Initially these phonons propagate quasi-diffusively through the crystal due to two dominant processes, anharmonic decay and isotopic scattering [61, 62]. During anharmonic decay, a single phonon decays into two, each with approximately half the original energy. This process occurs at a rate proportional to the -5th power of frequency:

$$\tau_d \propto (1\,THz/\nu)^5 \tag{2.1}$$

where τ_d is the anharmonic decay time constant and ν is the phonon frequency. Isotopic scattering occurs when phonons elastically scatter with isotopic impurities in the germanium or silicon crystals. Like anharmonic phonon decay this process is strongly frequency-dependent, occurring with a rate proportional to the -4th power of frequency:

$$\tau_I \propto (1\,THz/\nu)^4 \tag{2.2}$$

where τ_I is the isotopic scattering time constant and ν is the phonon frequency.

Isotopic scattering and anharmonic decay cause high energy phonons to have short mean free paths and quickly decay into lower energy phonons. After a few microseconds primary phonons decay to frequencies below 1 THz and have mean free paths greater than the thickness of the detector. At these energies phonons are considered "ballistic" as they travel freely through the crystal until they reflect on bare surfaces or are collected in the aluminum collection fins.

Relaxation phonons are produced when energy stored in electron-hole pairs is deposited into the phonon system at the detector surface. This energy is equivalent to the number of electron-hole pairs times the energy of the semiconductor band gap.

So called "Luke" phonons are generated as electrons and holes drift across the crystal by an applied electric field. Energy caused by the charge carrier acceleration

is dissipated into the crystal as phonon radiation [63], in much the same way as the emission of Cherenkov radiation. This effect was first measured by Neganov-Trofimov [64] and Luke [65]. The additional energy added into the phonon system by Luke phonons is equal to:

$$E_{Luke} = eV_b \sum_i \frac{d_i}{d} \tag{2.3}$$

where E_{Luke} is the Luke phonon energy, e is the magnitude of the carrier charge, V_b is the applied bias voltage across the detector, d_i is the distance covered by charge i, and d is the detector thickness. For full ionization collection this expression becomes:

$$E_{Luke} = eV_b N_Q = eV_b \frac{E_Q}{\epsilon} \tag{2.4}$$

where N_Q is the number of electron-hold pairs, E_Q is the ionization energy, and ϵ is the average energy to produce an electron-hole pair (3.0 eV in germanium and 3.8 eV in silicon). These Luke phonons are generated at ballistic frequencies [63] and therefore create a prompt signal. Since phonon signal timing information, especially from the primary phonons, gives important discrimination power (see Section 2.6.1), it is important that the applied bias voltage is low enough so that the prompt Luke phonon signal contribution does not overwhelm this information.

The total phonon energy measured is:

$$E_P = E_R + E_{Luke} = E_R + eV_b \sum_i \frac{d_i}{d} \tag{2.5}$$

where E_P is the total measured phonon energy and E_R is the phonon recoil energy due to primary phonons from the particle interaction.

2.3.2 Phonon Collection

In order to maintain good signal to noise and energy resolution, the heat capacity of the tungsten transition-edge sensors (TESs) must be optimized. For this reason tungsten TESs cannot cover the entire detector surface. The CDMS ZIP detectors use the concept of quasiparticle trapping, first proposed by N. Booth [66], to

maximize the phonon collection area. This quasiparticle trapping is achieved using aluminum collection fins arranged around tungsten TESs (Figure 2.4). Phonons entering the aluminum collection fins with energy greater than 2 times the aluminum superconducting band gap ($2\Delta_{Al} = 340\,\mu\text{eV} = 82\,\text{GHz}$) break Cooper pairs creating quasiparticles. These quasiparticles diffuse through the aluminum until a fraction of them enter the transition region and tungsten TES at the end of the fin. Since both the transition region, where the tungsten overlaps the aluminum, and tungsten have smaller band gaps than aluminum, quasiparticles which have lost energy so that they have less than $2\Delta_{Al}$ will be trapped and unable to re-enter the aluminum. Quasiparticles reaching the tungsten TES form the phonon signal.

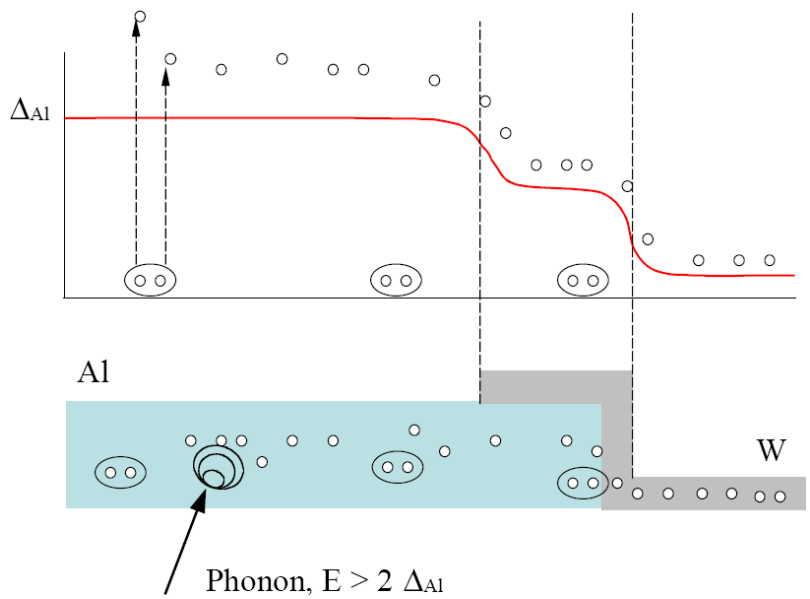

Figure 2.4: Cartoon of a Quasiparticle-assisted Electrothermal-feedback Transition-edge sensor (QET) showing the quasiparticle production and diffusion. Phonons break Cooper pairs in aluminum fins creating quasiparticles that diffuse through the aluminum. Quasiparticles that reach the tungsten enter a region with lower bandgap (top diagram), get trapped, and create the phonon signal.

The tungsten TES operates in electrothermal feedback (ETF) mode [67]. In this mode the detector is maintained at a temperature, ~40 mK, well below the TES transition temperature, 70-90 mK. The TES is voltage biased at the low end of its narrow superconducting transition region (Figure 2.5) so that small changes in

temperature correspond to measurable changes in resistance, and therefore current, which is readout by Superconducting Quantum Interference Devices (SQUIDs).

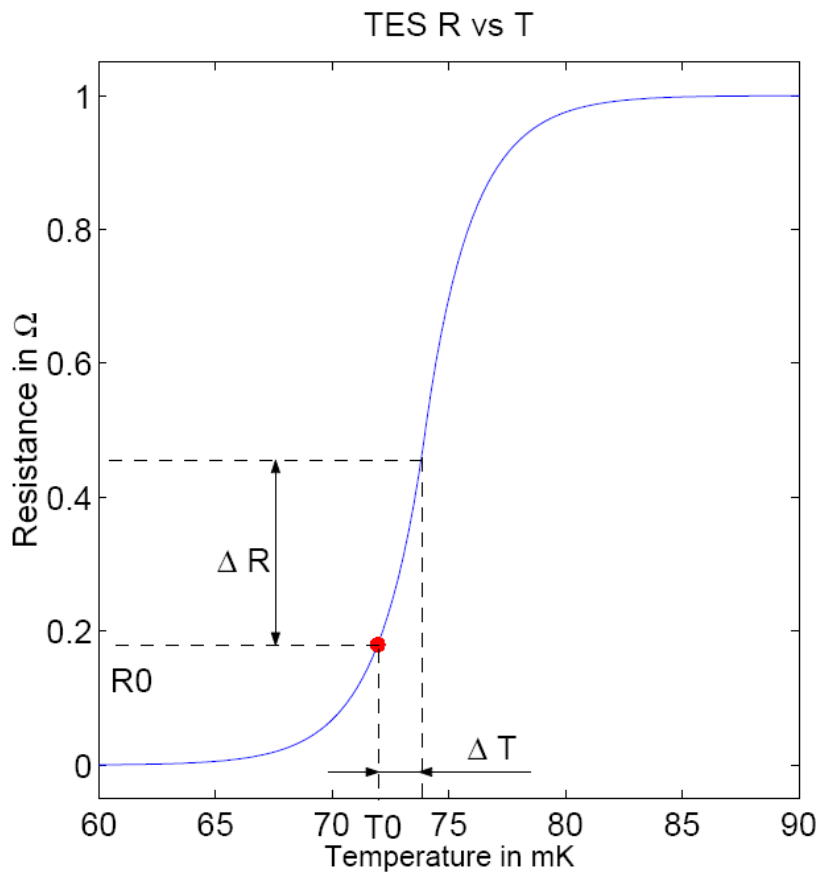

Figure 2.5: Plot of resistance as a function of temperature for a superconducting Transition-Edge Sensor (TES) showing the bias point and how a small temperature change causes a large change in resistance.

The thermal differential equation for the TES system is:

$$C\frac{dT}{dt} = -P_{bath} + P_{Joule} + P \tag{2.6}$$

where C is the TES heat capacity, $\frac{dT}{dt}$ is the differential temperature change with time, P_{bath} is the power flowing from the TES to the heat bath, P_{Joule} is the Joule power dissipation, and P is the signal power. By substituting for the power terms this equation becomes:

$$C\frac{dT}{dt} = \frac{V_{bias}^2}{R(T)} - \kappa(T^n - T_s^n) \tag{2.7}$$

where T is the TES temperature, V_{bias} is the TES bias voltage, $R(T)$ is the TES resistance, T_s is the substrate or heat bath temperature, κ is the thermal coupling coefficient, and n is the conductivity exponent, empirically verified to be 5. When quasiparticles enter the TES and increase the resistance, T (and P) increase. Since the TES is voltage biased, V remains constant while R (and P_{Joule}) decreases keeping the TES in a stable state.

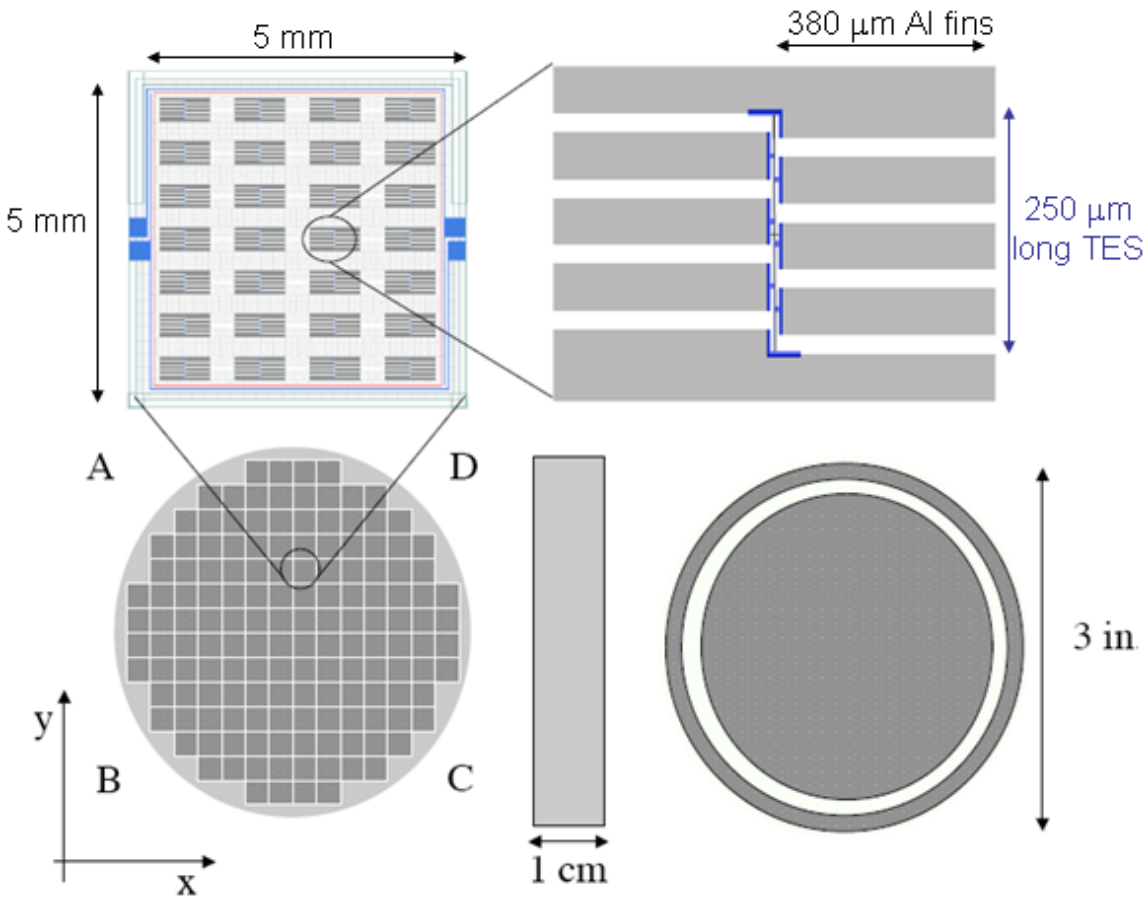

Figure 2.6: Schematic of the CDMS-II ZIP detector configuration. *Bottom right:* detector ionization face depicting the inner and outer electrodes. *Bottom left:* detector phonon face illustrating the large-scale photolithographic patterning, naming scheme of the four sensor quadrants (A-D), and the x-y reference coordinate system. *Top left:* close-up of one of the 37 "dies" making up each of the phonon sensors. Each die consists of 28 individual Quasiparticle-assisted Electrothermal-feedback Transition-edge sensors (QETs). *Top right:* a single QET consisting of a 1 μm wide by 250 μm long tungsten Transition-Edge Sensor (TES) connected to 8 aluminum collection fins.

Figure 2.6 shows the configuration of the CDMS-II ZIP detector. This figure illus-

trates the geometry of both the ionization and phonon channels. The top schematics show the 37 "dies", each with 28 individual quasiparticle-assisted electrothermal-feedback transition-edge sensors (QETs), that make up the phonon sensors and a single QET with its 8 aluminum collection fins around the tungsten TES [68].

2.4 Ionization Measurement

Besides creating phonons, particle interactions deposit energy into the electronic system. Valence electrons are liberated from bound states into the conduction band when there is sufficient energy, on the order of the semiconductor band gap. While the germanium (silicon) band gap is only 0.743 eV (1.12 eV), it is an indirect gap and 3.0 eV (3.8 eV) is required to generate an electron-hole pair.

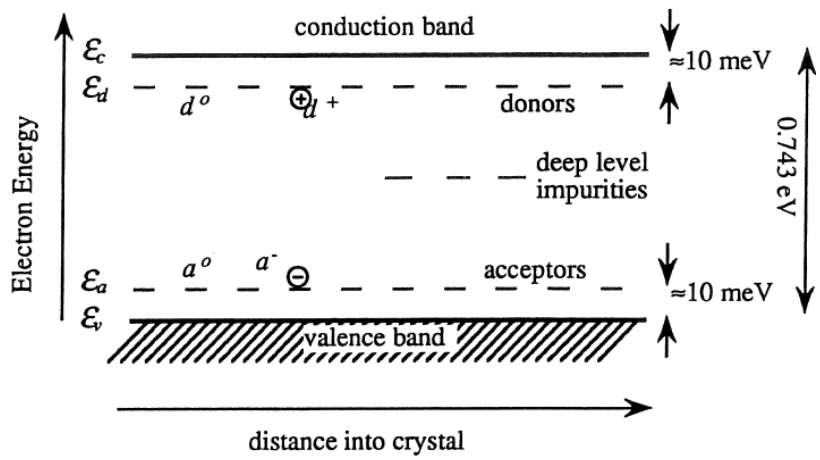

Figure 2.7: Diagram of germanium energy bands and levels. From [12].

Initially the freed electrons undergo quasi-diffusive motion near the interaction site. By applying an electric field across the detector, charge carriers are drawn across the crystal before they can recombine or diffuse into a trap (localized energy state in the band gap, see Figure 2.7). As the electron and hole charge carriers drift across the crystal they induce image charge on the conducting electrodes and a voltage across the coupling capacitor C_C in the ionization read out circuit (Figure 2.8). The feedback capacitor C_F is charged to maintain zero voltage at the amplifier input (and

subsequently discharged through the feedback resistor R_F). The measured ionization signal is created at the feedback capacitor [13].

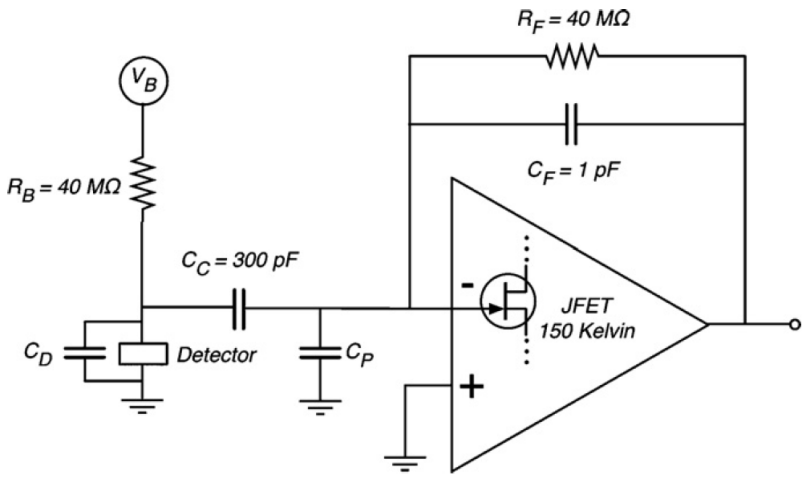

Figure 2.8: Schematic of the CDMS charge amplifier. From [13].

Since the ionization signal is proportional to the distance traveled, charge carrier recombination and trapping reduce the measured energy. Therefore it is critical to apply a sufficiently strong electric field to overcome these mechanisms. Field-dependent ionization collection in 1 cm thick germanium (silicon) devices has been studied and is shown in Figure 2.9a (Figure 2.9b) [12, 14]. These studies show that full ionization collection at mK temperatures is achieved in 1 cm thick germanium (silicon) devices by ∼200 mV/cm (<2 V/cm). This is well below the operational bias of -3 V (-4 V).

2.5 Ionization Yield Discrimination

Nuclear recoils produce fewer electron-hole pairs than electron recoils with the same phonon recoil energy. Thus the simultaneous measurement of both phonon and ionization energy allows event-by-event discrimination between bulk electron recoil background and nuclear recoil signal events.

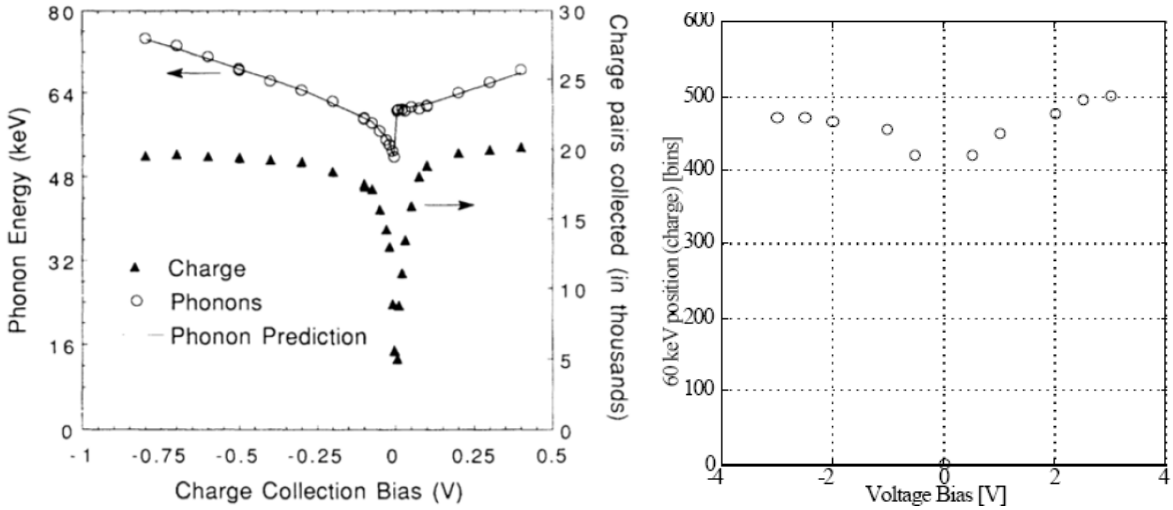

(a) (b)

Figure 2.9: Absolute ionization collection of 60 keV photons as a function of applied electric field for 1 cm thick (a) germanium and (b) silicon devices. This shows that full ionization collection is achieved in germanium (silicon) devices by ∼200 mV/cm (<2 V/cm), well below current operational bias voltages. Additionally (a) shows the agreement between the observed (circles) and predicted (curve) phonon amplitude based on phonon recoil and Luke phonon production. From [12, 14].

CDMS's primary discrimination parameter is ionization yield, defined as the ratio of ionization to phonon recoil energy:

$$y \equiv \frac{E_Q}{E_r} = \frac{E_Q}{E_P - E_L} = \frac{E_Q}{E_P - \frac{eV_b}{\epsilon} E_Q} \tag{2.8}$$

where E_Q is the ionization energy, E_r is the phonon recoil energy, E_P is the total phonon energy, E_L is the Luke phonon energy, e is the magnitude of the carrier charge, V_b is the applied bias voltage across the detectors, and ϵ is the average energy to produce an electron-hole pair (3.0 eV in germanium and 3.8 eV in silicon). E_Q is calibrated to be equal to E_r for electron recoils. Therefore electron recoils have an ionization yield ∼1 while nuclear recoils have ionization yield ∼0.3 due to the production of less ionization energy. Figure 2.10 plots ionization yield as a function of phonon recoil energy for calibration data sets showing the discrimination power of ionization yield, rejecting electron recoils $>10^4$.

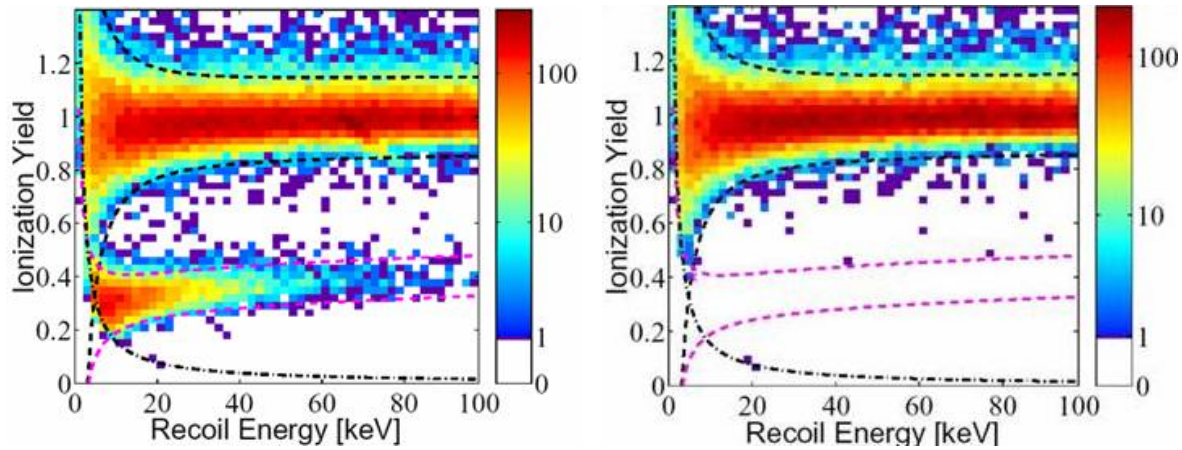

(a) (b)

Figure 2.10: Density plots showing ionization yield as a function of phonon recoil energy. The dashed curves represent the $\pm 2\sigma$ electron recoil (upper) and nuclear recoil (lower) bands as defined by calibration data. (a) Density plot of electron and nuclear recoil events from a ^{252}Cf neutron calibration source. (b) Density plot of electron recoil events from a ^{133}Ba gamma calibration source. After removing the neutron source the nuclear recoil band is clear of any events. This illustrates the ionization yield electron recoil rejection power of $>10^4$.

2.6 Charge Trapping

Ideally, ionization yield would provide complete discrimination of electron recoils. However that is not the case and one of the most significant sources of backgrounds in CDMS detectors is due to charge trapping. This trapping can occur through several mechanisms, either in the bulk or at the surface of the crystal. In both cases charge trapping reduces the total ionization signal causing electron recoil background events to occur at lower ionization yield, looking like nuclear recoil signal events. This section discusses the physics behind surface and bulk charge trapping and then describes how these events are rejected.

2.6.1 Surface Trapping, Dead Layers, and Phonon Timing Discrimination

Surface trapping creates a "dead layer," which is characterized by interactions with incomplete charge collection, along the flat detector faces. This surface trapping is caused by the back-diffusion of charge carriers into the adjacent ionization electrode (Figure 2.11). When a particle interaction occurs, freed electrons and holes gain kinetic energy. In order to separate and drift charge carriers to the electrodes, an applied electric field must overcome the initial kinetic energy imparted to the charge carriers. If the interaction occurs near the detector surface the electric field is not strong enough to separate all the charge carriers before some reach the adjacent ionization electrode. Since these carriers do not drift across the crystal they do not contribute to the ionization signal, therefore causing a reduction in the total ionization energy measured for that interaction.

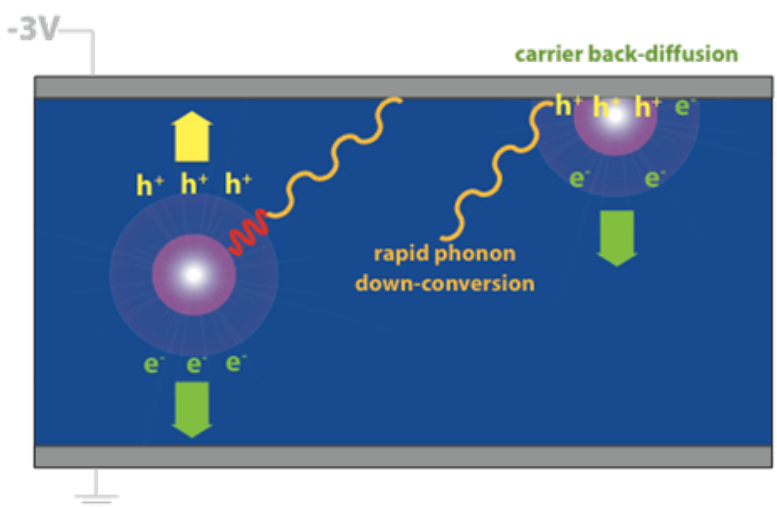

Figure 2.11: Cartoon depicting events occurring in the ZIP detector bulk (left) and surface (right). Electron (e^-) and hole (h^+) charge carriers from the bulk event are fully collected while some from the surface event may be lost in the adjacent electrode. The metal at the surface also causes high-frequency phonons (red curve) to quickly decay to low-frequency ballistic phonons (orange curve). From [15].

Another effect that impacts the dead layer is geometric. After an interaction free electron and hole carriers are initially confined to a spherical volume of radius R_p.

With time this sphere expands as the carriers move diffusively until the applied electric field drifts the electrons and holes in opposite directions. Since the charge carriers are not produced in an infinitely small region, if an interaction occurs at a distance from the surface (R) that is smaller than the charge cloud (R_p) a reduced number of carriers will be freed (Figure 2.12), [16] leading to a reduction in the ionization signal. Kyle Sundqvist is currently studying the magnitude of this effect, including a comparison with back-diffusion and a determination of R_p, through simulation and data comparison.

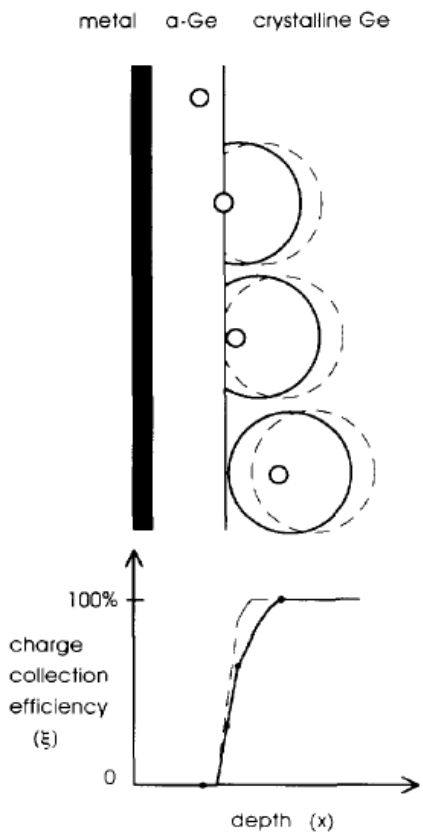

Figure 2.12: Illustration of the geometric effect of the charge carrier cloud which reduces ionization collection near the detector surface. The dashed curve shows how the carrier cloud moves away from the surface with time and the subsequent reduction in the dead layer depth (bottom). From [16].

Adding amorphous silicon between the detector crystal and aluminum layer reduces the size of the dead layer. This occurs because the effective amorphous silicon band gap is larger than the germanium and silicon band gaps and acts as a blocking

layer to low energy charge carriers [69, 70]. While this solution reduces the dead layer, electron recoils occurring in the first ∼5-10μm (depending on detector side and applied electric field) of the detector surfaces still suffer low ionization yield that can mimic the bulk nuclear recoil signal (Figure 2.13). These surface electron recoils are rejected by taking advantage of phonon timing information.

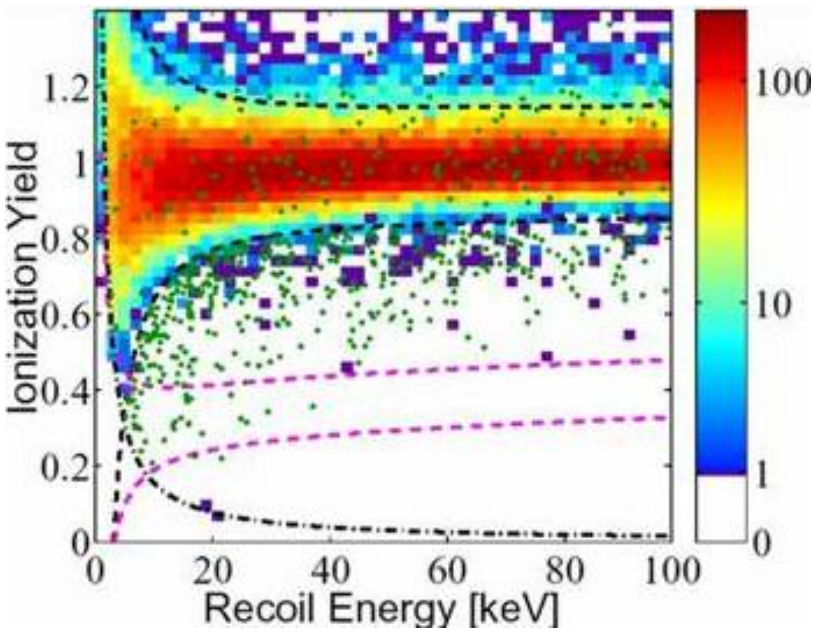

Figure 2.13: This plot shows the same density plot of ionization yield as a function of phonon recoil energy for electron recoil events from a ^{133}Ba gamma calibration source as Figure 2.10b. Additionally this plot shows electron recoil surface events (green points representing single events) that have reduced ionization yield.

As discussed in Section 2.3.1, primary phonons are produced at high frequencies and propagate quasi-diffusively until they decay to lower energies and travel ballistically through the crystal. Primary phonons reaching metal detector surfaces rapidly decay to lower energies and enter the ballistic regime faster than bulk primaries. This causes a difference in the phonon timing distributions between bulk and surface interactions which is used to reject between surface events (Figure 2.14).

Phonon timing discrimination primarily relies on two parameters, the phonon delay and risetime from the primary phonon channel, the channel with the largest phonon signal and the sensor under which the event occurred (Figure 2.15). Phonon

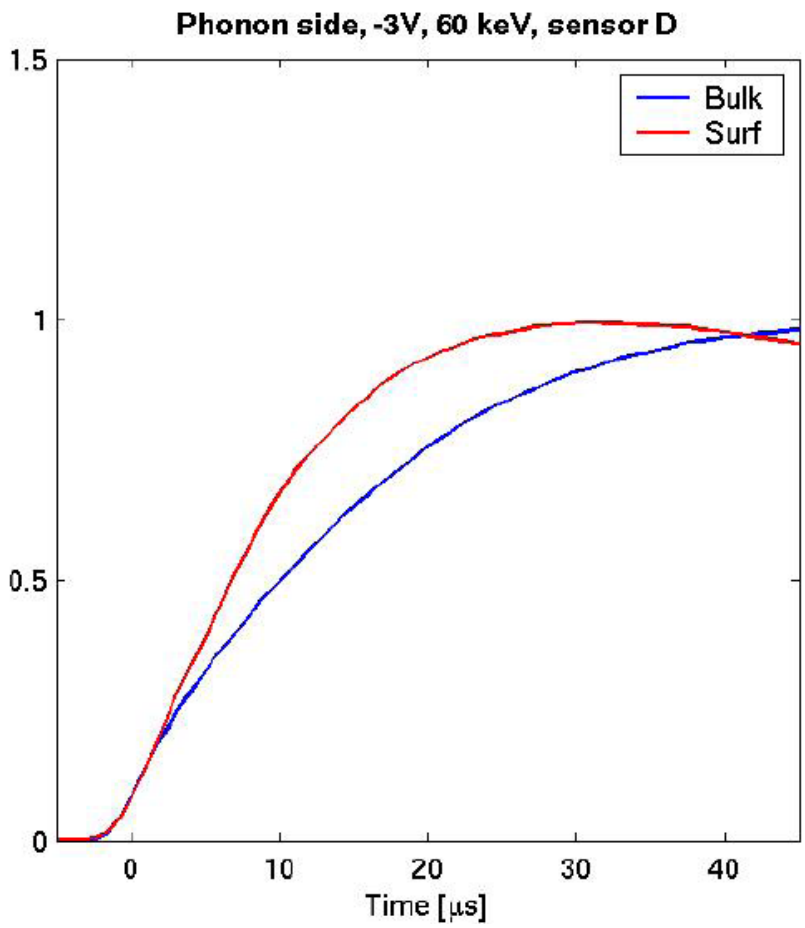

Figure 2.14: Comparison of the leading edges of the primary phonon pulse from 60 keV bulk (blue) and surface (red) electron recoil events.

delay is defined as the difference between the start of the ionization and primary phonon pulses. In this definition the start of the primary phonon pulse is taken to be the point on the pulse's rising edge where the amplitude is 20% the maximum height. Phonon risetime is defined as the difference between the 10% and 40% points along the primary phonon pulse's rising edge. During the Soudan 2-tower and 5-tower data analyses, the phonon "timing parameter" used to discriminate surface events was the sum of the primary phonon delay and risetime (Section 5.4.6).

Using phonon timing discrimination along with ionization yield increases the overall electron recoil rejection to $>10^6$. Figure 2.16 illustrates the power of using both ionization yield and phonon timing information to discriminate between electron and nuclear recoils.

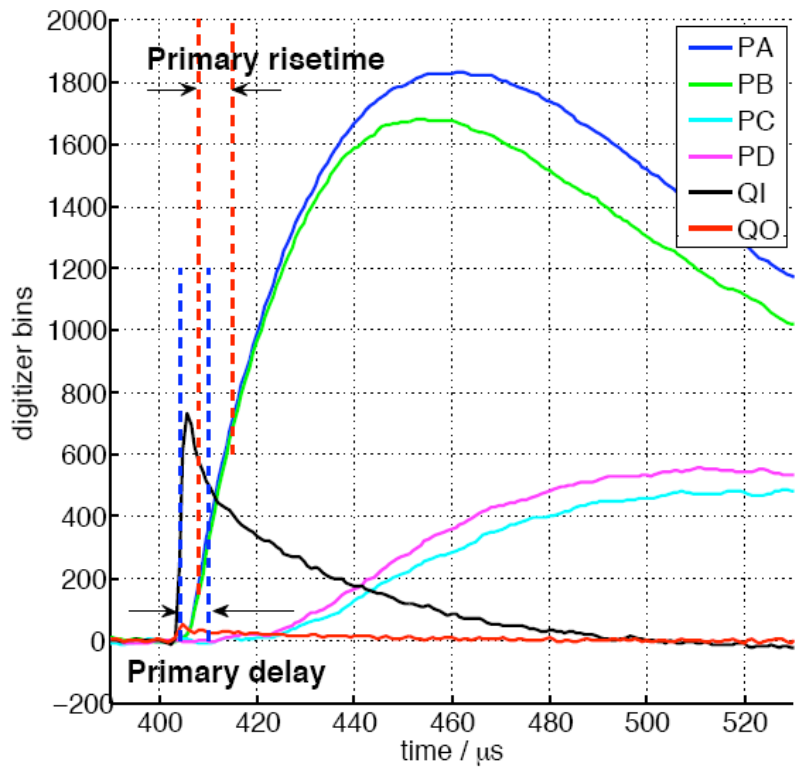

Figure 2.15: Raw ionization and phonon pulses illustrating the phonon delay and risetime parameters. Channel A (blue), the largest and fastest phonon pulse, is the primary phonon channel and the channel where the event occurred. The blue vertical dashed lines represent phonon delay, the difference between the ionization and primary phonon pulse start times. The red vertical dashed lines represent phonon risetime, the difference between the 10% and 40% points on the primary phonon pulse rising edge.

2.6.2 Bulk Trapping and Neutralization

Bulk trapping reduces the ionization signal (Figure 2.17) by trapping charge carriers at impurities caused by crystal lattice defects. This bulk trapping is a dynamic process due to both impact ionization and Coulomb attraction. If the detector crystal begins in a "neutralized" state, where all of the impurity sites have no net charge, some free charge carriers have enough energy to impact ionize at the impurity, knocking out a weakly bound electron, and ionizing the impurity. As charge carriers continue to drift, some carriers have low enough energy so as not to impact ionize but rather get attracted, and trapped, at the ionized impurity. In order to fully understand and model these processes, it is necessary to understand the charge carrier energy

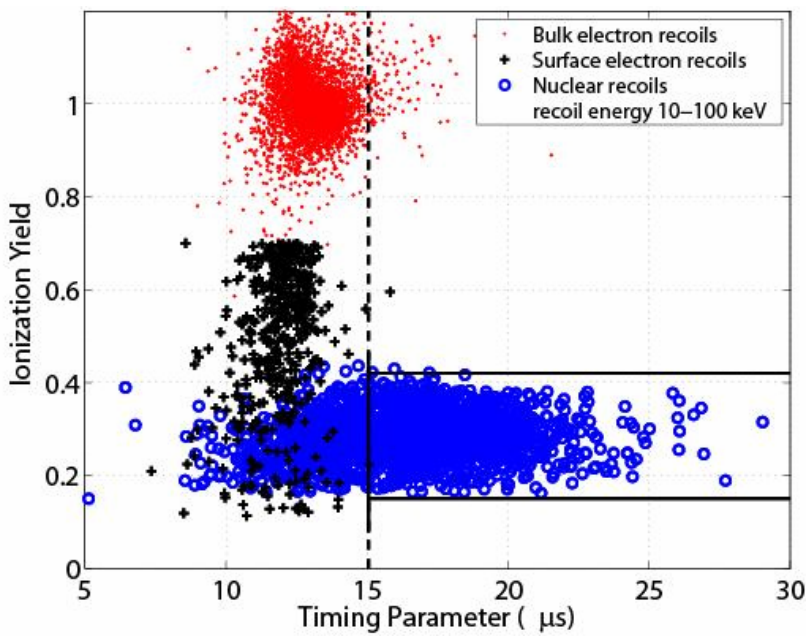

Figure 2.16: Ionization yield as a function of the phonon timing parameter showing the ZIP detector electron recoil discrimination power. Plotted here is calibration data from one of the Soudan germanium detectors. Red dots are bulk electron recoils and black crosses are surface electron recoils from ^{133}Ba calibration data while blue circles are nuclear recoils from ^{252}Cf calibration data. The vertical dashed line indicates the minimum value of the phonon timing parameter allowed for candidate dark matter events and the box shows the approximate signal region combining both ionization yield and phonon timing discrimination. From [17].

distribution to determine the numbers of particles which impact ionize and undergo Coulomb attraction. As an aside, impact ionization at an impurity site is possible with either electron or hole carriers, depending on energy and cross sections (there are 8 different cross section cases to consider, all combinations of charge polarity, impurity polarity, and electric field polarity). In addition, holes have more energy to impact ionize than electrons [71, 72]. Besides impact ionization and Coulomb attraction, other mechanisms that can affect charge collection include: built-in and time-varying electric fields, ionized regions in the bulk, and physical material contacts where charge layers or impact ionization occur [73, 74].

In order to reduce the impact of bulk trapping, CDMS detector crystals have low impurity and dislocation concentrations ($\sim 10^{10-11}$ impurities/cm^3 and $<$5000 dislocations/cm^2 in germanium). Operationally, data taking occurs on time scales

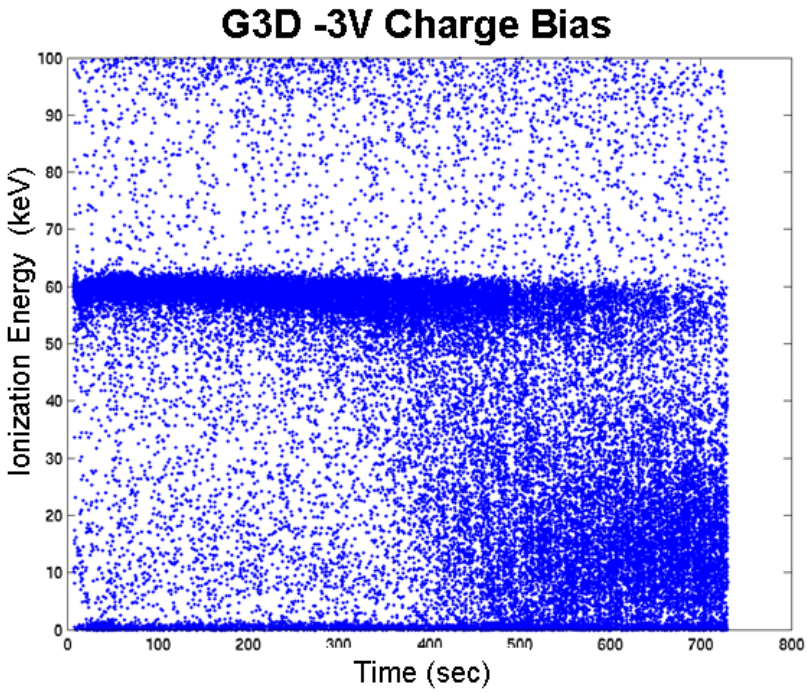

Figure 2.17: Ionization collection as a function of time for 60 keV ^{241}Am events taken at a test facility. This shows reduced ionization collection after a period of time as the detector becomes "de-neutralized" due to bulk trapping.

shorter than the time when bulk trapping affects ionization collection. In addition, detectors routinely undergo a neutralization process to reduce the effects of bulk trapping (Figure 2.18). During the neutralization process detectors are grounded while excess electrons and holes are generated. These free charge carriers execute a random walk through the crystal undergoing Coulomb attraction with ionized impurity sites which neutralize these sites. This minimizes bulk trapping because neutral impurity sites have a lower trapping cross section than ionized sites. Details on how neutralization is executed using internal infrared LEDs and external radioactive sources can be found in Chapter 6.

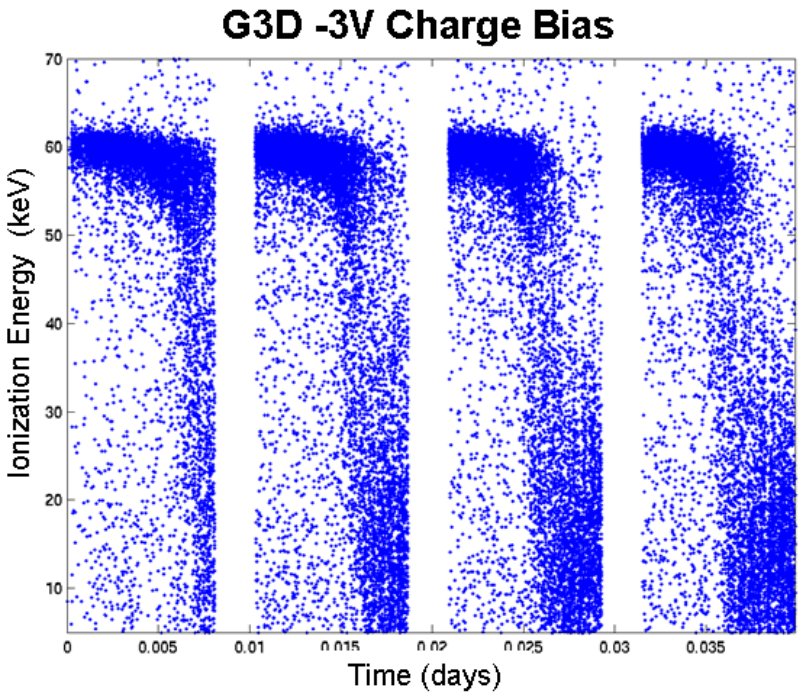

Figure 2.18: Like Figure 2.17 the plot shows ionization collection as a function of time for 60 keV ^{241}Am events taken at a test facility. Neutralization occurred during the periods of time showing no events. Notice how, despite losing full ionization collection prior to neutralization, after neutralization full ionization collection is regained.

Chapter 3

CDMS-II Experimental Setup in the Soudan Underground Laboratory

3.1 Introduction

While the CDMS detection technique achieves discrimination between electron and nuclear recoils (Chapter 2), the experimental location and setup were designed to satisfy additional requirements (outlined in Section 1.4) necessary for a successful direct detection WIMP search experiment. Specifically the experimental environment reduces the event rate of background interactions and maintains stable operation. This chapter describes the CDMS location, setup, shielding, and readout.

3.2 Location - Soudan Underground Laboratory

The CDMS-II experiment has operated in the Soudan Underground Laboratory since 2003. The Soudan Underground Laboratory is in the Soudan Underground Mine State Park (Figure 3.1), an old iron mine located in the Iron Range region of northern Minnesota, about a 3.5 hr drive north of Minneapolis. CDMS is located in the physics laboratory 2341 ft (713 m) below the surface, at a water equivalent depth of

2090 m. This underground location is important because the rock overburden above the experiment reduces the cosmic ray muon flux by a factor of ∼50,000 from its value at the surface. This flux reduction decreases the number of neutrons generated through muon-induced particle showers (see Section 5.6.1), limiting the background rate experienced by the detectors and increasing the experimental sensitivity.

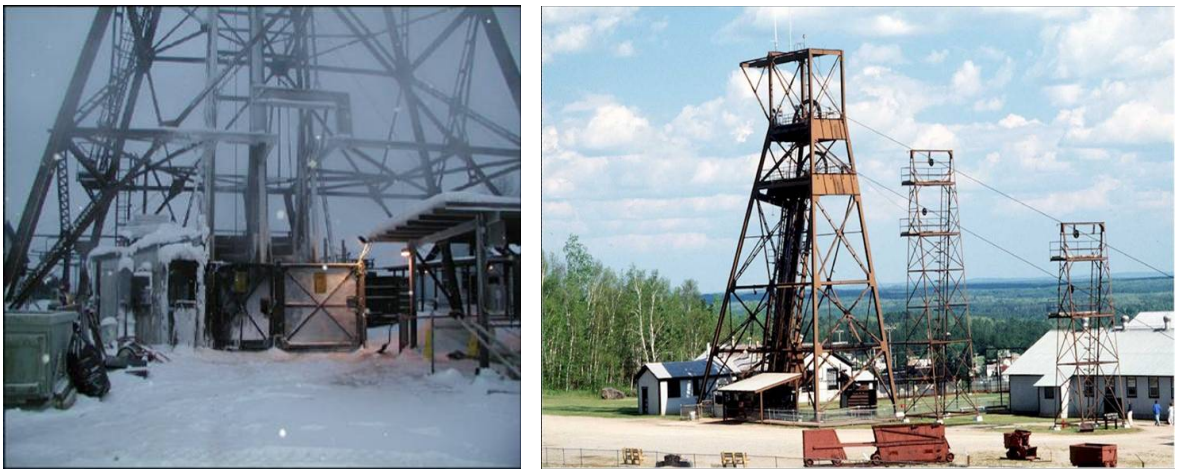

(a) (b)

Figure 3.1: Photos of the headframe at the Soudan Underground Mine taken in (a) winter and (b) summer.

3.3 Cryogenics

Detectors are cooled by an Oxford Instruments 400S ^{3}He-^{4}He dilution refrigerator to achieve the millikelvin temperatures necessary to operate the phonon sensors. To satisfy the requirements of having a large detector mass operated under stable conditions for long periods of time, and in a clean environment, a number of custom modifications were made to the refrigerator.

The detectors are located in a cold volume, called the "icebox," which is mounted beside the refrigerator. The icebox consists of nested, cylindrical copper cans thermally coupled to the various temperature stages of the dilution refrigerator. Each can is made from oxygen-free high thermal conductivity (OFHC), low-radioactivity cop-

per to minimize contamination that would produce backgrounds in the detectors. An additional copper cylinder connects the icebox to an electrical breakout box, called the "e-box," which allows wiring to run from the detectors in the cold volume out to room temperature. This entire setup resides inside an RF shielded class-10,000 clean room to maintain a clean, low-noise environment.

Additional readout electronics (Section 3.6) for both the detectors and veto (Section 3.4) systems are located outside the RF room in an electronics room.

Vacuum pumps, cryogenic supplies, and control systems are placed outside the RF room on the "cryo-pad." To sustain system stability at all times, even when not underground, there are several systems that continuously monitor temperatures, pressures, and flows in the refrigerator. In the case of abnormal readings, email and phone warnings are automatically issued to people on site ("shift-takers"). Additionally, liquid helium and nitrogen cryogen transfers are programmed to automatically occur as necessary.

Figure 3.2 shows a schematic of the CDMS experimental setup at the Soudan site.

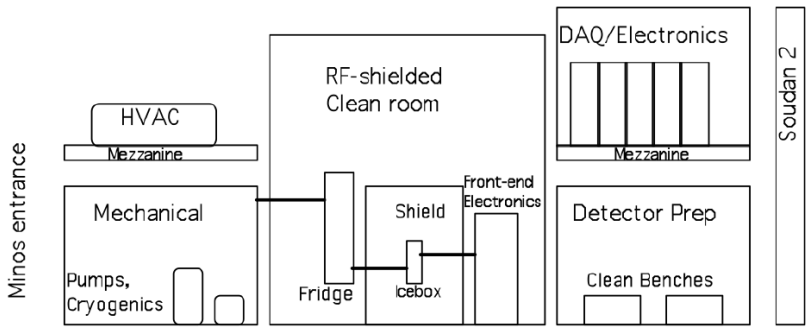

Figure 3.2: Schematic of the CDMS experimental setup at the Soudan site.

3.4 Shielding

While the rock overburden at the experimental location reduces the cosmic ray muon flux, the CDMS cryostat is surrounded by additional layers of passive and active

shielding (Figure 3.3) to further reduce the rate of cosmogenic and radioactive particles.

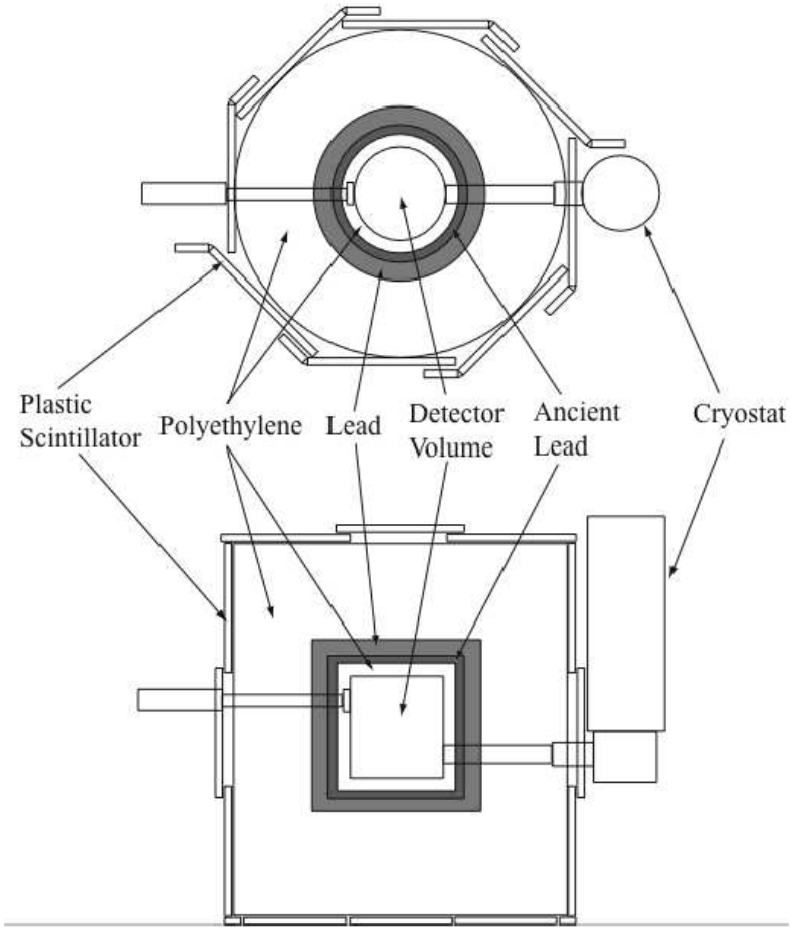

Figure 3.3: Schematic of the active and passive shielding surrounding the icebox at the Soudan site. This drawing shows the refrigerator (right), icebox (middle), and electronics e-stem (left). From closest to the detector volume the icebox is surrounded by a layer of polyethylene, ancient lead, ordinary lead, polyethylene, and finally the active muon veto. From [18].

The outermost shield is an active veto used to tag muons and particle showers originating outside the cryostat. This shield consists of 40 scintillator panels that provide almost 100% coverage around the icebox. Each panel is a 5 cm-thick sheet of plastic scintillator with one or two 2 inch R329-02 photomultiplier tubes. Any events that are coincident with this veto are rejected (Section 5.4.1).

Inside the active veto are several layers of passive shielding. The first of these

layers is 40 cm of polyethylene. This moderates low-energy neutrons preventing them from causing nuclear recoils above the detector energy threshold. Within the polyethylene is 22.5 cm of lead bricks used to shield the detectors from external gamma rays. Since normal lead itself is noticeably radioactive the inner 4.5 cm is made up of low-activity "ancient" lead that was recovered from a sunken ship. The innermost layer of shielding is made of another 10 cm of polyethylene for additional neutron moderation. This is particularly important for moderating neutrons generated by fissions and spallation processes within the lead.

As mentioned in Section 3.3, the icebox is made of a series of nested copper cans. Between this copper, and the other copper surrounding the detectors (Section 3.5), the total thickness is sufficient to stop alpha and beta radiation from outside the cans.

A final technique used to decrease the detector background rate is to purge the volume of air inside the lead shield with either "old" air or nitrogen. This reduces the radon level in the volume nearest the detectors from the relatively high level ($\sim$700 Bq/m^3) found in the laboratory. Even though the detector volume is maintained at vacuum, this continuous purge has been found to reduce the detector gamma rate by a factor of $>$4 and cut the surface event rate in half.

3.5 Cold Hardware

The requirements of maintaining a low background environment at millikelvin temperatures presents a challenge for creating the detector support and wiring structures. Cold hardware are the components inside the cryostat used for detector mounting and readout [13]. To maintain low backgrounds it is necessary to use radioactively pure materials for all these parts. In addition, the unique low temperature environment requires careful material selection to ensure the creation of either solid thermal joints or thermal isolation as appropriate.

Figure 3.4 shows a schematic of the detector assembly and readout inside the

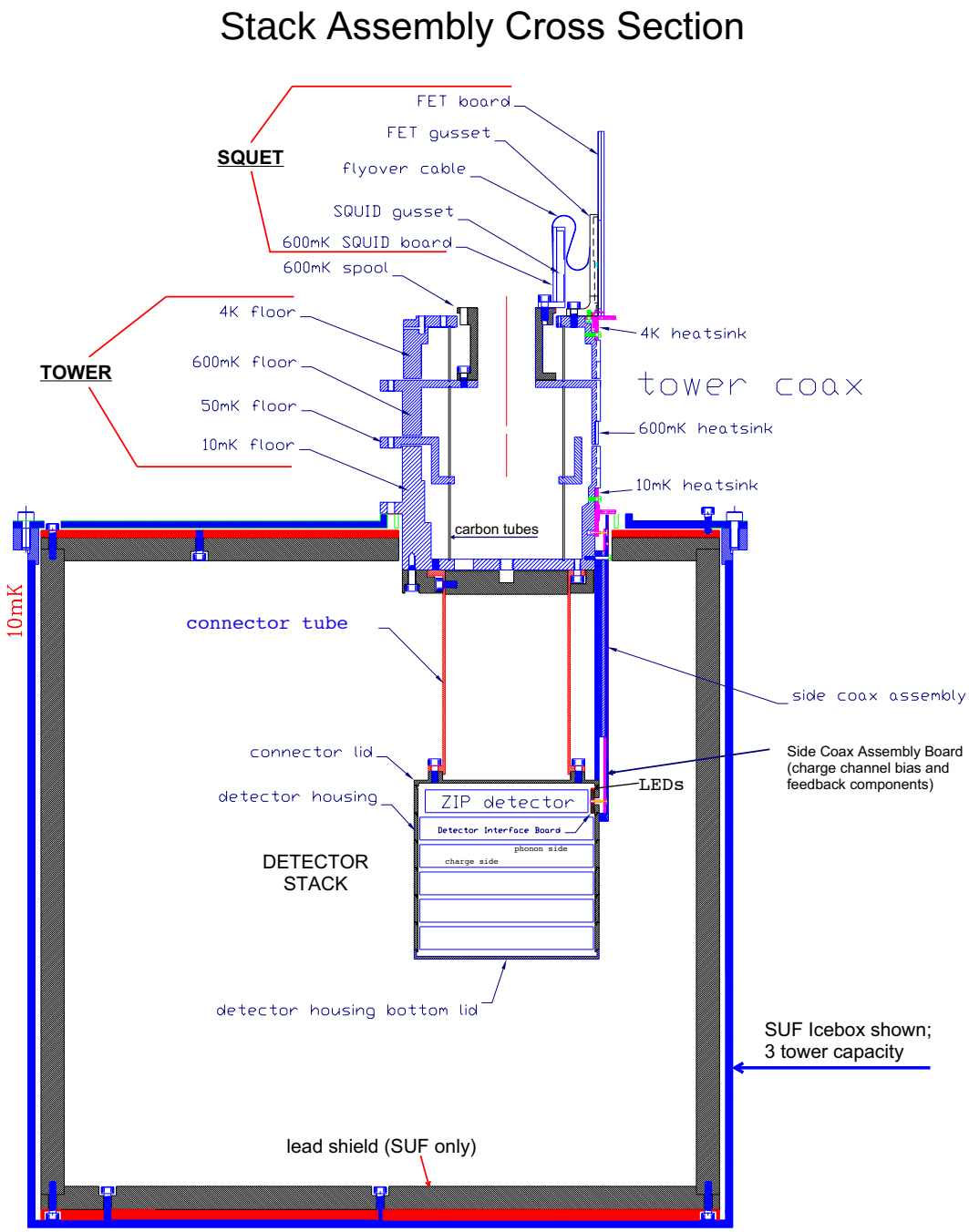

Figure 3.4: Schematic of a tower assembly in the innermost icebox can along with the cold hardware discussed in this section. Note that the icebox shown in this drawing is the one previously used at the Stanford Underground Facility (SUF). The major different between the icebox at the Stanford and Soudan sites is that the Soudan icebox can hold seven Towers and does not have inner lead or polyethylene (not shown) shields. Courtesy of Dennis Seitz.

innermost copper icebox can. Detectors are mounted in copper housings. Six detectors are stacked on top of one another and attached to the tower support structure. Wiring travels from the detector to the side coax, tower, SQUET card, and stripline out to room temperature through the e-box. These individual components of cold hardware are each described briefly in this section.

3.5.1 Detector Housing

Each detector is mounted in a hexagonal ring-shaped housing made of high-purity copper (Figure 2.1). A detector interface board ("DIB") is located on one of the hexagonal surfaces allowing the signal to travel from the detector to the side coax. The DIB also houses LEDs (Appendix A) used for detector neutralization.

Six detectors are mounted on top of each other to form the detector stack, which is attached to the tower. Within a single stack there is no material between the flat detector faces, 3.5 mm away from each other. This increases the proportion of events, especially due to radioactive contamination, that scatter in multiple detectors. These events are easily rejected by a multiplicity cut during the analysis (Section 5.4.3).

3.5.2 Tower

The tower (Figure 3.5a) is the main detector support structure, thermally and mechanically connecting the detectors to the refrigerator.

Physically the tower is a hexagonal copper structure composed of four copper stages. These copper stages are mechanically held together by central thin-wall graphite tubes which maintain relative thermal isolation. Each copper stage is heat-sunk to the 4 temperature stages of the dilution refrigerator (mixing chamber, cold plate, still, and 4 K) through the icebox cans and "cold" stem.

Each hexagonal surface is called a tower face and corresponds to one of the six detectors. The tower face contains wires which connect the side coax and SQUET card.

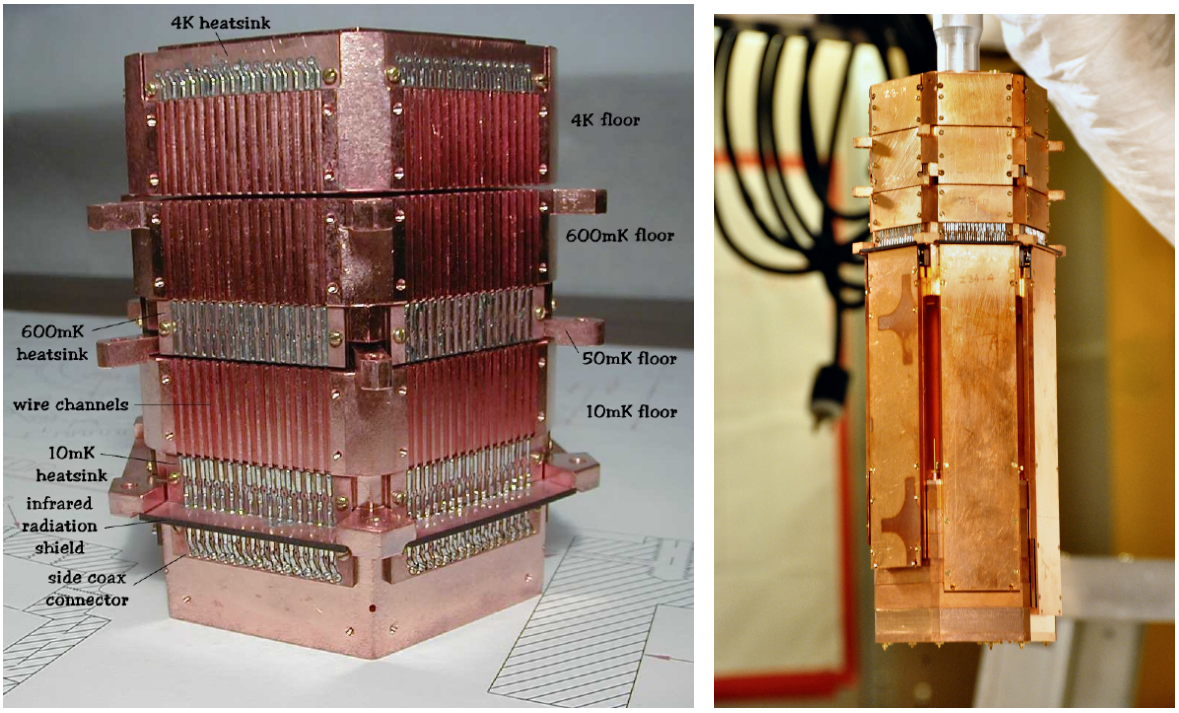

(a) (b)

Figure 3.5: (a) Photo of a tower. Picture and annotations courtesy of Dennis Seitz. (b) Photo of an assembled "tower" with the tower and detector stack along with the side coaxes connecting the two.

To reduce microphonics, these wires running along each tower face are tensioned. The wires are also heat sunk at the mixing chamber ("10 mK"), still ("600 mK"), and 4 K temperature stages to maintain the necessary thermal profile.

While the term "tower" technically only refers to the copper support structure described here, it is also commonly used for the entire detector assembly including the tower and detector stack as shown in Figure 3.5b.

3.5.3 Side Coax

A side coax (Figure 3.6a) connects each detector to its respective tower face. The side coax is a rigid structure made of copper with tensioned wires, like the tower faces, to carry phonon and ionization signals. Additionally, the coupling capacitors and bias and feedback resistors for the charge amplifiers are mounted in the side coax, which is

at base temperature, so that the Johnson noise contribution to the ionization signal is reduced.

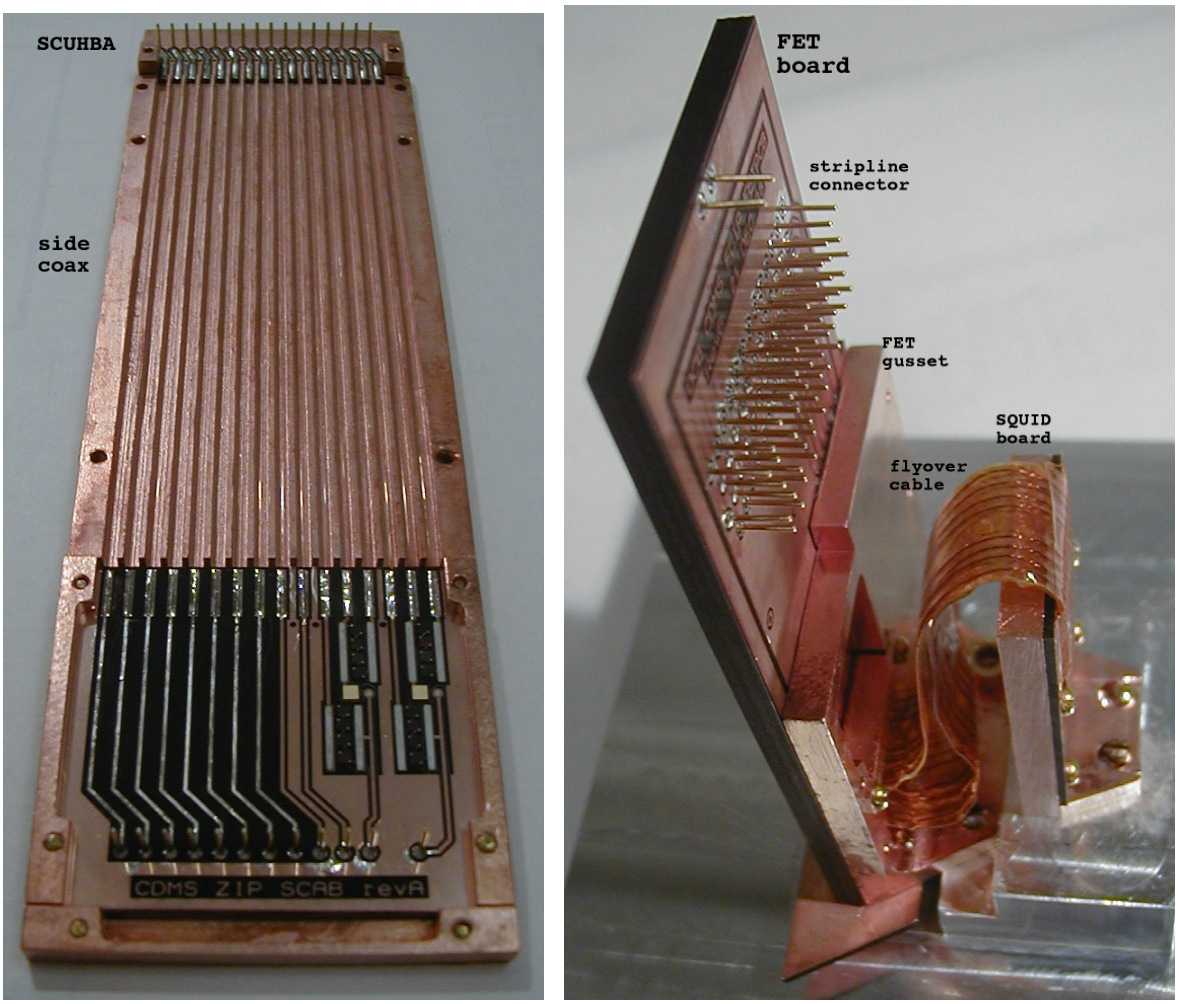

(a) (b)

Figure 3.6: (a) Photo of a side coax. (b) Photo of a SQUET with the separate FET (left) and SQUID (right) cards connected by a copper and kapton "fly-over" cable. Picture and annotations courtesy of Dennis Seitz.

3.5.4 SQUET

The SQUET card (Figure 3.6b) gets its name from housing both the SQUIDs for the phonon readout and FETs for the ionization readout. The SQUET is made up of two cards, one which holds the FETs and the second where the SQUIDs, shunt resistors,

and input and feedback coils of the phonon amplifiers are mounted. The larger FET card is mechanically and thermally connected to the tower on the 4 K thermal stage while the SQUID card is mounted to the 600 mK stage to improve SQUID signal-to-noise. On the FET card, the FETs themselves are thermally isolated by a kapton membrane within a copper bracket (or "gusset"). This allows the FETs to self-heat to their operating temperature of ∼140 K, where the FET noise is at a minimum, while applying a minimal heat load to the 4 K thermal stage.

3.5.5 Stripline

Finally the cold hardware is linked to the warm electronics by striplines (Figure 3.7). A stripline is a 3 m long flexible circuit made of kapton and copper. Each consists of 50 copper traces between 2 copper ground planes, all surrounded by kapton insulation. One stripline is used for each detector, connecting the SQUET card to the e-box.

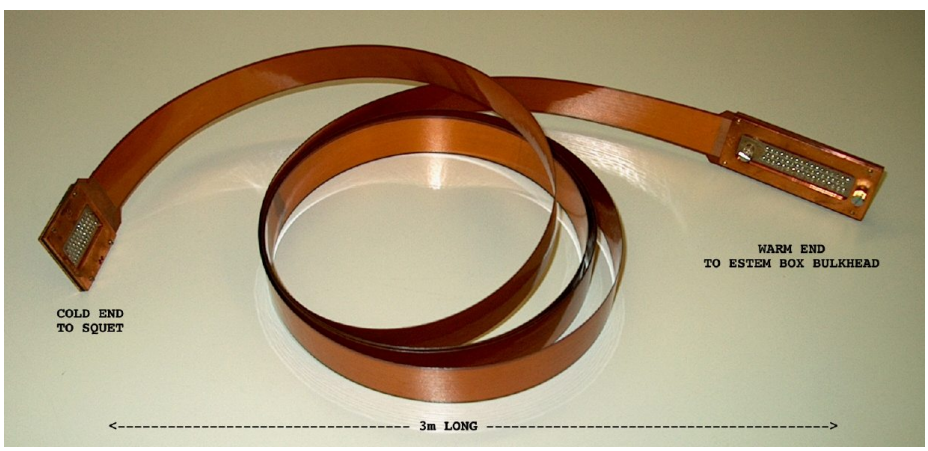

Figure 3.7: Photo of a stripline. Picture and annotations courtesy of Dennis Seitz.

3.6 Warm Electronics

On the warm end of the e-box the detector signal goes through a series of electronics boards containing readout circuits, signal filtering, triggering, and digitization.

The first warm electronics board the signal enters is the front-end board, or "FEB." This board is located in the RF clean room and connected directly to the e-box connectors through 50-wire cables. The FEB holds the second- and later-stage amplifiers and other components of the charge and phonon readout circuits. Besides containing signal readout electronics, the FEB also holds the control circuits for biasing the FETs, SQUIDs, TESs, and LEDs. All control is handled by the data acquisition system (Section 3.7) through GPIB (General Purpose Interface Bus) control.

After passing through the FEB, the signal goes through the receiver-trigger-filter ("RTF") board. This board is located outside the clean room in the electronics room. The RTF board filters the signal and generates 5 logic-level trigger signals, P_{hi}, P_{lo}, $P_{whisper}$, Q_{hi}, and Q_{lo}. P_{lo} is the primary trigger used during data taking, issued when the sum of the four phonon signals exceeds the software defined threshold set just above the noise level, typically 3-4 mV. P_{hi} and $P_{whisper}$ are similar to P_{lo} except with different thresholds. The P_{hi} threshold is set much higher ($\sim$500 mV) to be used to reject high-energy events while the $P_{whisper}$ threshold is set lower than P_{lo} to be used for tagging multiply-scattered events. Q_{hi} and Q_{lo} are similar to P_{hi} and P_{lo}, only for the summed ionization signals.

The trigger logic board determines when to initiate data acquisition and issue a "global" trigger. A global trigger is issued by:

- A P_{lo} trigger from any detector
- A "veto multiplicity" trigger where there is a simultaneous hit in multiple veto panels. This is used for muon background characterization and event rejection
- A "random" trigger issued at the beginning and end of a data set, as well as intermittently during data taking. These are used to measure and monitor the noise environment and detector performance

When a global trigger is broadcast, all ionization and phonon channels are recorded by an array of 14-bit Struck SIS 3301 analog-digital converters and written to disk. These Struck digitizers operate at 1.25 MHz and record a 1.6 ms trace, including 409 μs preceding the trigger.

3.7 DAQ and Data Handling

The Soudan data acquisition system (DAQ) is controlled by a system of JAVA and C++ programs that are described in detail in [75]. There is full data acquisition control from both underground in the mine and from the local surface control building at the Soudan site. Remote monitoring of the system is available off-site.

Raw data is stored to local disks in the mine and then transferred to the surface cluster of computers (the Soudan Analysis Cluster or "SAC") and written to tape. Initial data processing occurs on the SAC immediately after transfer to the surface. This data is used for automatic and manual data quality checks (Section 4.6). The final data processing is done on the Fermilab FermiGrid computing cluster.

Chapter 4

5-Tower Run

4.1 Introduction

The CDMS-II experiment began operation at the Soudan Underground Laboratory in 2003. The first data taken was from 1 tower between October 2003 and January 2004 [18]. An additional tower was added and data were taken with 2 towers worth of detectors between March and August 2004 [76, 77]. After the 2-tower data were complete, the CDMS-II target mass was more than doubled as an additional 3 towers were added to the Soudan icebox. This chapter discusses the Soudan system improvements, detector testing and selection for the new towers, and operation of the 5-tower runs at Soudan.

4.2 Detector Testing and Selection

Like the first two towers in the Soudan icebox, the last three towers are each comprised of a stack of six detectors. Before being installed in the Soudan icebox these detectors were tested and characterized [78]. Following the detector fabrication [59, 79] at Stanford University's Nanofabrication Facility, preliminary 77 K and 4 K electrical checks were completed. After successful initial evaluations the detector was sent to

either the University of California - Berkeley or Case Western Reserve University test facility. At these facilities the detector is cooled down to its operating temperature of approximately 20 mK in a ^{3}He-^{4}He dilution refrigerator for a thorough set of tests. These assessments include electrical and continuity checks, noise evaluations of all readout channels, and characterization of the tungsten superconducting transition temperature distribution in each phonon channel [80]. The W T_c mapping is a critical step in order to ensure optimal performance of the phonon channels. Based on the analysis of the W T_c distribution, detectors whose T_c's are too high or not uniform enough are doped with ^{56}Fe ions implanted into the detector surface [81, 82]. This ^{56}Fe ion implantation lowers the W transition temperature. W T_c gradients can be removed with this technique by varying the implantation dosage across the detector surface.

In addition to completing standard characterization measurements, test facilities perform studies with some detectors to gain information on device performance and discrimination. For example, before being installed in Tower 2 and placed in the Soudan icebox, the detector named G31 underwent an intensive series of studies at the UC Berkeley test facility [83, 79]. These tests probed the detector surface layers to provide important information regarding dead layer depths, surface event ionization yield and phonon timing discrimination, and input for which operating conditions produce the best detector performance. Test facility detector performance studies are also used to gain fundamental detector understanding, for research into modifications to improve discrimination in future detector designs, and assisting troubleshooting activities at Soudan. Studies aimed at detector fundamentals and detector R&D were completed at the Case Western test facility focusing on detector neutralization and ionization collection and are discussed in detail in Chapters 6 and 7.

Towers 3, 4, and 5 were built in February, July, and September 2004 with the best performing detectors that had been verified at that time. After each tower was constructed the entire assembly, including all of the detectors, was tested together

at one of the test facilities to check the configuration to be installed in the Soudan icebox.

Detector (Z)	Tower / ZIP	Detector Number	Detector Name
1	T1Z1	401	G6
2	T1Z2	402	G11
3	T1Z3	403	G8
4	T1Z4	404	S3
5	T1Z5	405	G9
6	T1Z6	406	S1
7	T2Z1	411	S14
8	T2Z2	412	S28
9	T2Z3	413	G13
10	T2Z4	414	S25
11	T2Z5	415	G31
12	T2Z6	416	S26
13	T3Z1	421	S17
14	T3Z2	422	G25
15	T3Z3	423	S30
16	T3Z4	424	G33
17	T3Z5	425	G32
18	T3Z6	426	G29
19	T4Z1	431	S12
20	T4Z2	432	G37
21	T4Z3	433	S10
22	T4Z4	434	G35
23	T4Z5	435	G34
24	T4Z6	436	G38
25	T5Z1	441	G7
26	T5Z2	442	G36
27	T5Z3	443	S29
28	T5Z4	444	G26
29	T5Z5	445	G39
30	T5Z6	446	G24

Table 4.1: Table of Soudan Detectors.

Table 4.1 lists the detectors used in the Soudan 5-tower runs. Each detector is given a name when it is fabricated. This name begins with a G or S denoting whether it is a germanium or silicon detector substrate and is followed by a number which references the order in which that detector was made. When built into a tower for installation in the Soudan icebox each detector gets a new name which refers to its

tower number and stack location. For example detector G31 is also known at T2Z5 because it is the fifth lowest detector in Tower 2.

4.3 Soudan Preparation

In order for the existing Soudan infrastructure to easily transition from 2 to 5 towers, there were several system upgrades. These improvements were important to enhance cryogenic stability, even with the additional demands placed on the system by the additional detectors and corresponding readout electronics.

Prior to installing the three new towers there were upgrades made to the vacuum system, computing infrastructure, and data acquisition and processing [15]. The cryogenic system was also improved with the addition of a Gifford-McMahon cryocooler. By adding this cryocooler the time between cryogen transfers was cut in half from approximately every 12 hours during Run 119 with 2 towers to about every 24 hours with 5 towers.

The three new towers, Towers 3, 4, and 5, were installed in the Soudan icebox during October and November 2004. Unfortunately, there were several major setbacks that delayed reaching base temperature and beginning data taking. These delays resulted from a blockage in the dilution refrigerator's circulation loop caused by a small piece of copper sinter between the 1 K pot and primary impedance, very high noise on the ionization channels due to vibrations from the cryocooler, and non-superconducting phonon channels due to poor thermal conductivity between the base temperature layers of the refrigerator and tower [15].

In order to fix the ionization channel noise and poor thermal conductivity, the refrigerator and detectors had to be warmed to room temperature. The ionization channel noise was dramatically improved (Figure 4.1) by replacing the hard couplings between the cryocooler drive head and the E-stem with annealed copper braids (Figure 4.2). Thermal conductivity between the refrigerator and tower base temperature

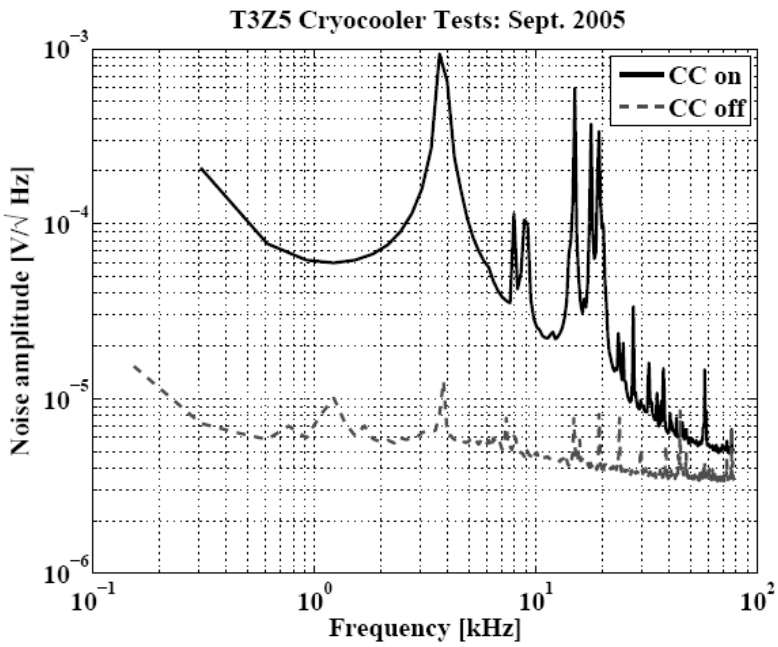

Figure 4.1: The inner ionization channel noise spectrum from T3Z5 taken with the cryocooler on (top, solid) and off (bottom, dashed). Notice the improvement in noise performance when the cryocooler is turned off. This was one indication that led to replacing the hard cryocooler couplings with annealed copper braids. From [15].

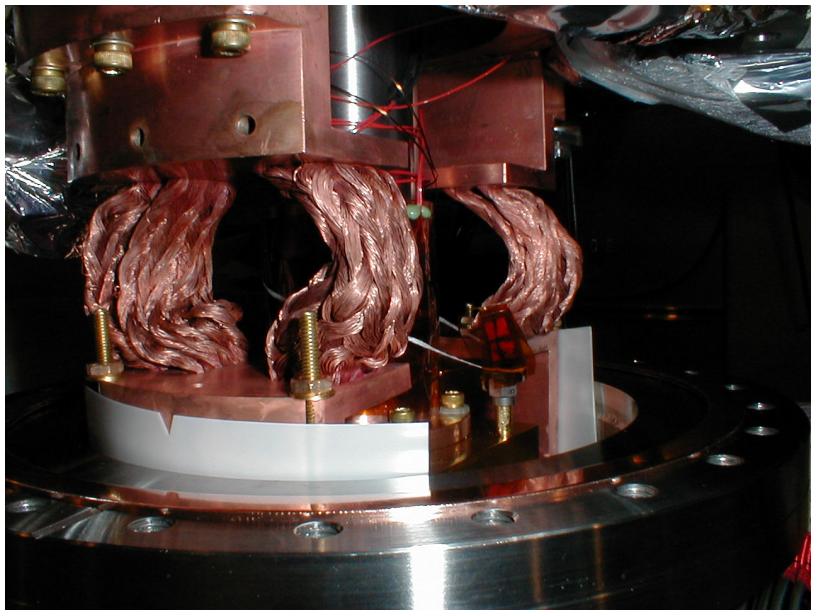

Figure 4.2: Photo of the annealed copper braids forming the flexible coupling between the cryocooler drive head and the E-stem.

layers was degraded due to the combination of two things: screws that were loosened by multiple thermal cyclings and copper-to-copper contacts that had an oxide layer formed on the surfaces (Figure 4.3a) and now sat between the metal. After opening the icebox to re-torque all screws and scrub the oxide off the copper surfaces (Figure 4.3b) which were used as thermal joints, the phonon channels acted as superconductors. The five towers (Figure 4.4) reached base temperature on June 26, 2006 after the dilution refrigerator repair and system modifications to fix the ionization channel noise and thermal conductivity.

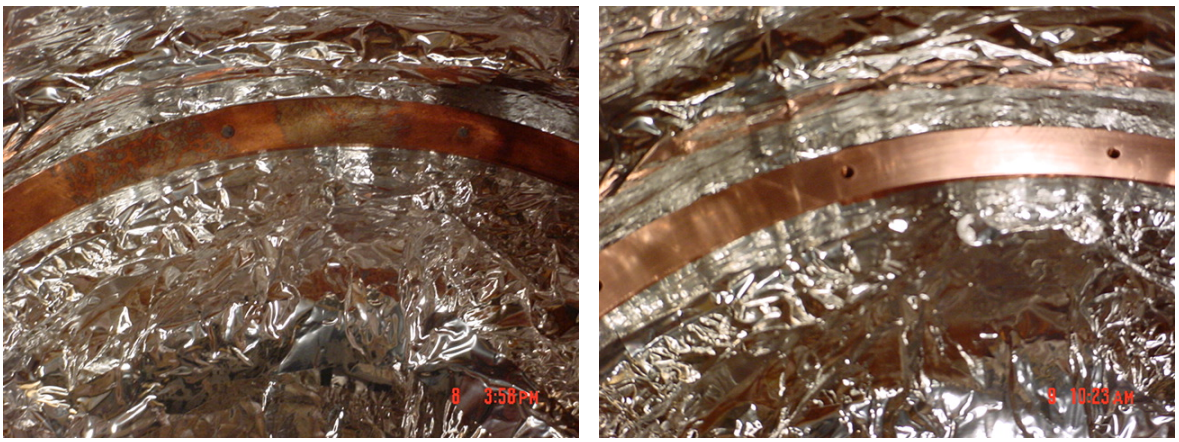

(a) (b)

Figure 4.3: 600 mK can (a) with oxide (b) and clean after scrubbing.

4.4 Detector Tuning

Following the successful cool down to base temperature detector tuning began as bias points were chosen for all 120 SQUIDs and TESs. Due to the large number of channels there was much effort placed on making both the SQUID and TES tuning processes more systematic and efficient [84]. Two LabView programs were developed for the Soudan tuning and were vital to the endeavor, allowing consistent and real time analysis.

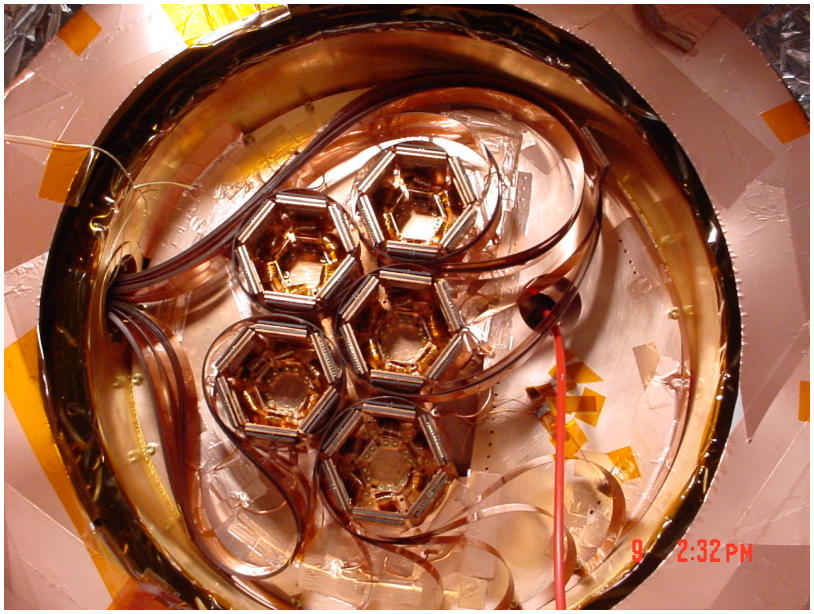

Figure 4.4: Photo of the final Soudan 5-tower installation showing the 4K lid.

While tuning the SQUIDs, the most important concerns were to achieve stability and sufficiently high bandwidth. Operationally, this meant ensuring that the SQUIDs were biased to have "good" V-Φ modulation curves that were sufficiently responsive [13]. The following criteria were followed when choosing the SQUID lock point on the modulation curve:

- There is no resonance or kink in the modulation curve in the SQUID's dynamic range around the lock point
- The SQUID responsivity at the lock point is between 100 and 150 Ω
- The SQUID bandwidth at the lock point is at least 250 kHz and ideally approximately 350 kHz

Figure 4.5 is a screen capture of the LabView SQUID tuning program with results after tuning the SQUID of channel A on T4Z1. The large bottom left window shows the V-Φ modulation curve, the variation of the voltage across the SQUID with the change of flux Φ through the SQUID. SQUID responsivity is given by the slope of the V-Φ curve. Large responsivity reduces the impact of amplifier noise and increases

the SQUID signal-to-noise ratio. SQUID responsivity is shown, as a function of lock point on the modulation curve, in the large top left window. The SQUID dynamic range is represented by the vertical lines along the V-Φ and responsivity curves. By looking at these two windows one can identify resonances, like the one seen on the left side of this SQUID's modulation curve, which tend to significantly increase SQUID noise. Although this SQUID has a resonance, the lock point is far from it on the upper right side of the modulation curve.

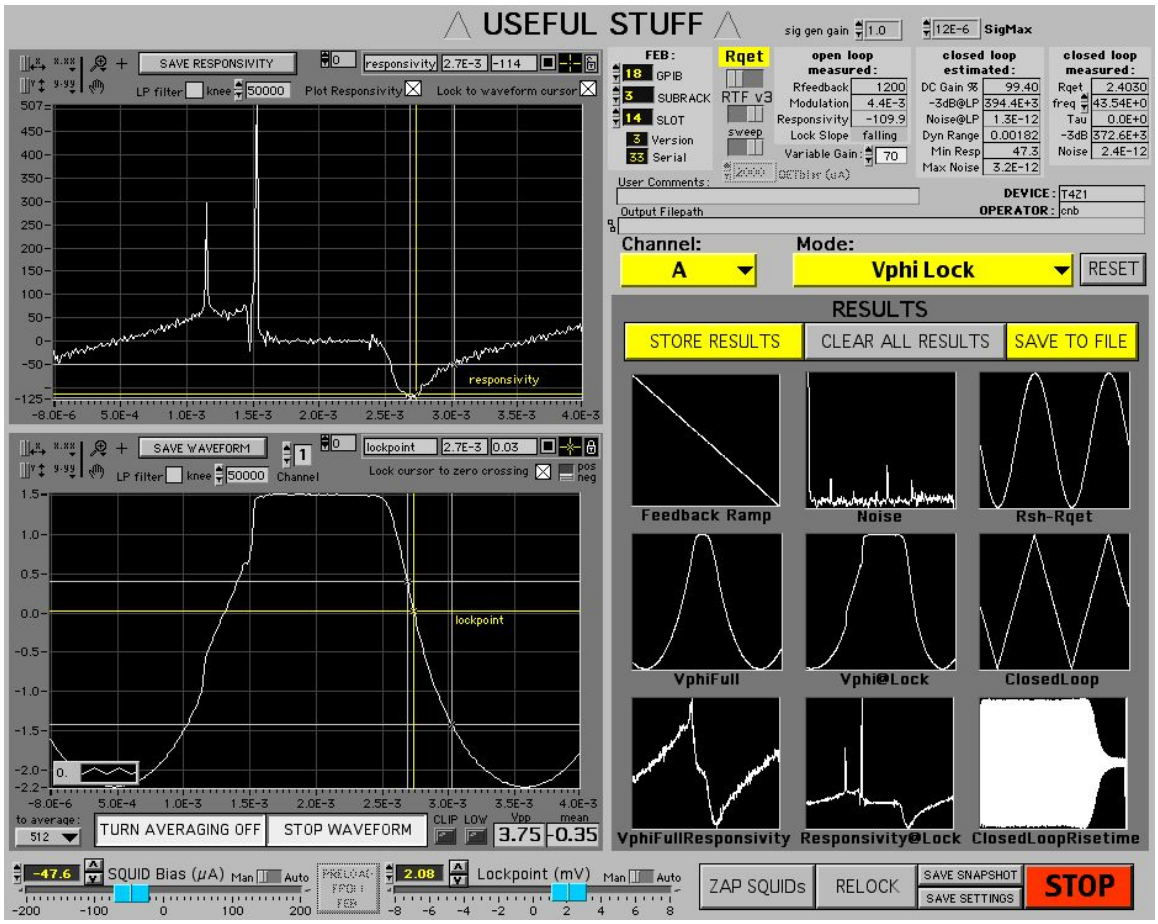

Figure 4.5: Screen capture of the LabView SQUID tuning program with results after tuning the SQUID of channel A on T4Z1. The large bottom left window shows the V-Φ modulation curve, while the large top left window represents the SQUID responsivity as a function of lock point. Although this SQUID has a resonance (left side of modulation curve), the SQUID operates far from it (as indicated by the vertical lines in the bottom left window). The numbers on the top right and smaller windows show the results of SQUID checks that ensure proper configuration. For example, this SQUID is tuned to a bandwidth of ~370 kHz.

The TES tuning procedure was based on gaining the maximum signal-to-noise without losing timing information used for surface event identification. The LabView TES tuning program allowed real time data monitoring and analysis of important parameters affected by the tuning such as the noise spectrum, bandwidth, and uniformity of timing parameters among the 4 phonon sensors. The TES procedure followed is outlined below [85]:

1. Initially bias the TES so that its resistance is approximately 200 mΩ for germanium detectors and 250 mΩ for silicon detectors

2. Determine the bandwidth each of the phonon channels based on the noise spectrum and adjust the TES bias current so that the bandwidth for all the channels are matched at approximately 100 kHz for germanium detectors and 140 kHz for silicon detectors

3. Take a short data set (of several thousand events) and use the LabView TES tuning program to make analysis cuts and evaluate timing parameters

4. If necessary, adjust the TES bias current so that the timing parameters are balanced for all the phonon channels

5. Repeat steps 3 and 4 as needed

6. Take a long dataset with the final tuning parameters for later comparison and documentation

Figure 4.6 is a screen capture of the LabView TES tuning program with results after tuning T3Z4. This LabView program allows the graphical creation of data selection cuts to be made and immediately applied to the data to determine appropriate TES parameters which balance the timing distributions from the 4 individual TESs (as instructed in step 3 above). Graphical analysis cuts are made using the plots in

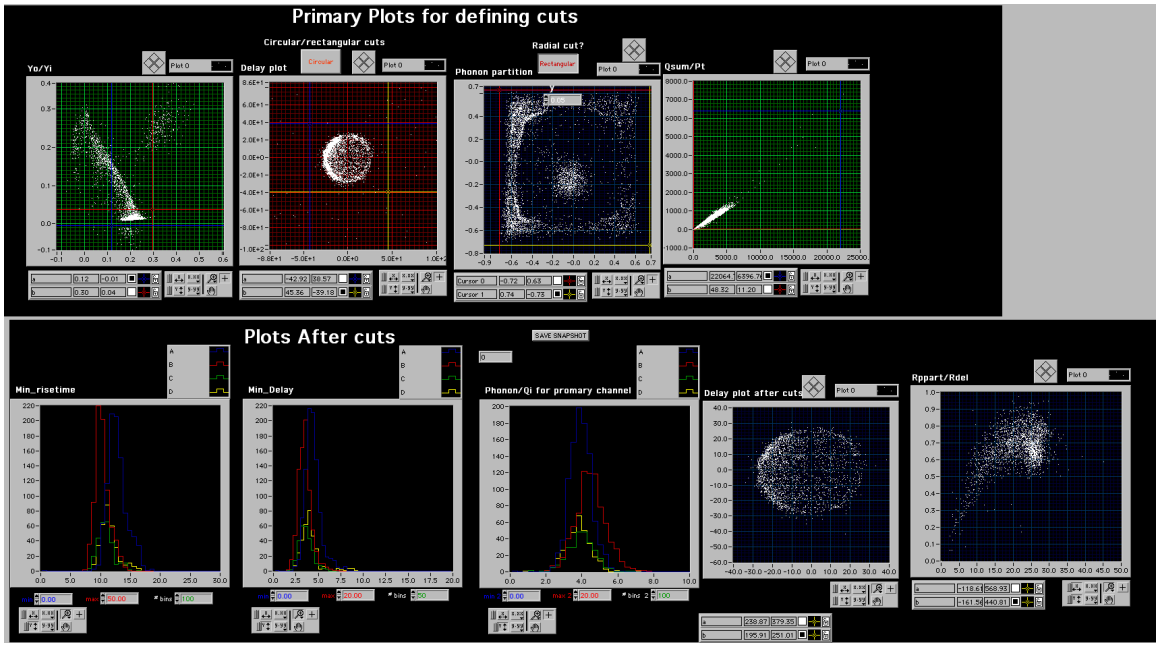

Figure 4.6: Screen capture of the LabView TES tuning program with results after tuning T3Z4. The plots in the top row allow the graphical creation of data selection cuts that are then applied to the data before creating the plots in the bottom row. The plots shown here represent a well tuned detector. Notice how the risetime and delay distributions of the four phonon sensors (the two bottom left windows) are balanced with each other. Also notice the middle two plots in the top row. These are the phonon delay ("delay") and partition ("box") plots which provide approximate event position reconstruction.

the top row and applied to the data before creating the plots in the bottom row. The plots in the top row show (in order from left to right):

- The ratio of ionization energy collected in Q_{outer} to phonon energy as a function of the ratio of ionization energy collected in Q_{inner} to phonon energy
- The phonon "delay" plot
- The phonon partition, or "box", plot
- Ionization energy as a function of phonon energy

The delay and box plots provide approximate event position reconstruction based on phonon delay parameters (as defined in Section 2.6.1) and the partitioning of phonon energy between the four sensors. The two most significant plots in the bottom row are

the first two on the left. These histograms show the risetime and delay distributions of the four phonon sensors. It is important to select TES parameters which "balance" these distributions so that the timing parameters of all four phonon channels are consistent for creating surface event rejection cuts based on risetime and delay.

While tuning the detectors there were several interesting observations and trends. First, when choosing the initial TES bias current so that the sensor resistance was approximately 200 mΩ (250 mΩ) for germanium (silicon) detectors, the bias current usually had to be raised in order to achieve the desired bandwidth of approximately 100 kHz (140 kHz) for germanium (silicon) detectors.

When biasing the SQUIDs there would sometimes be a bump in the SQUID bandwidth near the roll-off frequency (Figure 4.7). This bump can cause instabilities and problems in the TES tuning. This led to reducing the SQUID bandwidth from the desired 350 kHz, sometimes to as low as 250 kHz, in some sensors to get rid of the bump, which compromises the phonon risetime measurement.

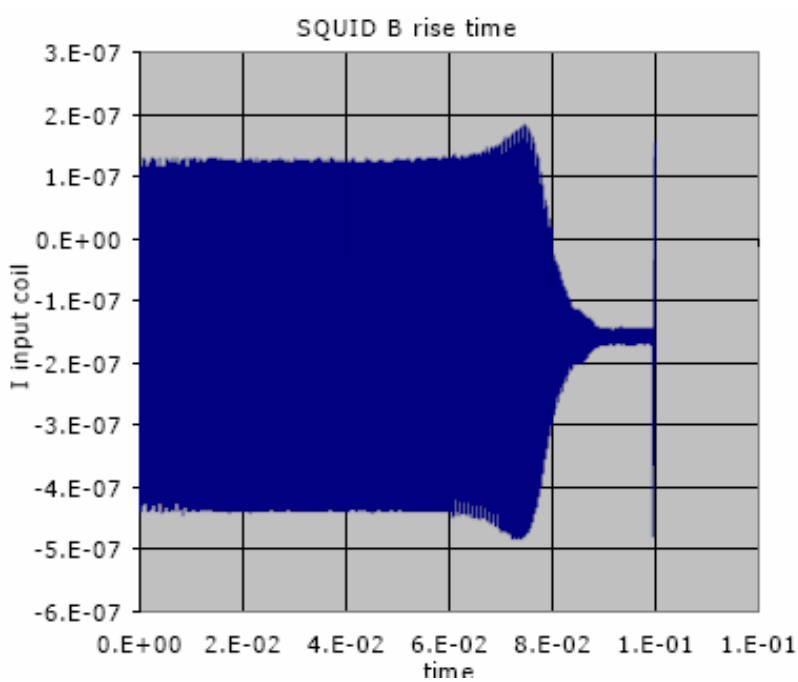

Figure 4.7: An example of the bump sometimes seen in the SQUID bandwidth near the roll-off frequency.

Besides occasionally seeing a bump in the SQUID bandwidth near the roll-off frequency, there would also sometimes be a bump in the noise spectrum near the roll-off (see the yellow trace in Figure 4.8). In an attempt to understand this excess noise there were some studies looking at the effects of changing SQUID bandwidth and TES bias. While changing the SQUID bandwidth had no effect, raising the TES bias tended to lower the excess noise (Figure 4.8). This indicates that the excess noise bump is due to the L/R pole being too close to the frequency of the electro-thermal feedback (ETF) pole at low TES biases. During these studies it was also found that this excess noise has an impact on phonon timing as seen in the delay plot.

Yellow (160810_0125): chD = 80uA QET bias
Cyan (160810_0132): chD = 85uA QET bias
Blue (160809_2352): chD = 88uA QET bias (these were final tuning settings)
Magenta (160810_0044): chD = 108uA QET bias
Green (160810_0106): chD = 128uA QET bias

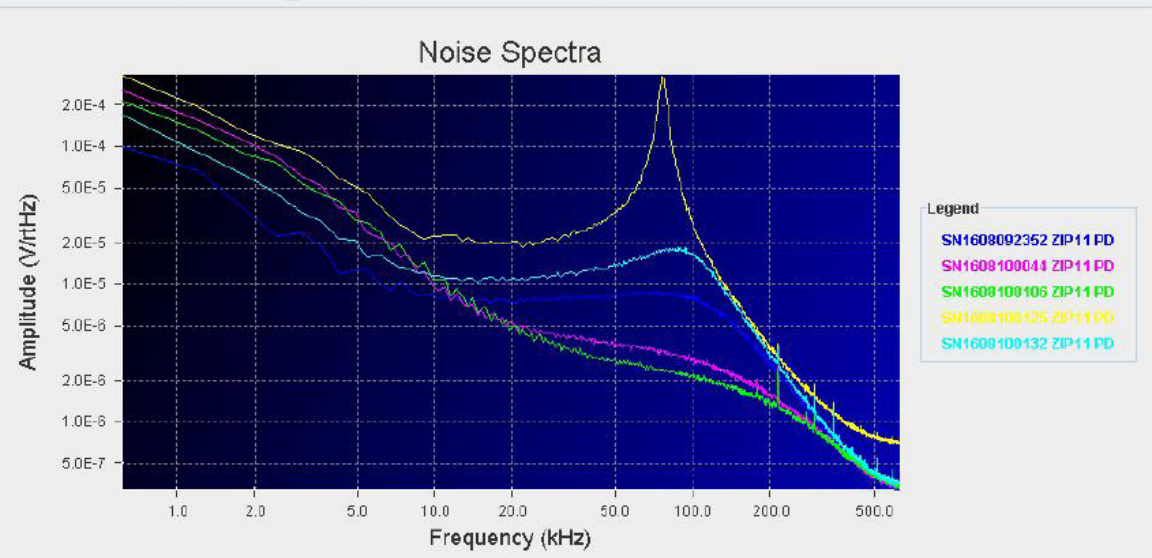

Figure 4.8: An example of how changing the TES bias current affects the noise spectrum for a detector showing large excess noise (the large bump near the roll-off) under specific bias conditions. Notice how increasing the TES bias current decreased the excess noise. This is dramatically seen by comparing the amplitude of the yellow (lowest TES bias current) and green (highest TES bias current) traces near their roll-off frequencies.

During occasional data sets certain phonon channels did not work. When looking at the noise spectrum they exhibited a very low frequency roll-off, often around 10 kHz, and elevated low frequency noise floor (see the green trace in Figure 4.9). The

cause was that the TES bias point was too close to the superconducting transition causing the channel to go superconducting.

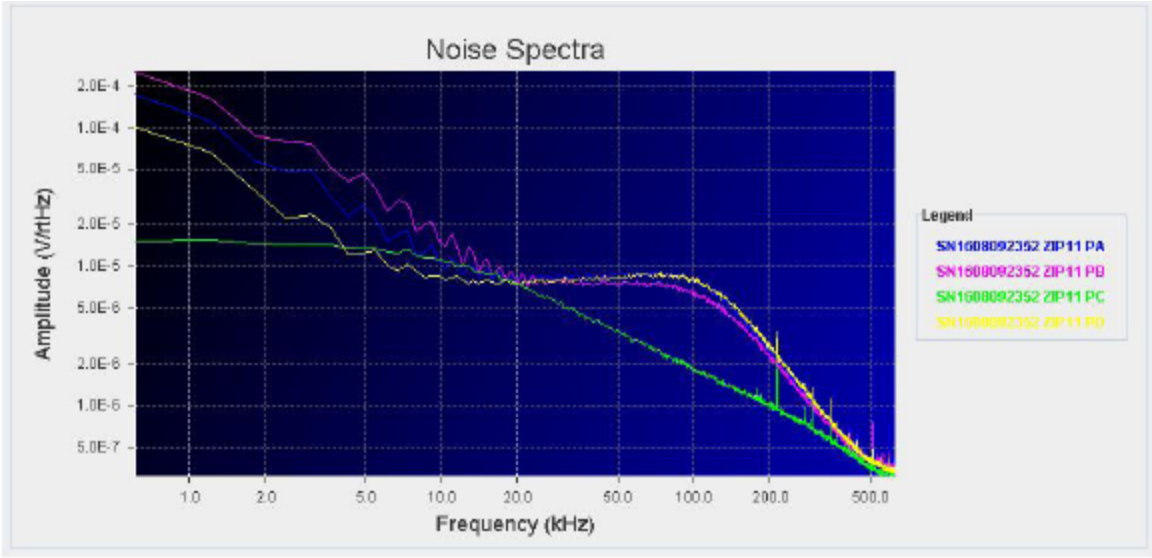

Figure 4.9: An example of a detector's phonon noise spectrum where one of the channels, channel C (green), went superconducting due to its bias point being too close to the superconducting transition. Phonon channels that are biased in their superconducting transition (like the blue, magenta, and yellow traces) have a noise spectrum that is relatively flat at low frequencies and then decreases at a roll-off frequency (∼100 kHz for germanium). The fact that the green trace shows elevated noise and no flat spectrum at low frequencies indicates that the TES is superconducting.

While tuning the phonon channels there was a brief period where the base temperature was elevated by approximately 15 mK. While this rise in detector temperature did not significantly affect the phonon performance, it did cause a noticeable difference in the phonon noise spectrum. This temperature increase produced an elevated phonon bandwidth and decreased low frequency plateau in the noise spectrum (Figure 4.10).

4.5 Operations

The Soudan 5-tower runs consisted of 30 CDMS-II ZIP detectors, 19 germanium and 11 silicon (as listed in Table 4.1). The science runs with this setup lasted from October 2006 to March 2009. Due to various cryogenic and maintenance reasons data taking

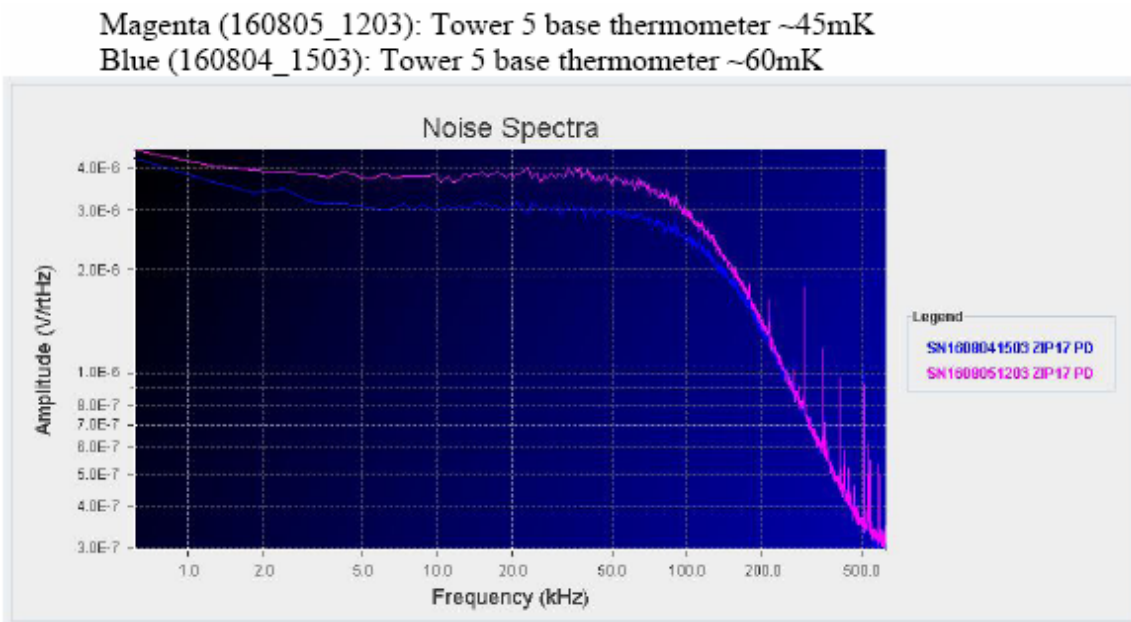

(a)

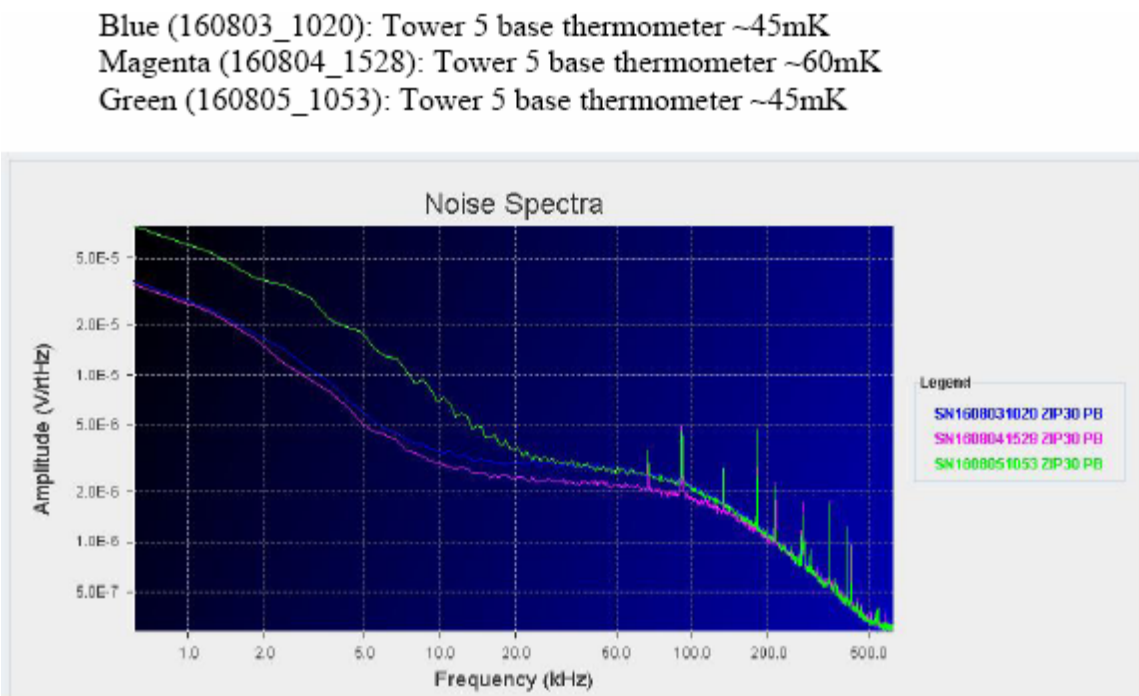

(b)

Figure 4.10: Examples of how the phonon noise spectrum is affected by a 15 mK difference in temperature from (a) T3Z5 channel D and (b) T5Z6 channel B. Notice how, in (a), the blue trace has a slightly lower amplitude and higher roll-off frequency than the magenta trace. This indicates a higher TES resistance caused by to the increased temperature. The same trend can be seen in (b) when comparing the magenta trace with the blue and green traces.

was halted for brief periods during this time. Therefore data collected occurred in 7 runs, the breaks between them identified by warming the cryostat above its 40 mK base temperature. Appendix D defines the time periods for each of the individual 5-tower runs along with additional information.

This Chapter and Chapter 5 focus on the first two of the Soudan 5-tower runs, known as Run 123 and Run 124. During Run 123 data were taken from October 2006 until March 2007. Run 124 began after warming to 9.5 K for cryogenic maintenance and data were taken between April and July 2007. The analysis and results based on this data are discussed in Chapter 5.

During the 5-tower runs WIMP search data were taken continuously, with exceptions being for the daily cryogen transfers for the dilution refrigerator, LED flashes to maintain detector neutralization (see Section 6.5 for frequency), and calibration data sets. In stable conditions and on a day with no calibration data set, WIMP search data would be taken for approximately 22 hours a day.

In addition to WIMP search data, extensive calibrations with γ-ray (^{133}Ba) and neutron (^{252}Cf) sources were taken to define the WIMP signal region and characterize detector performance and stability (see Chapter 5). Barium calibration data sets were taken regularly throughout the runs. During the first half of Run 123 there was only one ^{133}Ba source. In order to achieve more uniform statistics for all detectors (Figure 4.11), data were taken alternating the source between calibration source tubes on opposite sides of the icebox. In early February 2007 two ^{133}Ba sources arrived at Soudan and after that time barium calibration data sets were taken using both sources, one in each of the calibration source tubes for more uniform illumination across the detectors. These barium calibration data sets generated over 28×10^6 electron-recoil events between 10-100 keV, over 30 times greater than the number of similar events in the WIMP search data i.e., due to residual backgrounds. Californium calibration data sets occurred during three periods in Run 123 (November 2006 and January and March 2007) and two periods in Run 124 (April and July 2007). During

each of these calibration periods two data sets were taken, one with the ^{252}Cf source in the calibration source tubes on opposite ends of the icebox. These californium calibration data sets produced more than 10^5 nuclear recoils which mimic the WIMP nuclear recoil signal.

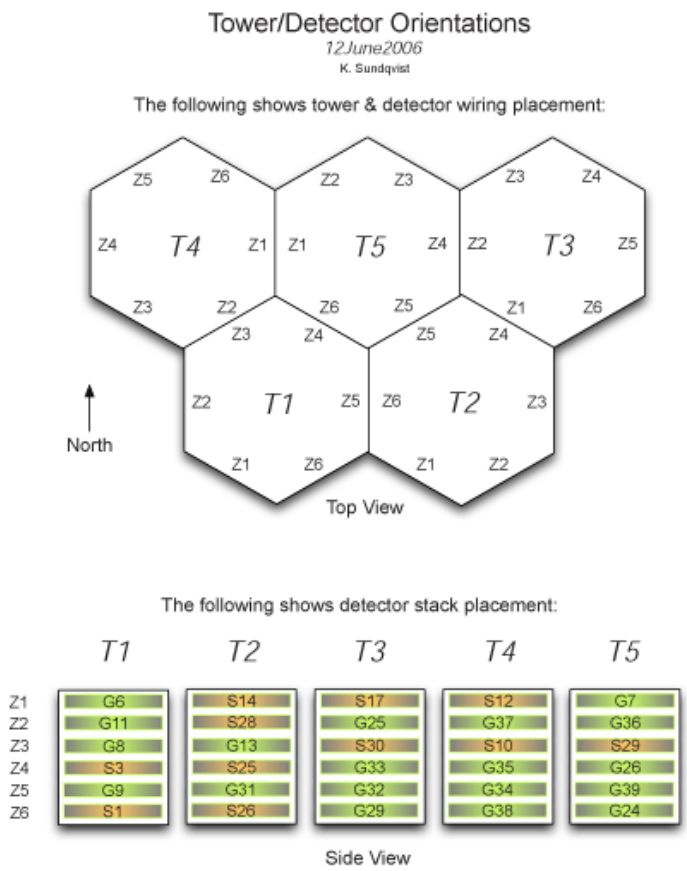

Figure 4.11: Schematic of the Soudan 5-tower detector orientation in the icebox and towers. The two calibration source tubes are located at the northeast and southwest ends of the icebox. Courtesy of Kyle Sundqvist.

4.6 Real-Time Data Quality

While taking data it is important to constantly monitor the data quality to ensure proper running conditions. During Run 123 there were many automated checks that gave real time feedback to ensure good data. In addition, the collaboration instituted a series of systematic tasks and studies for people on shift at Soudan as well as designated shift takers off site to monitor data quality. This section summarizes some of these data quality methods used during the Soudan 5-tower runs.

4.6.1 Noise

The noise spectrum can give information on how that detector channel is performing. In general, high noise in either the phonon or ionization channel indicates a change in the detector environment. More specifically, shifts in features in the phonon noise spectrum can tell about changes in the SQUID performance or stability, TES state, and even detector temperature. In order to monitor noise performance, 500 random triggers are recorded at the beginning of every dataset.

There are two methods to look for changes in the detector noise spectrum. First, in order to get immediate feedback, a script automatically runs after taking the random triggers. This script removes any traces with pulses, or events, generates the noise spectrum, and then looks for deviations by comparing the noise spectrum for each detector channel to a template spectrum for that channel (Figure 4.12). If there are significant changes in the noise spectrum a warning is issued notifying the operator of the discrepancy. This allows the operator to intervene and fix the problem if needed.

Beginning in Run 125 there was an addition to this monitoring protocol. Besides taking the 500 random triggers at the beginning of every data set, an additional 500 random triggers were taken at the end of every data set. These "end-of-run randoms" were also automatically processed into noise spectrum and compared with the template noise spectra. These "end-of-run randoms" help monitor any changes

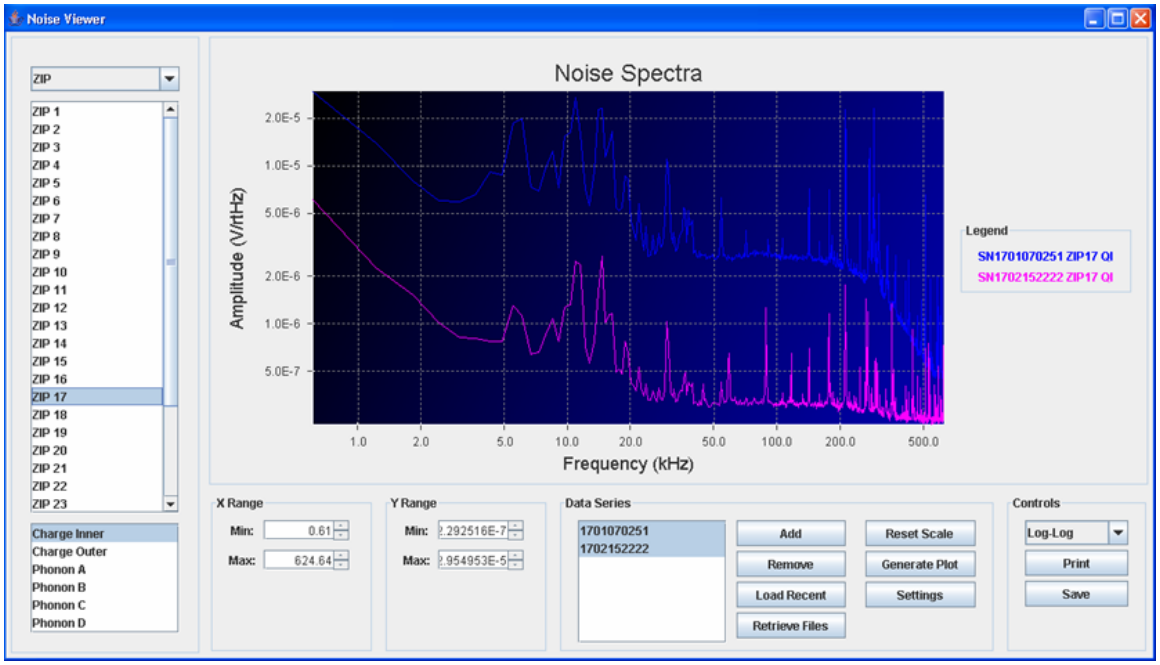

Figure 4.12: An example of the automatically generated noise spectrum for the inner ionization channel of T3Z5. The two traces shown here are from two different runs to give an illustration of what would generate a warning message based on this technique.

that may occur to a detector channel during an individual data set.

The second method of evaluating noise is completed during data processing. Similar to the real-time automatic noise evaluation, this method uses the first 500 triggers, runs a pulse rejection algorithm, and creates noise spectra. These noise spectra are automatically linked to the web for review.

4.6.2 Diagnostic Plots

Diagnostic plots are another way of evaluating data quality and detector performance. Similar to the noise assessment, a series of diagnostic plots are generated in real time and during data processing.

The real-time analysis routine generates diagnostic plots using a fraction of the events in the data set (Figure 4.13). Diagnostics recorded in real time include:

- The number of each detector's triggers

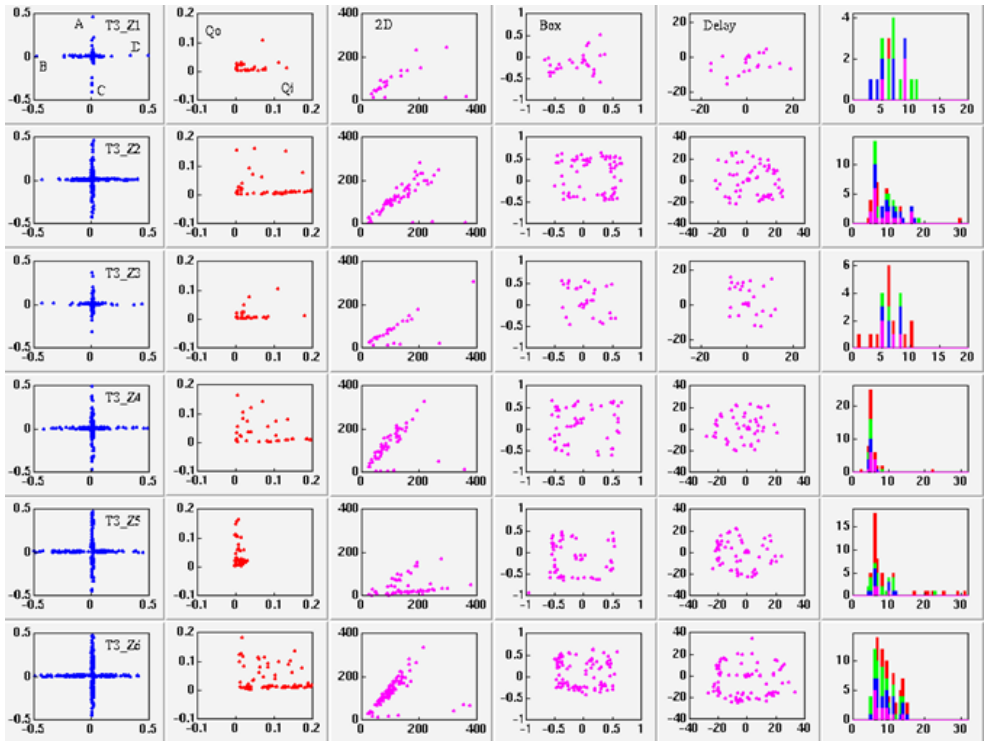

(a)

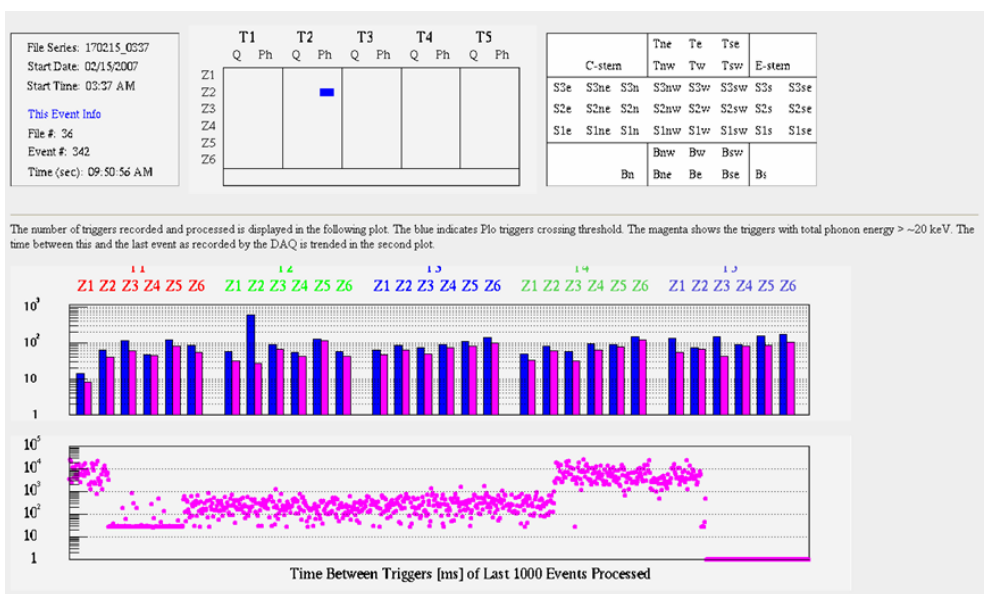

(b)

Figure 4.13: An example of the real time diagnostic plots showing (a) phonon and ionization channel and (b) trigger information. These graphical interfaces allow quick checks on detector performance. For example, by looking at the plots in (a) one can identify phonon and ionization channels that are not working properly. The bottom panel in (b) shows trigger rate as a function of time and illustrates rate changes that could cause an adjustment to a detector's trigger threshold (Section 4.6.3).

- Total trigger rate
- Phonon channel raw pulse heights
- Ionization channel raw pulse heights
- Phonon timing information
- Veto pulse height distributions

These diagnostic plots allow the operator to see problems in detector performance, triggering, or vetoing.

While processing each data set, another set of diagnostic plots are produced and automatically linked to the web next to a reference set of plots for review. These monitoring plots include:

- Phonon noise spectrum
- Charge noise spectrum
- Phonon timing and relative amplitude information

4.6.3 DAQ Monitoring

The data acquisition software constantly monitors the stability of select quantities. If there is a change in these quantities a warning is sent out to alert the operator. Some warnings require operator intervention if deemed necessary while others lead to automatic and immediate action. Below is a summary of these quantities.

DC Offsets

The phonon DC offsets, the difference between the raw phonon trace's baseline and zero, are a measure of the SQUID and TES stability. If the offset is greater than the value of one flux quanta, approximately 0.2 V, it indicates that the SQUID has likely

lost its stable lock point compromising the SQUID noise performance and possibly the phonon risetime measurement (due to lower bandwidth). These DC offsets are measured and recorded for each detector channel every minute. During each data set the offset for each detector channel is averaged. If at any point during the data set a detector channels DC offset is greater than 0.2 V, the data set is paused and all of the SQUIDs are relocked to restore stable SQUID operation.

Trigger Thresholds

During a data set, the trigger thresholds are read from the trigger board and compared to the values set by the operator through input files. If the value read from the board does not match the set value a warning is sent out.

Trigger Rates

During WIMP search data sets the trigger rates for all triggers are measured and recorded every minute. If any trigger rate increases by a factor of 10 a warning message is sent for the operator to investigate. If the primary phonon trigger rate increases by a factor of 10, then the trigger threshold for that detector is raised by a factor of 2 in order to keep the overall trigger rate from drastically increasing. A rise this large may be due to increased noise and will cause excess noise events to be recorded.

4.6.4 KS Tests

Kolmogorov-Smirnov, or KS, tests compare distributions of detector quantities for each data set with a reference set to look for anomalies. A KS test is run on the Soudan Analysis Cluster (SAC) for every WIMP search data set with over 1500 events immediately after processing. A summary table for each data set is automatically

generated and posted to the web. These tables record how well matched a detector's distribution is with its reference distribution.

An additional round of KS tests is run on both the final processed WIMP search and barium data sets. A cut is then made to remove data sets or certain detectors in a data set based on these KS tests. This cut maintains data stability by removing periods of time where a detector is underperforming i.e., due to noise.

Detector quantities and distributions that the KS tests study include:

- Noise
- Relative phonon amplitudes
- Timing information
- Ioinzation yield
- Phonon recoil energy
- Charge Chi-Square
- Total ionization energy

4.6.5 PipeDisplay

PipeDisplay is a series of automatically generated webpages designed to monitor detector performance and provide an easy, visual method for study (Figure 4.14). These webpages show (and archive):

- Phonon and ionization traces for each detector
- Veto panel pulses
- Noise spectrum
- DC offsets

- Trigger thresholds
- Number of triggers
- Fridge base temperature
- Experiment live time

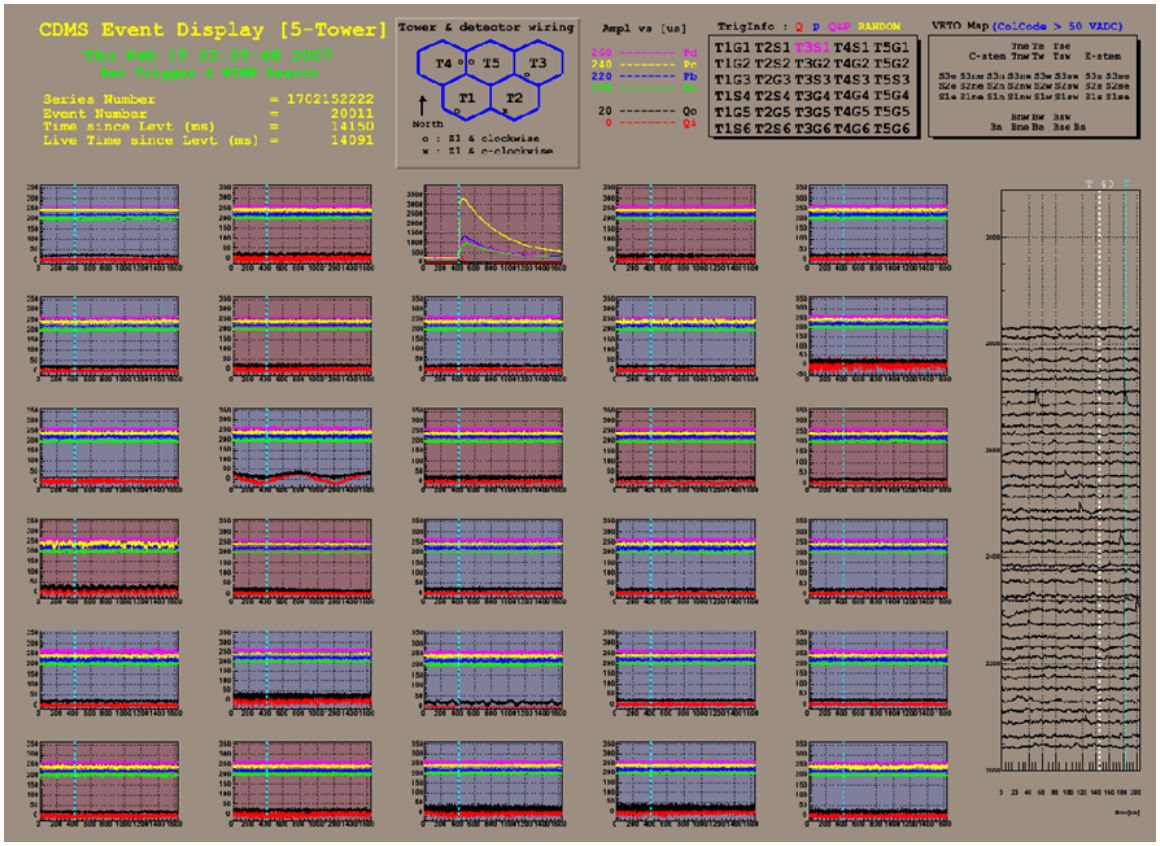

Figure 4.14: An example of the PipeDisplay webpage showing raw traces for each detector and veto panel.

4.6.6 Neutralization

During the Run 123 and Run 124 analysis a quantitative figure-of-merit that traces detector neutralization was developed (Section 6.3.3) and used to remove poorly neutralized events (Section 5.3.5). Briefly, this quantity measures the fraction of low

yield events (ratio of the number of events with ionization yield lower than the electron recoil band to the total number of events). Poorly neutralized detectors have a higher fraction of low yield events than when they measure full ionization collection. Following these studies and the experience in Run 124 that some of the detectors were not as well neutralized as in Run 123 (Section 5.3.1), it was evident that an automated and nearly real-time neutralization code would be possible and beneficial.

An automated script was developed based on the analysis completed for the Run 123 and Run 124 neutralization cut. By Run 127 this code began being implemented at Soudan. Following the processing of each new data set taken at Soudan, the script calculates the fraction of low yield events, re-calculates the mean fraction of low yield events (with the additional data), tags datasets with a low probability of having the observed number of low yield events given the expected number, and plots all of the information so that it is easily viewed on the webpage. With this information, shift-takers are able to review the webpage in order to see which data sets have poor neutralization and quickly identify problem periods to intervene as needed.

Chapter 5

5-Tower Analysis and Results

5.1 Introduction

The Run 123 and 124 data, taken between September 2006 and July 2007, underwent a series of processing, analysis cuts, and studies. This was all performed through a blind analysis resulting in a zero background experiment with the world leading WIMP-nucleon spin-independent cross section limit for WIMP masses above 44 GeV/c^2. This chapter summarizes the analysis work completed for the first 5-tower runs at Soudan along with a discussion of backgrounds and results.

5.2 Blinding

To perform an unbiased analysis, data were blinded and a protocol was established for setting and checking cuts. This section outlines the blinding method used for the Run 123 and 124 analysis.

5.2.1 Blinding Method

The method used to blind the data for the Run 123 and 124 analysis was decided upon prior to beginning data analysis and consisted of two main parts, procedures

for masking the signal region in the WIMP search data and using statistically independent data samples to create analysis cuts and verify their performance.

Signal Region Mask

A blinding proposal [86] was accepted by the collaboration in early 2006 that detailed the method of masking the signal region in WIMP search data. The highlights of this proposal include:

- Using only stable quantities so that there are no dependences on other cuts or derived quantities that may be changed over the course of the analysis through more detailed energy calibrations, position corrections, and studies
- Performing persistent checks that the signal regions is masked as intended
- Producing an auditable trail of any and all changes to the signal mask

In addition to these general blinding guidelines the proposal outlined the guidelines for creating the actual cut that masks the signal region in WIMP search data (also known as the blinding cut). This procedure was used in the blinding cut development and is discussed in Section 5.2.2.

Statistically Independent Data Samples

Besides masking the signal region in WIMP search data, using statistically independent data samples to create and test cuts adds an additional means for the analysis to remain unbiased. Cuts used to define the signal region, including recoil bands and phonon timing, were all developed using the extensive calibration data sets taken with ^{133}Ba and ^{252}Cf sources (Section 4.5). Two statistically independent samples of the ^{133}Ba gamma calibration data were created by placing every other event into each set. One sample was identified to be "open" and used for creating analysis cuts

while the other was designated as "closed" and used for checking cut performance and calculating efficiencies.

The following analysis procedure was discussed and adopted in February 2007 [87, 88]:

1. Define data selection cuts
    - Ensure that the performance of all data selection cuts is checked
2. Define all cuts to identify the WIMP signal region using californium and open barium calibration data
    - Estimate the expected phonon timing cut leakage (Section 5.4.6) for the closed barium data
    - All cuts must be reviewed
    - Comprehensive documentation should be completed
3. Apply cuts to the closed barium calibration data in order to verify performance and calculate efficiencies
    - Count the actual number of leakage events (background events that are not rejected) for the different cuts and compare with the estimated number of leakage events
    - Determine where discrepancies between the numbers of estimated and measured leakage events come from
    - Estimate the discrimination power or "passage fraction," ratio of the number of events in the 2σ nuclear recoil band to the total number of events, for the analysis cuts on the barium data
    - Estimate systematic uncertainties between barium and WIMP search data

4. Look at the non-masked WIMP search data, especially the surface events below the electron recoil band and above the masked signal region in the plot of ionization yield as a function of phonon recoil energy (similar to Figure 2.13), to do a final check that the cuts were created and are performing correcting
    - Count the actual number of leakage events for the different cuts
    - Determine where discrepancies between these leakage events and the predicted barium passage fractions come from
    - Estimate the expected sensitivity for all cuts
    - If multiple techniques were used to create several versions of a cut, decide on the best cut to be applied to the signal region based on the expected sensitivities
5. Apply cuts to the WIMP search blinded signal region to determine the number of candidate events

5.2.2 Blinding Cut

The blinding cut [89, 90] was developed by following the prescription in the blinding proposal to mask the signal region in the WIMP search data. Events masked by this cut satisfy the following criteria, a simplified and conservative version of the WIMP-search analysis:

- Veto-anticoincident: there is no signal in the veto panels immediately preceding the event trigger
- Event in the inner ionization electrode: the amplitude of the energy measured in the outer ionization electrode is consistent with noise
- Energy range: the measured phonon recoil energy is between the detector's analysis threshold and 130 keV

- Ionization yield: lies within the 3σ nuclear recoil band
- Multiplicity: the event was a "single" event, meaning that the phonon energy in all but one detector was consistent with noise

As decided upon in the blinding proposal, this cut follows the same form as the blinding cut used for the previous Soudan 2-tower analysis with one main difference. The Run 123 and 124 blinding cut relies solely on uncalibrated, raw quantities so that it remains self-consistent despite any changes during the analysis process, such as variations in energy calibrations and the addition of position correction.

The blinding cut was developed using barium and californium data taken between October 2006 and January 2007 [91, 92] and processed during the first round on the SAC. The cut was finalized and in use by the end of January 2007.

5.2.3 Blinding Implementation

The WIMP search signal region in the Run 123 and 124 data was masked using the blinding cut, which was applied during the final processing of the WIMP search data at Fermilab. Therefore the data in the official data distribution was blinded. Data checks confirmed that this blinding was implemented correctly and that the cut worked as constructed [90, 93, 94].

One of the final checks found that there were single-scatter events in the nuclear recoil band of the WIMP search data, even after applying the blinding cut. These events were not masked because the multiplicity criteria in the blinding cut was not as strict as the final singles cut (Section 5.4.3) during noisy data periods. In order to maintain blindness these events were not studied until after the analysis was complete. As a precautionary measure a secondary blinding cut was created. This secondary cut used the final 3σ nuclear recoil band and singles cut definitions and was applied when looking at WIMP search data prior to unblinding the signal region.

5.3 Data Quality Cuts

During the data analysis there are two general classes of cuts created, those that pertain to data quality and those that identify the WIMP signal region. Data quality cuts are crucial to maintaining a zero background experiment. They are necessary for use in calibration data so that the signal region can be defined using the most accurate information and in WIMP search data to ensure appropriate stability. These cuts are based on detector pathologies and systematic performance studies. This section describes some of the data quality cuts created for the Run 123 and 124 analysis.

5.3.1 Detectors Problems

During Runs 123 and 124 some detectors suffered poor performance: three germanium detectors due to fundamental readout failures which resulted in partial loss of functionality, one silicon detector with an unstable phonon channel, and two silicon detectors that never achieved sufficient neutralization. In addition, during Run 124 two germanium detectors suffered poor performance due to inadequate neutralization. These detectors were excluded from the analysis as detectors used to look for WIMP interactions. However, these detectors were included in the analysis as multiplicity veto detectors.

A summary of the detectors excluded in both Runs 123 and 124 is listed below:

- T1Z1 (germanium) because it only had one working phonon channel and no working LEDs
- T1Z3 (germanium) because the outer ionization electrode could not be biased
- T1Z6 (silicon) because it had no working LEDs and could not be neutralized (without strong source baking)
- T2Z6 (silicon) because it had no working LEDs and could not be neutralized (without strong source baking)

- T3Z1 (silicon) because it had an unstable phonon channel
- T5Z2 (germanium) because the inner ionization electrode could not be biased

In Run 124 T2Z5 (germanium) and T3Z6 (germanium) were not used as WIMP search detectors due to poor neutralization.

5.3.2 Detector Pathologies

There are several known pathologies that affect some detectors impacting their performance. The effects of these pathologies were studied and resulted in specific cuts to reject affected events.

Holiday islands

"Holiday islands" [95, 8] are areas near the outer edge of the inner ionization electrode that fall under uninstrumented regions on the phonon side that are electrically floating instead of being grounded. While this is not a problem for the ionization readout, it leads to different crosstalk properties between the inner and outer ionization electrodes for these events as opposed to other Q_{inner} events. In particular this leads to the misidentification of holiday island electron recoil events as low ionization yield events. Holiday island events only appear in Tower 1 and Tower 2 because detectors fabricated at later times have the uninstrumented phonon regions grounded. An ionization crosstalk data quality cut appropriately corrects these events.

T3Z2 floating segment

During the analysis of Run 123 and 124 data it was discovered that T3Z2 had an anomalously high population of low yield events in phonon channels C and D (Figure 5.1a), [96, 15]. Upon further investigation, these events were found to lie along an arc at the outer detector rim (Figure 5.1b). This is likely due to a region of disconnected TESs where the floating metal distorts the local electric field. Events

occurring in phonon sensors C and D in this detector were removed from the WIMP search analysis.

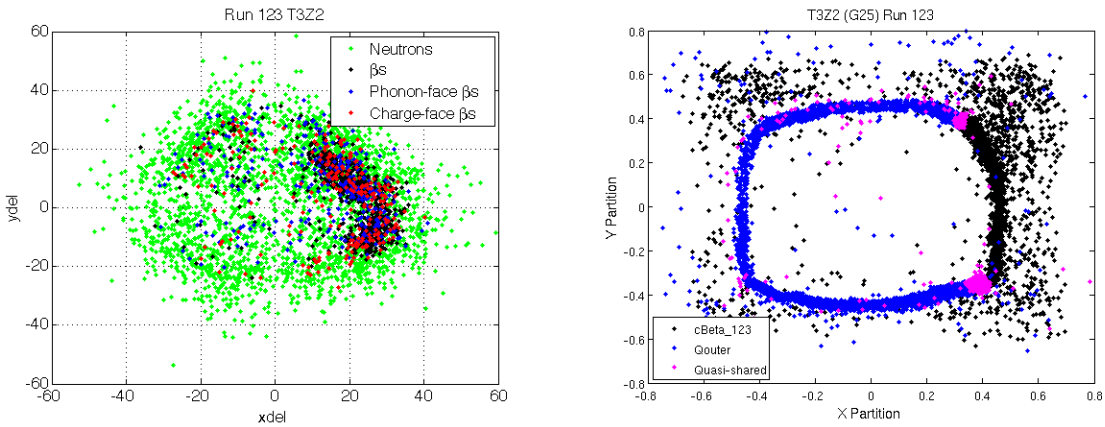

(a) (b)

Figure 5.1: (a) Delay plot for T3Z2 highlighting neutrons (green) and low-yield events (black, with blue and red indicating phonon and ionization face selections). (b) Phonon partition plot for T3Z2 illustrating the bad detector region at the right. Black points show inner ionization electrode events, blue outer ionization electrode events, and magenta events shared between the two electrodes. The right half of this detector is excluded from the WIMP search analysis.

Pucker on T5Z1 channel D

T5Z1 channel D has a distortion in delay and phonon partition plots (Figure 5.2) which affects the phonon timing distribution. This section of the detector was not included in the WIMP search analysis so that it would not impact phonon timing discrimination.

5.3.3 Stable Tuning

Official WIMP search data began on October 21, 2006. However a few detectors had changes made to their TES tuning between this official start date and the end of October. To ensure stable performance, detectors which had tuning changes were excluded from the WIMP search analysis until the final tuning was established.

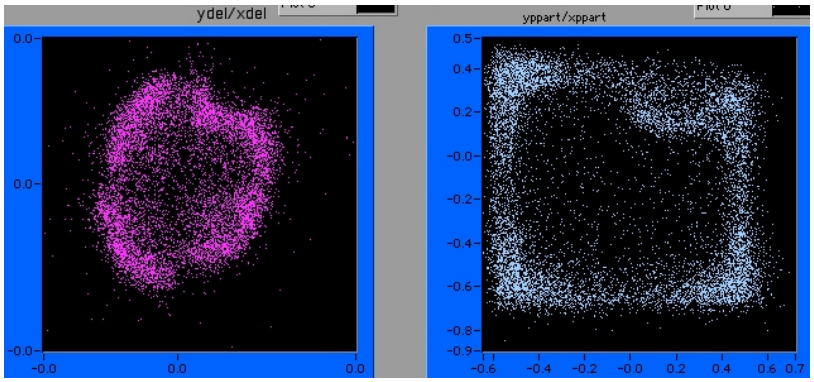

Figure 5.2: Phonon delay (left) and partition plot (right) for T5Z1 illustrating the distortion in channel D (top right).

5.3.4 Stable Performance

To ensure stable detector performance there were a number of studies performed [15]. These included evaluating

- Ionization channel goodness of fit (chi-square)
- Phonon pre-pulse baseline
- Ionization pre-pulse baseline
- Glitches in signal traces
- Trigger stability
- Phonon and Ionization noise
- Phonon bandwidth
- Trigger information

In addition to the individual studies, KS tests (discussed in Section 4.6.4) evaluated a number of diagnostic detector distributions. The information from the individual analyses and the KS tests resulted in data quality cuts which removed specific detectors during particular periods of time when they were not performing with the expected stability.

5.3.5 Neutralization

During the analysis of the first Soudan 5-tower data, quantitative analyses looking at neutralization stability, in both barium calibration and WIMP search data, throughout Runs 123 and 124 were completed. The results of these analyses were used to produce a data quality cut removing poorly neutralized data. The Run 123 and 124 analysis was the first time this type of quality cut was developed, however the motivation for creating this cut came from the previous Soudan 2-tower analysis results.

When the Soudan 2-tower data from, Run 119, was unblinded there was one candidate event [76]. This event was scrutinized to determine whether it was a true candidate WIMP-induced nuclear recoil. Through this scrutiny it was discovered that the candidate event was part of a data set suffering poor neutralization for a period of a few hours prior to an LED flash (Figure 5.3) and should have been removed from the analysis [19, 76]. This showed the importance of developing improved neutralization monitoring (discussed in Sections 4.6.6 and 6.3.3) and the benefit of applying a specific neutralization data quality cut.

Despite knowing that a neutralization cut was needed at the beginning of Run 123 there was not a good, quantitative method for selecting those data sets. Since detectors become poorly neutralized after being biased too long without neutralization, the first pass at the neutralization cut was to remove WIMP search data sets that hadn't been neutralized with an LED flash for 20 or more hours and WIMP search data sets that occurred after barium calibration data sets with more than 100,000 events when there was no LED flash between the two [97, 98].

After additional studies a quantitative figure-of-merit, the fraction of low yield events, was found to trace detector neutralization. This resulted in quantitative studies of neutralization stability in barium calibration [20], and WIMP search [99, 100] data. Both of these analyses calculated the fraction of low yield events for each data set and found the mean fraction of low yield events for each detector (where the

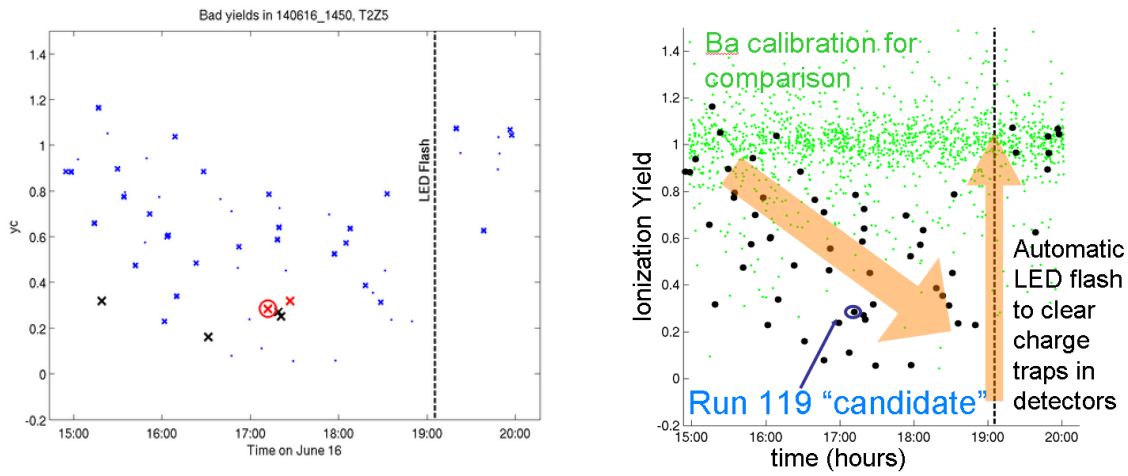

(a) (b)

Figure 5.3: Both of these plots show ionization yield as a function of time for T2Z5 during the Run 119 data set with the candidate event that exhibited poor neutralization. (a) Shows WIMP search data only. The blue crosses are single events, black crosses are 7-10 keV events passing all cuts except phonon timing, the red cross is an event above the phonon analysis threshold passing all cuts except phonon timing, and the red cross with a circle around it is the candidate event. From [19]. (b) Shows WIMP search data (black) along with barium data (green) for comparison with well neutralized data as a function of time.

mean was based on all the data). Data sets whose fraction of low yield events was 2σ above the mean, where σ is the binomial error on the fraction of low yield events for each individual data set, were tagged (Figure 5.4a). In addition to calculating the fraction of low yield events for each barium calibration data set, the fraction of low yield events was calculated for 100,000 event bins from tagged barium sets (Figure 5.4b). This allowed tagged barium data sets to undergo further study to determine whether the entire set suffered from poor neutralization or if only parts of it did. If the end of a barium data set suffered poor neutralization only that part was removed from the analysis rather than the entire data set.

By comparing the data removed based on the time since last LED flash and fraction of low yield event analyses, it was discovered that the time since last LED flash was more conservative than needed and the fraction of low yield events provides a more precise means of identifying poorly neutralized data sets.

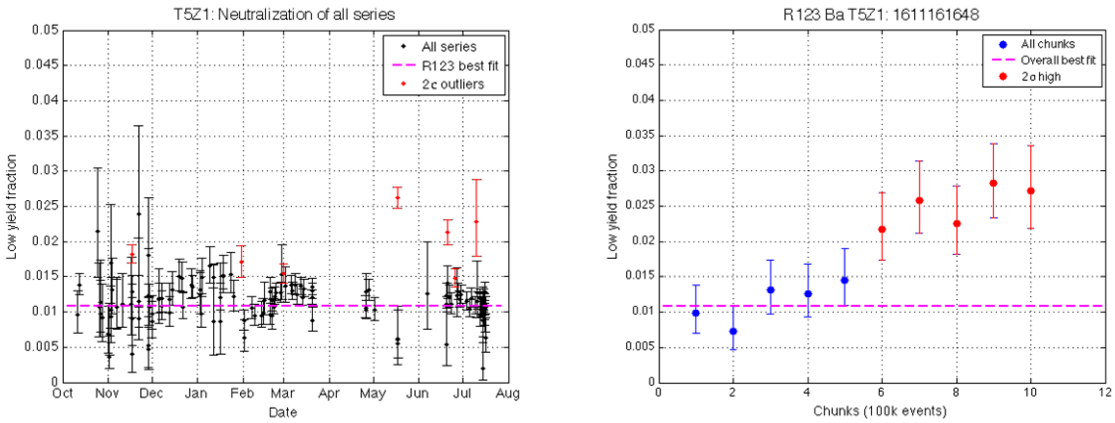

(a) (b)

Figure 5.4: Illustrations of the neutralization stability analyses using the fraction of low yield events. In both of these plots points in red are tagged as poorly neutralized and the horizontal dashed magenta line is the mean fraction of low yield events. (a) This plot shows the fraction of low yield events computed for each Run 123 and 124 barium data set as a function of time. (b) Plotted here is the fraction of low yield events for a single barium data set in 100,000 event bins. From [20].

After comparing the results of the three separate techniques for developing the Run 123 and 124 neutralization cut [101], a single cut [102] was created to remove:

- Entire WIMP search data sets that were tagged in the WIMP search neutralization stability analysis
- Entire or partial barium calibration data sets that were tagged in the barium calibration neutralization stability analysis
- Periods of time exhibiting poor neutralization, identified as periods of time where the majority of barium calibration data sets were tagged in the barium calibration neutralization stability analysis
- WIMP search data sets that were tagged in the analysis looking at the time since last LED flash and which occurred after a poorly neutralized barium calibration data set (as defined in the barium calibration neutralization stability analysis)

Since one of the reasons for creating the neutralization cut during the Run 123 and 124 analysis was to prevent a candidate event like that in the Run 119 analysis, a neutralization cut was created for the Run 119 data, using the same method as the Run 123 and 124 cut, to verify that the method satisfied that goal. Indeed, when applied to the Run 119 data, the "Run 119" neutralization cut did remove the data set containing the candidate event (Figure 5.5) [103].

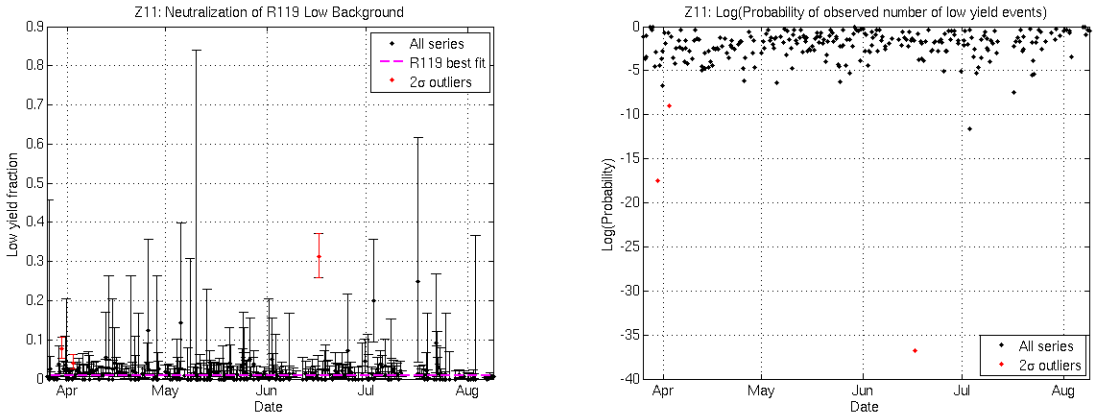

(a) (b)

Figure 5.5: Plots showing the results of applying the "Run 119" neutralization cut to the T2Z5 data. Red points are tagged as being poorly neutralized. The candidate event was in the red data set in the middle of June. (a) Like Figure 5.4a, this plot shows the fraction of low yield events computed for each Run 119 WIMP search data set as a function of time. (b) Plotted here is another way of looking at the same data. This shows the probability of a data set having the observed number of low yield events based on the expected number.

After unblinding the data from Runs 123 and 124 there was a study to determine the effect of the neutralization cut on the analysis [102]. This study showed that the Run 123 and 124 neutralization cut removed approximately 0 to 5% live time for each detector, except for T3Z6 which showed signs of losing neutralization faster than the other detectors and therefore had more data removed. The Run 123 and 124 neutralization cut did not remove any candidate events from this analysis (though it did remove several events that passed all cuts except phonon timing). While the cut did not remove any events, it provides an explicit check that removes potential backgrounds due to poor neutralization. The fact that no events were removed by

the neutralization cut also indicates improvements in the quality of data taken and quality cut development.

While reviewing the Run 123 and 124 neutralization cut there were discussions on improving the method of tagging poorly neutralized data sets for future analyses. In the Run 123 and 124 cut, data sets were tagged when the fraction of low yield events was 2σ above the mean, as calculated using all the data sets in the study (Figure 5.6a). The concern with this implementation was that σ was calculated individually for each data set based on the error of that data set's fraction of low yield events. An alternate method of tagging poorly neutralized data sets is to calculate the probability of a data set having greater than, or equal to, the number of observed low yield events, N, given the expected number of low yield events (calculated given the mean fraction of low yield events and the total number of events in the data set) and then place a cut on this probability distribution (Figure 5.6b). A third way to create the neutralization cut is to use the absolute fraction of low yield events and cut all data sets whose value is above a set threshold (Figure 5.6c). After comparing these different ways of selecting poorly neutralized events, I decided to set future cuts on the probability distribution. This technique takes the data set statistics into account and selects only the most poorly neutralized outlier data sets rather than some set percentage of the worst, as would be the case when using the absolute fraction of low yield events [104].

To make the development of future neutralization cuts faster and easier, the code used to do the Run 123 and 124 neutralization analysis was improved and automated. This automated code calculates and saves the fraction of low yield events for every barium calibration and WIMP search data set as well as the fraction of low yield events for every 50,000 barium calibration events. After calculating all of these values the code calculates and plots the mean fraction of low yield events for each detector and tags data sets which have a low probability, less than 10^{-10}, of having the observed number of low yield events (given the expected number). This information is saved and used to create the neutralization data quality cut.

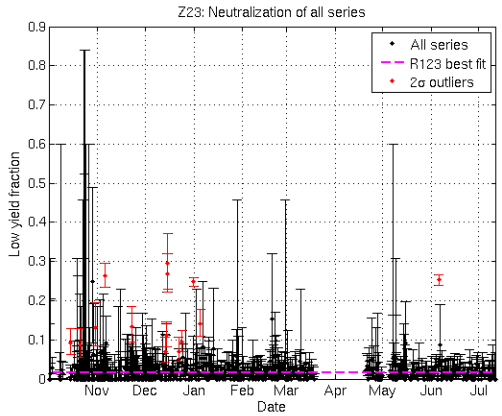

(a)

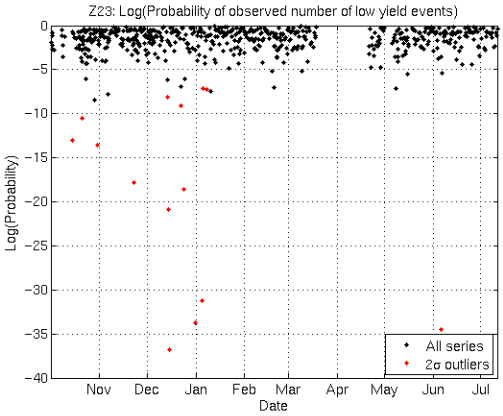

(b)

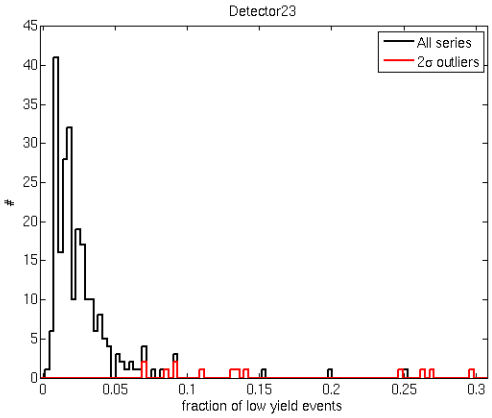

(c)

Figure 5.6: Plots comparing the different methods of looking at data from the neutralization analysis. In all of the plots the red points were tagged as poorly neutralized based on the method used in the Run 123 and 124 neutralization cut. (a) Like Figures 5.4a and 5.5a, this plot shows the fraction of low yield events computed for each WIMP search data set as a function of time. (b) Like Figure 5.5b, this is another way of looking at the same data. This shows the probability of a data set having the observed number of low yield events based on the expected number. (c) A histogram of the fraction of low yield events for all of the WIMP search data sets. This does not take statistical variations into account.

5.4 Science Cuts

The "science" cuts described in this section are those cuts used to identify the WIMP signal region. These cuts are defined using half of the calibration data taken throughout Runs 123 and 124. The cut performance is verified and the efficiency calculated using the second half of the calibration data.

5.4.1 Veto

Nuclear recoils due to cosmic-ray induced muon activity are rejected by applying a veto cut [21] to the data. This cut rejects events with a signal in the active muon veto shields (Section 3.4) surrounding the Soudan icebox. To maintain sufficient background rejection and adequate cut efficiency, events are removed when there is:

- A veto trigger within 50 μs before the detector trigger
- A reconstructed energy in the veto above a set threshold anywhere in the -180 to +20 μs window around the detector trigger for which veto pulses are recorded

The veto energy threshold used in the cut was set for each panel to maximize the muon detection efficiency while minimizing dead time caused by gamma interactions. Figure 5.7 shows an energy deposition histogram of 1 million Run 123 events for one of the top veto panels along with the cut position identifying the threshold near the upper edge of the gamma distribution and well below most muons.

5.4.2 Thresholds

To maintain acceptable discrimination at all energies there is a lower threshold placed in the analysis. This avoids performance degradation due to noise at low energies.

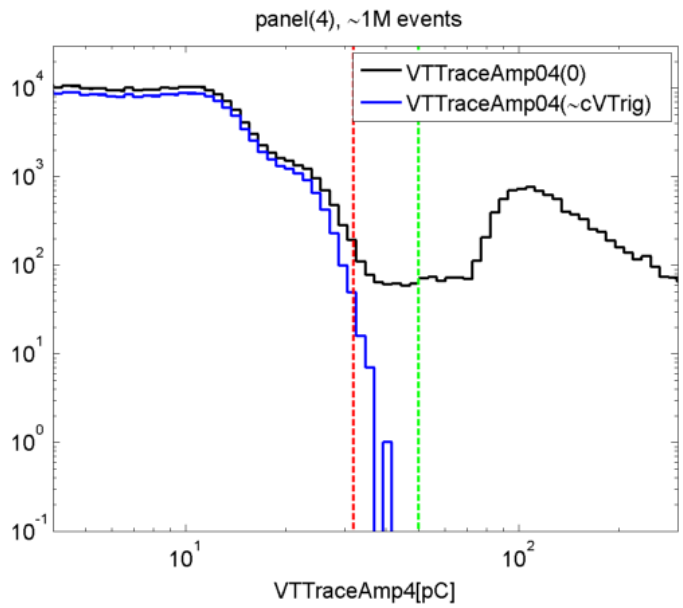

Figure 5.7: An energy deposition histogram of 1 million Run 123 events for one of the top veto panels along with the cut position. The dashed green vertical line is the 50 pC mark were the threshold was previously set for an old version of this cut and the red dashed is were it is now set for the Run 123 analysis. From [21].

Ionization Thresholds

The ionization threshold is set so that events whose ionization signal is consistent with noise are rejected. This ionization threshold is based on a gaussian fit of randomly triggered events at the 4σ upper edge of the Q_{inner} noise blob (Figure 5.8a) [22].

Since there were variations in the ionization resolution with time throughout Runs 123 and 124 (Figure 5.8b), the Q_{inner} noise blob was evaluated for every data set [23]. The final ionization threshold used in the analysis was defined as the maximum of the overall 4σ and the run-dependent 4σ upper edge of the Q_{inner} noise blob.

Phonon Thresholds

Since the phonon noise is lower than the ionization noise, the phonon threshold is set in phonon recoil energy to satisfy the following conditions:

- The surface event rejection cut must have significant efficiency

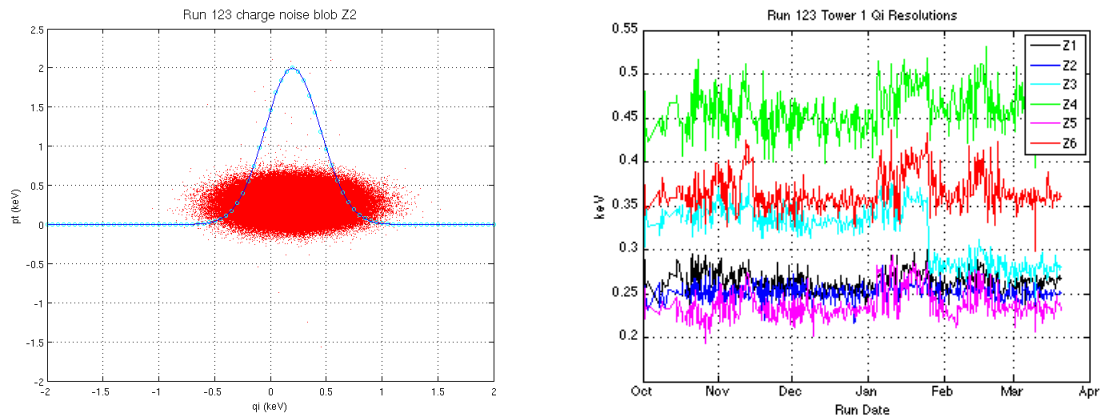

(a) (b)

Figure 5.8: (a) T1Z2's noise blob in phonon and ionization energy from the random triggered events in the Run 123 data along with the gaussian fit to the Q_{inner} noise blob that was used in the ionization threshold cut. From [22]. (b) The ionization energy resolution for Tower 1 as a function of time during Run 123. From [23].

- The ionization threshold cut and the edge of the electron recoil band must not eliminate the nuclear recoil band
- There must be a significant population of surface events on which to characterize the cut, particularly the systematic error in the background leakage

Table 5.1 shows the phonon recoil energy thresholds, imposing a mandatory minimum of 7 keV for silicon and 10 keV for germanium detectors [105].

Detector Number	Tower 1	Tower 2	Tower 3	Tower 4	Tower 5
Z1		7		10	**10**
Z2	**10**	7	**10**	**10**	
Z3		**10**	7	15	7
Z4	10	7	**10**	**10**	**10**
Z5	**10**	**10**	**15**	**10**	**10**
Z6			**10**	**10**	**20**

Table 5.1: Phonon recoil energy thresholds (in keV) for the Run 123 and 124 analysis. Germanium detectors are in bold.

5.4.3 Event Multiplicity

Since the WIMP interaction cross section is extremely small, WIMPs are not likely to interact multiple times. The requirement that any candidate event interact only once, otherwise known as a single scatter, allows a further level of rejection against backgrounds that multiple scatter.

In the Run 123 and 124 analysis an event is defined as a single scatter if it shows significant energy in one and only one detector. Specifically, a single-scatter event has a phonon recoil energy greater than 6σ of that detector's phonon recoil noise blob while all other detectors have a phonon recoil energy less than 4σ of their phonon recoil noise blob [106]. Even though some detectors are not suitable for use as WIMP search detectors, all detectors are used to identify single-scatter events.

After creating this singles cut it was discovered that the cut efficiencies had significant fluctuations with time and were generally much lower than expected [107]. This was due to variations in phonon resolution and noise (Figure 5.9), [23]. While this does not have a dramatic effect on detector performance, it does on the singles cut. Periods of poor resolution and higher noise, on even a single detector, cause the energy in that detector to appear higher than the 4σ phonon recoil noise blob and therefore look like a multiple scatter. To resolve this issue an approach was taken similar to that in defining the ionization thresholds (Section 5.4.2). Rather than calculating the phonon recoil noise blobs once for the entire analysis, they were calculated individually for every data set. Defining the 6σ and 4σ thresholds for each data set reduced the impact of the phonon resolution and noise instabilities. To veto multiple-scatter events, ionization signals, above the analogous 4σ thresholds, were used along with the phonon recoil signal for four detectors with relatively poor phonon performance (T1Z1, T3Z1, T5Z5, T5Z6) [108].

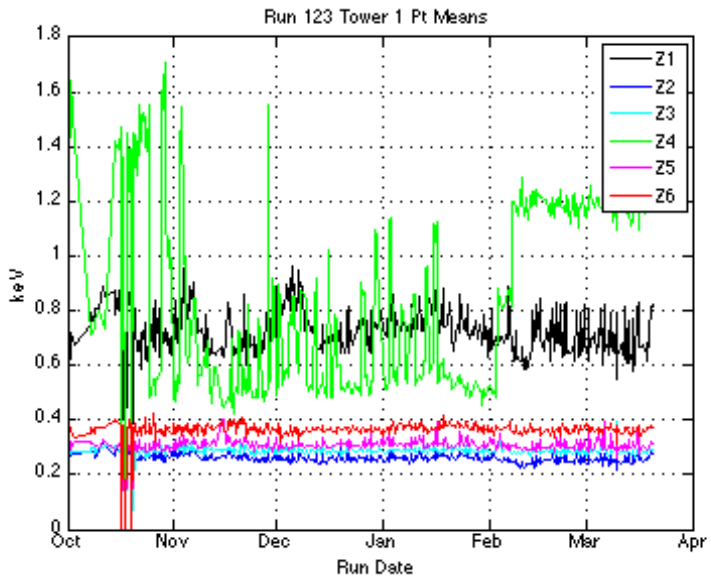

Figure 5.9: The mean of the phonon energy noise blob for Tower 1 as a function of time during Run 123. Note how the mean varies with time, especially for Z4. This caused many single-scatter events to appear as multiple-scatters during periods of high noise in the initial singles cut. From [23].

5.4.4 Fiducial Volume

Events near detector surfaces suffer from incomplete ionization collection. This incomplete ionization collection is caused by the electric field terminating on detector walls, intrinsic and space-charge induced distortions in the electric field configuration, and poor phonon sensor coverage. To maintain discrimination power a fiducial volume is defined within the detector. The cuts identifying the fiducial volume reject events at large detector radius.

Ionization Guard Ring

By design, the primary fiducial volume cut takes advantage of the energy information collected in both the inner and outer ionization electrode. Events where the Q_{outer} energy is consistent with noise, at the 2σ level, are in the detector's fiducial volume [109].

Phonon Manifold

An additional fiducial volume cut based on the combination of information from the outer ionization electrode and phonon channels was developed for the Run 123 and 124 analysis [24]. This new cut removes events that are miscorrected during phonon position correction due to degeneracies. Position correction is necessary to remove position dependent variations in discrimination quantities [18]. However this correction has degeneracies because the phonon partition and delay parameters, which identify event location, are not single valued. However, a combination of these parameters breaks most of the degeneracy, although some remains especially at high radius. This does not cause a problem except when a high radius event is position corrected along with low radii events (Figure 5.10). The differences in the phonon timing distributions for these two event classes can cause significant changes to the corrected values. This can allow high radii surface events to pass the phonon timing cut and not be rejected.

To remove miscorrected outlier events this cut uses the Q_{outer} event population as a tracer for the high radius region of the detector. This population of events is compared with the phonon position correction information. Events within a radius, R, of a Q_{outer} event are excluded from the analysis. The radius R was set on a detector by detector basis to remove a large fraction of outlier events while minimally affecting nuclear recoil efficiency.

5.4.5 Ionization Yield

As discussed in Section 2.5, ionization yield is the ratio of ionization to phonon recoil energy and is the primary discrimination parameter between bulk electron and nuclear recoil events. A WIMP candidate event must satisfy two criteria based on ionization yield determinations:

- The event's ionization yield must lie within the 2σ nuclear recoil band

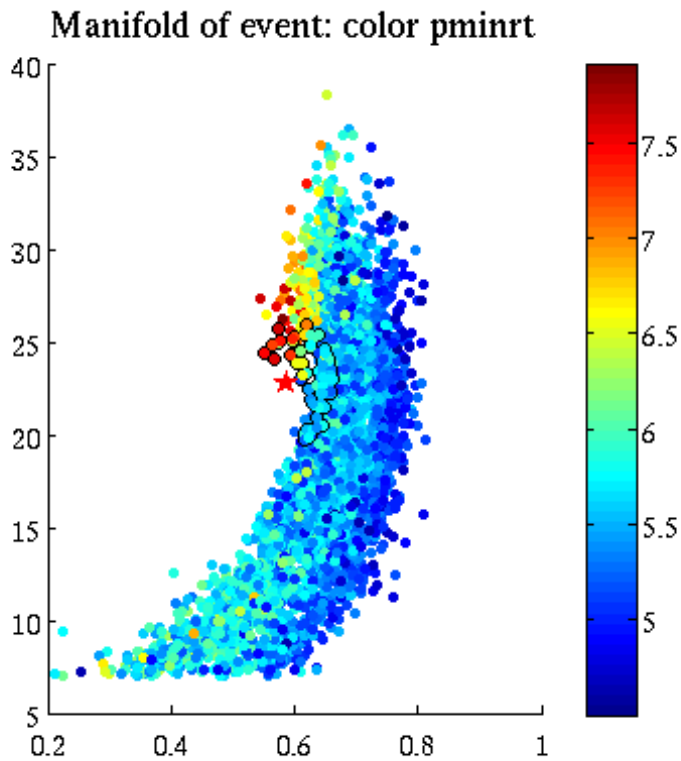

Figure 5.10: A slice of the phonon position manifold, phonon partition radius vs. delay radius, for T1Z5. The colors indicate values of the primary phonon risetime value. The star is a timing outlier event and the black circles show this event's nearest neighbors used during the position correction. This illustrates an example of mixing high (red and yellow) and low (blue) radius events during correction. From [24].

- The event's ionization yield must be less than the lower 3σ edge of the electron recoil band

The electron and nuclear recoil bands are calculated for each detector based on the ^{133}Ba gamma (Figure 5.11a) and ^{252}Cf neutron (Figure 5.11b) calibration data sets taken throughout Runs 123 and 124. After data selection cuts are applied to the calibration data, the data is binned in phonon recoil energy and gaussian fits of ionization yield are made for each bin. The means and sigmas are then fitted as a function of phonon recoil energy to define the recoil bands [25].

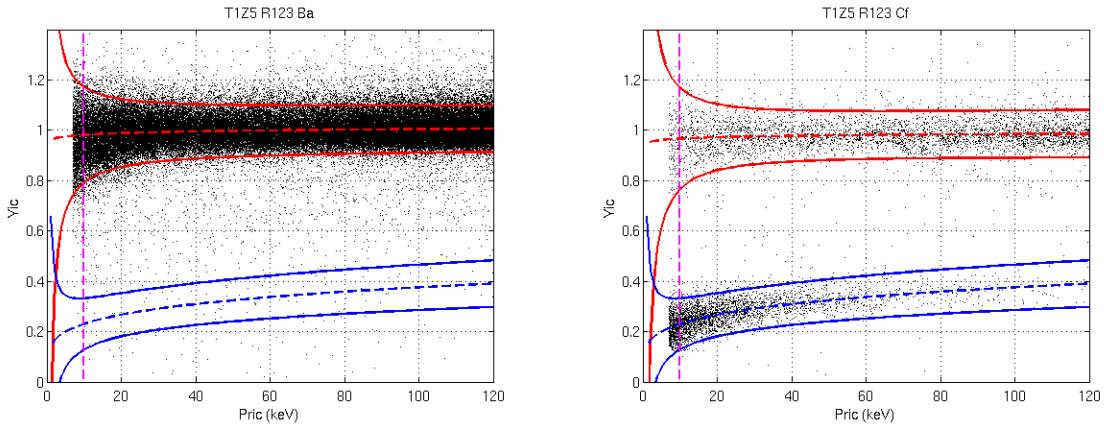

(a) (b)

Figure 5.11: Both of these plots show ionization yield as a function of phonon recoil along with the calculated electron (red) and nuclear (blue) recoil bands for the germanium detector T1Z5. The dashed points represent the center of the electron and nuclear recoil bands while the solid lines denote the 2σ bands. (a) Black points are events from ^{133}Ba gamma calibration data sets. (b) Black points are events from ^{252}Cf neutron calibration data sets. From [25].

5.4.6 Phonon Timing

To remove surface events, especially those that are not rejected by the ionization yield cut due to poor ionization collection (Section 2.6.1), a cut based on phonon timing is applied. The cut developed for Runs 123 and 124 [26] was based on the R119 Soudan 2-tower cut [110] using the primary phonon delay and risetime (Section 2.6.1).

There are two parts to the Run 123 and 124 phonon timing cut, the consistency and discrimination cuts (Figure 5.12). The consistency cut requires the difference between the phonon delay and risetime to be consistent with the neutron calibration population within 4σ. The discrimination part of the cut defines the sum of the phonon delay and risetime as the "timing parameter." WIMP candidate events must exceed a minimum timing parameter value. This threshold is determined for each detector to allow a passage fraction of no more than 0.3% for surface events from the ^{133}Ba calibration data in order to obtain an estimated background, due to surface events, of less than one event in the full WIMP search exposure.

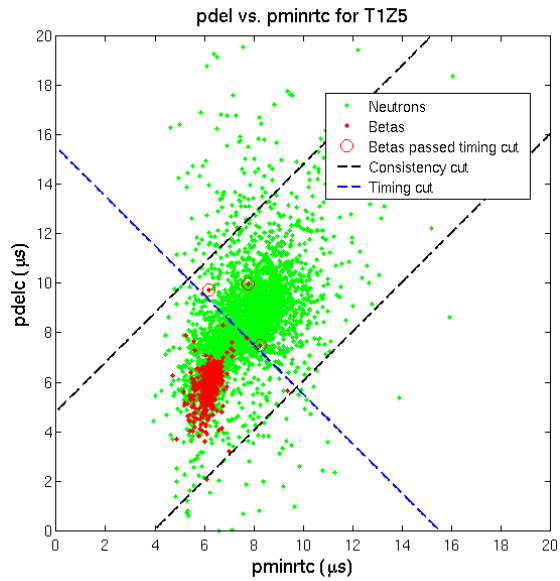

Figure 5.12: Phonon delay as a function of risetime for T1Z5 neutron (green) and surface (red) events. The acceptance region for bulk nuclear recoil events is defined to the upper right of the blue dashed line and between the black dashed lines. Surface events that pass the timing cut are represented by the circled red dots. From [26].

5.5 Analysis Exposure

The Run 123 and 124 analysis used the detectors listed in Tables 5.2 and 5.3 to look for WIMP interactions. As discussed in Section 5.4.3 all 30 detectors were used as veto detectors to identify single-scatter events. The analysis includes a smaller subset of Run 124 detectors due to time constraints placed on the analysis by the collaboration as to when the results should be presented and the decision to include Run 124 with Run 123 for this analysis. Run 124 detectors not selected to be used as WIMP search detectors were not necessarily bad or poorly performing. To meet the collaboration-imposed time constraints this analysis only includes Run 124 detectors which were in a state very similar to what they were during Run 123 so that creating a new set of cuts was not necessary for incorporating the two runs together.

The total live time of the Run 123 and 124 WIMP search analysis, after all data quality cuts, was [15]:

- Germanium : 421.43 kg-d

				T5Z1
T1Z2	T2Z2	**T3Z2**	**T4Z2**	
	T2Z3	T3Z3	T4Z3	T5Z3
T1Z4	T2Z4	**T3Z4**	**T4Z4**	**T5Z4**
T1Z5	**T2Z5**	**T3Z5**	**T4Z5**	**T5Z5**
		T3Z6	**T4Z6**	

Table 5.2: The 15 germanium and 6 silicon Run 123 detectors included in the analysis. Germanium detectors are bold.

T1Z2				
			T4Z3	
	T2Z4		**T4Z4**	**T5Z4**
T1Z5			**T4Z5**	**T5Z5**
			T4Z6	

Table 5.3: The 7 germanium and 2 silicon Run 124 detectors included in the analysis. Germanium detectors are bold.

- Silicon : 53.47 kg-d

The total efficiency, as a function of phonon recoil energy, of the science cuts in the Run 123 and 124 germanium [17] and silicon [27] WIMP search analyses is shown in Figure 5.13.

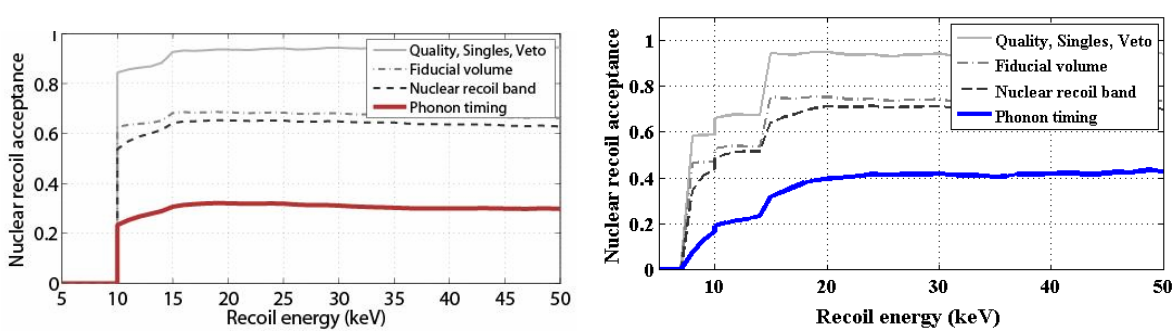

Figure 5.13: The efficiency of the R123 and 124 (a) germanium and (b) silicon WIMP search analysis as a function of phonon recoil energy. Curves represent the total efficiency after the subset of cuts described in the caption were applied to the data. From [17] and [27].

In order to compare multiple experiments with different exposures and efficiencies the spectrum-averaged exposure for a given WIMP mass is calculated. This takes an

experiment's live time and efficiency function into consideration. For this analysis the spectrum-averaged exposure for a 60 GeV/c^2 WIMP is 119.9 kg-d for the germanium detectors and 25.9 kg-d for the silicon detectors [15].

5.6 Background Estimate

Before looking at the WIMP signal region it is critical to understand the experimental backgrounds. For CDMS the two main backgrounds to consider are nuclear recoil and surface events.

5.6.1 Nuclear Recoil Background Events

Nuclear recoil backgrounds are the most dangerous to a WIMP dark matter search because they cannot be distinguished from WIMP interactions. The major sources of nuclear recoil backgrounds are from neutrons generated through cosmic ray interactions or radioactive decays. As discussed in Chapter 3 the experimental location and setup is designed to minimize these types of interactions in the detectors. Detailed studies and simulations of these backgrounds have been carried out to estimate their impact on the sensitivity [111, 110, 60].

Cosmogenic neutrons are generated by energetic cosmic ray induced muons. The most dangerous cosmogenic neutrons have energies in the MeV range and can produce nuclear recoils in the ZIP detectors with keV energies, the same energies expected from a WIMP interaction. Monte Carlo simulations of the CDMS background due to these neutrons have been performed using the GEANT 4 and FLUKA + MCNP packages. Analysis of these results predict <0.1 single-scatter veto-anticoincident cosmogenic neutron in the Run 123 and 124 exposure. The simulations were cross checked by comparing their predictions with the Run 123 and 124 data looking at veto-coincident nuclear recoil events. The predicted number, based on simulations, was consistent with the number seen in the data [60].

Another source of MeV energy neutrons is from radioactive processes, particularly through spontaneous fission and (α, n) reactions. To estimate the background from these radiogenic neutrons it is necessary to understand material contamination [112] and experimental geometry and perform Monte Carlo simulations [113]. Based on these studies the expected radiogenic neutron background is <0.1 event in the Run 123 and 124 data [114].

5.6.2 Surface Events

While the cuts applied to the WIMP search data sets were designed to reject surface electron recoil events there remain some outlier events which are misclassified as nuclear recoils. The background due to these misclassified surface events was estimated based on the combination of several methods [15]. All of these methods calculated the ratio r_i, the fraction of events passing the timing cut to those failing, for each detector. Once r_i is known the estimated number of surface events falling in the nuclear recoil band mimicing a WIMP signal is calculated by multiplying r_i by the total number of events failing the timing cut.

The surface event background for internal detectors was estimated using two methods. The first method calculated r_i by looking at the multiple-scatter events within the nuclear recoil band. While this class of events should have the same ionization yield distribution as events within the signal region the statistics are poor. To increase statistics for determining r_i the timing cut performance of multiple-scatter events outside of the nuclear recoil band were considered. Although this event population increased the statistics there were additional differences between it and the singles distribution, particularly in ionization yield. These differences were accounted for in the r_i calculation based on the results of systematic studies between the multiple and single event distributions.

Detectors at the end of a tower have only one face adjacent to a neighboring

detector. This presents additional complications in calculating r_i due to the difference between single- and multiple-scatter events across the two detector faces. The exterior detector face only has single-scatter surface events making it impossible to determine which detector face these events occurred on. For these detectors r_i is calculated based on the multiple-scatter events within the nuclear recoil band (on the internal detector face) and weighted by the inferred division between the two faces.

Based on these methods the surface event background was estimated to be:

- Internal Ge surface event background: $0.26^{+0.18}_{-0.11}(\text{stat})^{+0.11}_{-0.10}(\text{syst})$
- External Ge surface event background: $0.29^{+0.41}_{-0.20}(\text{stat})^{+0.3}_{-0.1}$ (syst)
- Total Ge surface event background: $0.59^{+0.49}_{-0.27}(\text{stat})^{+0.32}_{-0.15}(\text{syst})$
- Total Si surface event background: $1.08^{+0.93}_{-0.56}(\text{stat})\pm0.12$ (syst)

5.7 Unblinding

After all cuts and leakage estimates were finalized the WIMP search data were unblinded. Due to the time constraints placed on the Run 123 and 124 analysis, that were discussed in Section 5.5, the germanium and silicon detectors were unmasked separately. For both the germanium and silicon data, prior to looking into the signal region the conservative blinding cut was removed so that the number of single-scatter events failing the phonon timing cut, and therefore not signal events, could be compared with expectations. This step allowed for a final verification that all cuts, especially data quality, were applied correctly and performed as expected. After checking that the number of single-scatter events failing the phonon cut were consistent with expectation (Table 5.4), the phonon timing cut was applied.

The germanium detectors used for the WIMP search analysis, as listed in Section 5.5, were unblinded on February 5, 2008 and the internal silicon detectors were

Detector Number	Tower 1	Tower 2	Tower 3	Tower 4	Tower 5
Z1					**18±10 (30)**
Z2	**1.4±0.5 (9)**	6.8±3.0 (6)	**3.2±0.8 (1)**	**3.6±0.9 (4)**	
Z3		**2.4±0.7 (5)**	7.1±3.1 (9)	5.0±2.3 (2)	11.2±4.7 (10)
Z4	6.5±2.9 (7)	6.8±3.0 (14)	**3.5±0.9 (4)**	**5±1.1 (3)**	**5.8±1.3 (3)**
Z5	**4.3±1 (8)**	**4.3±1 (2)**	**2.2±0.6 (0)**	**4.4±1 (5)**	**3.8±0.9 (4)**
Z6			**4.5±1.7 (6)**	**14±4 (13)**	

Table 5.4: The predicted number of single-scatter events failing the phonon timing cut along with the observed number in parentheses. Germanium detectors are bold.

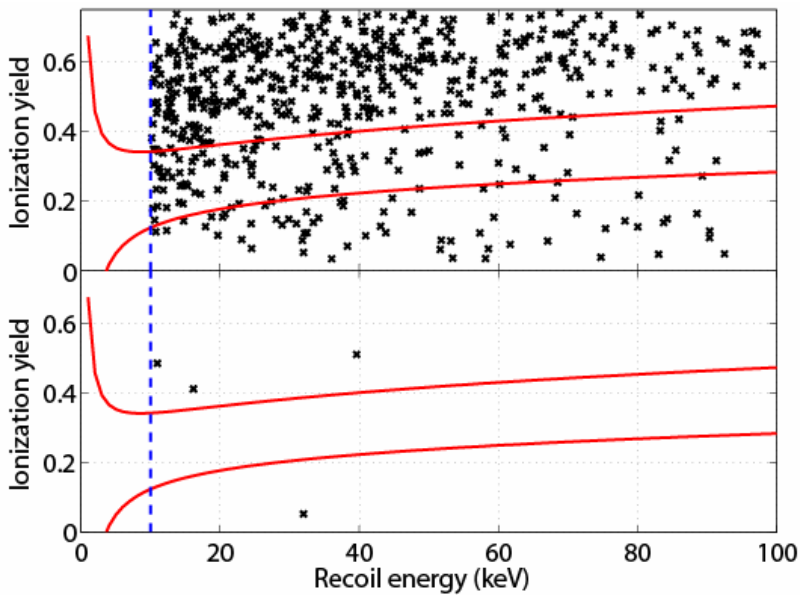

Figure 5.14: Ionization yield as a function of phonon recoil energy for the Run 123 and 124 germanium WIMP search data. These plots focus on the nuclear recoil band region. Events in the top plot pass all cuts except ionization yield and phonon timing while events in the bottom plot include all cuts. From [17].

unmasked on December 3, 2008. No signal events were observed in any detector, as illustrated in Figure 5.14 for the germanium data.

5.8 Results

Based on the null results from the first 5-tower Soudan germanium and silicon detector data, upper limits can be placed on the WIMP-nucleon cross section. The upper limits assume the standard halo model: including a Maxwellian velocity distribution,

characteristic velocity of 270 km/s, and local density of 0.3 GeV/c^2.

Figure 5.15 shows the 90% confidence level upper limits on the spin-independent WIMP-nucleon scattering cross section for the first 5-tower Soudan data along with previous CDMS results. The dashed curve shows the results from this analysis and the dot-dashed curve represents the reanalysis of the Soudan 2-tower data from Runs 118 and 119 [8]. Combining all the Soudan data produce the results shown by solid curves. The results from the germanium combined results are 3.4 times stronger than the previous Soudan 2-tower results at the curve minimum while the silicon results from the Run 123 and 124 5-tower data is 3 times stronger than Soudan 2-tower results at the curve minimum.

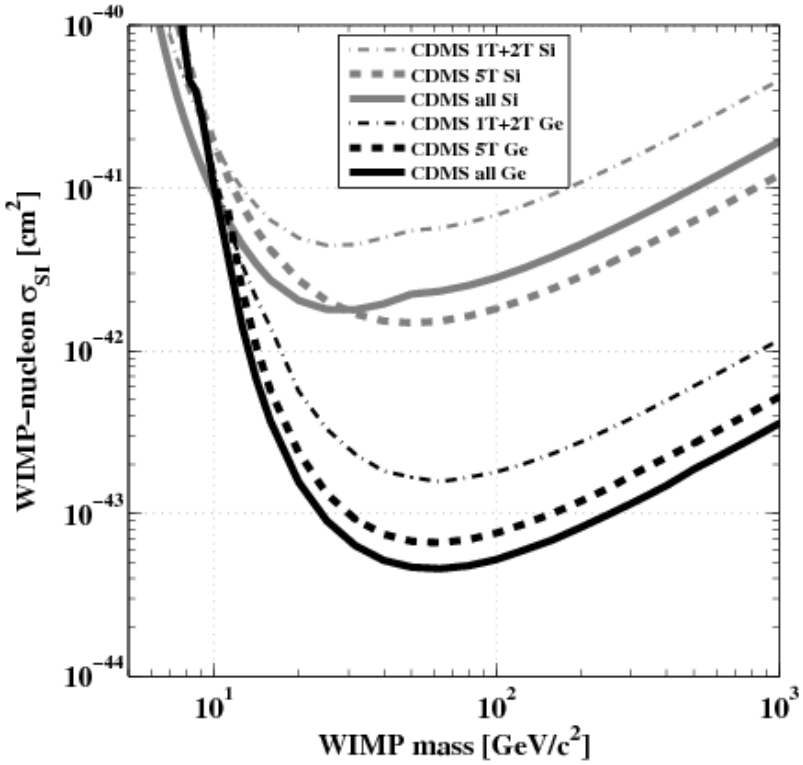

Figure 5.15: 90% confidence level upper limits on the spin-independent WIMP-nucleon scattering cross section as a function of WIMP mass for CDMS-II germanium (black) and silicon (gray) data showing the results of the Soudan 2-tower reanalysis (dot-dash), the 5-tower analysis (dash), and the combination of the two (solid). Courtesy of Jeff Filippini, from [28].

Figure 5.16 compares the CDMS combined germanium and silicon results from

Figure 5.15 with the results from other leading dark matter experiments: including EDELWEISS I [48], WARP [52], ZEPLIN III [51], and XENON10 [115, 50, 116]. The CDMS combined germanium upper limit currently places the strongest constraints on WIMP cross section for masses above 44 GeV/c^2.

Along with these results Figure 5.16 shows three regions of WIMP parameter space based on supersymmetric models [117, 118]. The light gray region at higher cross sections represents the 3σ annual modulation detection by the DAMA/LIBRA experiment [58] as interpreted within the standard halo model [119]. This region is inconsistent with the results of all other dark matter experiments within this model framework.

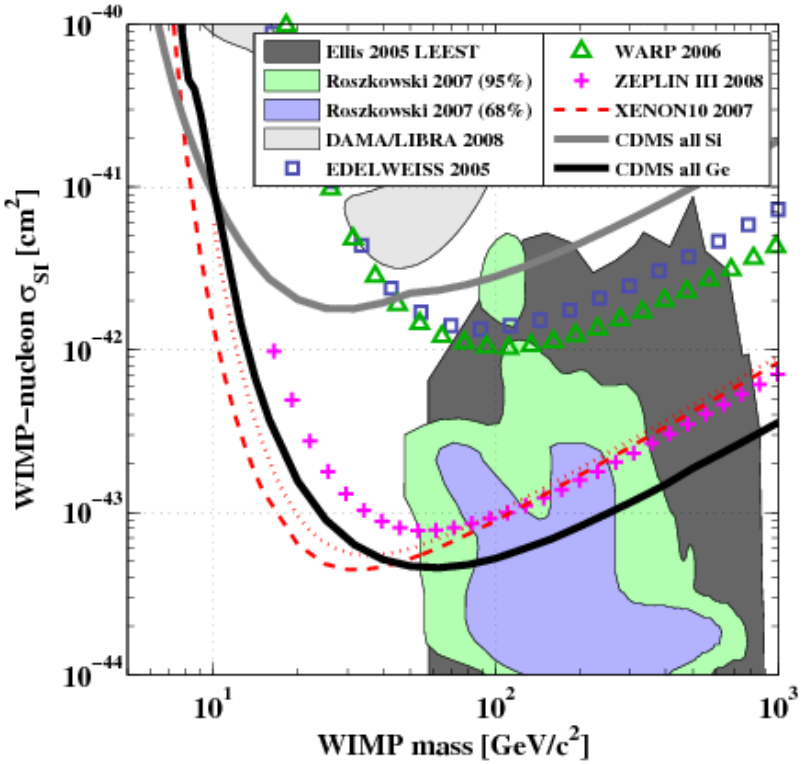

Figure 5.16: Like Figure 5.15, this shows the 90% confidence level upper limits on the spin-independent WIMP-nucleon scattering cross section as a function of WIMP mass. The curves represent the results from the combined CDMS Soudan data (solid black, germanium, and gray, silicon), XENON10 (red dashes, red dots indicate the effect of the newest scintillation yield measurements on the XENON10 result), ZEPLIN III (magenta crosses), WARP (green triangles), and EDELWEISS (blue squares) while the shadded regions indicate parameter ranges expected from the DAMA/LIBRA modulation result and supersymmetric models. Courtesy of Jeff Filippini, from [28].

Figure 5.17 shows the CDMS combined Soudan data results as interpreted for spin-dependent WIMP interactions with ^{29}Si and ^{73}Ge isotopes. Figure 5.17a assumes couplings to neutrons only and Figure 5.17b to protons only. Both of these figures compare the CDMS combined results with those from other experiments: including XENON10 [120], COUPP [10], KIMS, Super-Kamiokande [121], and DAMA/LIBRA [58, 119]. As in Figure 5.16, these results are plotted along with regions representing possible WIMP parameter space based on supersymmetric models [118].

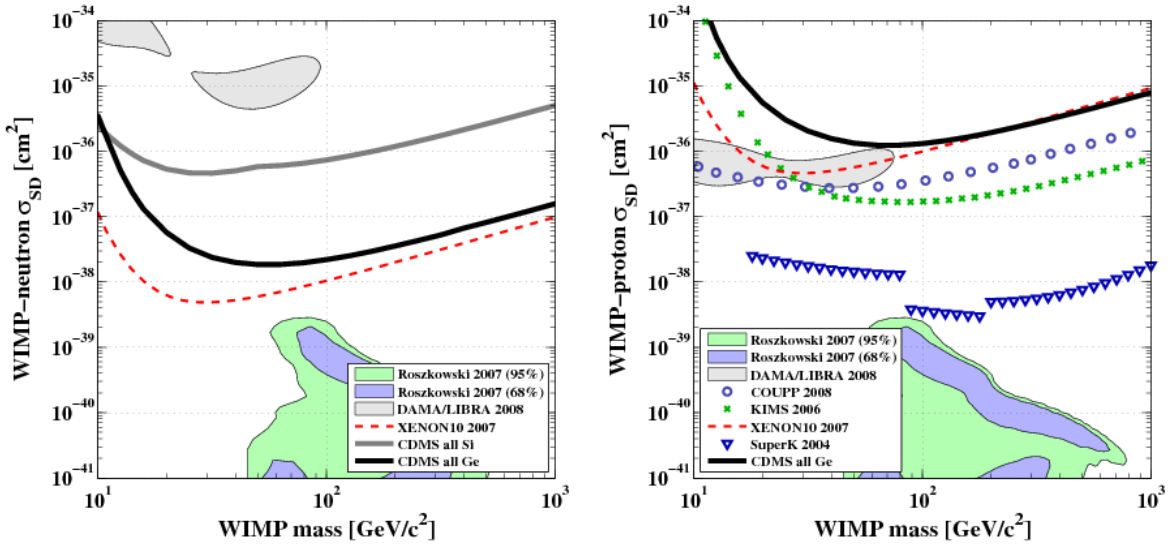

(a) (b)

Figure 5.17: 90% confidence level upper limits on the spin-dependent (a) WIMP-neutron and (b) WIMP-proton scattering cross section as functions of WIMP mass. The curves represent the results from the combined CDMS Soudan data (solid black, germanium, and gray, silicon), XENON10 (red dashes), Super-Kamiokande (blue triangles), KIMS (green crosses), and COUPP (blue circles) while the shadded regions indicate parameter ranges expected from the DAMA/LIBRA modulation result and supersymmetric models. Courtesy of Jeff Filippini, from [28].

Chapter 6

Neutralization

6.1 Introduction

To maintain good ionization-yield discrimination in each detector, charge trapping, which leads to incomplete ionization collection, must be minimized. To reduce bulk trapping by defects and lattice impurities, detectors routinely undergo neutralization. During this process the detector is grounded and bombarded with energetic particles (which CDMS calls "baking," or, when used for short periods of time, "flashing"). These particles create electron-hole pairs in the crystal which diffuse to neutralize ionized impurities or recombine. Neutralizing ionized impurities causes these sites to have a smaller trapping cross-section than if they were charged, therefore reducing bulk trapping in the detector.

Operationally it is important to ensure and maintain proper detector neutralization. Among other things this requires using the appropriate neutralization procedure based on the detector location and circumstances, determining the optimal interval between neutralization while taking data, and monitoring data quality. This chapter discusses these operational aspects as well as recent tests which have increased our understanding of neutralization.

6.2 Neutralization Methods

There are several methods for generating the energetic particles used to bombard the detector crystals during neutralization. The techniques that CDMS uses include the use of LED photons, radiation from radioactive sources, and ambient background radiation. Each of these methods is particularly well suited for certain circumstances and each has its own set of variables to take into consideration. Depending on the testing location, a combination of LED and source neutralization techniques should be used together. The specific operational implementations of these methods are discussed later in Appendix C.

6.2.1 LED Neutralization

From the beginning of CDMS ZIP detectors, LEDs have been used for detector neutralization (Figure 6.1). These LEDs are mounted on the detector housing and the emitted photons create electron-hole pairs in the detector crystal (for additional details on the CDMS LEDs, see Appendix A).

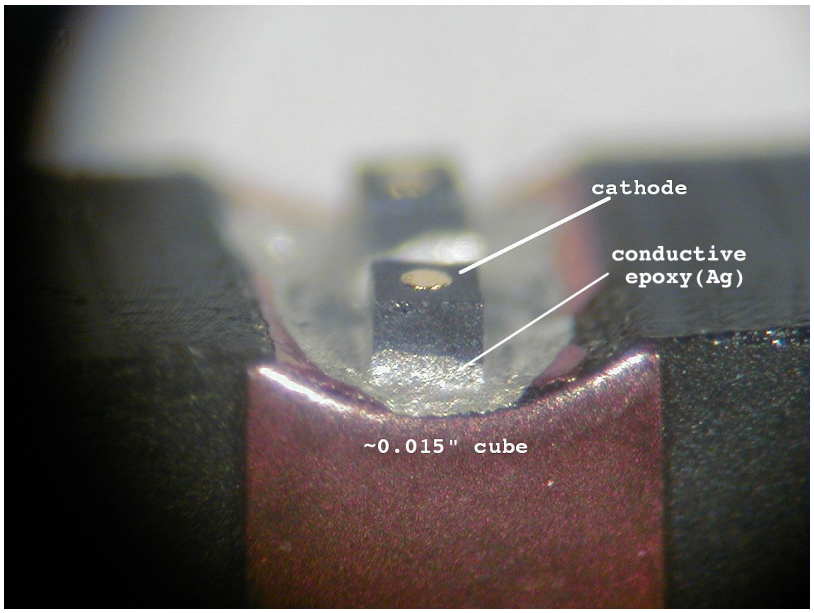

Figure 6.1: Close-up photo of LED mounted in CDMS ZIP detector housing. Picture and annotations courtesy of Dennis Seitz.

LEDs have historically been the primary method of neutralization in the CDMS-II experiment and have done this job well. The use of LEDs does require some optimization, especially in the Soudan set-up with many detectors. A fundamental consideration is the effect of the LED generated heat load on the cryostat. This requires a balance between achieving effective neutralization and minimizing the cryostat heat load [122]. To achieve this, the number of LEDs used at one time and length of time they are used is tuned. At the beginning of many of the Soudan 5-tower runs systematic studies were conducted to understand how the detectors become neutralized and the effectiveness of different neutralization techniques. As discussed later in this chapter, some of these tests focused on determining the appropriate LED settings to achieve this balance between effective neutralization and heat load.

6.2.2 Strong Source Neutralization

Another technique for neutralizing detector crystals is to take advantage of ambient background radiation (at the surface sites) or to use strong radioactive sources to create electron-hole pairs in the detector crystal. The effectiveness of neutralization using strong sources is discussed here.

The first time this technique was used in CDMS-II was at the end of Run 124 and the beginning of Run 125. This technique was suggested to supplement LED baking, especially for detectors that had no working LEDs due to equipment failures, and was based on the neutralization procedure used in CDMS-I [123, 12] and by the Edelweiss dark matter experiment. Using strong cobalt and cesium sources worked remarkably well the first time they were used on the 5-towers of detectors at Soudan. There were several silicon detectors that were not usable in the previous runs because they had no working LEDs, and therefore were poorly neutralized, which were able to be used in Run 125 after the strong source neutralization.

However, there are some issues involved with neutralizing using only strong sources.

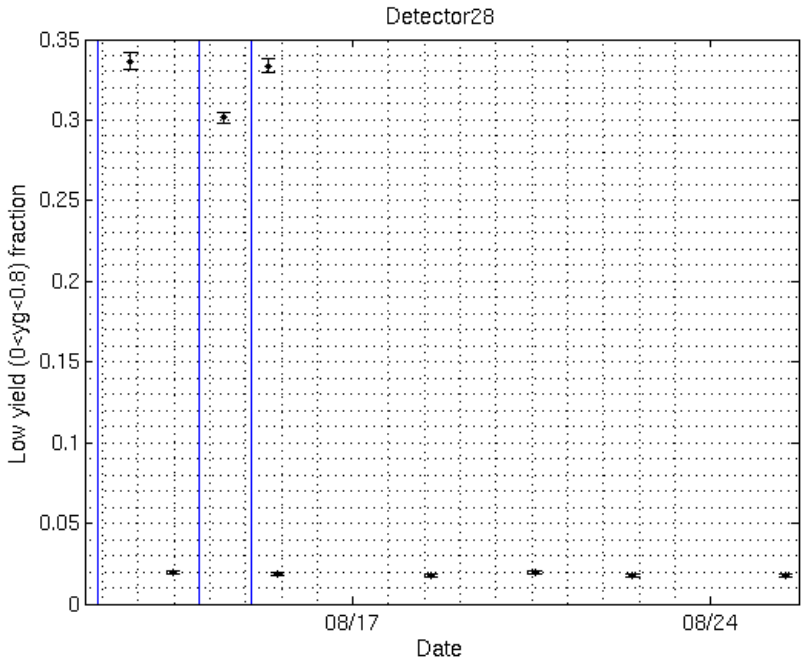

Figure 6.2: Plot showing a figure-of-merit of good neutralization (fraction of low yield events) for Ge Boule B detector Z28 (T5Z4) for barium calibration data sets taken at the beginning of Run 128. Each point represents a single data set and the vertical blue lines represent when strong source neutralization occurred. Note how the fraction of low yield events is high (indicates poor neutralization) after each strong source bake and then becomes low (indicates good neutralization) due to LED neutralization.

Probably the most important issue is that for some detectors using strong sources worsened the detector neutralization state (Figure 6.2). While this is not entirely understood, the detectors made worse by strong sources were germanium detectors made from the same boule (Boule B) of germanium. There are not many differences in the germanium properties between Boule B and the other boules except for a slight difference in the impurity concentration. Boule B has a higher impurity concentration than the other boules by at least a factor of 2 ($2.7\times10^{+11}$ to $4.7\times10^{+11}$ impurities per cm^3 as compared to $9.5\times10^{+10}$ to $1.0\times10^{+11}$ impurities per cm^3 or $8.5\times10^{+10}$ to $1.9\times10^{+11}$ impurities per cm^3). Despite these detector neutralization states worsening after using strong sources, performing a LED flash afterwards caused the detector neutralization to return to a good state. It is interesting to consider whether this phenomenon with the Boule B detector neutralization states points to an upper limit

on the germanium impurity concentration which can be sustained with this type of detector. To study this, future tests could be performed in a controlled experiment comparing the neutralization states of crystals with different impurity concentrations.

6.3 Assessing Neutralization

To determine whether settings or procedures are effectively neutralizing a detector, it is important to find a figure-of-merit that traces good neutralization. During the Soudan 5-tower runs there was considerable effort put into finding this type of figure-of-merit. One direction that was pursued was to find a feature in the charge pulse shape that would indicate when the LEDs begin emitting photons and started neutralizing the detector crystals. Another direction pursued was to determine a quantitative figure-of-merit that could be used to compare detector neutralization states. This section describes these studies.

6.3.1 Pulse Shapes

Despite the detector charge channels being grounded during LED neutralization, LED pulsing induces coincident charge pulses. A series of studies were conducted at the Case Western and UC Berkeley test facilities, as well as at the Soudan underground site, which attempted to make a correlation between effective detector neutralization and these charge pulses seen during LED pulsing. While this study collected many pulses and observed some similarities, it did not find a clear connection in the charge pulses between all the various detectors and LEDs. These charge pulses are messy as they contain not only information from the LEDs and neutralization process, but also from pick-up due to the GPIB commands and cross-talk. Figure 6.3 shows a sample charge pulse (black) along with the FEB front panel voltage monitor trace of the LED (red). The charge pulse begins coincident with the LED pulse starting and shows a spike, in the opposite polarity as the initial pulse direction, coincident

with the LED pulse ending. The spike coincident with the end of the LED pulse is most likely due to GPIB pick-up or cross-talk. If the LED pulse is long enough, the charge pulse often changes polarity and has a bump in it. This is possibly related to the emission of LED photons, but this feature is not consistent between all detectors and LEDs, so it is difficult to make a concrete conclusion.

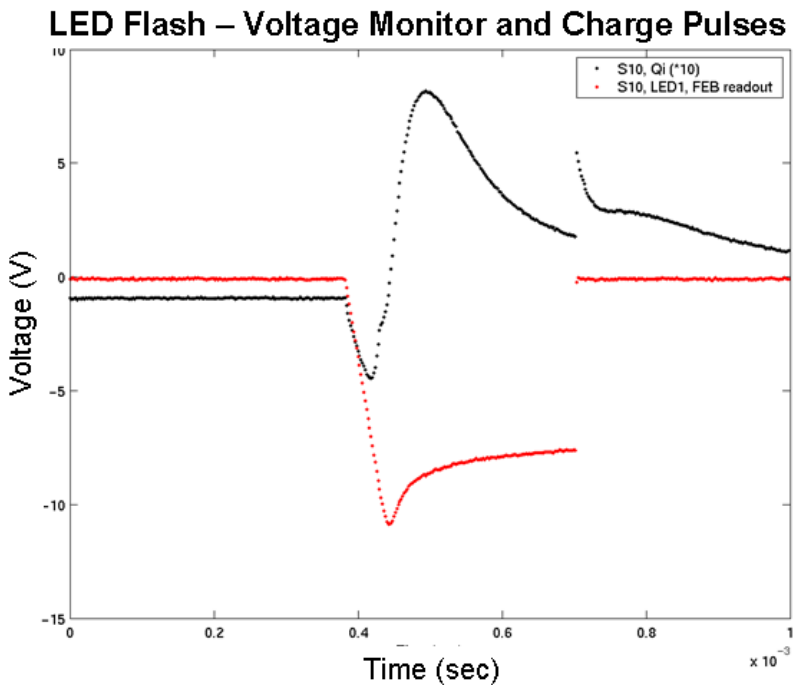

Figure 6.3: Oscilloscope trace showing voltage as a function of time for a charge pulse due to a LED flash (black) and the FEB front panel voltage monitor trace showing the voltage through the LED (red).

6.3.2 Voltage Monitoring

The FEB warm electronics board has a test point on its front panel which can be used to measure the voltage across the LED. Since each LED is unique, it would be advantageous to correlate characteristic features in this voltage monitor trace (red curve in Figure 6.3) with the time at which the LED provides effective detector neutralization. Details on this voltage monitor trace can be found in Appendix A. At the beginning of Soudan Run 127, a study involving a series of LED bakes was

performed to make this connection between the voltage monitor trace and detector neutralization via LEDs. Section 6.4.1 describes these results.

6.3.3 Low Yield Events

During the early Soudan 5-tower runs, one area where there was substantial effort was to determine a quantitative method for monitoring the neutralization states of the detectors. This is of particular importance for determining when a detector has reached a fully neutralized state at the beginning of a run, for ensuring that a detector maintains good neutralization throughout an entire run, and for verifying that detector neutralization is consistent between multiple runs.

Prior to these quantitative techniques, the method for determining whether a detector had reached a fully neutralized state was to do a series of LED bakes with barium calibration data taken between each bake. Then, by looking at the charge and yield distributions as well as several 2-D scatter plots (Figure 6.4), if the detector properties have not changed between the last two barium calibration datasets, it is considered to be neutralized. To monitor neutralization, KS tests of yield distributions were performed.

To determine a variable that traces detector neutralization states, several event populations were studied. In the end, looking at low yield events has proven to be a powerful method for establishing and comparing detector neutralization states. Additionally, two other event populations, those of the detector "funnel" and "ear" (Figure 6.5a), may also provide useful neutralization information. Scatter plots show that these populations could give "coarse" neutralization information as they appear to have a larger number of events when a detector has very poor neutralization (Figure 6.5b). To be able to use these funnel and ear event populations, there would need to be work on creating good, likely automated, cuts to select these events.

Looking at low yield events has proven to be a powerful quantitative tool for de-

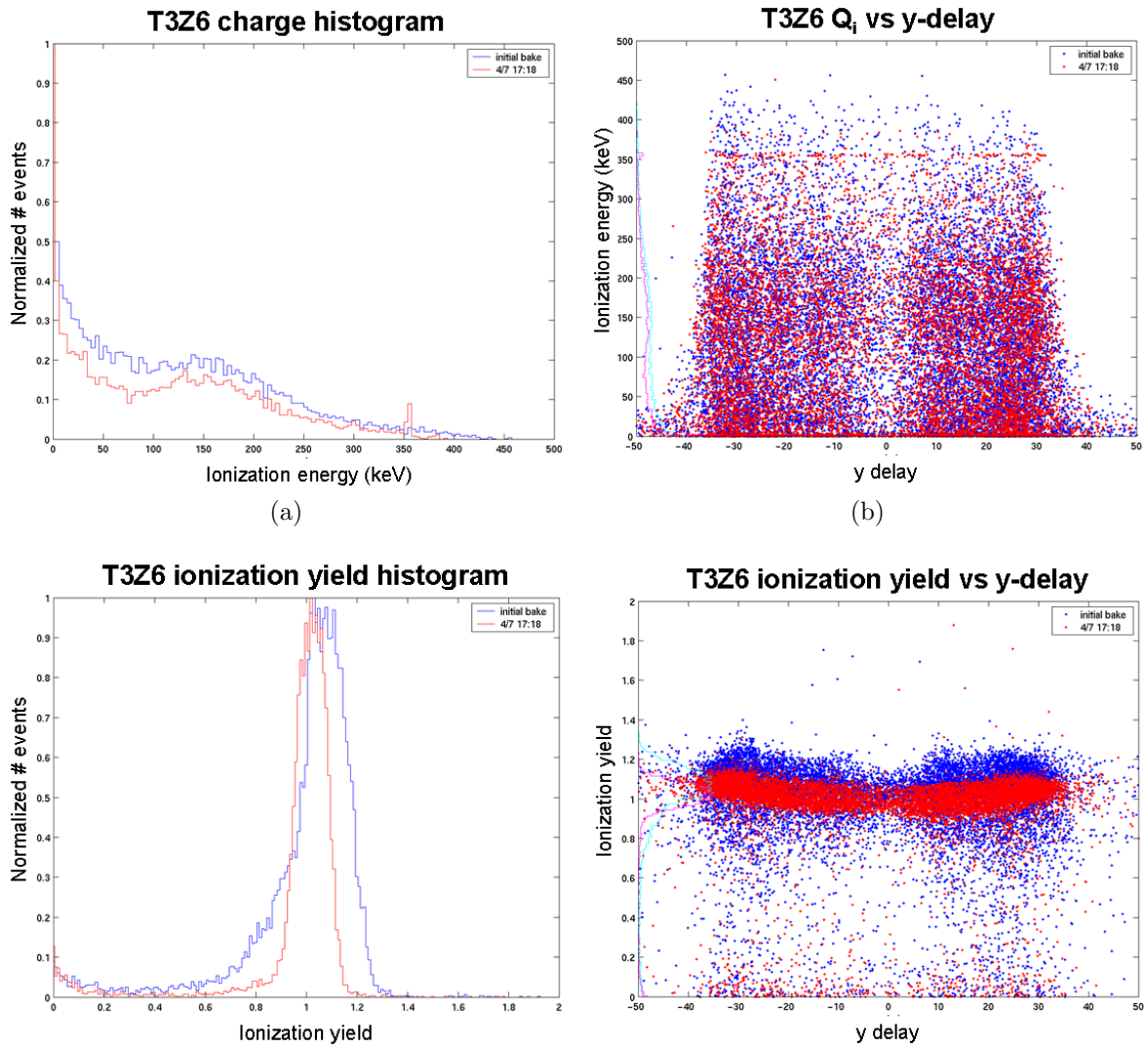

Figure 6.4: Histograms of charge (a) and ionization yield (c) and 2-D scatter plots of charge (b) and ionization yield (d) as a function of detector y-position comparing the neutralization states of two barium calibration data sets, one (blue) taken prior to any neutralization and the other (red) after an initial LED bake.

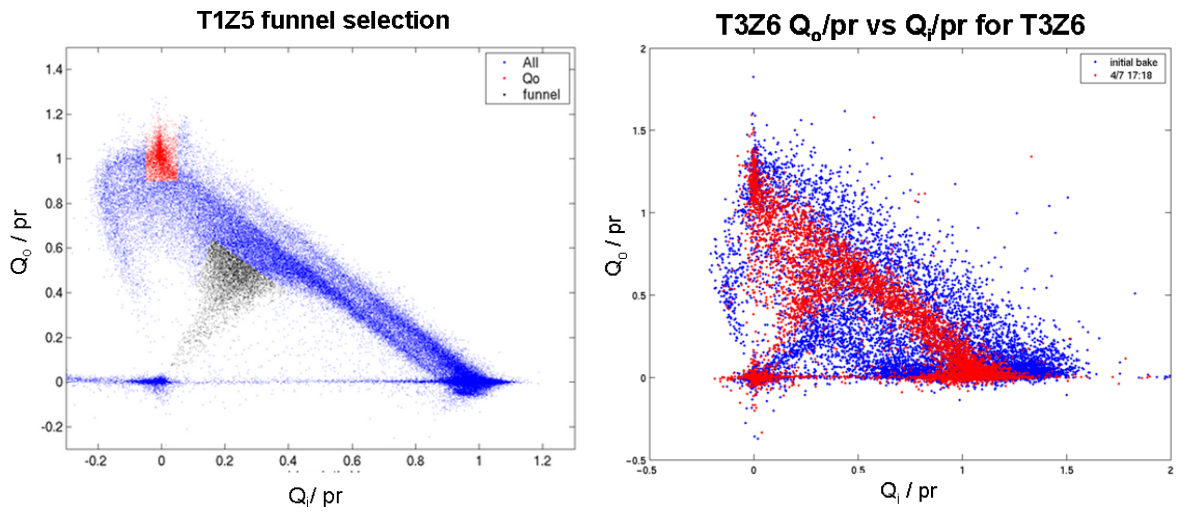

(a) (b)

Figure 6.5: 2-D scatter plots of ionization yield defined using only q-outer energy vs. ionization yield defined using only q-inner energy. (a) The black events make up the event population known as the "funnel" and the blue events to the left of the red (q-outer events) make up the event population known as the "ear". (b) Compares the neutralization states of two barium calibration data sets, one (blue) taken prior to any neutralization and the other (red) after an initial LED bake. Notice how the "funnel" and "ear" event populations shift between the blue and red data sets.

termining and tracing detector neutralization states. The specific quantity studied is actually the fraction of low yield events, or the ratio of the number of low yield (ionization yield below the electron recoil band) events to the total number of events, for each detector. Since this quantity is used at various times during the data processing and analysis, and usually early in the analysis, there are relatively few cuts placed on the data prior to calculating this ratio. Typically the only cuts placed on the data are to place a loose energy range and select only Q^{inner} events. These cuts are:

- total phonon energy >10
- Q^{inner} ionization energy <500
- Q^{inner} fiducial volume cut

In addition, the definition of low yield events is very general, usually between 0 <ionization yield <0.8. However, it is useful to use several different definitions of low

yield events, such as:

- 0 <ionization yield <0.2
- 0.2 <ionization yield <0.4
- 0.4 <ionization yield <0.6
- 0.6 <ionization yield <0.8

in order to see very poor neutralization or fine changes in neutralization. These various low yield event definitions tend to be especially useful when watching silicon detectors go from an extremely poor neutralization state to a good one (Figure 6.6). These various low yield event definitions can also provide information to determine how neutralization changes and if there is something odd occurring in the detectors.

While the fraction of low yield events gives a quantitative measure of detector neutralization states, it is still not particularly clear what the absolute value for a perfectly neutralized detector is. Comparison between datasets and runs has been particularly useful in ensuring good detector neutralization during the Soudan 5-tower runs and has shown remarkably consistent neutralization states despite the different neutralization procedures (Figure 6.7) [124].

From all of these studies, empirically the fraction of low yield events tends to be between approximately 0.01 - 0.05 for detectors with good neutralization. However this does vary somewhat by detector and would change if the low yield event definition were changed or different cuts were used. Also, using the strategy of defining good neutralization as when the yield distribution no longer changes after LED or strong source baking does not give an absolute measure of detector neutralization. The fact that the yield distribution, or fraction of low yield events, no longer changes could say just as much about reaching the neutralization limit achievable with that technique as about reaching the absolute good neutralization level.

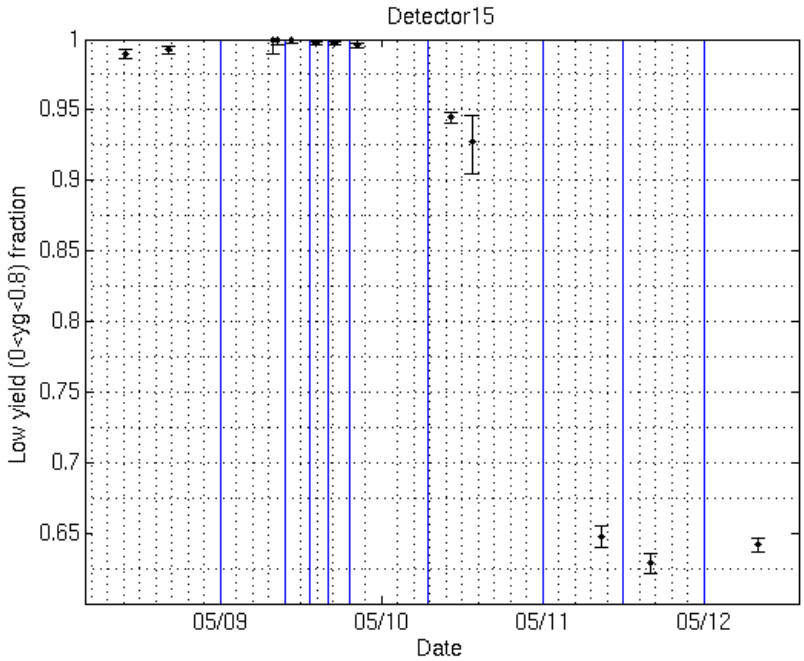

(a)

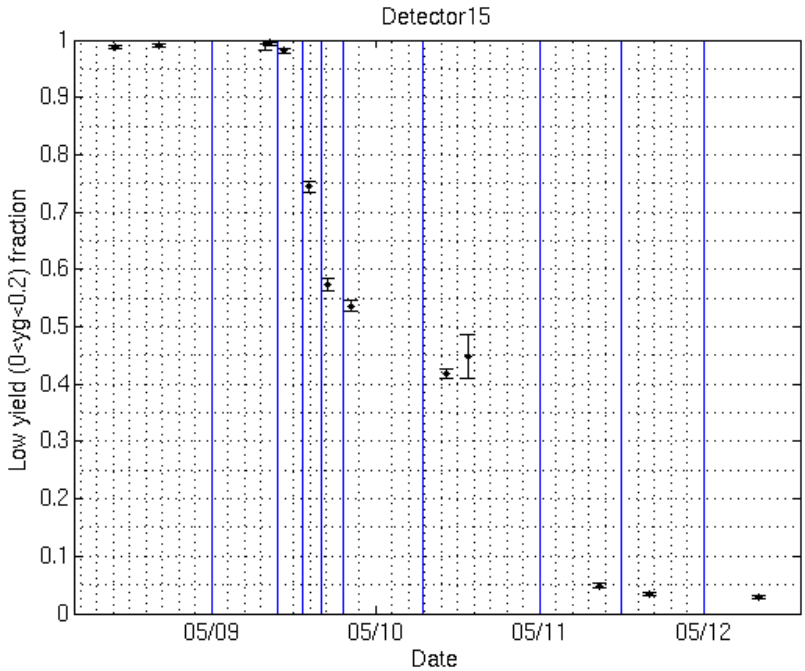

(b)

Figure 6.6: Like Figure 6.2, these plots show the fraction of low yield events as a function of time. These plots are for Si detector Z15 (T3Z3) barium calibration data sets taken at the beginning of Run 127. Each point represents a single data set and the vertical blue lines represent when LED neutralization occurred. (a) uses the fraction of low yield event definition of 0 <ionization yield <0.8. (b) uses the fraction of low yield event definition of 0 <ionization yield <0.2. Note how the fraction of low yield events decreases after fewer LED bakes using the low yield definition in (b). While this does not indicate good neutralization, it shows that the LED neutralization is beginning to work and affect the detector's ionization collection.

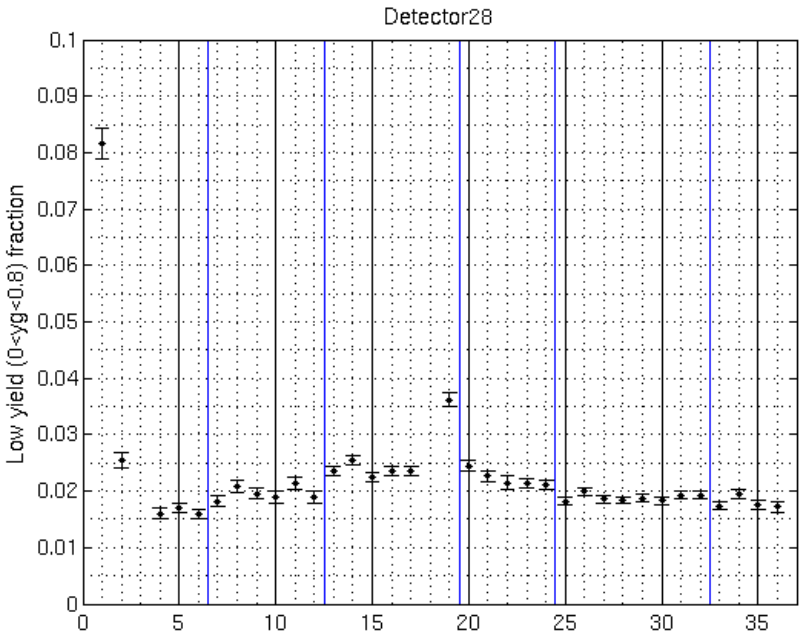

Figure 6.7: Like Figure 6.2, this plot shows the fraction of low yield events as a function of time. This plot is for Ge detector Z28 (T5Z4) barium calibration data sets taken throughout the Soudan 5-tower Runs 123 through 128. Each point represents a single data set and the vertical blue lines represent the division between each of the runs. Despite a few outlier data sets, the fraction of low yield events, and neutralization, remained fairly constant throughout.

While the fraction of low yield events is a good neutralization tracer, it is notable that neutralization is not the only detector phenomenon that affects this quantity. Some specific examples include:

- Phonon channel changing states (Figure 6.8)
- Charge channel bias changes (Figure 6.9)
- "helium film" zero-charge events (Figure 6.10)

In these examples the fraction of low yield events change, but not due to neutralization changes. Instead other external influences affect the ionization or phonon collection. During the Soudan 5-tower runs this occurred when T3Z1 phonon channel A changed states, T5Z2 charge bias was adjusted, and when there were zero-yield events caused by helium films on the detectors.

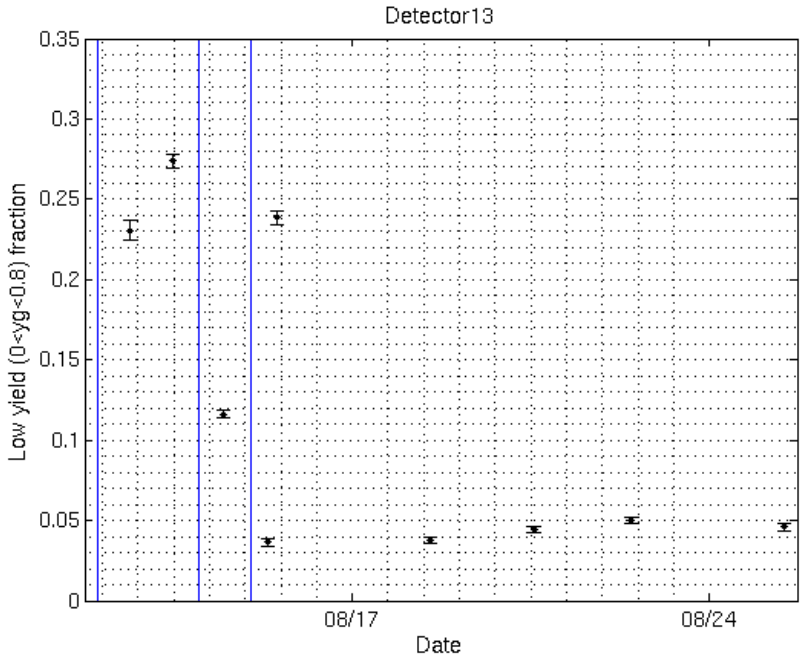

Figure 6.8: Like Figure 6.2, this plot shows the fraction of low yield events as a function of time. This plot is for Si detector Z13 (T3Z1). Each point is a single data set and the vertical blue lines represent times strong source neutralization occurred. Notice that the fraction of low yield events was very high during the fifth data set. This correlates with a change in T3Z1 phonon channel A state.

6.4 Optimizing running conditions

To most effectively neutralize detectors, one should optimize the procedures used. This section highlights how some of these optimizations are determined and what the most effective neutralization procedure should be comprised of.

6.4.1 LED Optimization

As discussed earlier, when using LEDs for detector neutralization, one must choose appropriate settings which produce effective neutralization while minimizing the heat load on the cryostat.

At the beginning of Run 127 there was a systematic study performed to better characterize the LEDs and LED detector neutralization. This study focused on finding a characteristic feature of a LED which corresponds to settings producing effective

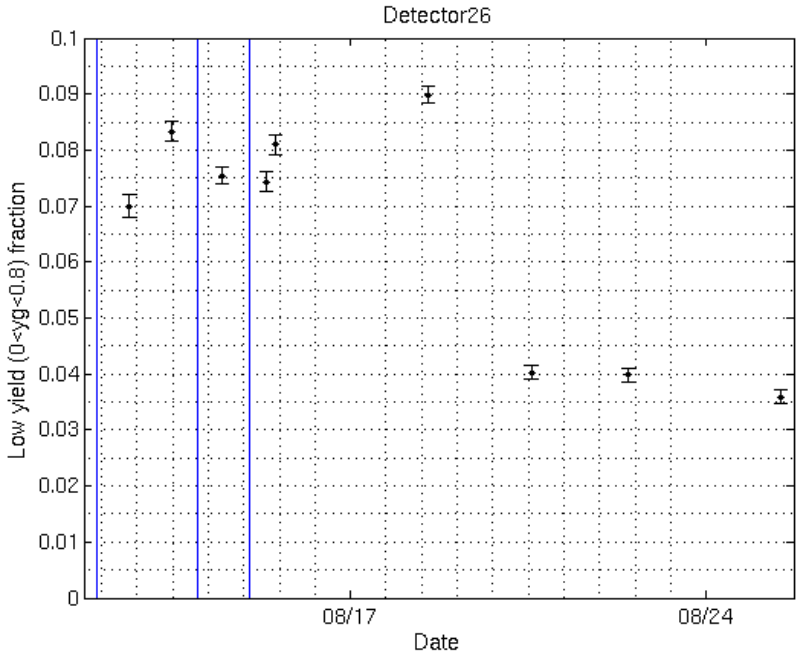

Figure 6.9: Like Figure 6.2, this plot shows the fraction of low yield events as a function of time. This plot is for Ge detector Z26 (T5Z2). Each point is a single data set and the vertical blue lines represent times strong source neutralization occurred. Notice that the fraction of low yield events suddenly decreased after the sixth data set. This correlates with a change in T5Z2 charge bias.

neutralization and determining if LEDs neutralize adjacent detectors. The results of this study are discussed below and the details are outlined in Appendix B.

LED on-time

Neutralization studies performed at the beginning of Run 127 were performed to correlate characteristic features in the voltage monitor trace (Section 6.3.2) with the time at which the LED provides effective detector neutralization. At the beginning of these studies, the detectors were in a de-neutralized state (because they had just experienced an extreme temperature excursion; see Section 6.6.1). After the detectors reached base temperature, a series of LED bakes were performed on six detectors. During each of these LED bakes the length of time the LEDs remained on was increased where the LED on-times were uniquely defined for each LED as determined by features in the voltage monitor trace. By evaluating the detector neutralization

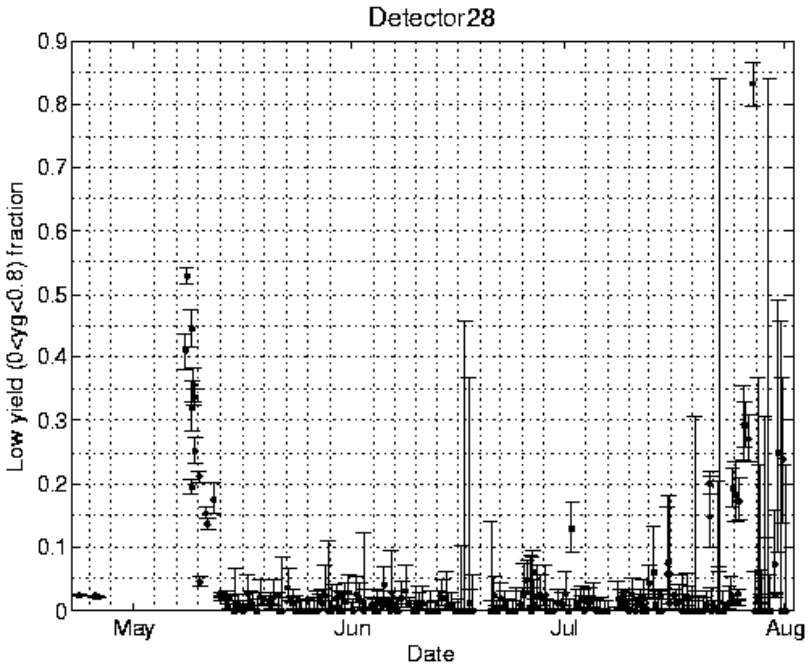

Figure 6.10: Like Figure 6.2, this plot shows the fraction of low yield events as a function of time. This plot is for Ge detector Z28 (T5Z4). Each point is a single data set. Notice that the fraction of low yield events was very high in May and again in August. The high fraction of low yield events in May was due to bad neutralization at the beginning of the run, prior to any LED or strong source bakes, while in August was due to zero charge events caused by helium films.

states after each LED bake, features in the voltage monitor trace corresponding to detector neutralization were determined.

The data from this series of LED bakes show that detectors began neutralization between LED test bake #2 and #3 (Figure 6.11), which correspond to the 90% and maximum amplitude of the voltage monitor trace [125]. This was determined by watching for changes in the fraction of low yield events in the datasets taken between each LED bake (see Section 6.3.3 for more details). Due to the coarseness of the available LED pulse on-times (10 μs steps), some LEDs were on slightly longer or slightly shorter than the 90% or maximum amplitude (as determined on the LED voltage monitor trace) time. Based on this study, by the time the LED voltage monitor trace is at its maximum amplitude, the LEDs are causing detector neutralization. In fact, the minimum LED pulse on-time, for LEDs to neutralize the detectors, is (approxi-

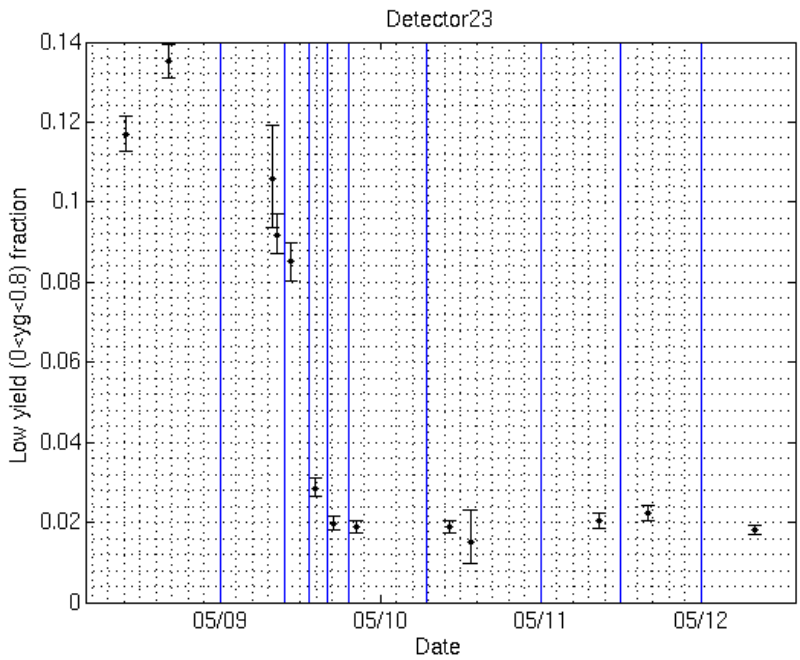

Figure 6.11: Like Figure 6.2, this plot shows the fraction of low yield events as a function of time. This plot is for Ge detector Z23 (T4Z5) barium calibration data sets taken during the LED tests at the beginning of Run 127. Each point represents a single data set and the vertical blue lines represent when LED neutralization (using T4Z5 LED) occurred. Note how the fraction of low yield events began dramatically decreasing, showing effective neutralization, after the third LED bake.

mately halfway) between 90% and maximum amplitude of the LED voltage monitor trace. The Soudan 5-tower LED on-times (that were used beginning with Run 124) were set to be 5 μs past the maximum amplitude of the LED voltage monitor traces. Based on this study, this on-time should be long enough for detector neutralization and appears to be a reasonable guideline for setting a minimum length for a LED pulse on-time.

Adjacent LED Neutralization

In addition to determining what feature in the FEB front-panel voltage-monitor trace corresponds with the start of LED detector neutralization, the Run 127 studies determined which detectors a given LED is able to neutralize. Base on this study, a LED neutralizes both the detector on which it is mounted as well as the detector

above it (adjacent to the phonon side, where the LED is mounted). However a LED is unable to neutralize the detector below it (adjacent to the charge side, the side opposite the LED) [125]. These results provide strong evidence that the LED photons reflect on detector surfaces (Figure 6.13) and are able to provide adjacent detector neutralization (Figure 6.12).

6.4.2 Strong Source Optimization

A series of optimizations could be done to modify the strong source neutralization procedure to make it more efficient. These optimizations include determining the optimal usage time and temperature dependence.

During the Soudan 5-tower runs, neutralization using the strong sources always occurred overnight, for at least 14 hours. In the future it would be interesting to perform a series of strong source "bakes" where the sources are used for progressively longer periods of time. This type of study would determine if there is an optimal length of time and if neutralization improves with the length of time the strong sources illuminate the detectors.

At the beginning of Run 125 strong sources were used while cooling the detectors to base temperature from approximately 8 K and, at the beginning of Run 128, while cooling the detectors to base temperature from approximately 67 K. In Run 125 the silicon detectors were all very well neutralized, but in Run 128 they needed much more neutralization after reaching base temperature (Figure 6.14). While there are many other variables in this comparison, such as differences in the initial neutralization states, it is notable that simply using the strong sources while cooling the detectors to base was not able to provide sufficient neutralization. This may give indication of a temperature dependence where neutralization using strong sources only work below a certain temperature.

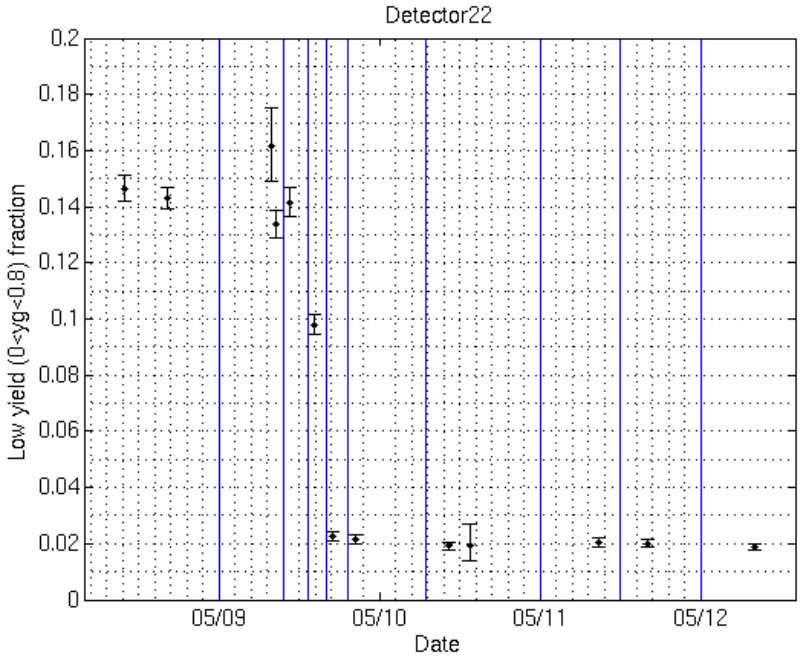

(a)

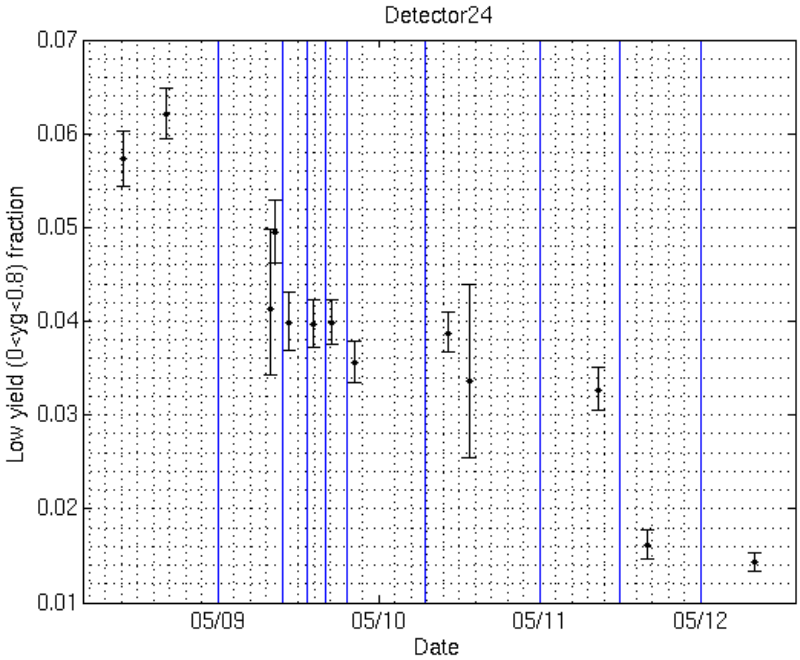

(b)

Figure 6.12: Like Figure 6.2, these plots show the fraction of low yield events as a function of time. (a) This plot is for Ge detector Z22 (T4Z4) barium calibration data sets taken during the LED tests at the beginning of Run 127. (b) This plot is for Ge detector Z24 (T4Z6) barium calibration data sets taken during the LED tests at the beginning of Run 127. Each point represents a single data set and the vertical blue lines represent when LED neutralization (using T4Z5 LED) occurred. Note how the fraction of low yield events began dramatically decreasing, showing effective neutralization, after the third LED bake for Z22 (T4Z4, adjacent to Z23's LED) but not Z24 (T4Z6, opposite from Z23's LED).

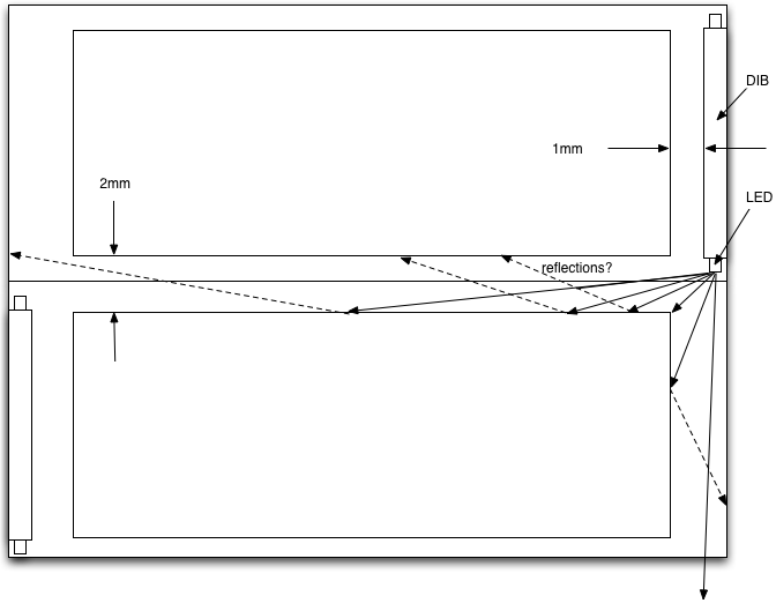

Figure 6.13: Diagram showing the possible LED reflection pattern allowing for neutralization of both the detector it is mounted on as well as the adjacent detector. Courtesy of Dennis Seitz.

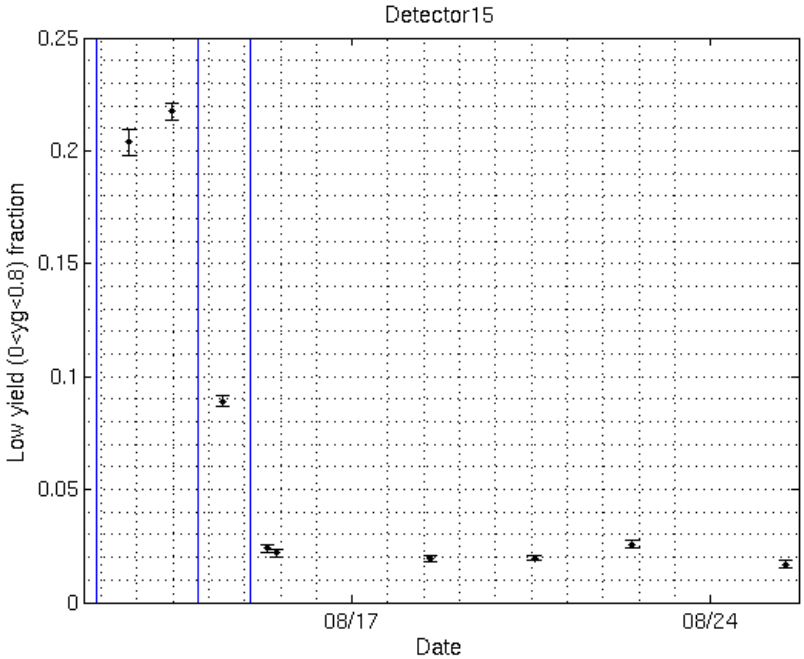

Figure 6.14: Like Figure 6.2, this plot shows the fraction of low yield events as a function of time. This plot is for Si detector Z15 (T3Z3) barium calibration data sets taken at the beginning of Run 128. Each point represents a single data set and the vertical blue lines represent when strong source neutralization occurred. Note how the fraction of low yield events did not indicate good neutralization after the first strong source bake that occurred during the cooldown.

6.4.3 Neutralization Effectiveness

LED and strong source bakes are approximately equally effective at neutralizing detectors, however, there are advantages and disadvantages to each method. Neutralization using LEDs adds a heat source in the fridge and only one tower or six detectors' LEDs should be used at one time to avoid excessively heating the fridge, while using strong sources does not add a heat load to the fridge and neutralizes all detectors at the same time. However using strong sources worsens the neutralization state of some detectors and a LED bake is required to restore neutralization for those detectors. Therefore, the most efficient and effective neutralization procedures use a combination of the different methods. In addition, barium or gamma calibration datasets which have sufficient statistics, at least several hundred thousand events, should be taken throughout the neutralization process, especially between individual bakes, to evaluate and monitor the neutralization states of the detectors.

Besides operational advantages to the different neutralization methods, there may also be differences in the physical neutralization process with the various methods. In particular, LEDs may be much better at surface neutralization while strong radioactive sources and ambient background radiation may be much better at bulk neutralization due to the different energies. This hypothesis also suggests that the best detector neutralization is achieved using a combination of methods.

6.5 Maintaining Neutralization

Once the detectors reach a well neutralized state, it is necessary to keep them neutralized throughout data taking. There are several ways for a detector to lose neutralization, where the primary cause is having detector charge channels biased for extended periods of time or increasing the detector temperature (see Section 6.6). The focus here will be on neutralization stability while at base temperature.

As previously mentioned, neutralization can degrade while the detectors are at base temperature if the charge channels are biased for extended periods of time. To maintain neutralization, it is necessary to determine the maximum length of time the detectors can be biased. This time varies for different run conditions, i.e., WIMP search versus barium calibration datasets, due to the different interaction rates. During the 5-tower Soudan data runs, the neutralization states of the detectors were monitored during long WIMP search and barium calibration datasets to evaluate the neutralization stability.

While taking WIMP search data it was determined that there was not a significant change in the detector neutralization states over the course of 12 hours. This was verified near the beginning of Run 123 [29] by looking at the mean and standard deviation of ionization yield (Figure 6.15a) as well as using fraction of low yield events [126], in Run 125 [127], and in Run 127 [128] by looking at the fraction of low yield events, both binning events in 1 hour bins (Figure 6.15b).

To maintain detector neutralization over long periods of time during WIMP search running there were two LED flashes each day. One of these LED flashes occurred automatically during the daily cryogen transfers and the other occurred after approximately 11 hours of data taking.

While taking barium calibration data it was determined that there was not a significant change in the detector neutralization states over the course of a dataset containing 1 million events. This was verified in Run 124 [129] and Run 127 [130] by looking at the fraction of low yield events, with 100,000 event bins (Figure 6.16). Note that the 1 million event limit is based on computing resources. Based on the number of detectors and file sizes, taking more than 1 million events in a single dataset could create problems with large file sizes and slow processing. To maintain detector neutralization over long periods of time, a LED flash automatically occurred at the end of every barium calibration dataset longer than 30 minutes.

In addition to maintaining neutralization during a single dataset, it is important

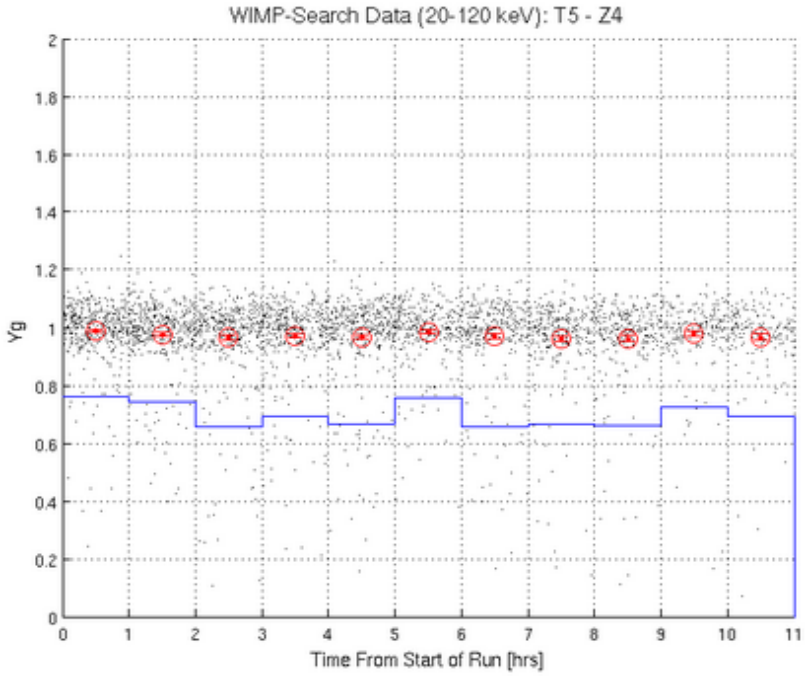

(a)

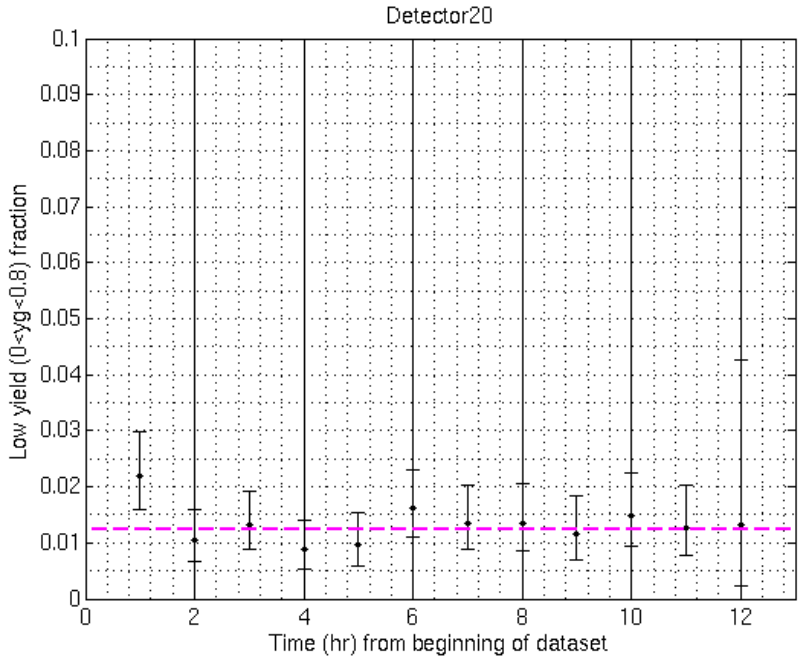

(b)

Figure 6.15: (a) Plot of several weeks of Run 123 WIMP search data ionization yield as a function time from the beginning of the data set for Z28 (T5Z5). The black points are individual events and the red points show the ionization yield mean and one standard deviation error bars for 1 hr time bins. Note how the ionization yield is stable with time. From [29]. (b) Plot showing the fraction of low yield events for Ge detector Z20 (T4Z2) for 2 months of Run 127 WIMP search data. Each point represents a 1 hr time bin measured from the beginning of the data set. Note how the fraction of low yield events remains stable with time.

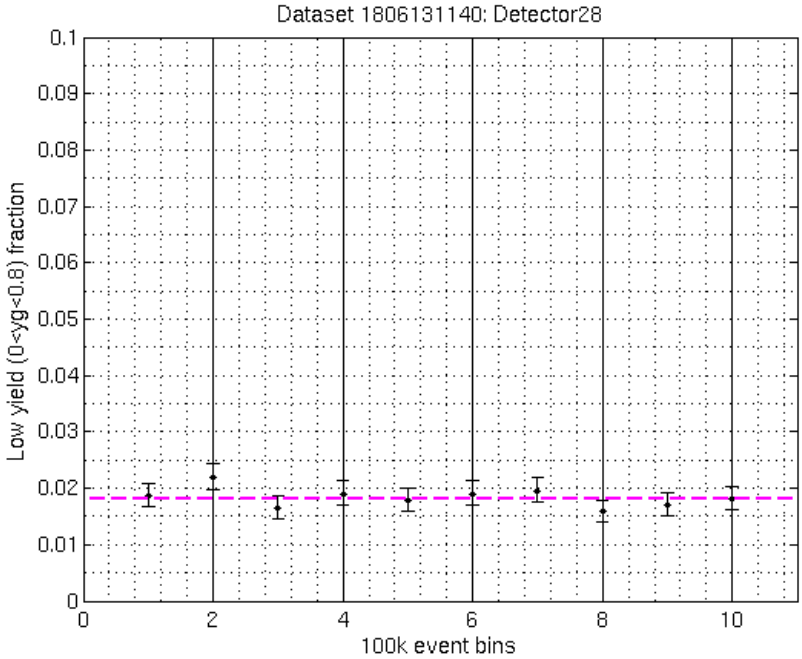

Figure 6.16: Plot showing the fraction of low yield events for Ge detector Z28 (T5Z4) for a long Run 127 barium calibration data set. Each point represents a 100,000 event bin. Note how the fraction of low yield events remains stable throughout the entire data set.

to regain good neutralization states at the beginning of each run after a large temperature excursion. A study was conducted which compared the detector neutralization states from Soudan 5-tower Runs 123 through 128 [124]. This showed that each of these runs, even with different initial neutralization procedures, had very consistent detector neutralization states (Figure 6.7). The few exceptions were usually silicon detectors which take a longer time to neutralize, especially with inoperable LEDs.

6.6 External Influences on Neutralization

This section discusses some of the ways that detector neutralization can be affected. The most important influences include increasing the temperature of the detector crystal, event rate, and charge bias.

6.6.1 Temperature

One external condition that affects detector neutralization states is temperature. Empirically, detectors lose neutralization when they are extensively heated. In between many of the Soudan 5-tower runs, the detectors were heated to different temperature points for cryogenic maintenance purposes. This allowed for studies detailing how the detector neutralization states were affected as a function of temperature. In parallel with these studies, a simple model was created to predict the relation between charge collection and temperature.

The model predicting the relationship between charge collection and temperature is based on the expectation for impurity ionization to vary with temperature. In this simple model, charge carriers are treated equally with the assumptions that donors and acceptors are equal in concentration and impurity ionization energy. In addition, energy and field dependences on capture cross-sections and geometry electrostatics are neglected. After computing the ionized impurity concentration as a function of temperature (Figure 6.17a), it is assumed that carrier trapping only occurs via capture and ionized impurities and the charge collection as a function of temperature is calculated (Figure 6.17b). [30]

During the Soudan 5-tower runs, data were taken to benchmark this model. The data were all taken at base temperature after thermal cycling the detectors to a given maximum temperature and then cooling them back down and prior to any attempts at neutralizing the detectors. Four temperature points were studied, each taken at the beginning of four separate runs. These four temperature points studied were approximately 10 K (data taken at the beginning of Run 124), 40 K (data taken at the beginning of Run 126), 70 K (data taken at the beginning of Run 127), and room temperature (data taken at the beginning of Run 129). The detector neutralization states were studied using the fraction of low yield events for each barium calibration dataset (Figure 6.18), where the lower the fraction of low yield events corresponds to

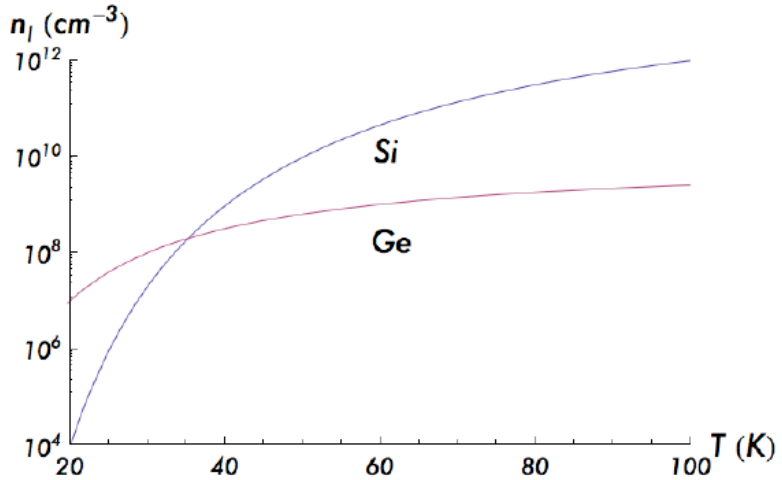

(a)

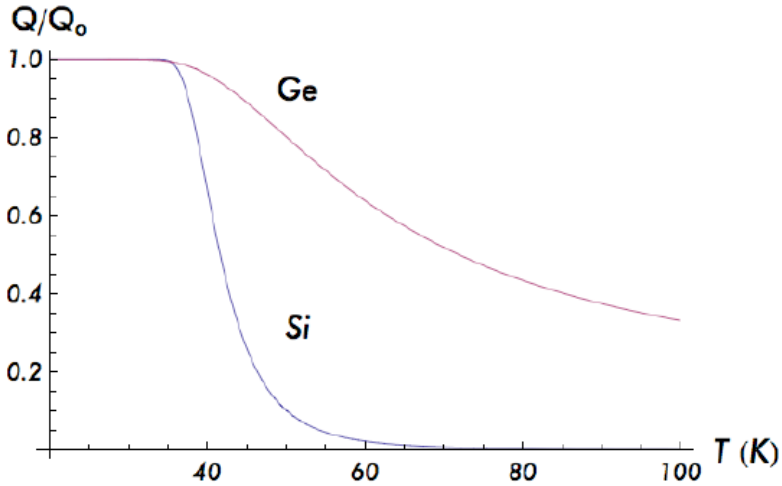

(b)

Figure 6.17: (a) Prediction for the concentration of ionized impurities as a function of temperature. (b) Prediction for partial charge collection as a function of temperature. From [30].

better neutralization [131]. These values for each temperature point were compared. For both silicon and germanium detectors, the biggest change in detector neutralization states comes after warming the detectors to temperatures between 10 and 40 K. Warming detectors to approximately 10 K has no significant effect on their neutralization state and warming detectors above 40 K does not cause their neutralization state to substantially further worsen.

Comparing data from the Soudan 5-tower temperature studies to the model based on ionized impurities shows that the model appears to have the correct trends for temperature dependent neutralization loss. Most notably, the model predicts that charge collection will become practically non-existent for silicon detectors while it will plateau at some finite, non-zero collection for germanium detectors. The data from the temperature studies confirms this by seeing the silicon detectors' fraction of low yield events going to 1 while the germanium detectors' fraction of low yield events remains less than 0.5. The most obvious flaw in the model, when compared to the data, is that the model predicts the detector neutralization state to worsen at higher temperatures than seen in the data. However this is not surprising as this model only considers neutralization loss and temperature dependencies due to ionized impurities. This model neglects such things as impurity ionization by impact ionization due to carriers, carrier trapping by deep centers and neutral impurities, as well as energy-dependencies. To further isolate the temperature at which detectors begin to lose neutralization, and normalize the temperature axis in this simple model, it would be interesting to continue the studies looking at detector neutralization states as a function of temperature. Of particular interest would be studying the detector neutralization state immediately following warming the detectors to temperatures between 10 and 40 K to see silicon detectors partially neutralized, instead of fully neutralized or completed de-neutralized.

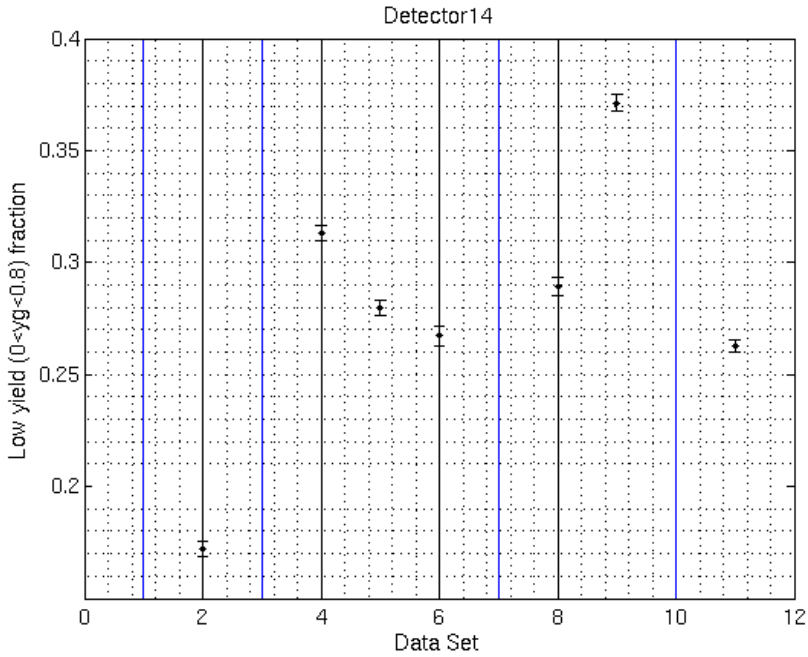

(a)

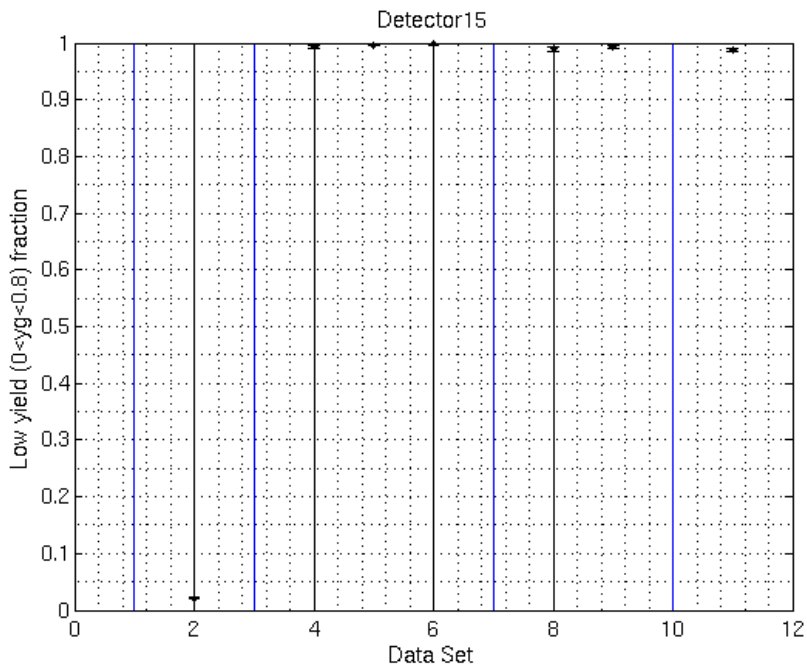

(b)

Figure 6.18: Like Figure 6.2, these plots show the fraction of low yield events as a function of time. Plots for Ge detector Z14 (T3Z2) (a) and Si detector Z15 (T3Z3) (b) barium calibration data sets taken at the beginning of Run 124, 126, 127, and 129 after cooling down from approximately 10 K, 40 K, 70 K, and room temperature (respectively) and before any neutralization occurred. Each point represents a single data set and the vertical blue lines represent the temperature excursions. Note how, for both the Ge and Si detector, the fraction of low yield events changes the most between points 2 and 4 (after warming to approximately 40 K). Also note how the Si detector loses all ionization collection (seen by a fraction of low yield events equal to 1) while the Ge detector maintains some ionization collection.

6.6.2 Event Rate

The event rate that a detector experiences affects the time that it maintains full ionization collection. For example, a detector operated underground and shielded will experience an event rate that is much less than a detector operated at a surface test facility. Due to the much larger event rate, the detector on the surface will lose neutralization sooner than the detector underground. This is empirically verified when comparing Soudan WIMP search data with test facility detector data. As discussed in Section 6.5, during the 5-tower Soudan runs, detectors maintained full ionization collection for at least 12 hours. For comparison, test facility testing with internal collimated sources shows detectors losing full ionization collection in as little as 5 minutes.

Neutralization dependence on event rate can be explained in terms of impurity site trapping cross-sections. Since even neutral impurity sites have a finite trapping cross-section, the more particle interactions creating charge carriers, the more likely trapping becomes. When combining this with rate, for a given number of particle interactions to cause a incomplete ionization collection, a detector experiencing a larger event rate will become de-neutralized faster than one with a low event rate.

6.6.3 Charge Bias

Bias conditions can also affect neutralization, especially the amount of time a detector is able to maintain full ionization collection. The lower the charge bias, the shorter amount of time the detector remains neutralized. This has been empirically seen in recent test facility data (Figure 6.19).

To understand how charge bias affects neutralization, one should first understand how electric field affects charge collection. At sufficiently low electric fields the ionization signal, even for full collection, is reduced due to charge carrier recombination in the bulk of the detector. As the electric field across the crystal increases, the

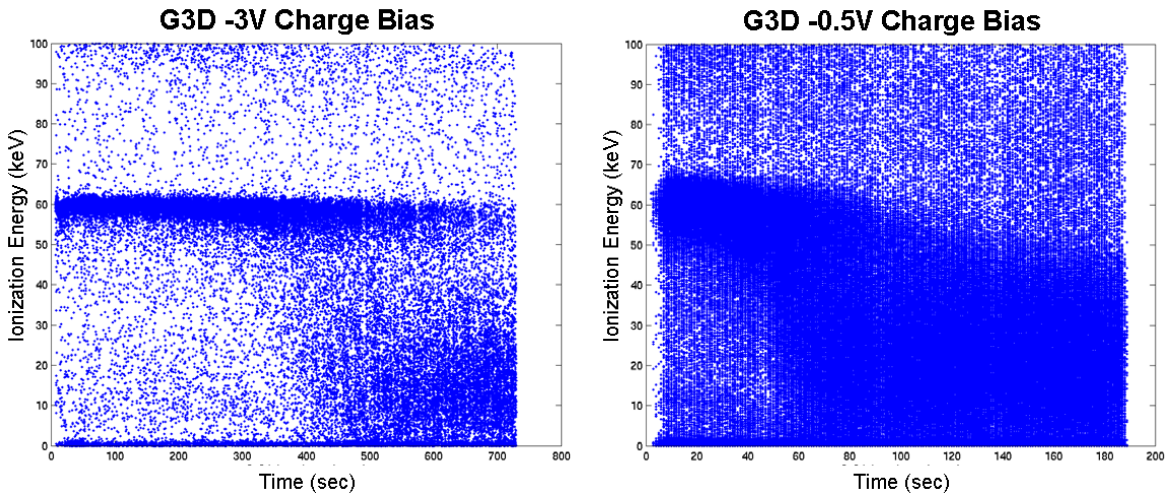

(a) (b)

Figure 6.19: Plots of test facility data showing the 60 keV ^{241}Am line ionization collection as a function of time for -3 V charge bias (a) and -0.5 V charge bias (b). Note how the 60 keV events lose full ionization collection after less time for the -0.5 V data than the -3 V data.

ionization signal increases until bulk recombination is negligible and the signal nearly plateaus. During detector operation, the charge bias is large enough to produce an electric field across the crystal which creates the maximum ionization signal (in the region that the signal plateaus when varying electric field). However, when charge trapping occurs, the bulk electric field is reduced. When this bulk field is weakened enough, the ionization signal will be decreased due to recombination. In the case comparing two initial charge biases, less trapping needs to occur to cause the bulk field to become low enough creating incomplete ionization collection for the smaller initial bias. Therefore the smaller initial charge bias will experience incomplete ionization collection sooner than the larger initial bias.

6.7 1 inch Detector Neutralization

One way to increase sensitivity to WIMP interactions is to increase an experiment's target mass. The next phase of the CDMS experiment, SuperCDMS, is not only

increasing its target mass by making new detectors, but also by using thicker detectors that are 1 inch instead of 1 cm thick. As described in Section 7.5, fabrication and testing of these new detectors has begun.

During the fabrication and packaging of the 1 inch detectors there were some changes to the LEDs. Due to the increased thickness of the detectors, instead of mounting both of the LEDs on the phonon side of the detector housing, 1 inch detector housings have one LED (LED1) on the phonon side and one LED (LED2) on the charge side. In addition, the LED supply used for the 1 cm detectors ran low and a new batch of LEDs was received. The LEDs in this new batch have the opposite polarity of those used for the 1 cm detectors. While this has no impact in the ability of the LED to neutralize a detector, it does have a slight operational impact. The new LEDs must be biased with the opposite polarity (bias current) as the 1 cm detector LEDs. Also important to note is that the early 1 inch detectors use a combination of the old and new LEDs, so it is necessary to test each 1 inch detector LED prior to use and record each bias polarity.

An important question remains with respect to 1 inch detector neutralization. Since, to date, all 1 inch detector testing has been conducted at the surface test facilities, it is unclear if a LED on one side of a 1 inch detector is able to effectively neutralize the entire crystal. When the first superTower of 1 inch detectors is installed underground at the Soudan site, it will be important to learn if the LEDs on both sides of the detector are necessary. To learn this, a test strategy similar to what was used at the beginning of Run 127, as discussed in Section 6.4.1 and Appendix B, should be suitable. Since the beginning of Run 127 LED tests showed that a LED on the phonon side of a 1 cm detector neutralizes both the detector it is mounted on as well as the adjacent detector, a reasonable approach to use with 1 inch detector LED neutralization is to use the same LED (i.e., LED1) for every detector in the stack. This way every face of the detectors will be illuminated and neutralized by a LED (i.e., LED1 on detector 3 will neutralize the phonon side of detector 3 as well as the

charge side of detector 2 and so forth). This technique would eliminate the necessity of performing multiple LED flashes, with both LED1 and LED2 of each detector, to ensure LED illumination and neutralization on both detector sides.

6.8 Neutralization Model

To better understand the microphysics when a detector loses full ionization collection, a series of tests were performed at the Case Western test facility. During these tests, three different detectors (Table 6.1) with internal collimated radioactive sources were studied. To learn about the de-neutralization process, we began with a fully neutralized detector and then took long data sets without performing any neutralization. This examines a regime not typically probed during normal running where it is operationally crucial that data does not exhibit poor ionization collection. From these data sets, studying the ionization, total phonon, and phonon recoil energy from x-ray lines with time can give information about the processes occurring in the crystal.

The ionization signal can be reduced through several mechanisms. First, for events occurring near the detector surface, carrier back diffusion into the adjacent contact can reduce the number of charge carriers drifting across the crystal thereby reducing the signal (Section 2.6.1). Second, bulk trapping can partially reduce the signal because carriers are trapped before traveling the entire distance across the crystal (Section 2.6.2). Finally, the signal can be reduced by changing the bulk electric field. As discussed in Section 6.6.3, if the bulk electric field is small enough, then the signal will be decreased due to carrier recombination.

In addition to looking at the ionization signal with time, studying the phonon signals can add information. This knowledge can be particularly useful in understanding which of the above processes is responsible for changing the ionization signal. The main reason for this is that the total phonon signal is made up of energy from both the interaction recoil and the Luke phonons. Due to the Luke phonon energy depen-

Detector	Thickness	Doping Type	Impurity Concentration	Phonon Side Surface	Charge Side Surface
G3D	1 inch	p-type	$7.7\times10^{+10}$ to $7.6\times10^{+10}$	amorphous Si	amorphous Si
G2E	1 inch	n-type	$1.5\times10^{+10}$ to $8.0\times10^{+10}$	amorphous Si	20% hydrogenated amorphous Si
G28B	1 cm	n-type	$2.7\times10^{+11}$ to $4.7\times10^{+11}$	8% hydrogenated amorphous Si	amorphous Si

Table 6.1: Detectors used to study loss of ionization collection along with important properties.

dence on ionization signal and electric field, the total phonon energy should change if the bulk electric field changes. This is especially useful when determining if the loss of ionization signal is due to a change in the bulk electric field. While the ionization signal will not change until the bulk electric field has decreased substantially, the phonon signal should change continuously with the changing electric field and thus be affected before the ionization signal. In addition to the total phonon energy, changes in the phonon recoil energy also give information about the bulk electric field. Since the phonon recoil energy is calculated based on the collected ionization energy and inferred bulk electric field from the applied charge bias, if the phonon recoil energy is not constant with time, the bulk electric field must be changing.

While this study turned out a wealth of complex information, some trends emerged from the data. Two of the three detectors showed extreme loss of ionization collection while the third detector, G2E, only showed small changes with time. This extreme loss of ionization collection indicated a charge carrier dependence. However, under closer data inspection the carrier dependence between these two detectors, G3D and G28B, was different. For G3D, extreme loss of ionization collection occurred when electrons were the dominant carrier responsible for creating the signal (Figure 6.20). Conversely, G28B experienced extreme loss of ionization collection when holes were the dominant carrier creating the signal (Figure 6.21). This carrier dependent nature of signal loss indicates that the detector preferentially traps one charge carrier over

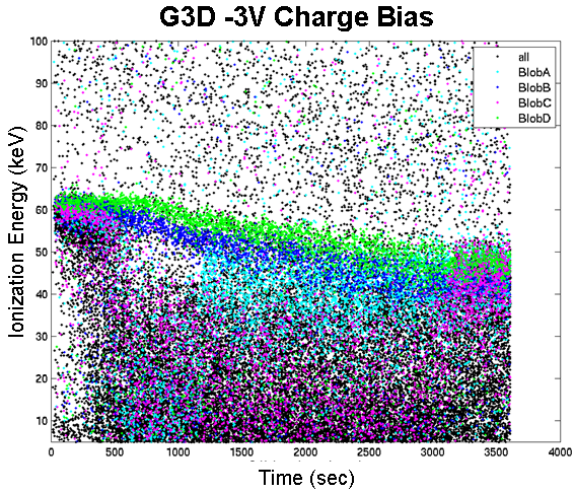

(a)

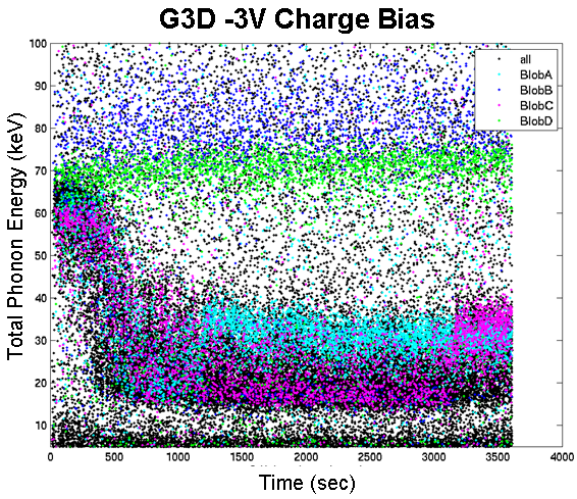

(b)

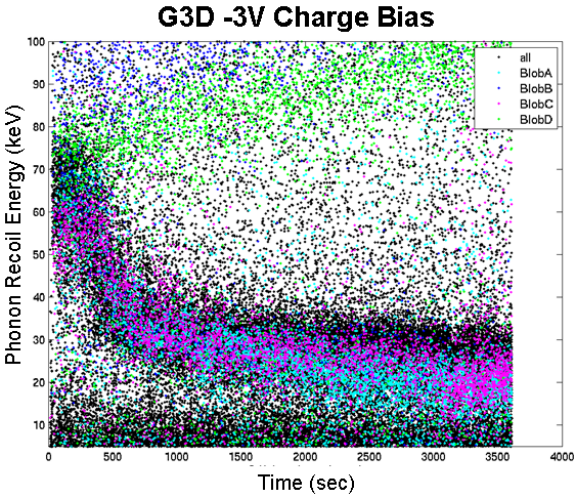

(c)

Figure 6.20: Plots of test facility data of p-type G3D showing how the 60 keV ^{241}Am line changes as a function of time in ionization energy (a), total phonon energy (b), and phonon recoil energy (c). The primary charge carrier for events from sources over phonon sensors A (cyan) and C (magenta) were electrons while the primary charge carrier for events from sources over phonon sensors B (blue) and D (green) were holes.

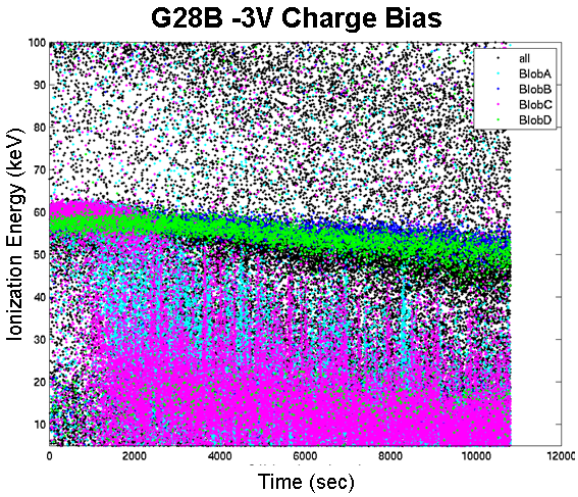

(a)

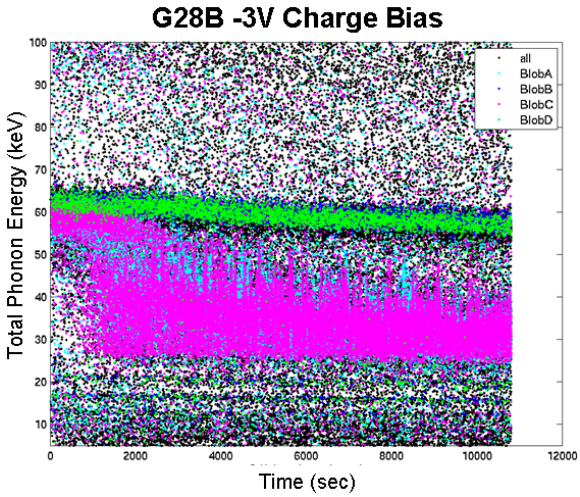

(b)

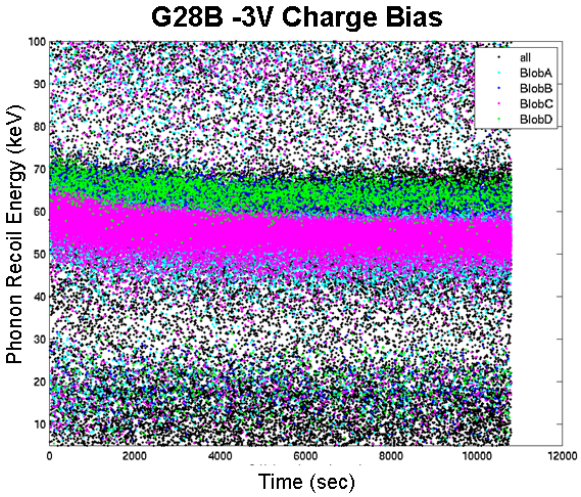

(c)

Figure 6.21: Similar to Figure 6.20, except for n-type G28B, showing ionization energy (a), total phonon energy (b), and phonon recoil energy (c). Unlike Figure 6.20, the primary charge carrier for events from sources over phonon sensors A (cyan) and C (magenta) were holes while the primary charge carrier for events from sources over phonon sensors B (blue) and D (green) were electrons.

the other. The fact that G3D and G28B have opposite carrier dependencies may be explained by looking at the crystal properties. G3D and G28B have different doping properties: G3D is a p-type crystal while G28B is a n-type crystal.

Considering charge transport in 40 mK CDMS detectors [132, 12] indicates that the contacts act like Schottky contacts [133] where the semiconductor band bends near the contact in order to align Fermi levels. This contact model provides a natural explanation for surface trapping that would change the bulk electric field and then could cause incomplete ionization collection due to bulk recombination. This model could also explain why there are differences between detectors made from n-type and p-type crystals. The semiconductor band gap in a Schottky contact between a n-type material and metal will bend in the opposite direction as a Schottky contact between a p-type material and metal (Figure 6.22). If this is happening at the contacts of our detectors, then a n-type crystal would naturally trap the opposite charge carrier than a p-type crystal at the detector surfaces.

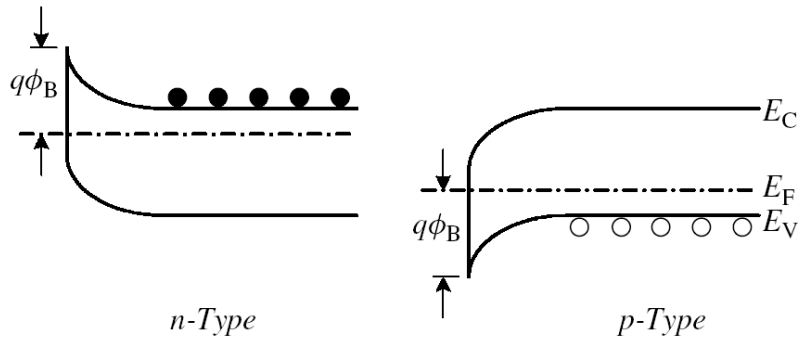

Figure 6.22: Semiconductor band gap diagram for Schottky contacts between metal and a n-type crystal (left) and a p-type crystal (right). Notice how the band gap bends, near the metal-semiconductor interface, in different directions for n-type and p-type materials. This "band bending" creates a depletion zone near the contact for electrons (n-type) or holes (p-type). For CDMS detectors this could mean electrons get "trapped" at the contact in n-type crystals while holes get "trapped" at the contact in p-type crystals. From [31].

While a Schottky contact model provides some insight into why one might expect different behavior for n-type and p-type crystals, bulk trapping models may also explain some differences. If bulk trapping were the cause of the incomplete ionization

collection, then the crystal doping may affect the preferred trapping carrier as the majority impurity in a n-type crystal are acceptors while in a p-type crystal are donors.

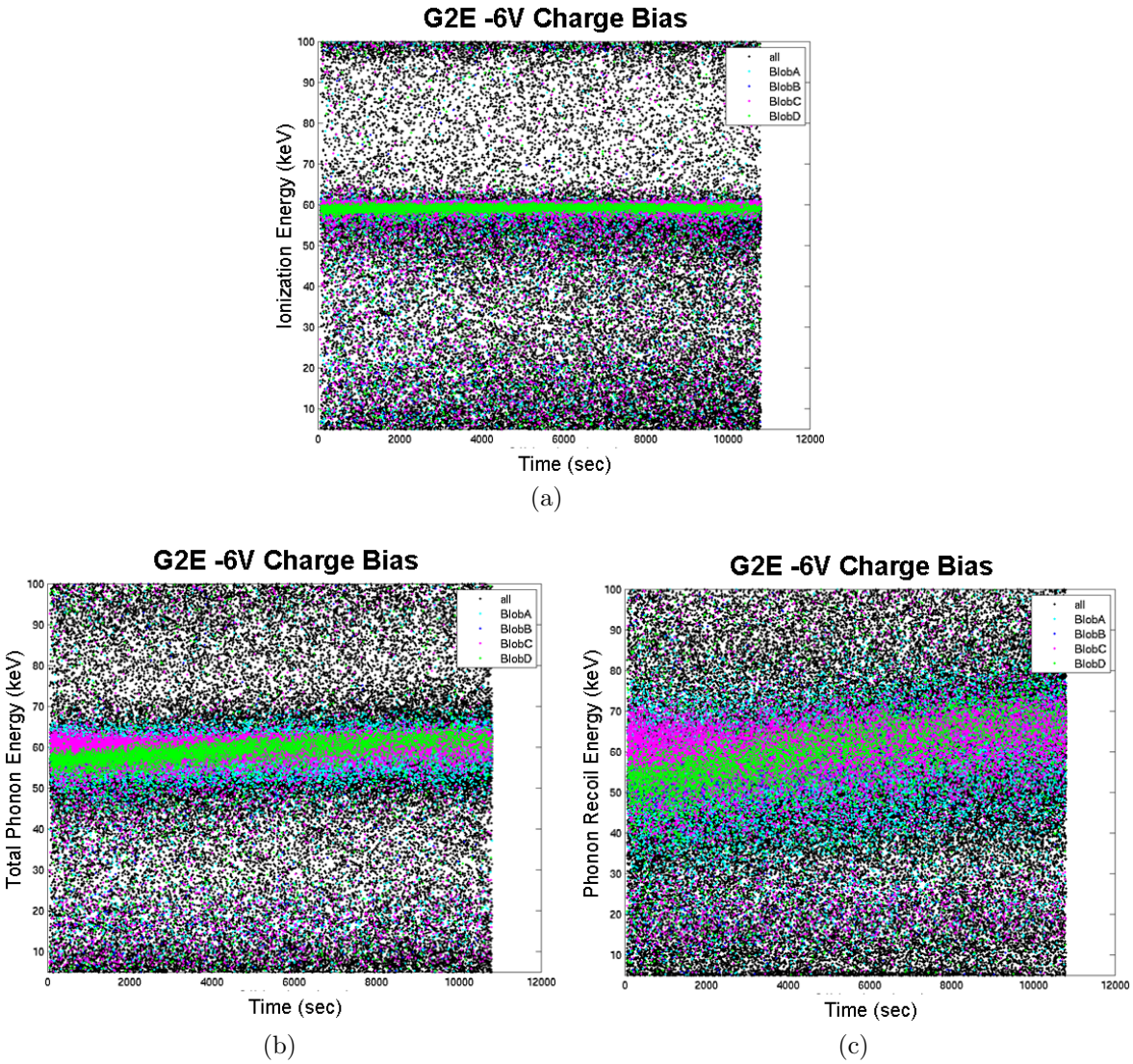

Figure 6.23: Plots of test facility data of n-type G2E showing how the 60 keV ^{241}Am line changes as a function of time in ionization energy (a), total phonon energy (b), and phonon recoil energy (c). The primary charge carrier for events from sources over phonon sensors A (cyan) and C (magenta) were holes while the primary charge carrier for events from sources over phonon sensors B (blue) and D (green) were electrons.

Based upon this data, while electron (hole) carriers cause extreme loss of ionization signal in p-type (n-type) crystals, hole (electron) carriers also create some effect in the ionization and phonon signals. This effect is generally much more subtle, but

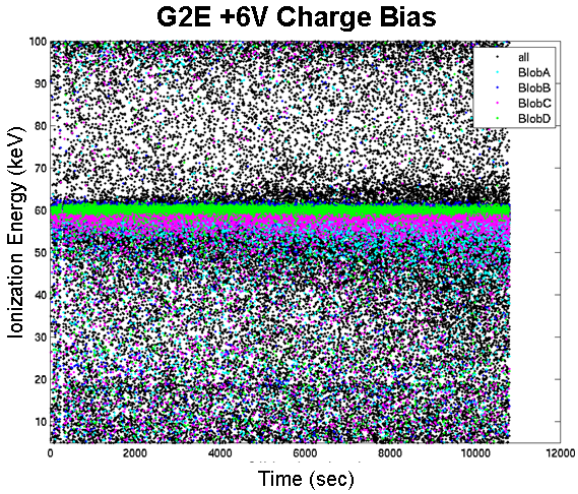

(a)

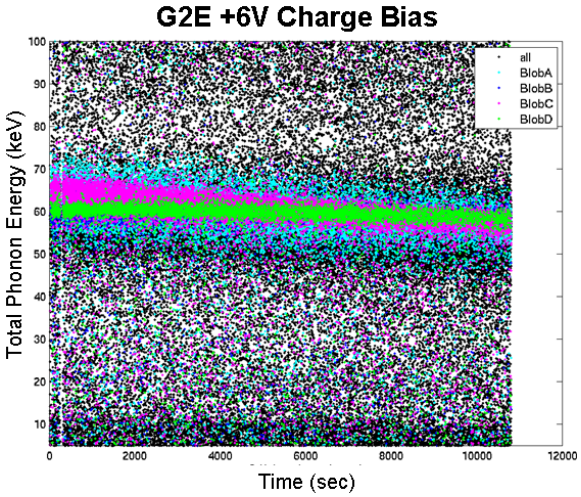

(b)

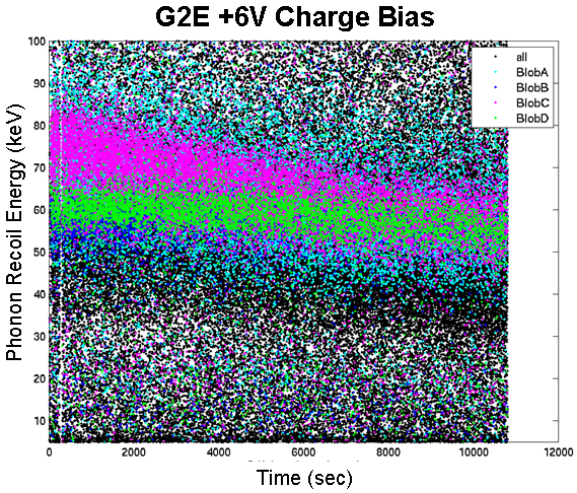

(c)

Figure 6.24: Similar to Figure 6.23, this shows n-type G2E ionization energy (a), total phonon energy (b), and phonon recoil energy (c). Unlike Figure 6.23, the primary charge carrier for events from sources over phonon sensors A (cyan) and C (magenta) were electrons while the primary charge carrier for events from sources over phonon sensors B (blue) and D (green) were holes.

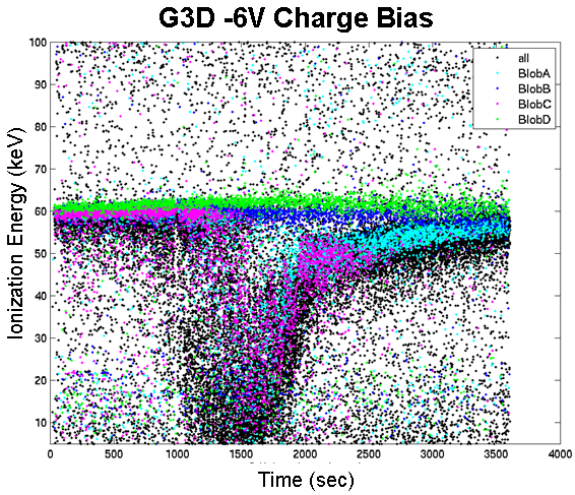

(a)

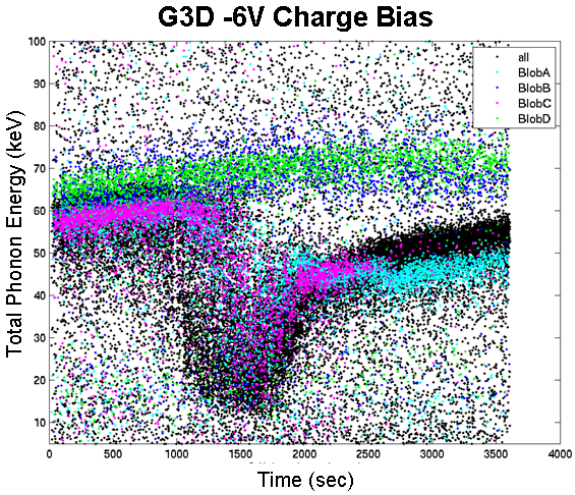

(b)

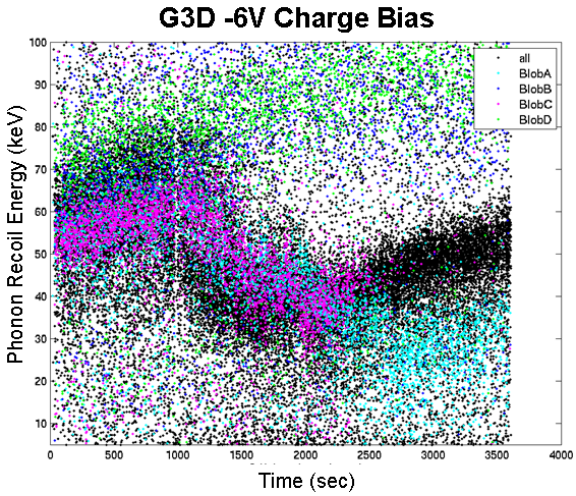

(c)

Figure 6.25: Plots of test facility data of p-type G3D showing how the 60 keV ^{241}Am line changes as a function of time in ionization energy (a), total phonon energy (b), and phonon recoil energy (c). The primary charge carrier for events from sources over phonon sensors A (cyan) and C (magenta) were electrons while the primary charge carrier for events from sources over phonon sensors B (blue) and D (green) were holes.

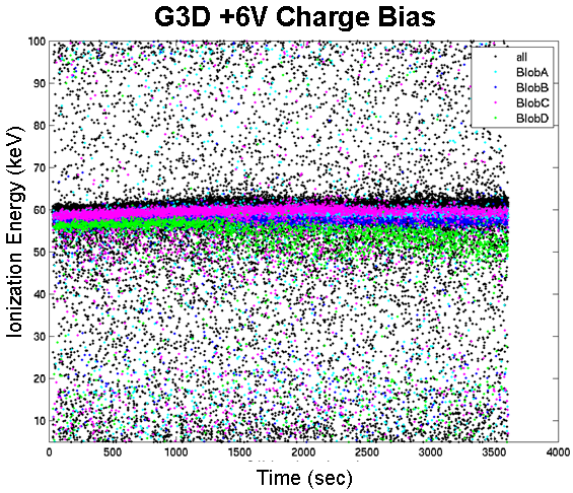

(a)

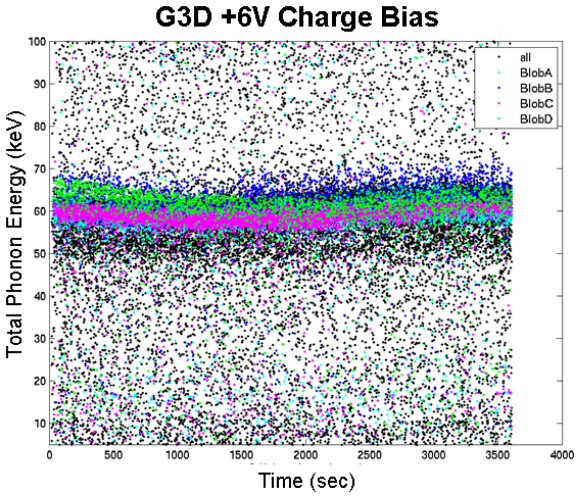

(b)

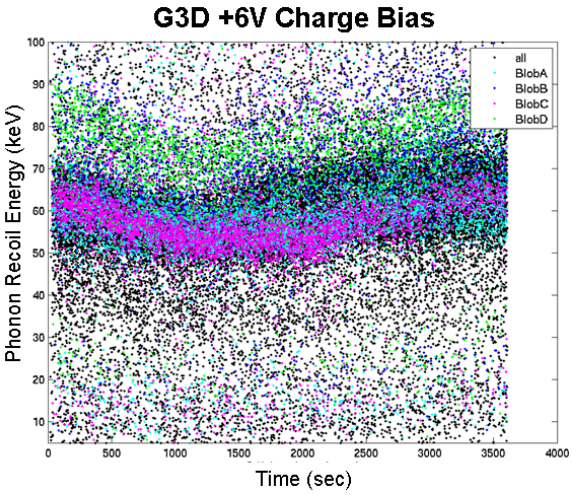

(c)

Figure 6.26: Similar to Figure 6.25, this shows p-type G3D ionization energy (a), total phonon energy (b), and phonon recoil energy (c). Unlike Figure 6.25, the primary charge carrier for events from sources over phonon sensors A (cyan) and C (magenta) were holes while the primary charge carrier for events from sources over phonon sensors B (blue) and D (green) were electrons.

it is present. Hole carriers in p-type G3D and electron carriers in n-type G28B and G2E cause a slight change in the slope of the ionization line as a function of time. More noticeable than the effect on the ionization signal is the change in the phonon signal. In this data the phonon signal for a line source (i.e., ^{241}Am 60 keV events) has a gradual slope with time. Depending on the polarity of the charge bias, the plot of phonon recoil energy versus time will slope upwards or downwards. The direction of this slope (in the plot of recoil versus time) seems to be dependent on the polarity of the charge bias and of the crystal doping type. The plot of phonon recoil energy versus time for G2E, an n-type crystal, slopes upwards under positive charge bias (Figure 6.24) and downwards under negative charge bias (Figure 6.23) while the trend is exactly the opposite for p-type G3D (Figure 6.26 and Figure 6.25).

Another diagnostic to explain the microphysics in the crystal is to look at the reconstructed event position with time to see if the positions change. Since the data were taken with collimated sources, events from a single source are localized. These localized regions in the phonon delay plot are called "blobs." In many of the data sets, the delay plot blobs appear to get larger with time. One particularly interesting phenomenon is seen in the blobs of G3D when the holes are the primary charge carrier and the events occur primarily on the charge side of the detector. These data sets show the subtle changes in the ionization energy with time. In these data sets, at later times, the blobs form voids where there are no events in the middle of them (Figure 6.27).

There are, at least, two possible explanations for the lack of events in the middle of blobs, one relying on surface trapping and another on bulk trapping. As holes are drifted across the crystal, some of them are trapped at the far surface. The concentration of trapped holes becomes higher until they begin affecting the electric field lines, and therefore the path of hole carriers, to bend around them. A similar effect could occur around a localized region in the bulk.

One final collection of data that was taken as part of this study was to take data

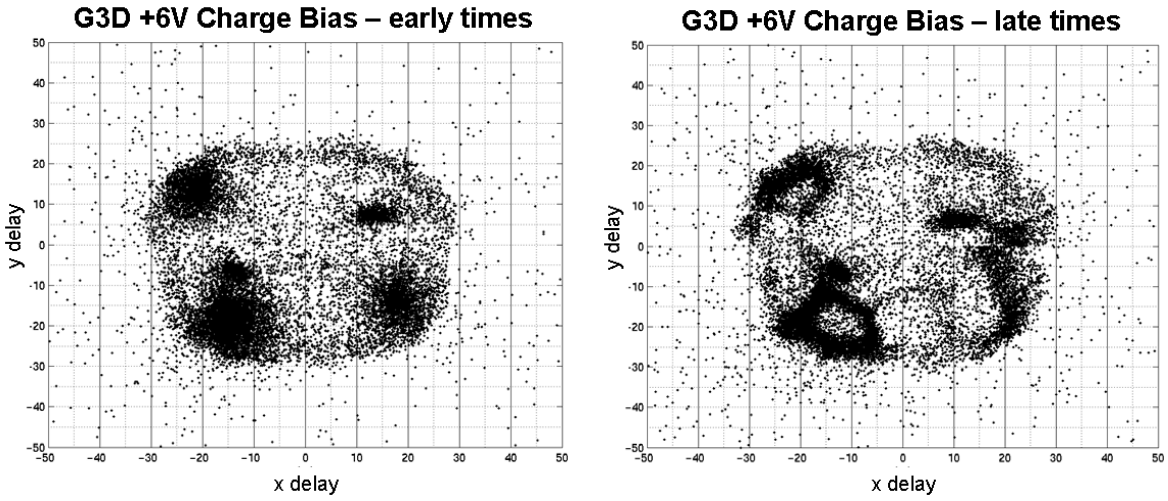

(a) (b)

Figure 6.27: Plots of test facility data showing delay plot blobs forming voids with no events at the end of long data sets which had no explicit neutralization or grounding and where holes were the dominant charge carriers. (Note that the primary charge carrier for events from sources over phonon sensors A, B, and C were holes while the primary charge carrier for events from sources over phonon sensors B and D were electrons.) (a) Delay plot blobs at the beginning of the run. (b) Delay plot blobs at the end of the run.

overnight with no explicit neutralization or grounding to study very long term affects. The data were taken with p-type detector G3D for -3 V and +3 V charge biases. For electron carriers, the long data set showed basically the same trend as the shorter data sets (Figure 6.29): the ionization signal decreased to almost zero and then increased to approximately full signal (perhaps a little higher in the overnight data, but with much worse resolution). However, the data set with hole carriers has more features than in the shorter data sets (Figure 6.28). In the overnight data set, the ionization line with time for hole carriers showed three branches. For the entire data set there was a population of events that remained at approximately full ionization collection. Approximately halfway through the data set, a population of events began losing ionization signal and remained at very low collection. Following this low signal population, a third event population appeared, this population increasing in ionization energy.

Trying to understand the long data set with three event populations is an inter-

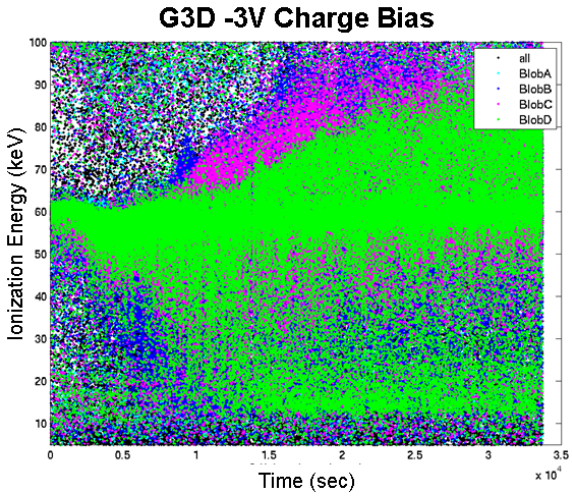

(a)

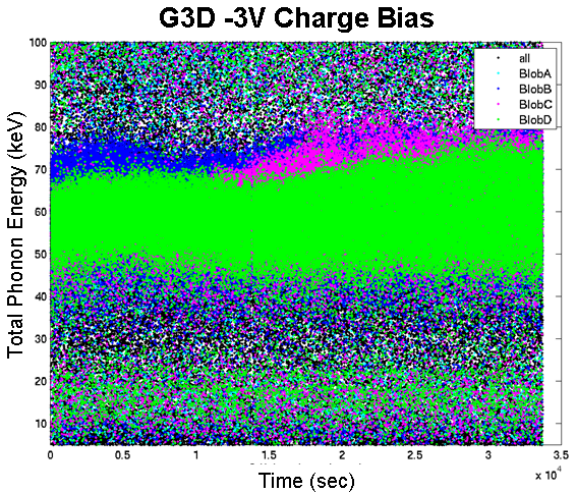

(b)

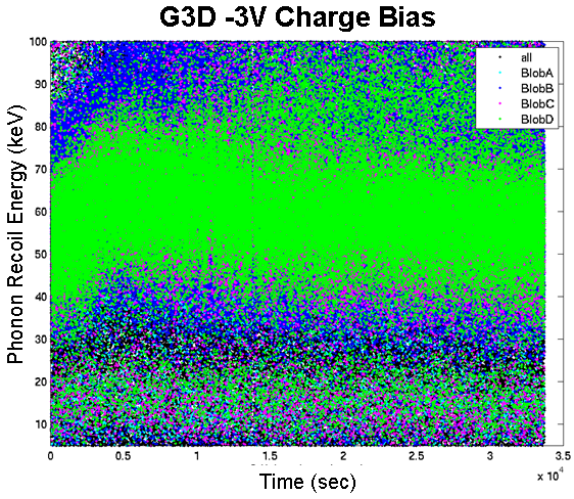

(c)

Figure 6.28: Plots of test facility data of p-type G3D showing how the 60 keV ^{241}Am line changes as a function of time in ionization energy (a), total phonon energy (b), and phonon recoil energy (c) overnight. The primary charge carrier for all events were holes. (Events from the source over phonon channel A are cyan, channel B are blue, channel C are magenta, and channel D are green)

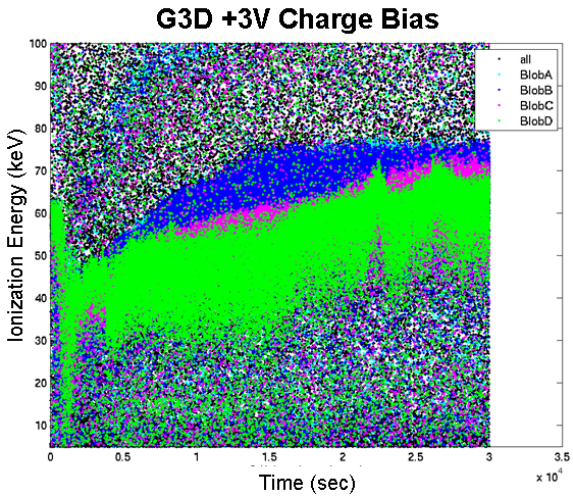

(a)

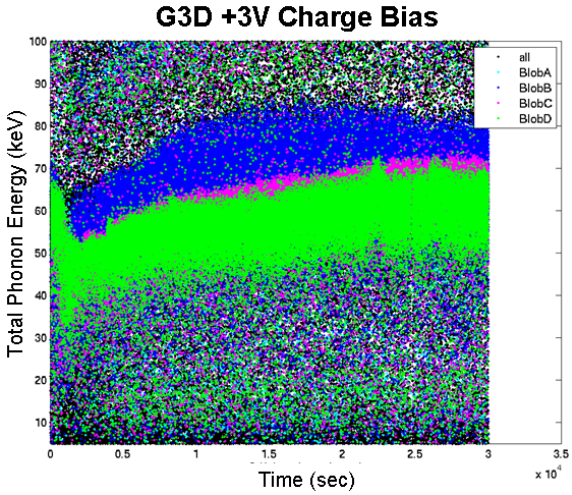

(b)

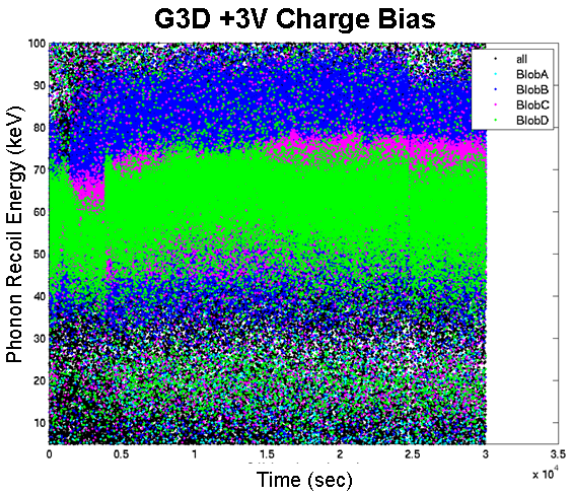

(c)

Figure 6.29: Similar to Figure 6.28, this shows p-type G3D ionization energy (a), total phonon energy (b), and phonon recoil energy (c) overnight. Unlike Figure 6.28, the primary charge carrier for all events were electrons. (Events from the source over phonon channel A are cyan, channel B are blue, channel C are magenta, and channel D are green)

esting problem, especially explaining how to get events with extra energy. Again we could consider surface and bulk trapping cases. Like the explanation of generating voids with no events in the blobs, hole carriers get trapped at the surface with an increasing concentration. In addition to the electric field lines getting bent around the high concentration of holes, additional holes are trapped forming a column. Holes that are trapped further from the surface begin to experience reduced ionization collection. Once enough holes are concentrated in this column, some hole carriers are able to impact ionize and cause an increased ionization signal. A localized bulk region could cause a similar effect. To break this degeneracy we need to recall how the ionization signal is created (Section 2.4). Since the signal is proportional to the distance carriers travel through the detector, impact ionization near the surface would have little impact on the collected ionization signal (since the extra carriers would not travel a significant distance). However, impact ionization in the detector bulk would create extra carriers that would add to the collected signal. Based on this argument, these long data sets imply bulk hole trapping.

While these long data sets were taken in an effort to further understand the microphysics involved in the loss of ionization collection, they illustrate the complex and dynamic processes involved. Loss of ionization collection likely comes from a combination of surface and bulk trapping and distinguishing between the two is complicated. It is possible that surface trapping is dominant for one charge carrier while bulk trapping dominates for the other. Also, the variations in the data from the different detectors indicates dependencies on many factors. While some preliminary conclusions can be drawn from this study, data with many more detectors would need to be taken before the entire process is fully understood. Then this data would have to be compared with the results of charge transport models, some of which are under construction as part of Kyle Sundqvist's thesis work [72].

Chapter 7

Design Studies toward Improving Surface Event Rejection

7.1 Introduction

To increase sensitivity to WIMP interactions, CDMS and other dark matter experiments are proposing and developing experiments with larger target mass to be run for long periods of time. In order for the next phase of CDMS, SuperCDMS, to continue running as a background free experiment, as the target mass is increased there must also be a proportionate reduction in the ability to reduce backgrounds. For this reason there has been a number of detector research and development studies ongoing to meet the requirements for the SuperCDMS experiment, discussed further in Section 7.5.

As discussed in Section 2.6.1, incomplete charge collection for events occurring near the detector surface creates a "dead layer" where electron recoil background events can look like nuclear recoil signal events. Improving surface event rejection, including reducing the size of this "dead layer," has been the focus of several design modifications, carried out on test detectors, which will be discussed in this chapter.

7.2 Interleaved ZIP

One method that was tested, and is currently under a second round of development, to improve surface event rejection is based on a surface rejection technique invented by Luke [134] to alter the electric field and ionization collection in the detector. In this detector design, the ionization electrodes are interleaved with the phonon sensors on both flat detector faces. Ionization electrodes on opposite detector faces are biased with an equal, but opposite, charge bias while the phonon sensors are maintained at ground. The resulting electric field creates two regions, one in the bulk and another along the detector surfaces (Figure 7.1). In the bulk region electric field lines extend across the detector causing bulk events to create a signal in both ionization electrodes. In the $\sim$700 μm surface region both ends of the electric field lines terminate on the same detector face, one end on the ionization electrode and the other at the phonon sensor. An event occurring in this surface region only creates a signal in one of the two ionization electrodes.

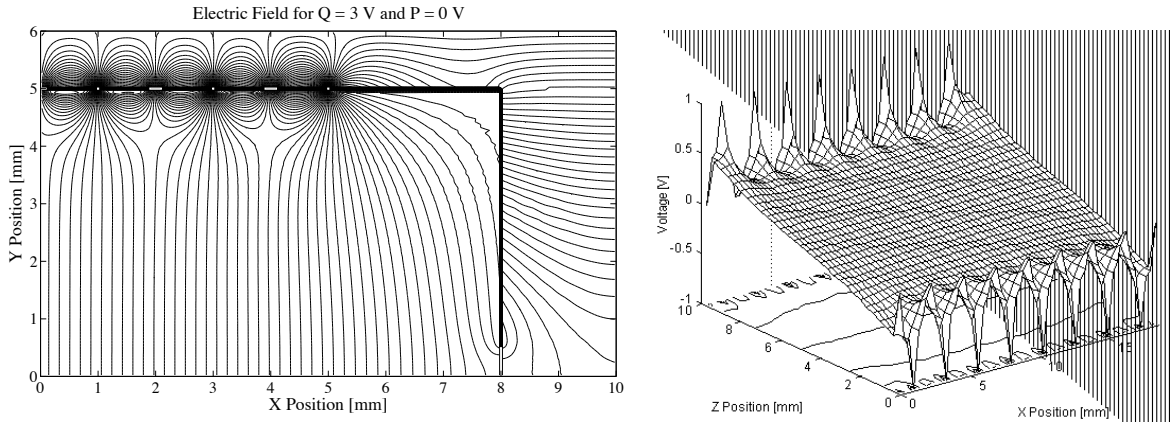

(a) (b)

Figure 7.1: Calculated electric field distribution for the interleaved ZIP electrode configuration. (a) 2-dimensional cross-section. From [32]. (b) 3-dimensional view. Courtesy of B. Cabrera.

Two prototype Si interleaved ZIP detectors were fabricated and tested between 2005 and 2006 [32]. Figure 7.2 shows a schematic of this detector. The four phonon

sensors are arranged on both sides of the detector to allow for 3-dimensional event reconstruction through relative timing and energy collection. The ionization electrode on the top detector face (Q_{top}) is interleaved with phonon channels AB and CD while the electrode on the bottom detector face (Q_{bottom}) is interleaved with phonon channels AD and BC. Figure 7.3 details the phonon channel design layout. The phonon sensors are contained within a 200 μm wide "ribbon" that snakes between interleaving 20 μm wide ionization rails. The spacing between the phonon ground and ionization bias electrodes is 1 mm throughout. This spacing is based on calculations [135] in order to achieve a capacitance in silicon below about 80 pF and in germanium below about 110 pF so that the detector maintains low ionization noise, which is proportional to the detector capacitance. The estimated detector capacitance of the prototype Si interleaved ZIP detector is 60 pF.

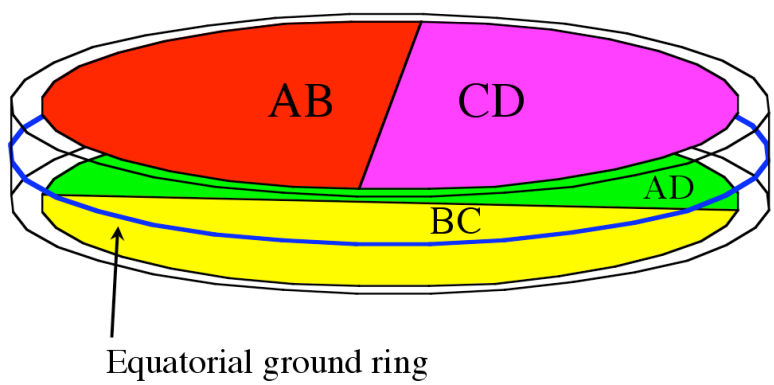

Figure 7.2: Schematic of the interleaved ZIP detector.

Analysis of data taken with the two prototype Si interleaved ZIPs resulted in a proof of principle of this detection technique. Figure 7.4 illustrates the discrimination power between bulk and surface events based on the ionization measurement alone. Using this method to reject surface events should increase the detector ionization yield discrimination ability as shown in Figure 7.5.

In addition to studying the ionization collection, some effort also went into studying how the interleaved ZIP geometry affects phonon energy collection and event

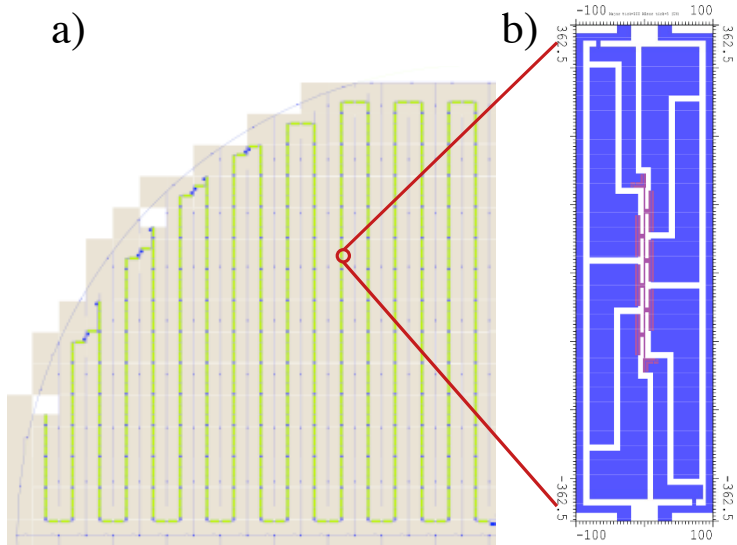

Figure 7.3: (a) Design layout for one of the phonon channels. (b) Close-up of one of the 1246 QETs that make up one of the phonon sensors. Eight Al collection fins are connected to the 1 μm wide W TES.

location reconstruction. With the phonon sensors on both sides of the detector the event location can be determined by the pattern of phonon energy collected on the two sides. Figure 7.6 shows a histogram of uncalibrated phonon energy collected in one of the four phonon sensors for 60 keV surface events. Comparing the bimodal distribution for top and bottom surface events indicates a depth dependence in the phonon energy distribution. Since there were two collimated sources, events in each peak can be correlated with the source they came from (events deposit the most energy in the primary phonon sensor, the sensor closest to the interaction site). The fact that the two higher energy peaks do not match indicates the depth of the interaction in the crystal affects the phonon collection. This shows promise that the interleaved ZIP geometry may produce better event location, especially depth, reconstruction than the standard CDMS-II ZIP detectors.

Since these first CDMS prototype tests were completed, the EDELWEISS experiment has developed prototype detectors based on this technique which have demonstrated high efficiency at rejecting low-energy β surface events, approaching 10^5 [136].

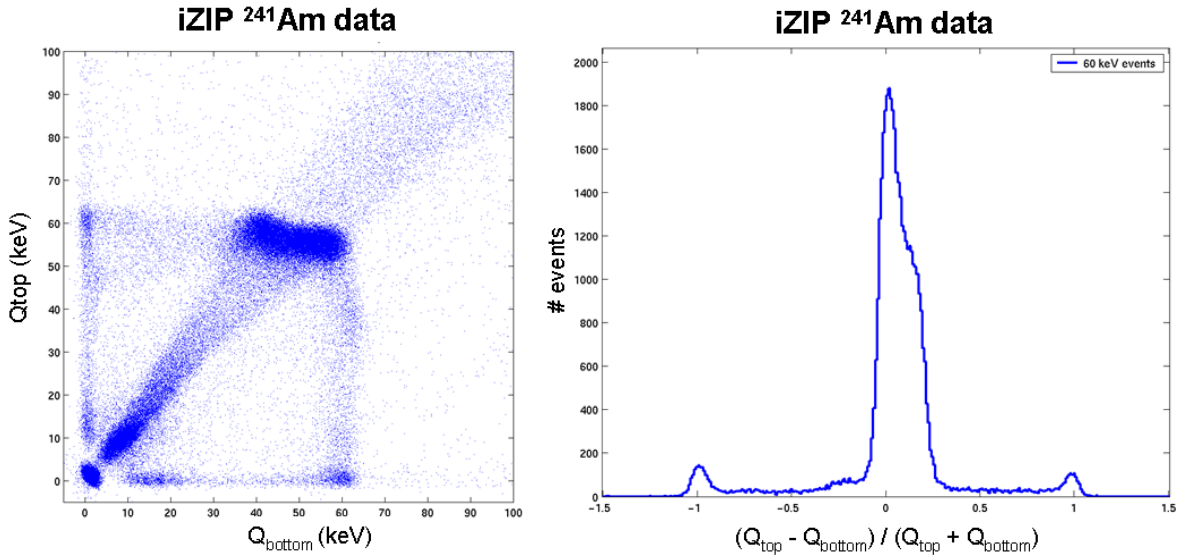

(a) (b)

Figure 7.4: (a) Ionization signal from the ionization electrode on the top detector face (Q_{top}) plotted again the electrode on the bottom detector face (Q_{bottom}) for data with internal ^{241}Am sources and no analysis cuts. Bulk events lie along the line down the middle of the plot with equal charge collection in both electrodes while surface events lie along the edges of this plot having ionization collection in only one of the two electrodes. (b) Histogram of a depth dependent position parameter based on ionization collection (the difference between the energy in Q_{top} and Q_{bottom} normalized by the sum of the two) for 60 keV events in (a). Surface events on the top detector face occur at 1 and on the bottom detector face occur at -1. Bulk events lie in the peak around 0.

Currently CDMS is fabricating a second set of prototype interleaved ZIP detectors. These new detectors are made from 1 inch thick Ge crystals. Based on results from the first CDMS interleaved ZIPs, the EDELWEISS demonstration, and further improvements, these detectors could be a candidate for a future large scale version of CDMS while remaining background free.

7.3 Phonon and Ionization Side Yield Discrimination Asymmetry

Besides working to improve the overall detector dead layer, effort has been invested in understanding and resolving the asymmetry between the dead layer on the phonon

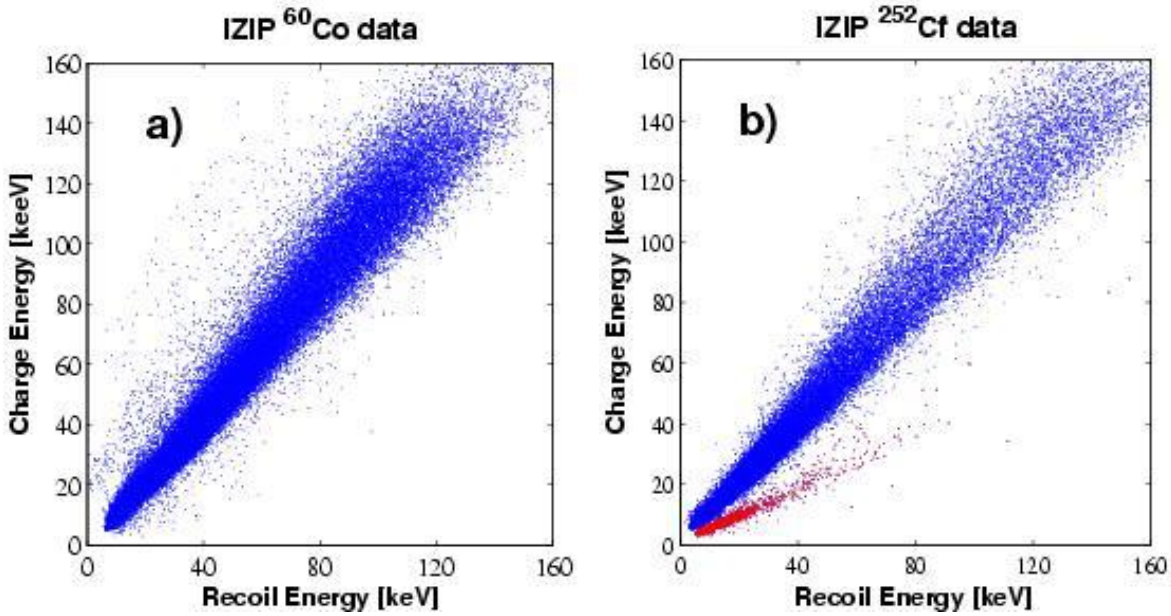

(a) (b)

Figure 7.5: Plots showing ionization energy as a function of phonon recoil energy for bulk events from (a) a ^{60}Co calibration source producing only gamma events and (b) a ^{252}Cf calibration source producing both electron and nuclear recoil events. Red nuclear recoil events are clearly identified in the band with reduced ionization collection. From [32].

and ionization side of the germanium ZIP detectors.

Calibration studies of one of the Ge ZIP detectors conducted at the UC-Berkeley test facilities found that the dead layer on the phonon side of the detector is approximately 15% larger than that on the detector's ionization side [83, 137, 138]. Figure 7.7 illustrates how this difference affects the ionization yield discrimination, the ^{109}Cd surface event population appears at much lower ionization yield on the phonon side (Figure 7.7b) than the ionization side (Figure 7.7a) of the detector. Subsequent performance studies of Soudan data show that the ionization yield based rejection factor (nuclear recoil band passage fraction) for surface events occurring on the phonon side is $\sim$4 times worse than for ionization side surface events in Ge detectors [139, 140]. It is interesting to note that Si detectors do not show this same asymmetry between phonon and ionization side surface events [141].

There have been several strategies devised that may provide possible methods of

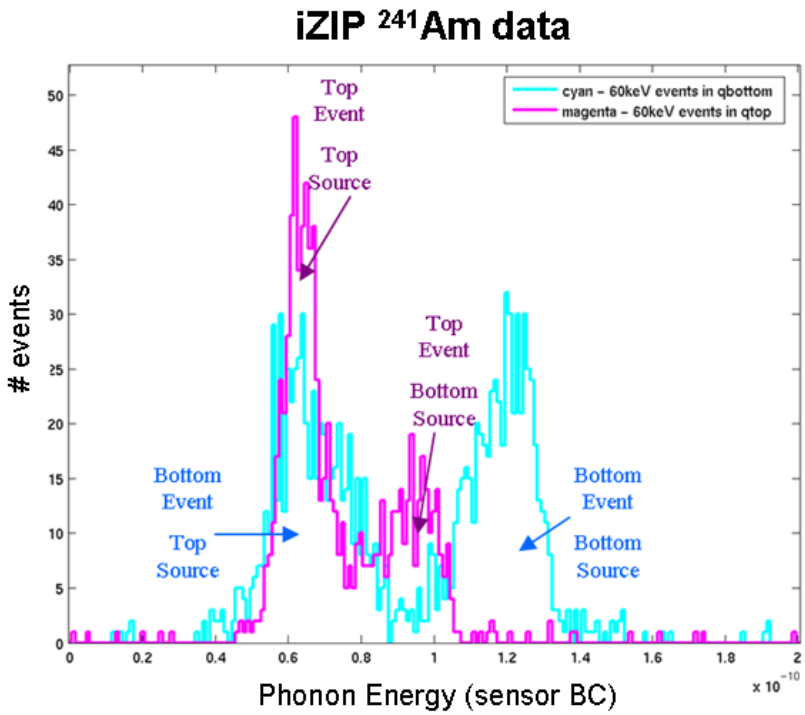

Figure 7.6: Histogram of the uncalibrated phonon energy collected in one of the four phonon sensors, sensor BC, of 60 keV surface events (as selected based on ionization energy), divided into events occurring near the top (magenta) or bottom (cyan) surface. The bimodal nature of these distributions can be understood to come from events occurring near the phonon sensor plotted (higher peak) versus those off sensor. In addition, since there were two collimated internal sources, one on sensor BC and one off sensor, the events in these peaks can be correlated with which source they came from. An interesting feature is that the higher energy peak of the top events does not match the top peak of the bottom events, indicating that the depth of the interaction in the crystal affects the phonon collection.

reducing this asymmetry between the phonon and ionization side dead layers. This section will discuss the rationale behind these strategies and show results based on evaluating test devices.

7.3.1 Hydrogenated Amorphous Silicon

One approach to decreasing the asymmetry between phonon and ionization side surface events was to passivate the amorphous silicon blocking layer between the detector crystal and Al layer with hydrogen. Previous experience with hydrogenated amorphous silicon blocking layers in early CDMS detectors [69, 70] indicate an im-

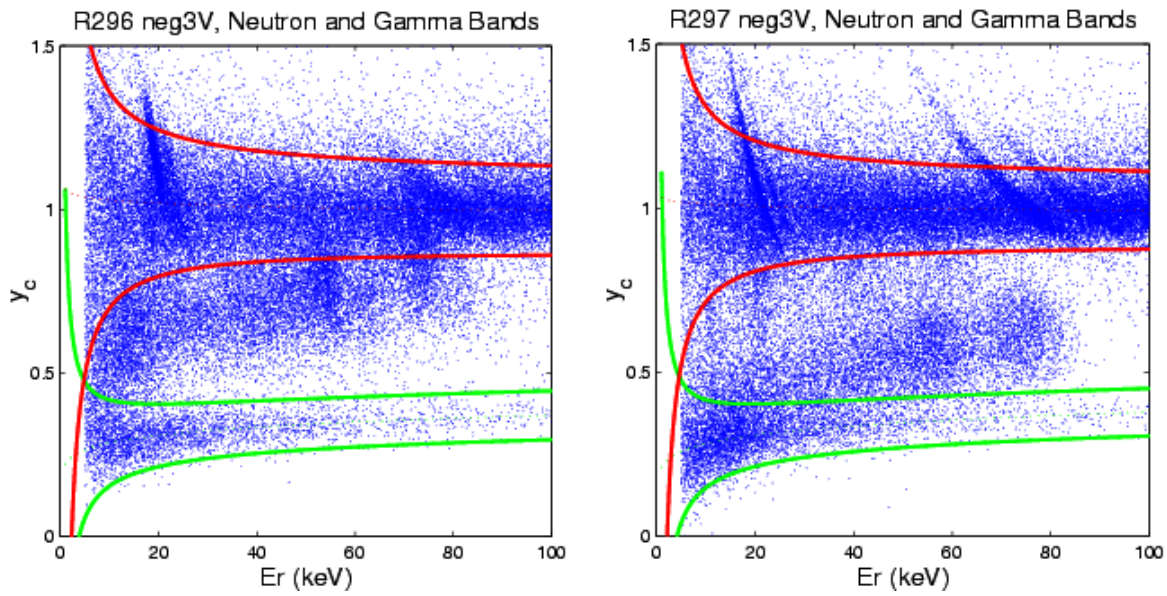

(a) (b)

Figure 7.7: Plots showing ionization yield as a function of phonon recoil energy for calibration data on a Ge ZIP detector using an external ^{252}Cf and internal ^{109}Cd source. The ^{109}Cd source produces many β events which probe the detector surface layer creating the event population with low ionization yield between the upper electron recoil and lower nuclear recoil bands. (a) ^{109}Cd source (and surface events) on the ionization side (b) ^{109}Cd source (and surface events) on the phonon side.

provement in ionization yield based surface event discrimination. This improvement is thought to be due to the passivation of interface defects in the amorphous silicon [142, 143], therefore increasing the layer's blocking ability and decreasing the detector dead layer.

To determine if hydrogenating the amorphous silicon layer in the CDMS-II ZIP detectors would improve the ionization yield based surface event discrimination, several test device surface layers were characterized at the Case Western test facility with internal collimated ^{241}Am sources. The first set of test devices included two 1 inch Si detectors, one with "standard" surface treatment (no hydrogen added to the amorphous silicon layers) and one with hydrogen passivation added to the surface treatment on both detector faces. A second set of test devices consisted of three Ge detectors, one with standard surface treatment (no hydrogen added to the amorphous

silicon layers), one with hydrogen passivation added in the ionization surface treatment, and one with hydrogen passivation added in the phonon surface treatment. During both sets of investigations the detectors with multiple treatments allowed the ionization and phonon side ionization yield rejection and dead layers to be compared. Additional Si detector properties are listed in Table 7.1 and Ge detector properties are listed in Table 6.1.

Silicon Test Devices

The first performance studies with hydrogenated amorphous silicon in CDMS-II detectors were completed using 1 inch silicon detectors (Table 7.1). In order to examine the effect the hyodrogenated amorphous silicon had on surface event discrimination, a similar test program was executed with both detectors so that the data could be compared. In order to probe the detector surface layer, collimated ^{241}Am sources were placed adjacent to each detector face. These sources emit 14, 18, and 21 keV x-rays which have penetration depths into silicon of approximately 345, 714, and 1111 μm respectively (linear attenuation coefficients of approximately 29, 14, and 9 cm^{-1} respectively). Since a fraction of the low energy x-ray events occur close to the detector surface, studying the tails of distributions can give information about these events and the poorly collected surface region. For surface events, the combination of the charge bias polarity and the event side determines the sign of the dominant charge carrier producing the ionization signal. For instance, electrons (holes) are the dominant charge carrier for ionization side surface events with a negative (positive) applied charge bias. Therefore, in addition to placing the ^{241}Am sources on both detector sides, data were taken with multiple charge bias amplitudes, both negative and positive polarity for each.

This silicon detector data analysis was accomplished by looking at the fraction of low yield events. Since surface events suffer from poor ionization collection and ionization yield is the ratio of the ionization to phonon recoil energy collected for each

Detector	Thickness	Phonon Side Surface	Charge Side Surface
S10C	1 inch	amorphous Si	amorphous Si
S06C	1 inch	20% hydrogenated amorphous Si	20% hydrogenated amorphous Si

Table 7.1: Si detectors used to study the effects of hydrogen passivating the amorphous silicon blocking layer along with important properties.

event, those with low ionization yield correspond to events occurring in the surface layer. By making a phonon selection of the 14 keV x-ray events and comparing the fraction of low yield events between the two detectors for data sets with different charge biases and especially different bias polarities, and for events from the sources on different detector faces, one is able to understand the surface event discrimination for the different conditions.

Unfortunately S10C, the "control" detector with no hydrogen added to the amorphous silicon layers, suffered from QET chassis shorts. While data were still able to be taken with this detector, these shorts complicated the direct comparison between S10C and S06C, the "test" detector with hydrogen added to the amorphous silicon layers on both detector faces. In addition, the data from both S10C and S06C suffered poor ionization resolution which is believed to be due to the QET chassis shorts on S10C. Although this poor ionization resolution made direct calculations of the dead layer impossible, comparisons of the fraction of low yield events were still possible and allowed for some analysis of surface event discrimination to be completed.

Analysis of the S06C data, with hydrogenated amorphous silicon layers on both detector faces, shows indications that hydrogenated amorphous silicon layers may decrease the ionization yield discrimination asymmetry of surface events between the ionization and phonon detector faces for silicon detectors under specific charge bias conditions. This is seen in the data in Figure 7.8. Under negative electric field the asymmetry between ionization and phonon side ionization yield discrimination can

be seen as the fraction of low yield events for the 14 keV ^{241}Am x-rays is higher for events occurring on the phonon side (red) than on the ionization side (blue). However, under positive electric field this asymmetry disappears. Based on this data, the ionization yield asymmetry appears to be gone when biasing this silicon detector with hydrogenated amorphous silicon with a positive electric field. Since the ionization and phonon side asymmetry exists under negative and positive electric fields in the current detectors with no hydrogenated amorphous silicon, this analysis indicates that adding hydrogen to the amorphous silicon layer on a silicon detector reduces the ionization yield discrimination asymmetry for positive charge bias.

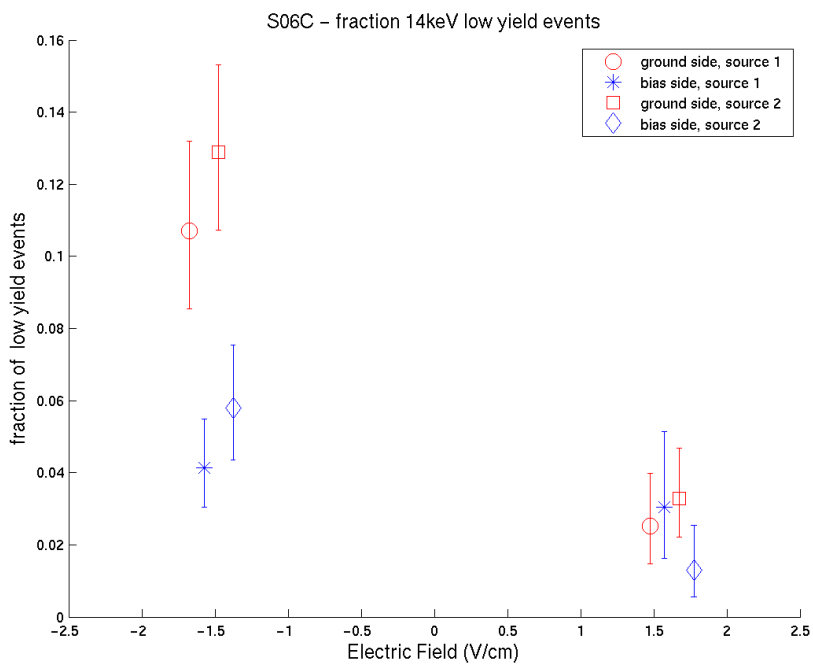

Figure 7.8: Plot showing the fraction of low yield events for 14 keV x-rays from ^{241}Am sources on the ionization detector face (blue) and the phonon detector face (red) for negative and positive 1.5 V/cm electric fields. Notice how the discrepancy in the fraction of low yield events between ionization and phonon side events for negative electric field disappears under positive electric field.

Germanium Test Devices

After the promising results with hydrogenated amorphous silicon on silicon detectors, the technique needed to be tested with germanium detectors (since all of the

SuperCDMS detectors will be germanium because of its greater sensitivity to WIMP interactions than silicon, Section 2.2). Initial tests using the same percentage of hydrogen (20%) with germanium on the phonon detector face failed because the surface conductivity at low temperatures was too high and there was not sufficient isolation between phonon sensors. Decreasing the percentage of hydrogen to 8% on the phonon detector face maintained a low enough surface conductivity to allow the functionality of the four individual phonon sensors.

This investigation included three 1 inch germanium detectors (Table 6.1) and data taken using the same strategy as the silicon detector study. Again, collimated ^{241}Am sources were placed on both detector faces to probe the surface layers and data were taken with multiple charge bias amplitudes, and both negative and positive polarity for each. The ^{241}Am x-rays have a much shorter penetration depth in germanium than in silicon. Therefore a larger fraction of events occur in the detector surface layer and the analysis can also consider the 60 keV gamma-ray. The 14, 18, 21, and 60 keV ^{241}Am lines have penetration depths into germanium of approximately 17, 33, 50, and 909 μm respectively (linear attenuation coefficients of approximately 590, 300, 200, and 11 cm^{-1} respectively).

The data from these 1 inch germanium detectors generally all did not have good phonon energy resolution. This phonon energy resolution was poor enough that a phonon energy selection to select the 14, 18, and 21 keV x-ray lines in an unbiased manner was impossible. Therefore this data analysis took advantage of using the 60 keV gamma-ray line which is well separated from other ^{241}Am spectral features. While using this 60 keV line means that a smaller fraction of events occur in the germanium detector surface layer, there are much better statistics than there are for the lower energy x-ray lines.

In order to quantify the depth of the detector surface layer and to better compare these three detectors, and previous detectors, this analysis determined the detector dead layer. The dead layer is calculated based on the distribution of measured

ionization energy of 60 keV ^{241}Am gamma-rays and event locations (based on the penetration depth of 60 keV in germanium). This method was previously used and described in [69, 70], and Appendix G.

By comparing the calculated dead layers for G3D (with no hydrogen added to the amorphous silicon on either detector face, Figure 7.9), G2E (hydrogen added to the amorphous silicon on the ionization side detector face, Figure 7.10), and G28B (hydrogen added to the amorphous silicon on the phonon side detector face, Figure 7.11), it appears that G3D has the smallest calculated dead layer for a given bias and both detector faces (Figures 7.12 and 7.13). This implies that adding hydrogen to the amorphous silicon layer "worsens" the dead layer for a germanium detector and is consistent with the theory that, unlike the case of a silicon substrate, hydrogen added on a germanium substrate does not passivate the interfacial dangling-bond defects [73].

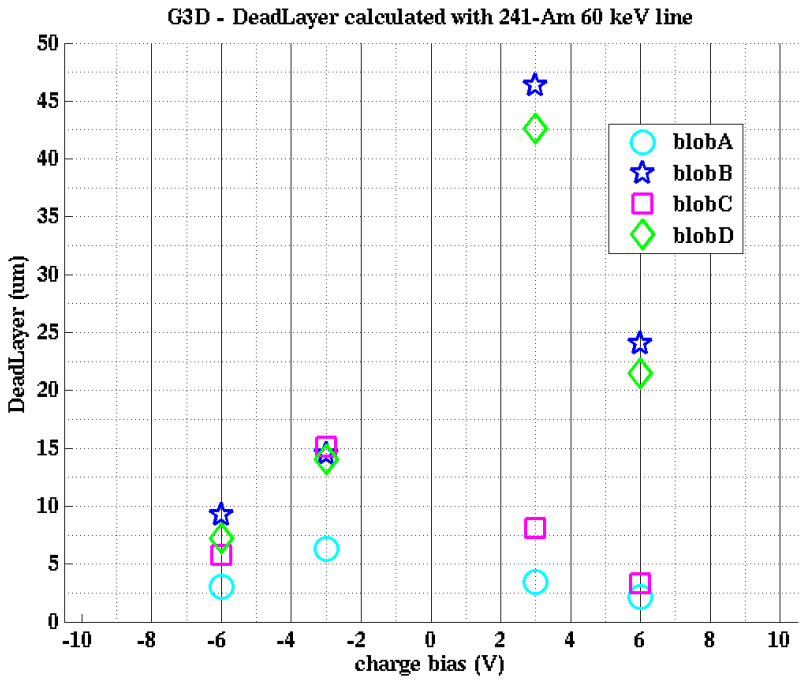

Figure 7.9: Plot showing the calculated dead layer for the 1 inch germanium detector G3D (no hydrogen added to the amorphous silicon on either detector face) as a function of charge bias. The detector side the ^{241}Am source was located on corresponds to the side the events occur on. Source A (cyan) and C (magenta) were located on the ionization side while B (blue) and D (green) were located on the phonon side.

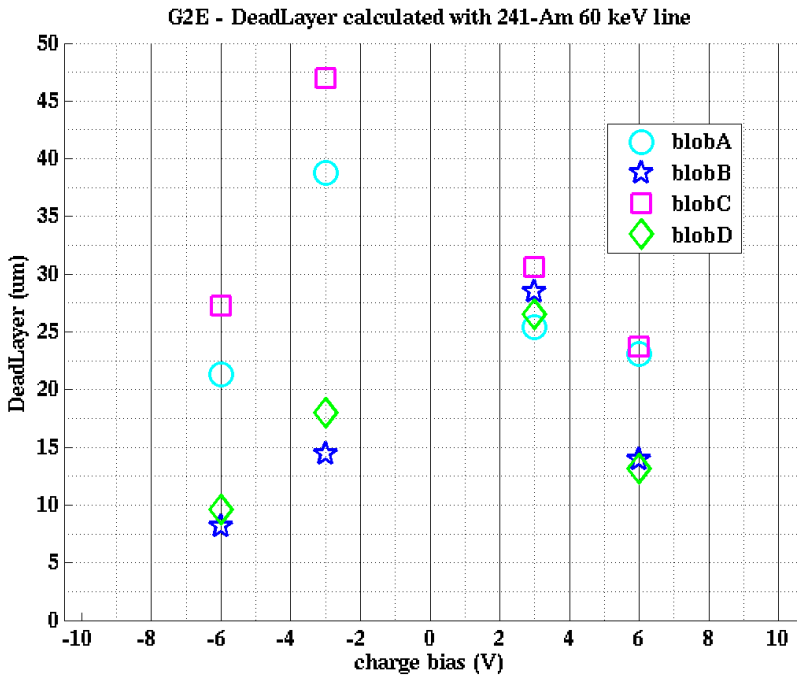

Figure 7.10: This is the same type of plot as Figure 7.9, only for the 1 inch germanium detector G2E (hydrogen added to the amorphous silicon on the ionization side detector face). Unlike Figure 7.9, source B (blue) and D (green) were located on the ionization side while A (cyan) and C (magenta) were located on the phonon side.

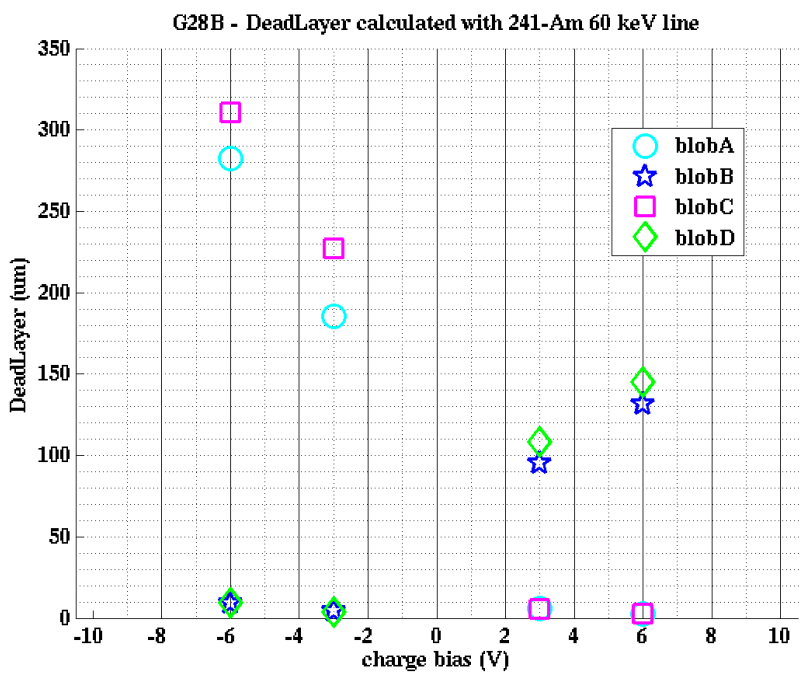

Figure 7.11: This is the same type of plot as Figure 7.9, only for the 1 cm germanium detector G28B (hydrogen added to the amorphous silicon on the phonon side detector face). Figure 7.9, source B (blue) and D (green) were located on the ionization side while A (cyan) and C (magenta) were located on the phonon side.

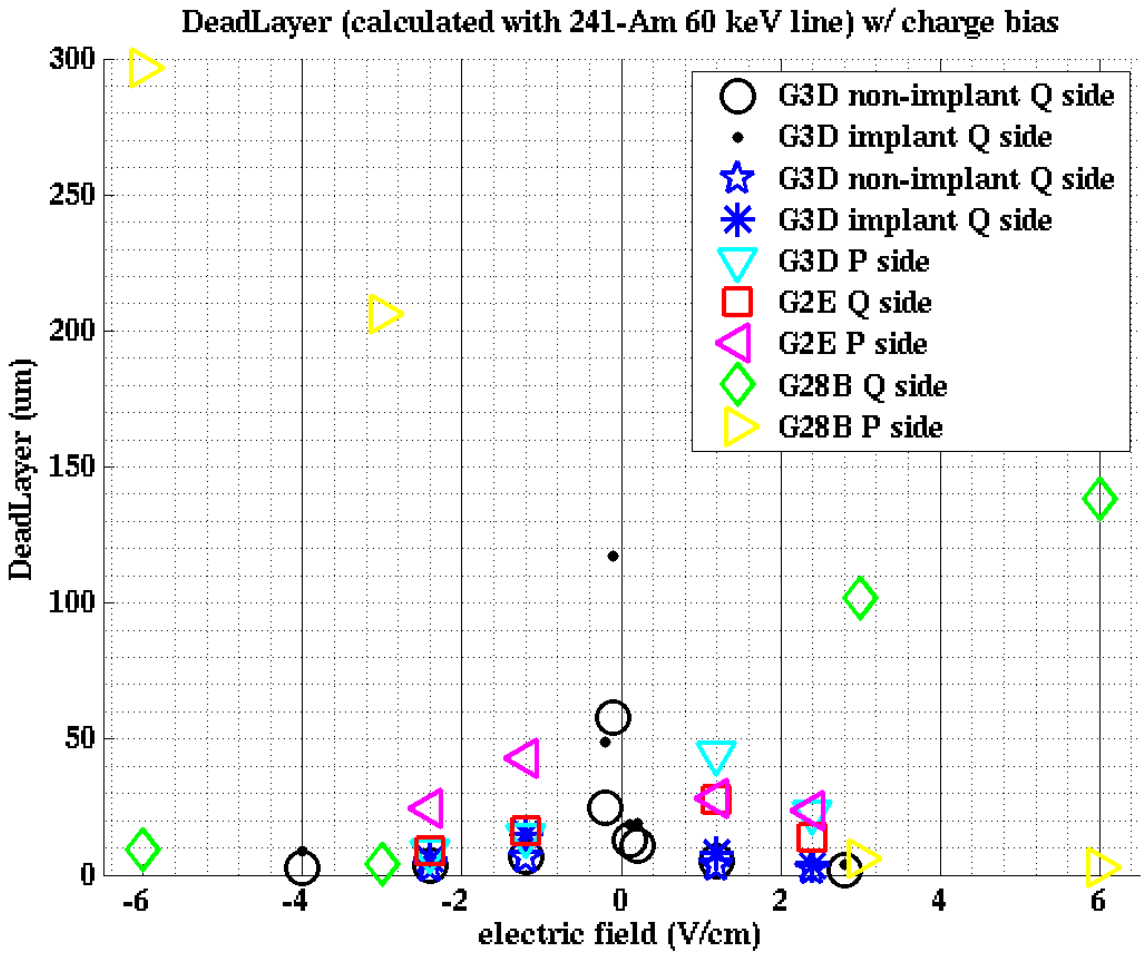

Figure 7.12: This is the same type of plot as Figure 7.9, showing the calculated dead layer as a function of electric field. This plot compares all three germanium detectors and demonstrates how G3D (no hydrogen in the amorphous silicon layer on either detector face) has the smallest dead layer for a given charge bias. To see how hydrogenating the ionization side (from 0% to 20%) amorphous silicon layer affects the detector dead layer, compare the charge side of G2E (red square) with G3D (black circle and blue open star) and compare the phonon side of G2E (magenta triangle) with G3D (cyan triangle). To see how hydrogenating the phonon side (from 0% to 8%) amorphous silicon layer affects the detector dead layer, compare the charge side of G28B (green diamond) with G3D (black circle and blue open star) and compare the phonon side of G28B (yellow triangle) with G3D (cyan triangle). To see how ion implantation affects the detector dead layer, compare G3D's non-implanted charge side (black circle and blue open star) with G3D's implanted charge side (black circle and blue closed star). To see how the applied electric field (charge bias) affects the detector dead layer, compare multiple biases of a single detector and single source side. The dead layer is inversely proportional to the applied electric field, to a certain point, and is then fairly independent of field.

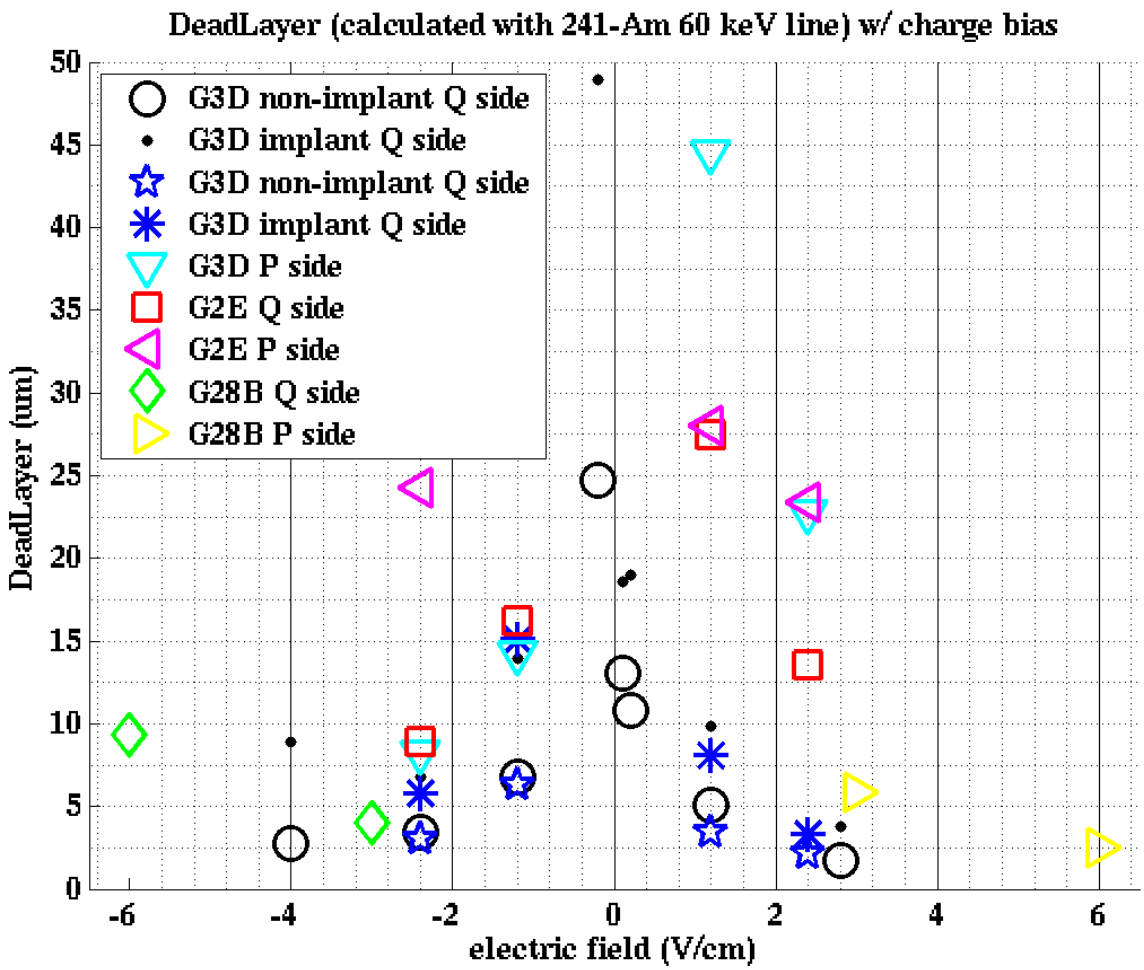

Figure 7.13: This is the same plot as Figure 7.12, except that it has a smaller y-axis ranges.

While the dead layer comparison between G3D, G2E, and G28B shows that G3D has the smallest dead layer, closer inspection of the data leads to a number of additional questions and caveats. One of the biggest questions that is not understood based on this data is how adding hydrogen to one detector face can affect the opposite face dead layer. This can be seen in the calculated dead layers for both G2E (Figure 7.10) and G28B (Figure 7.11).

In the course of analyzing and comparing the data taken with G3D, G2E, and G28B it was realized that the comparative study had more variables adjusted between the three detectors than just adding hydrogenation to the amorphous silicon processing. These three detectors were fabricated on germanium crystals that were each

from a different germanium Boule. Therefore each of the detectors have different impurity concentrations (detailed in Table 6.1). In particular, G28B has approximately twice the impurity concentration as the other two detectors. In addition, G3D is a p-type crystal while the other two detectors are n-type. While it is possible that neither of these have a significant impact on the dead layer calculation, both have possibly produced other significant phenomenon. Soudan data shows that Boule B germanium detectors are worsened by neutralization via strong source baking (Section 6.2.2). This suggests that the larger impurity concentration in this germanium may be the cause. Long data sets taken with G3D and G28B to study how detectors lose neutralization show a discrepancy between which charge carrier is responsible for losing full ionization collection first (Section 6.8). This points to a difference in charge carrier dynamics between n- and p-type germanium crystals (Section 7.4.5). Therefore, it is possible that variations in the calculated dead layers between the three detectors could be caused by something other than adding hydrogen into the amorphous silicon processing.

One final comment regarding this dead layer analysis has to do with comparing the dead layer calculated based on using the 60 keV gamma-ray line from an ^{241}Am source versus the 22 keV gamma-ray line from a ^{109}Cd source [138]. In addition to calculating the dead layer of G3D based on data taken with an internal ^{241}Am source, it was calculated based on data taken with an internal ^{109}Cd source. Despite testing the same detector and using the same analysis method, the calculated dead layer based on ^{241}Am data was larger than that calculated using ^{109}Cd data. The trend that dead layers calculated using the 60 keV line from ^{241}Am data is larger than dead layers calculated using the 22 keV line from ^{109}Cd data has been seen recently with several detectors that are nominally the same. This discrepancy makes it difficult to compare dead layers calculated based on the ^{241}Am 60 keV line with those based on the ^{109}Cd 22 keV line. The ^{241}Am calculation is likely over-estimating the dead layer depth due to the significant number of Compton scatter events. More than 10%

of 60 keV events Compton scatter while there are almost no Compton scatters for 22 keV events. Since the model used to calculate dead layer (Appendix G) assumes single scatters as opposed to multiple Compton scatters, the Compton scatters add an additional length scale that is not considered in the calculation. The comparisons of the calculated dead layer for G3D, G2E, and G28B done in this analysis are valid because systematic effects were controlled by always using the ^{241}Am 60 keV line. While an absolute dead layer measurement is important for background estimates, this study focused on evaluating the relative performance of different devices in a controlled environment.

7.3.2 Ion Implantation

Another way to solve the ionization yield discrimination asymmetry between the phonon and ionization detector sides is to determine the underlying cause and attempt to fix that. One hypothesis for the asymmetry is that it is due to the iron ion implantation used on the phonon detector side in order to create appropriate and uniform tungsten superconducting transition temperatures [81]. The iron ion deposition is optimized at 50 keV at 7° incidence so that the peak of the iron ion concentration is approximately 40% through the superconducting tungsten layer [82]. However, since the detector has only approximately 20% Al surface coverage (Section 2.2), roughly 60% of the iron ions make it through the 400 Å of bare amorphous silicon into the germanium crystal (Figure 7.14a). These ions are suspected to cause damage to the germanium surface (Figure 7.14b) by adding acceptors and creating a larger dead layer [71, 33].

To test this hypothesis, half of the ionization side of the 1 inch germanium detector G3D (additional details of this detector are listed in Table 6.1) was iron ion implanted with the same procedure as used on the phonon side during transition temperature tuning. The half of G3D's ionization side was implanted with a single

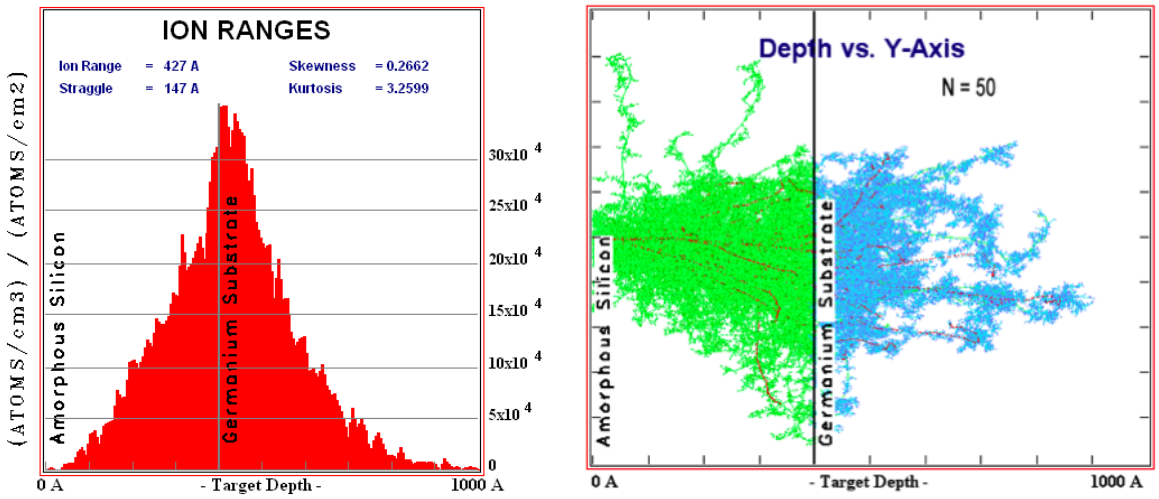

(a) (b)

Figure 7.14: (a) Plot showing a simulation of the iron ion concentration as a function of depth into the amorphous silicon and germanium substrate. (b) Plot showing a simulated distribution of dislocations created by a single iron ion. From [33].

dose of $6.54\times10^{+12}$ atoms/cm^2 ^{56}Fe$^+$ ions at 50 keV while G3D's phonon side was implanted with two doses for a total implantation of $7.85\times10^{+12}$ atoms/cm^2 ^{56}Fe$^+$ ions at 50 keV. Implanting half of G3D's ionization side allowed for a comparative study of the ionization yield discrimation and dead layer thickness between the implanted and non-implanted ionization side as well as between the ionization and phonon sides.

G3D data taking and analysis was conducted in much the same manner as the studies done looking at effects of hydrogenated amorphous silicon. G3D was cold tested multiple times, each with different configurations of internal collimated ^{241}Am sources. These configurations included four sources that were all on the ionization side with two on the implanted half and two on the non-implanted half (Figure 7.15a), two sources on the phonon side and two sources on the ionization side with one source on each side over the implanted and the non-implanted ionization half (Figure 7.15b), and four sources that were all on the phonon side (similar to Figure 7.15a except that all sources were on the phonon side instead of the ionization side). The multiple runs and configurations allowed the data to be cross-checked and verified.

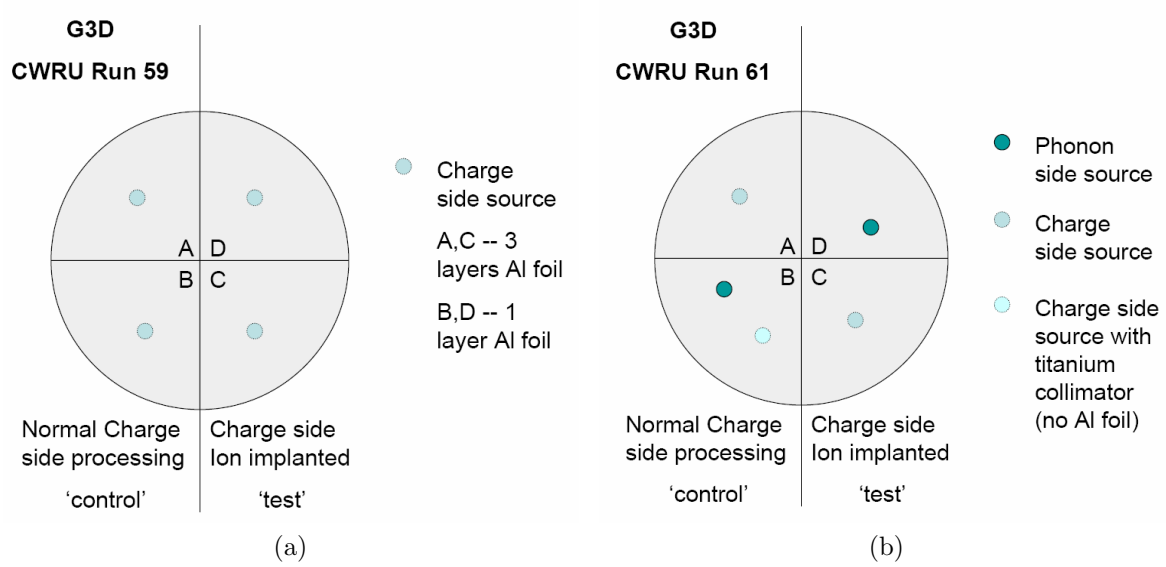

Figure 7.15: The internal collimated ^{241}Am source configuration for G3D during two test facility runs. (a) All sources were on the detector's ionization side. Two sources were over the detector half that had been iron ion implanted and two were over the control half. (b) Two sources were on the detector's ionization side and two on the phonon side. One source on each detector side was over the detector half that had been iron ion implanted and the other over the control half.

Like the analysis comparing effects of the hydrogenated amorphous silicon, during this investigation the fraction of low yield events and the detector dead layers were calculated and compared. While some analysis was done looking at the fraction of low yield events for 14 keV events, the majority of the analysis focused on studying 60 keV events in order to use the higher statistics and avoid bias because of the difficulty in making energy cuts due to the poor phonon energy resolution.

Based on comparing the ionization side dead layers between the implanted and non-implanted half of G3D, there is strong indication that adding iron ion implantation does make the dead layer larger and therefore worsen the ionization yield discrimination. Figure 7.16 shows the ionization side dead layer difference between the half with and without iron ion implantation for the data set taken with all four sources on the ionization detector side. In addition, this difference in the ionization side dead layer can be seen in Figure 7.9 (by comparing the green diamond, ioniza-

tion side with no implantation, and blue star, ionization side with implantation) and Figures 7.12 and 7.13 (by comparing the black circle and open blue star, ionization side with no implantation, with the black dot and closed blue star, ionization side with implantation).

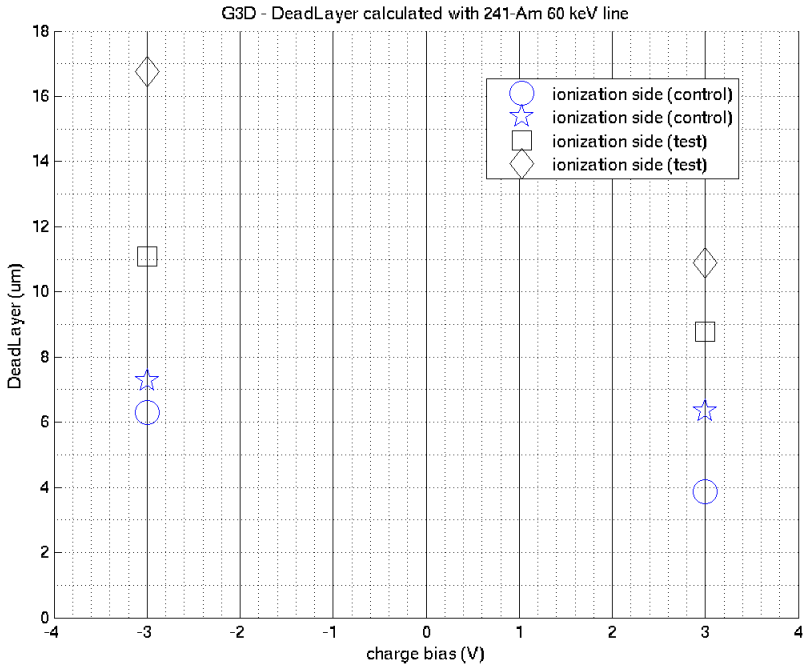

Figure 7.16: Plot showing the calculated dead layer for the 1 inch germanium detector G3D (no hydrogen added to the amorphous silicon on either detector face) as a function of charge bias. The detector side the ^{241}Am source was located on corresponds to the side the events occur on, that is, on the ionization side. Sources A (blue circle) and B (blue star) were located on the half with no iron ion implantation while C (black square) and D (black diamond) were located on the half with iron ion implantation.

Besides seeing the difference between the ionization side dead layer with and without iron ion implantation one can also compare the ionization side dead layer with iron ion implantation with the phonon side dead layer in Figure 7.9 and Figures 7.12 and 7.13. These two figures show that for negative charge bias the calculated dead layer for the ionization side with iron ion implantation is approximately consistent with that for the phonon side. However, for positive charge bias the calculated dead layer for the phonon side is larger than the ionization side with iron ion implantation. This may indicate that while iron ion implantation does affect the dead layer, it may

not be the only cause for the phonon and ionization side ionization yield asymmetry.

Since this study shows that iron ion implantation affects the dead layer, the ionization yield asymmetry between phonon and ionization side events could be reduced by modifications to the implantation procedure in future detectors. In particular, the damage to the germanium substrate by the iron ions can be lessened by applying a mask during implantation which would cover the entire detector surface except for the tungsten, which constitutes only a few percent of the surface area. Using this configuration the iron ions would not see any bare amorphous silicon and could not penetrate to the germanium substrate to cause damage. Future analysis comparing the phonon and ionization side dead layers and ionization yield discrimination of detectors with no iron ion implantation and iron ion implantation while masking off the bare amorphous silicon will further verify these results and the method to remove the asymmetry, and improve the phonon side ionization yield discrimination.

7.4 Other Phenomena Observed During Device Testing

The data taken to understand how hydrogenated amorphous silicon and iron ion implantation affect detector dead layers and ionization yield discrimination turned out to be very rich data sets. In addition to learning about the specific a priori questions, other aspects of the data turned out to be interesting and worth considering how they affect the data analysis as well. While some of these trends may not be fully understood, they are summarized in this section and may be considered for future follow-up studies.

7.4.1 Dead Layer Electric Field Dependence

Figures 7.12 and 7.13 demonstrates how the detector dead layer varies with the applied electric field for G3D, G2E, and G28B. From this data, the dead layer appears to be inversely proportional to applied electric field (the dead layer decreases with larger electric fields). However, once the charge bias has reached a certain level the dead layer does not seem to have much dependence on it.

This data and similar studies can be useful in determining what amplitude and polarity charge bias the detectors should be biased with for optimal background discrimination. By combining information about how the dead layer, as an indicator of ionization yield discrimination, and phonon timing information, as the other major background discriminator, vary with applied bias, the optimal charge bias can be determined.

7.4.2 Electric Field Dependent Ionization Collection

With the increased thickness of CDMS detectors (Section 7.5) from 1 cm to 1 inch thickness, it is important to ensure that the detectors operate with an electric field strength that achieves full ionization collection for bulk events. To do this test, data were taken with S06C (Figure 7.17), G3D (Figures 7.18 and 7.19), G2E (Figure 7.20), and G28B (Figure 7.21) with internal collimated ^{241}Am sources with multiple applied charge biases (at least -6 V, -3 V, +3 V, +6 V). Then "seagull" plots were created by individually fitting the ionization energy collected in the inner electrode from the 60 keV ^{241}Am line for each source with a gaussian functional form. The "seagull" plot shows the gaussian mean and 1σ error for each source as a function of applied charge bias or electric field.

The first important observation based on this data analysis is that the ionization collection as a function of electric field for the 1 inch detectors (Figures 7.17 and 7.18) is consistent with those from the CDMS-II 1 cm detectors [14, 12].

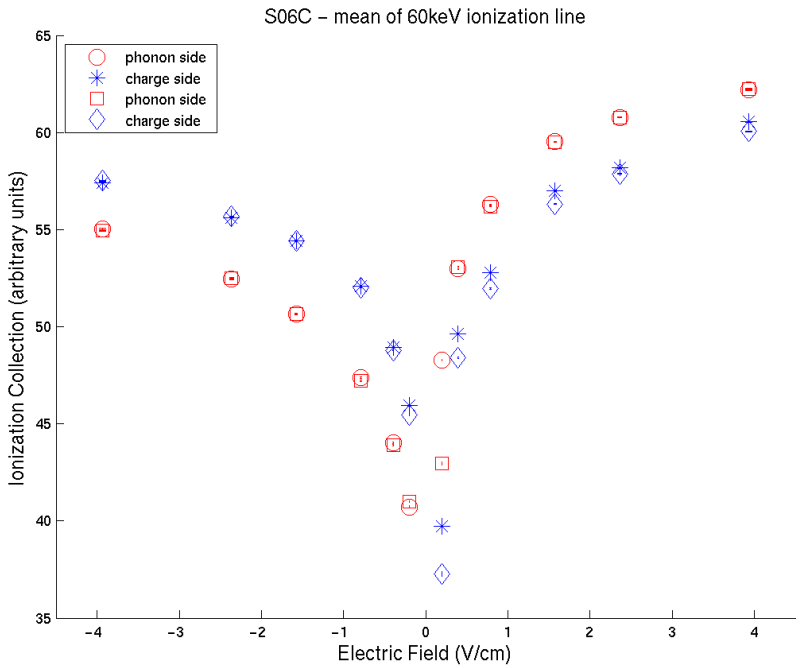

Figure 7.17: Plot showing the raw collected ionization energy of 60 keV ^{241}Am events, with 1σ error bars, as a function of applied electric field for the 1 inch silicon detector S06C. Two sources were located on the ionization side (blue) while another two were located on the phonon side(red).

A second feature to notice is that the absolute ionization collection is not always the same for negative and positive polarity charge biases. For the silicon detector S06C (Figure 7.17) the collected ionization energy from ionization side sources (blue) remain constant for negative and positive applied charge bias while the collected ionization energy from phonon side sources shows a significant difference for negative and positive applied charge bias. On the other hand, for the germanium detectors (Figures 7.18, 7.19, 7.20, and 7.21) the collected ionization energy from phonon side sources remains constant for negative and positive applied charge bias while the collected ionization energy from ionization side sources shows a significant difference for negative and positive applied charge bias.

This difference in the ionization collection for negative and positive charge bias might say something about bulk ionization trapping and the difference between electron and hole charge carrier transport. In particular, for Ge, under both negative

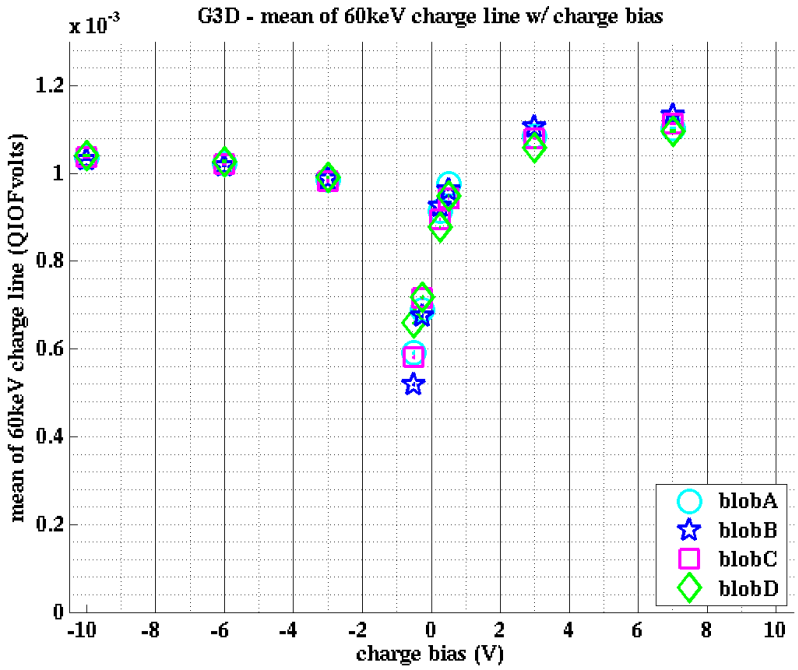

(a)

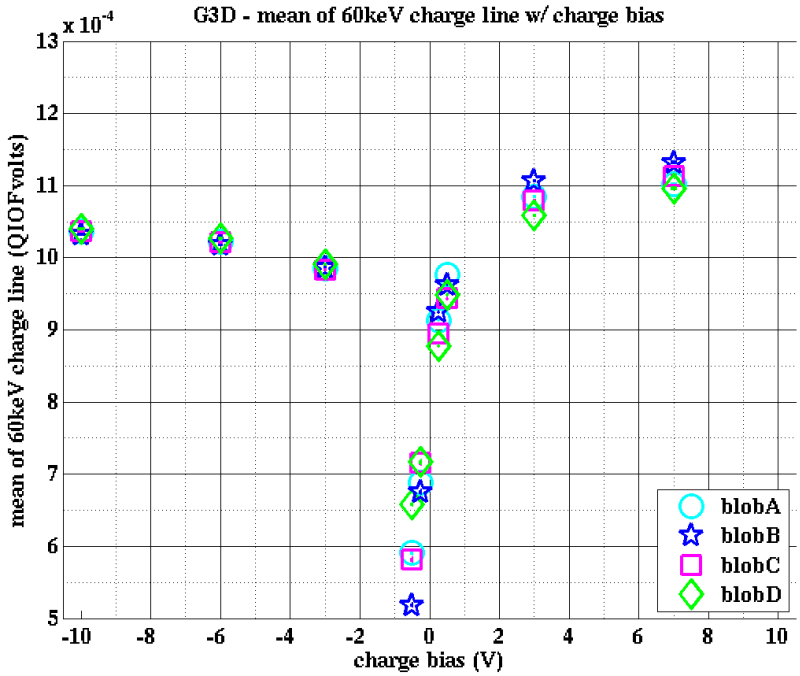

(b)

Figure 7.18: Plots showing the raw collected ionization energy of 60 keV ^{241}Am events, with 1σ error bars, as a function of applied charge bias for the 1 inch germanium detector G3D. (a) and (b) show the same data but have different y-axis ranges. The detector side the ^{241}Am source was located on corresponds to the side the events occur on. All of the sources were located on the ionization side.

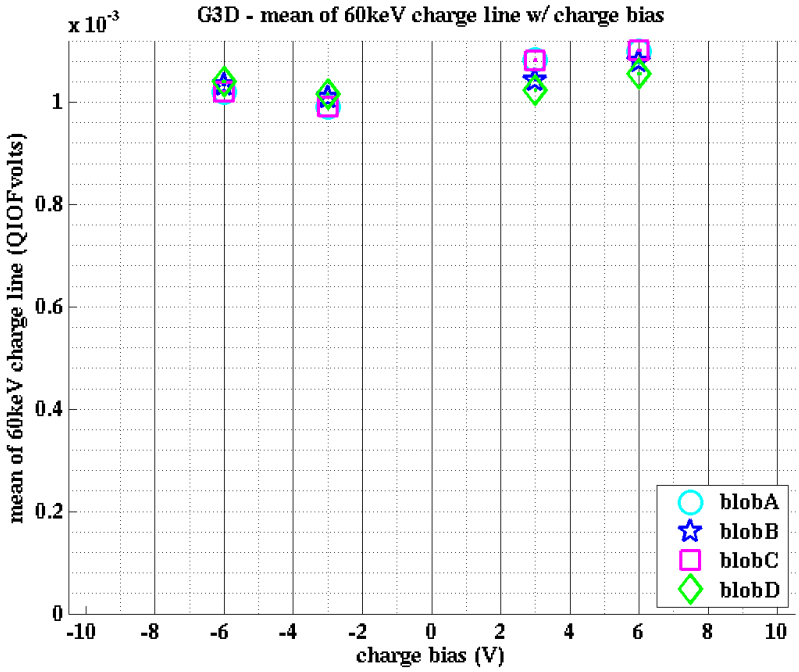

(a)

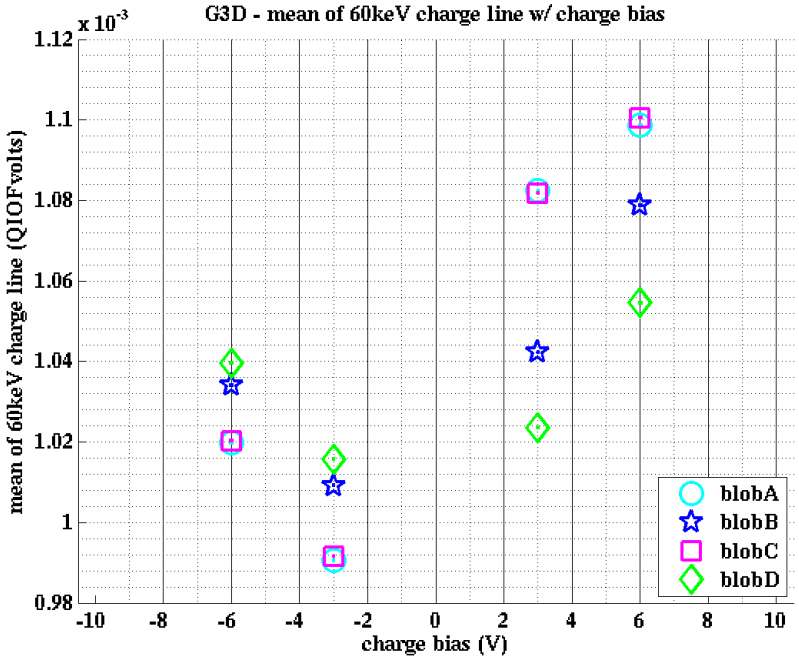

(b)

Figure 7.19: Similar to Figure 7.18, except that this is for the 1 inch germanium detector G3D and source A (cyan) and C (magenta) were located on the ionization side while B (blue) and D (green) were located on the phonon side.

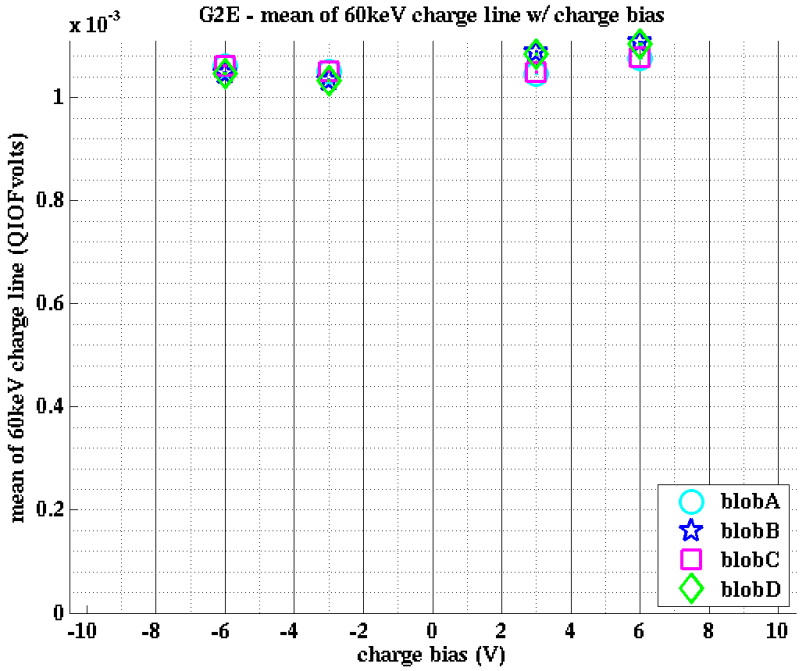

(a)

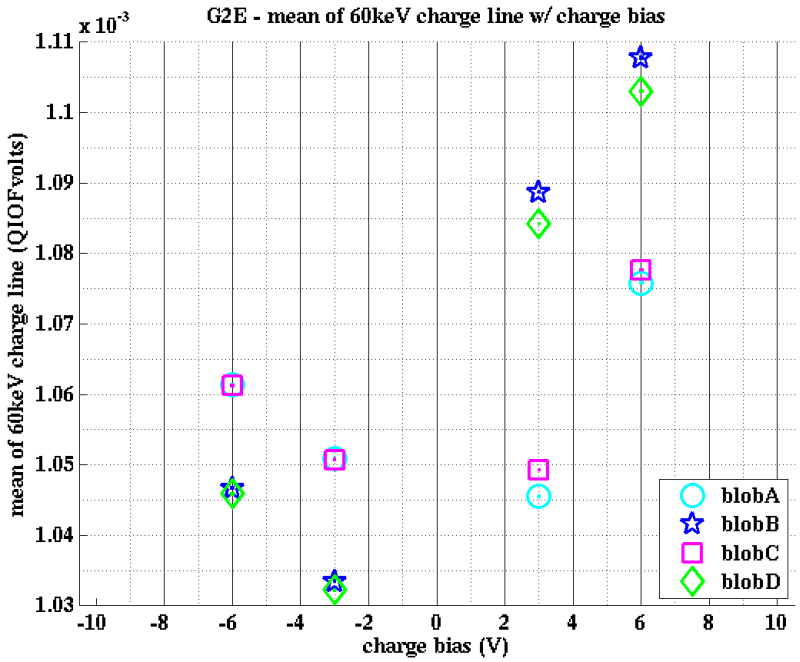

(b)

Figure 7.20: Similar to Figure 7.18, except that this is for the 1 inch germanium detector G2E and source B (blue) and D (green) were located on the ionization side while A (cyan) and C (magenta) were located on the phonon side.

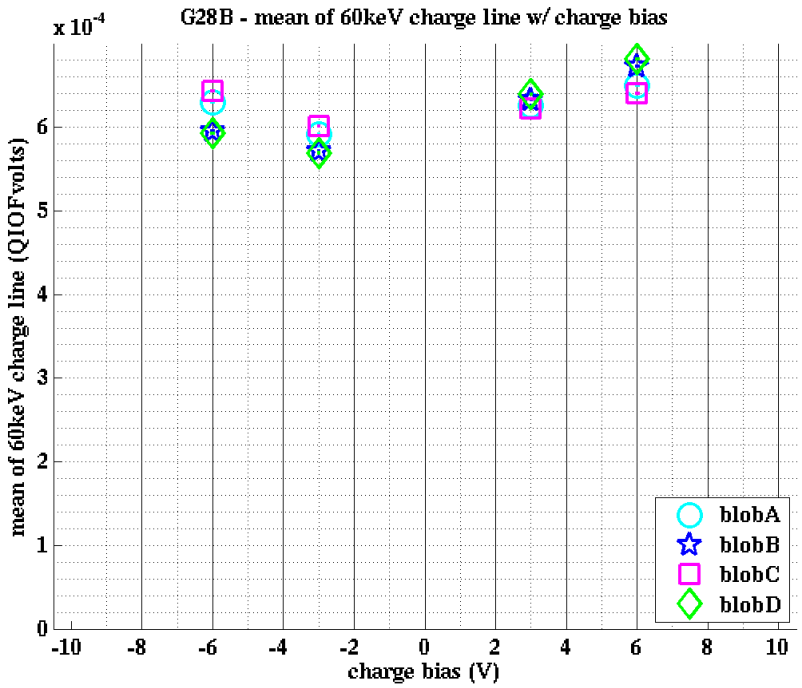

(a)

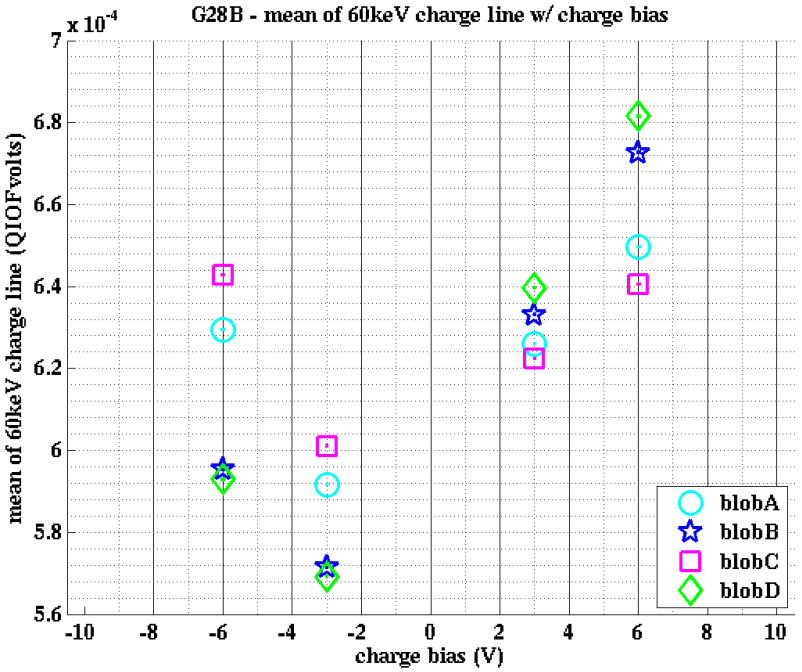

(b)

Figure 7.21: Similar to Figure 7.18, except that this is for the 1 cm germanium detector G28B and source B (blue) and D (green) were located on the ionization side while A (cyan) and C (magenta) were located on the phonon side.

and positive applied charge biases the ionization signal is greater when holes are the dominant charge carrier.

If this ionization collection dependence on charge bias polarity is indeed due to charge carriers, one possible reason for the differing results between germanium and silicon is the event distribution in the different materials. For example, the 60 keV event distribution is much more uniform throughout a 1 inch silicon crystal (where the 60 keV penetration depth is 1.3 cm) than a 1 inch germanium crystal (where the 60 keV penetration depth is 0.091 cm).

It is also interesting that, in both silicon and germanium and for both electron and hole charge carriers, the collected ionization energy is greater under positive applied charge bias than negative charge bias.

Finally it is important to note the difference between the ionization collection for events from sources on the ionization and phonon detector faces. This will be discussed further in Section 7.4.3 for the germanium detectors.

Note that the absolute amplitude of G28B lines is approximately half that of the other detectors due to a short between inner and outer ionization electrode and this analysis only uses the energy from the inner electrode.

7.4.3 Position Dependent Charge Collection

While analyzing the G3D data with two of the internal collimated ^{241}Am sources on the detector ionization side and two on the detector's phonon side, the 60 keV ionization line does not appear at the same energy for both ionization and phonon side source events. This offset in the collected ionization energy from ionization and phonon side source events is not only seen in the G3D data, but also in data taken with G2E and G28B.

Figures 7.22, 7.23, and 7.24 show histograms of calibrated ionization energy for G3D, G2E, and G28B for -3 V and +3 V applied charge biases. In all of the his-

tograms, the black curve is the total collected ionization energy from all sources and the colored curves show events from each individual source that was located on either the ionization or phonon detector face. While the ionization signal was individually calibrated for each detector and data set, the same calibration constant was used for all events within a single data set (there were not two separate calibrations, one for charge side and one for phonon side source events).

In the histograms look at the difference in the energy collected between ionization and phonon side source events for the two charge bias polarities. For positive applied charge bias polarities, the energy difference between sources located on the ionization and phonon sides is much larger than for negative charge bias polarities, so much so that the 60 keV peak looked bimodal under +3 V charge bias. Additionally, while not shown here, for lower applied charge bias amplitudes, the difference in the energy collected for ionization and phonon side sources appears slightly larger than for larger applied charge biases.

Another way of looking at this difference between the energy collected from ionization and phonon side source events is by looking at the seagull plots (Figures 7.19, 7.20, and 7.21) for G3D, G2E, and G28B. To see the difference in energy collected from ionization and phonon side source events, compare the ionization and phonon side data points for a specific detector and specific applied charge bias.

This difference in the ionization energy collected between ionization and phonon side source events is problematic because this appears as a depth dependence in the collected ionization energy. In WIMP search data the event depth is not known. With a depth dependence in the ionization energy, events with the same phonon recoil energy will have a range of collected ionization energy and therefore produce a spread in the ionization yield distribution and worsen the discrimination between electron recoil background and nuclear recoil signal events. Given the dependence on applied charge bias amplitude and polarity, this information can be used along with other discrimination studies to select the best detector settings that give the best

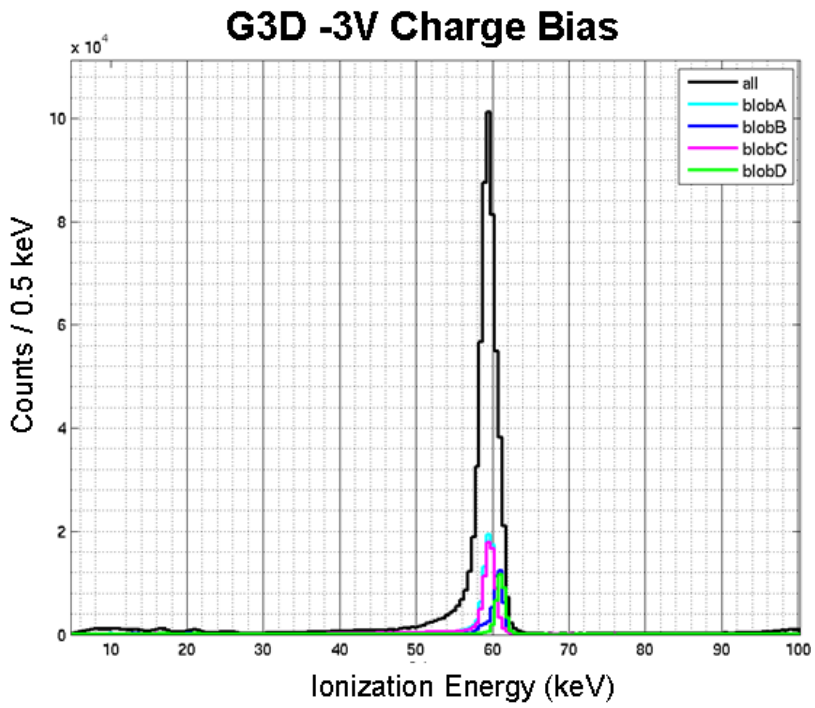

(a)

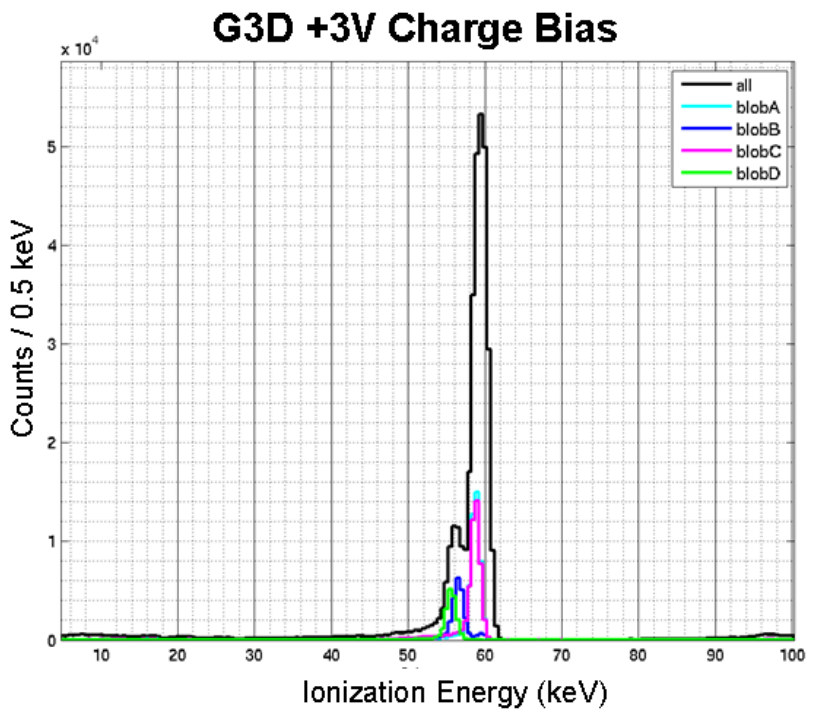

(b)

Figure 7.22: Histograms of the ^{241}Am 60 keV ionization energy in the inner charge electrode for 1 inch germanium detector G3D with (a) a -3 V charge bias and (b) a +3 V charge bias. The detector side the ^{241}Am source was located on corresponds to the side the events occur on. Source A (cyan) and C (magenta) were located on the ionization side while B (blue) and D (green) were located on the phonon side.

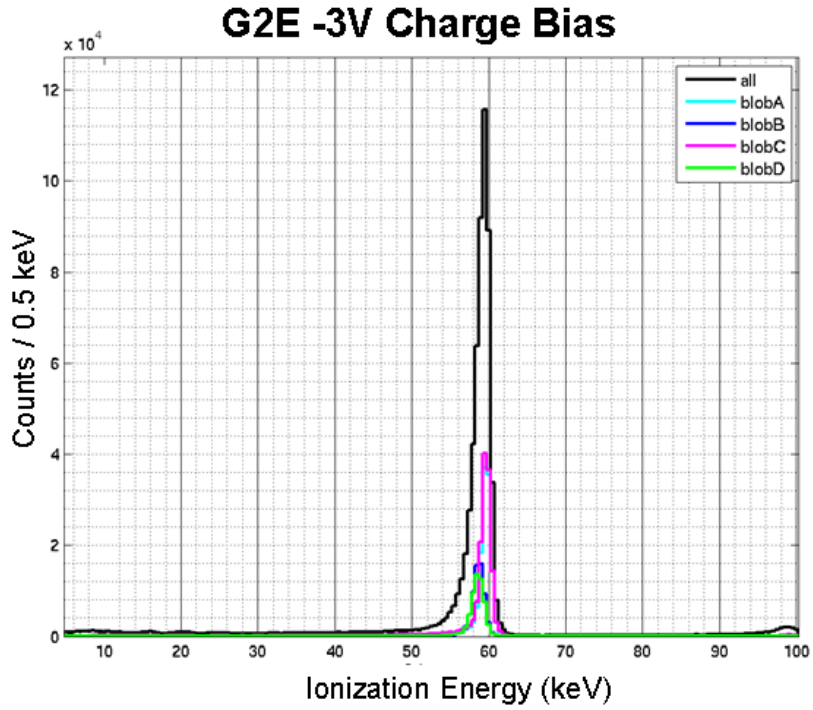

(a)

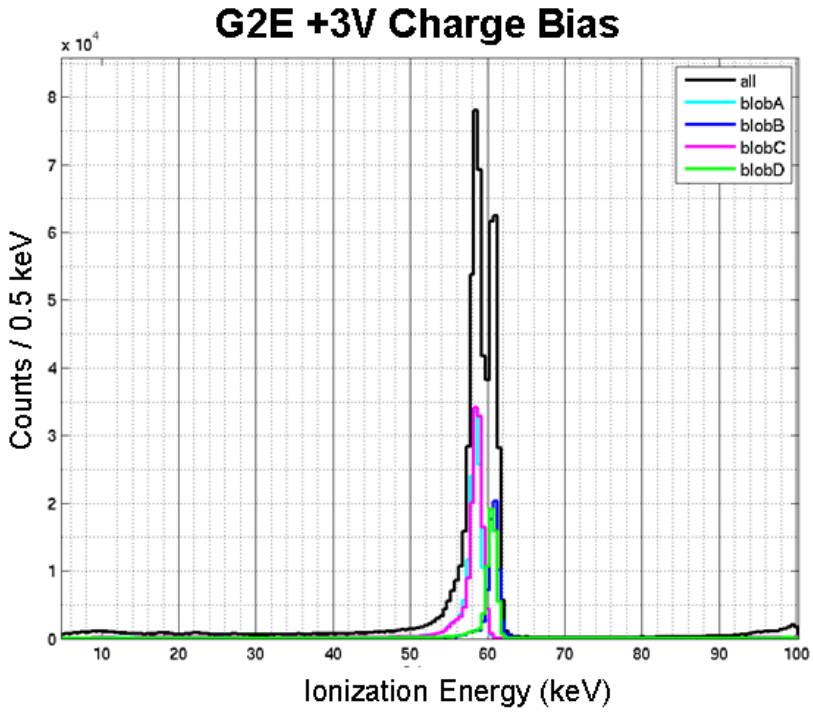

(b)

Figure 7.23: Similar to Figure 7.22, except for 1 inch germanium detector G2E. Again, (a) a -3 V charge bias and (b) a +3 V charge bias. Unlike Figure 7.22, source B (blue) and D (green) were located on the ionization side while A (cyan) and C (magenta) were located on the phonon side.

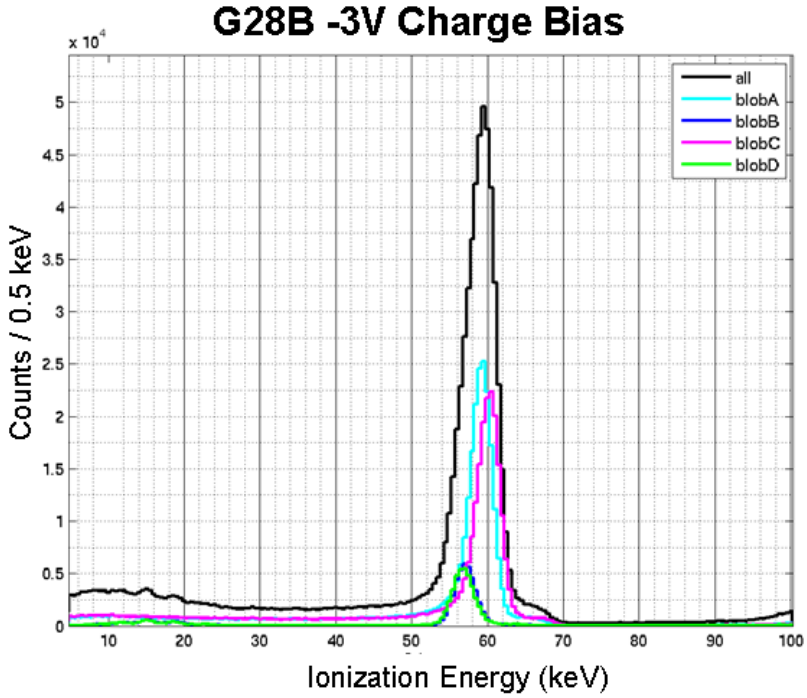

(a)

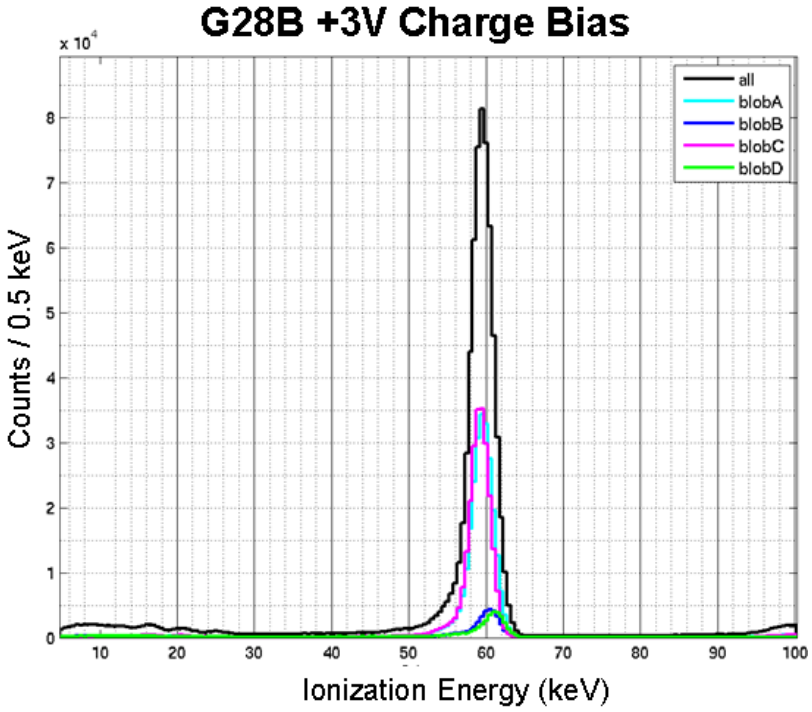

(b)

Figure 7.24: Similar to Figure 7.22, except for 1 cm germanium detector G28B. Again, (a) a -3 V charge bias and (b) a +3 V charge bias. Unlike Figure 7.22, source B (blue) and D (green) were located on the ionization side while A (cyan) and C (magenta) were located on the phonon side.

background rejection.

7.4.4 Charge Instability after Changing Charge Bias

While analyzing G28B data, it was discovered that there is to be a short period of time (on the order of 20 seconds) immediately after biasing the ionization channels (for example, applying a charge bias after grounding) where there is unstable ionization collection. This phenomenon is seen in plots of ionization energy as a function of time (Figure 7.25) for the 60 keV line from internal ^{241}Am sources. Note that there are other lines that also show this ionization instability.

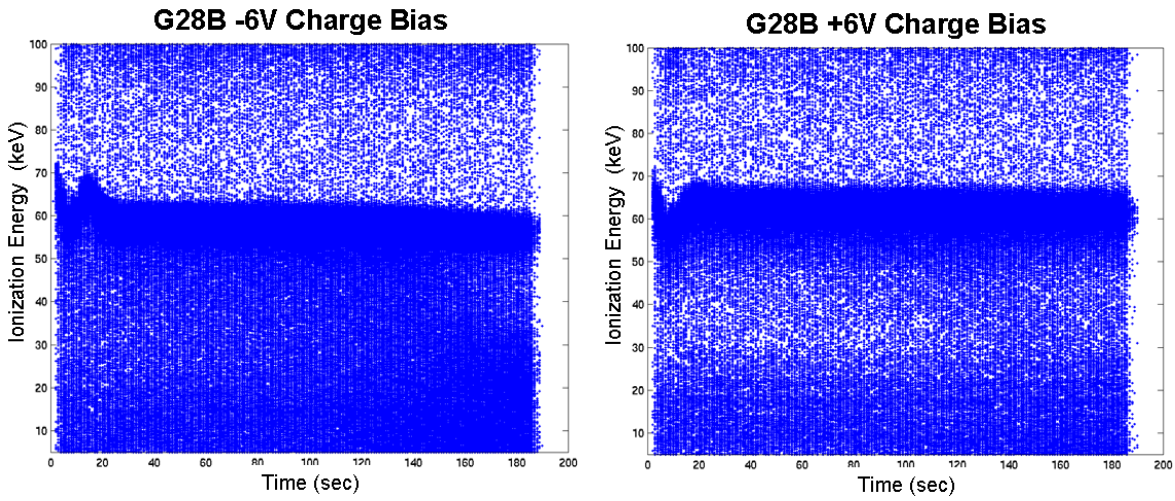

(a) (b)

Figure 7.25: Plots of the ^{241}Am 60 keV ionization energy in the inner charge electrode as a function of time for 1 cm germanium detector G28B with (a) a -6 V charge bias and (b) a +6 V charge bias.

After first noticing this instability in the ionization energy in G28B, other data were examined to look for trends. When comparing G28B data taken with different applied charge bias amplitudes and polarities, the behavior of the ionization instability differs slightly. The general trends are that for smaller applied charge bias amplitudes the instability doesn't last as long (compare Figures 7.25a and 7.26a or Figures 7.25b and 7.26b) and for opposite applied charge bias polarities the instabil-

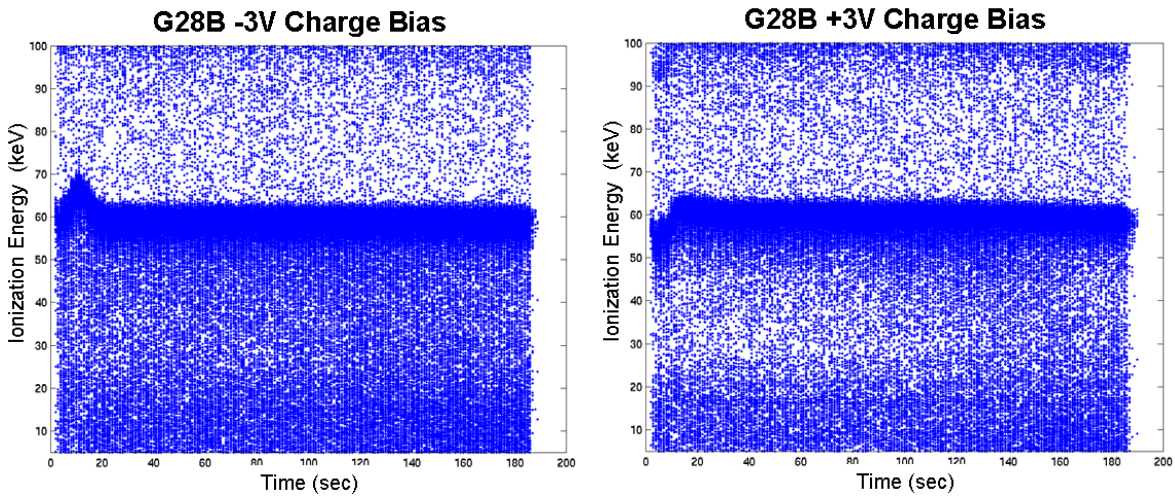

(a) (b)

Figure 7.26: Similar to Figure 7.25, except for (a) a -3 V charge bias and (b) a +3 V charge bias.

ity is inverted or "reverses" (compare Figures 7.25a and 7.25b or Figures 7.26a and 7.26b).

In addition to studying G28B data, data taken with other detectors was inspected for the same feature. The G3D (Figure 7.27) and G2E (Figure 7.28) data that was looked at also shows the same instability in ionization energy.

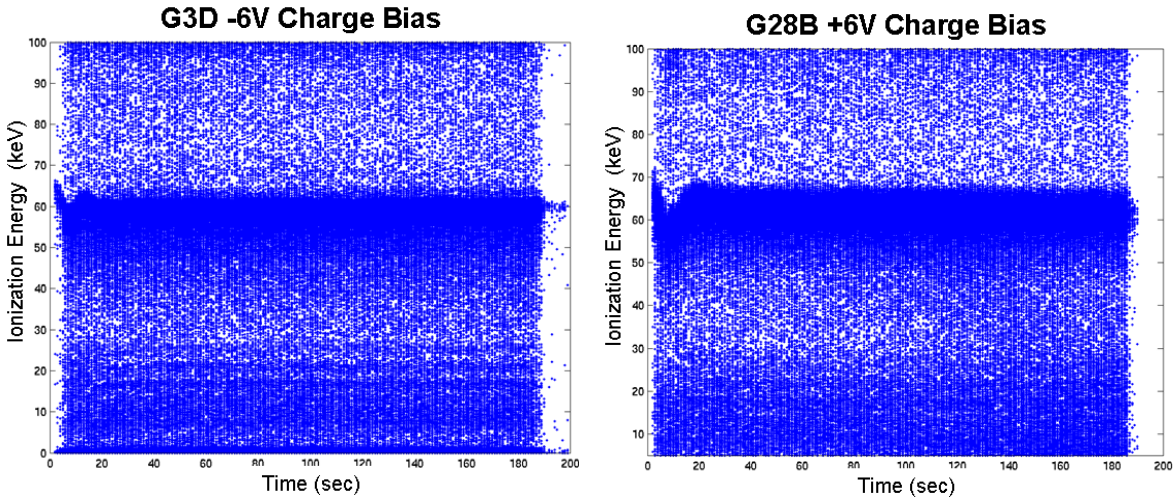

(a) (b)

Figure 7.27: Similar to Figure 7.25, except for 1 inch germanium detector G3D. Again, (a) a -6 V charge bias and (b) a +6 V charge bias.

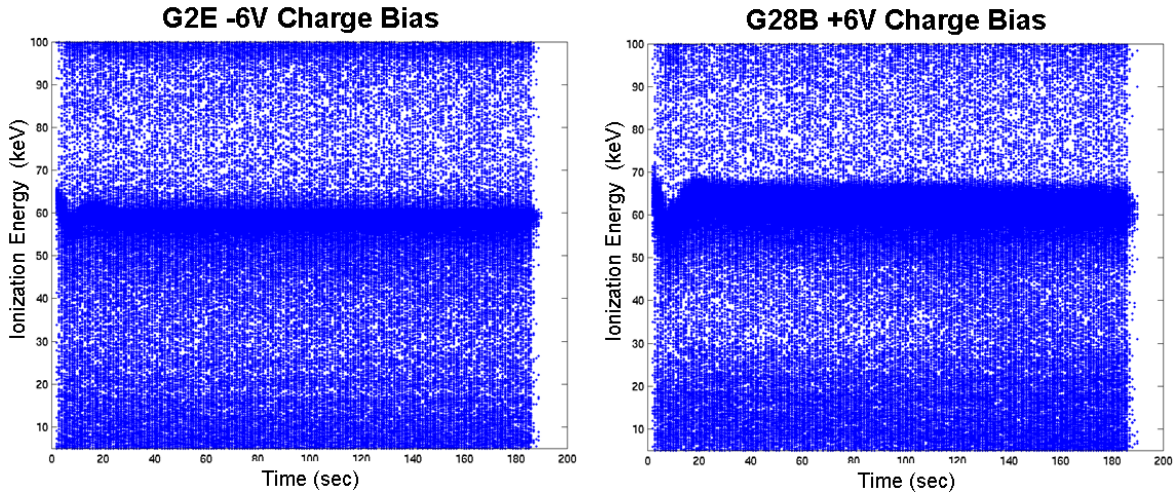

(a) (b)

Figure 7.28: Similar to Figure 7.25, except for 1 inch germanium detector G2E. Again, (a) a -6 V charge bias and (b) a +6 V charge bias.

In order to understand the origin of the instability with time, the total phonon energy and phonon recoil energy collection were studied as a function of time. Unlike the ionization collection with time (Figure 7.29a), the total phonon energy does not vary (Figure 7.29b). Since the total phonon energy collection does not vary with time, that means that the Luke phonons generated by drifting charge carriers is not varying with time. Therefore this indicates an electronic origin to the ionization instability rather than something occurring in the detector itself. Note that the phonon recoil energy does vary with time (Figure 7.29c). This is because the recoil energy is determined based on a combination of the total phonon and ionization energy collected.

The hypothesis for the cause of the ionization instability is that it is due to the FET auto bias [144, 13]. This keeps the gate voltage at zero and has a dominant time constant on the order of 4.4 sec. In order to test this hypothesis a study was completed which watched the baseline of the ionization channels on an oscilloscope while stepping the applied bias between ground and various charge biases. Figure 7.30 shows these oscilloscope traces and reveals an exponential change occurring on the

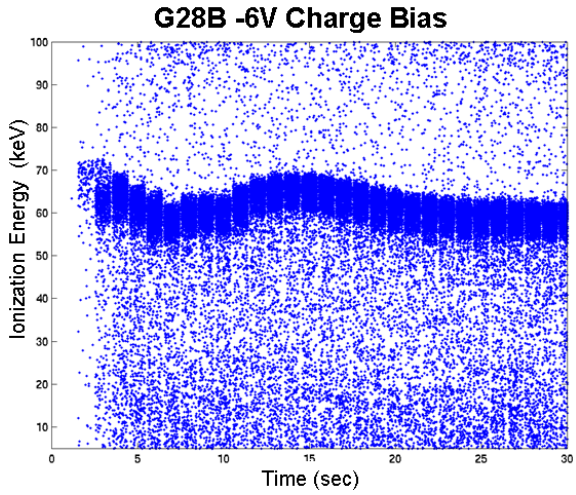

(a)

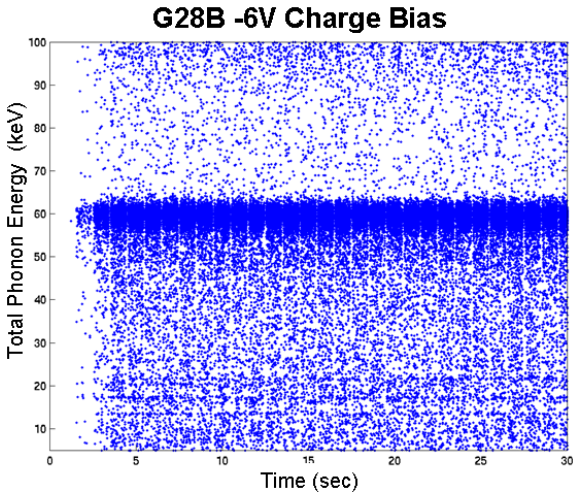

(b)

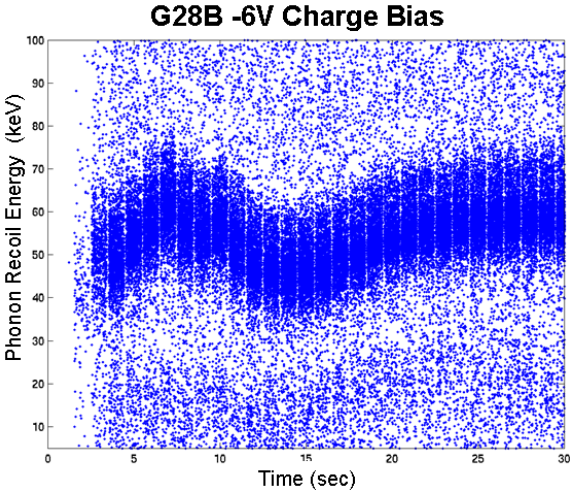

(c)

Figure 7.29: Plots of the ^{241}Am 60 keV (a) ionization energy in the inner charge electrode, (b) total phonon energy, and (c) phonon recoil energy as a function of time for 1 cm germanium detector G28B with a -6 V charge bias.

order of 20 sec when the applied charge bias changes. By comparing the sign and amplitude of the ionization channel variation when stepping the applied charge bias with different polarities and amplitudes it is observed that there is a larger variation for greater steps in the applied charge bias and that steps with opposite polarities produce variations in reverse directions.

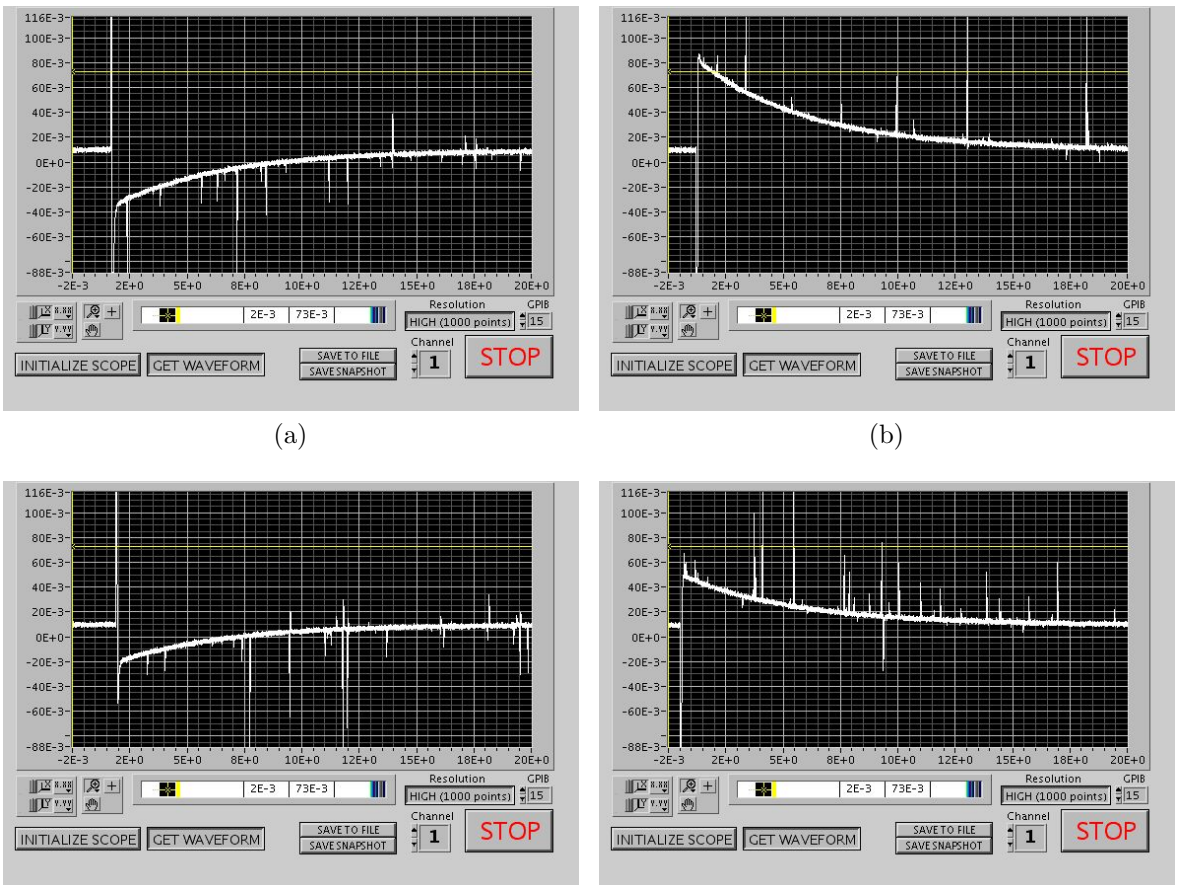

(a) (b)

(c) (d)

Figure 7.30: Oscilloscope traces of the ionization channel baseline changing when stepping the applied charge bias from ground to (a) -6 V, (b) +6 V, (c) -3 V, and (d) +3 V.

Looking at the baseline of ionization channel pulses in the G28B data at various times after stepping the applied charge bias from ground to -6 V (Figure 7.31) an exponential decrease consistent with the results from the oscilloscope traces (Figure 7.30) in seen.

It is not completely clear how the exponentially changing baseline in the ionization

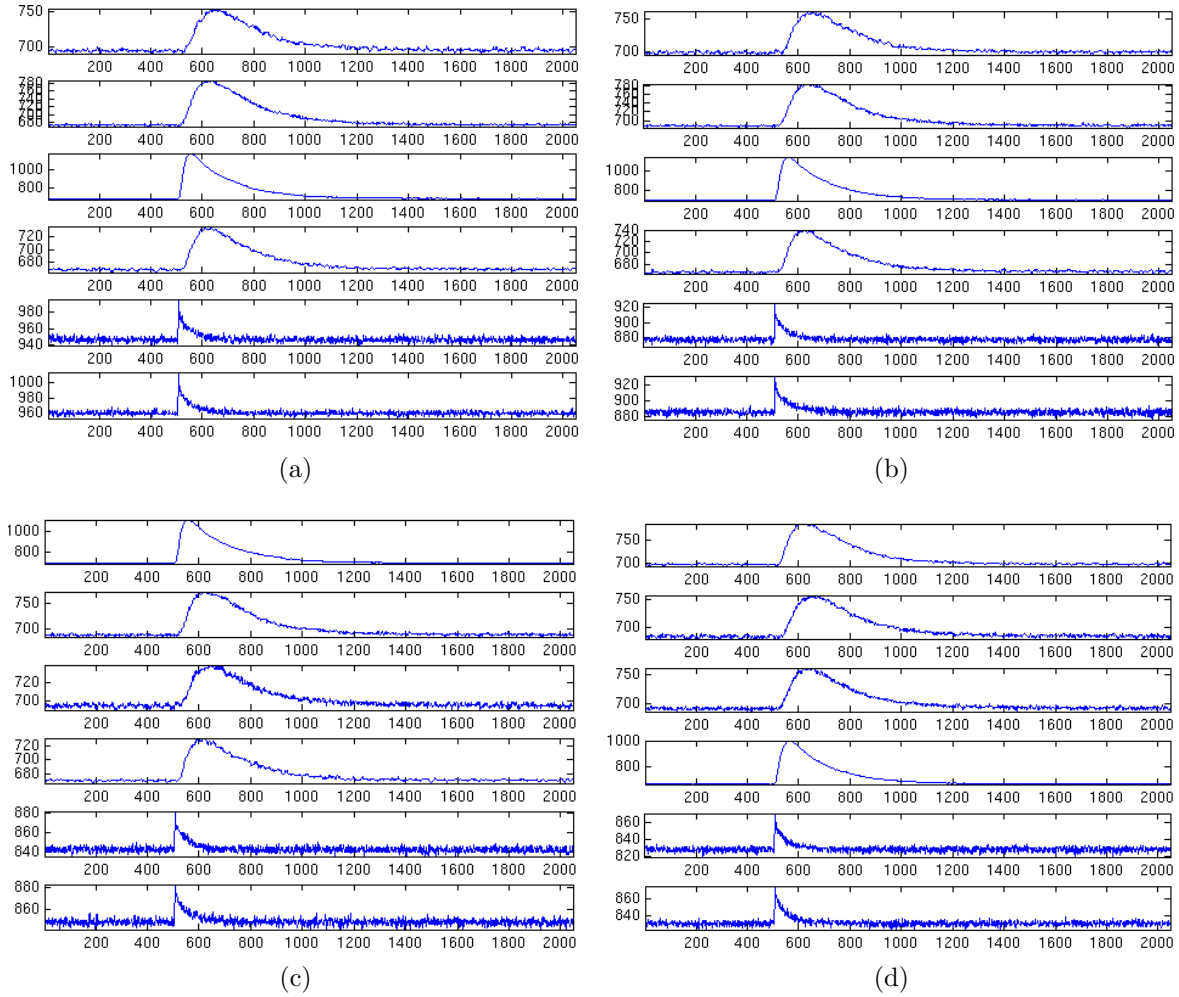

Figure 7.31: Raw traces of 60 keV pulses from G28B data of phonon channels A, B, C, and D, inner and outer ionization electrodes (from top to bottom) taken with a -6 V applied charge bias. The pulses were taken (a) 3 seconds, (b) 7 seconds, (c) 13 seconds, and (d) 25 seconds after stepping the applied charge bias from ground to -6 V.

channels causes an oscillatory instability in the ionization energy. An explanation is that the changing baseline creates a problem for the fitting algorithm in the data processing step and therefore these events have incorrect energy reconstruction.

7.4.5 N- vs. P-type Germanium

As discussed briefly in Sections 6.8 and 7.3.1, the type of impurity dominant in the germanium crystal may affect charge carrier transport through the detector and the effectiveness of background discrimination. In order to understand if the differences

between n- and p-type germanium crystals have a large impact on ionization yield discrimination of surface events, a study was carried out with the n- and p-type germanium detectors used in the Soudan 5-tower runs looking at surface events from barium calibration data [140, 145].

If the detector contacts are indeed like Schottky barriers, the semiconductor band bends near the contact to reach an equilibrium state with the metal differently for n- and p-type germanium (Figure 6.22). With pure Schottky contacts on both sides of the detector crystal, one charge carrier would preferentially be "trapped" at the surfaces (i.e., electrons for n-type crystals and holes for p-type crystals). While the Schottky barrier model of the detector contacts doesn't explain ionization and phonon side dead layer asymmetry (because switching the polarity of the applied charge bias doesn't switch the asymmetry), it does indicate that there may be some differences in the surface layer between n- and p-type germanium crystals.

The Ge detectors used in Run 123 come from three distinct Ge boules, each with different characteristics, including doping quantities and types (Table 7.2) [146]. Comparing the number of ionization and phonon side surface events for the n- and p-type germanium crystals can give some indication as to whether or not there is a significant difference in ionization yield discrimination or the ionization and phonon side asymmetry.

To compare the ionization and phonon side surface events for n- and p-type germanium detectors in the Run 123 barium calibration data, the ratio of the total number of phonon side surface events to the total number of ionization side surface events, $R_{p/i}$, was calculated for each detector. In order to compare $R_{p/i}$ for n- and p-type germanium detectors, the average ratio for determined for n- and p-type detectors. Based on this analysis, p-type germanium crystals show a larger asymmetry between phonon and ionization side ionization yield discrimination than n-type germanium. $R_{p/i}$ was 3.1 for p-type germanium detectors and 1.8 for n-type germanium detectors [140].

Detector Number	Tower 1	Tower 2	Tower 3	Tower 4	Tower 5
Z1	A n-type	Si	Si	Si	A n-type
Z2	A n-type	Si	B n-type	C p-type	C p-type
Z3	A n-type	A n-type	Si	Si	Si
Z4	Si	Si	C p-type	C p-type	B n-type
Z5	A n-type	B n-type	C p-type	C p-type	C p-type
Z6	Si	Si	B n-type	C p-type	B n-type

Table 7.2: Soudan Run 123 detectors along with the germanium crystal boule identification and doping type.

One question related to this finding is if the larger $R_{p/i}$ for p-type germanium detectors is due to a smaller number of charge side surface events or a larger number of phonon side surface events (as compared with n-type germanium detectors). This would give information as to which detector side is affected by the different doping and give insight into the behavior of band bending near the contacts.

By doing a simple average of the total number of phonon side and charge side surface events for n- and p-type detectors, it is seen that the larger $R_{p/i}$ for p-type germanium detectors is due to a larger number of phonon side events for p-type germanium as opposed to n-type germanium. The average total number of phonon side surface events in this data set was 320 for p-type and 254 for n-type germanium detectors while the average total number of ionization side surface events in this data set was 105 for p-type and 138 for n-type germanium detectors [145].

Note that one of the n-type germanium detectors seems to be an outlier with an unusually high number of both ionization and phonon side surface events as compared with other n-type germanium detectors. If this detector is removed the number of n-type and p-type germanium ionization side surface events becomes more even and the number of n-type and p-type germanium phonon side surface events become further

apart.

Besides looking at the difference between the number ionization and phonon side surface events for n- and p-type germanium detectors, it is interesting to look at the difference in ionization yield discrimination for n- and p-type detectors. The nuclear recoil band passage fraction is one estimator of this discrimination against surface events. Due to the ionization and phonon side discrimination asymmetry, the passage fraction is different for ionization and phonon side surface events. However, by individually comparing the ionization and phonon side passage fractions for n- and p-type germanium detectors, no difference is found in the ionization yield discrimination [140].

The analysis of the Run 123 barium calibration data shows that the germanium doping type appears to have an effect on the ionization and phonon side asymmetry but has no major impact on the ionization yield discrimination.

7.5 SuperCDMS Detector Design

To increase sensitivity to WIMP interactions, CDMS has proposed and begun the next phase of the experiment, SuperCDMS [147]. Generally the SuperCDMS goal is to increase the experimental target mass while maintaining a background free experiment by making proportionate reductions in the ability to reduce backgrounds. In parallel with the studies discussed in this section there have been several other modifications to the CDMS-II ZIP detectors that form the first version of SuperCDMS detectors. This section discusses this first version of the SuperCDMS detector which has been demonstrated at test facilities, fabricated, and installed in the Soudan icebox.

In order to take advantage of existing CDMS-II infrastructure and lead to cost-effective timely improvements, SuperCDMS detectors maintain a 4 phonon channel and 2 charge channel readout.

One of the three main differences between the CDMS-II and SuperCDMS ZIP detector is the latter is 1 inch thick (Figure 7.32), rather than 1 cm. By increasing the detector thickness there is more target mass per readout channel. In addition, the increased thickness improves surface event rejection by decreasing the surface to volume ratio.

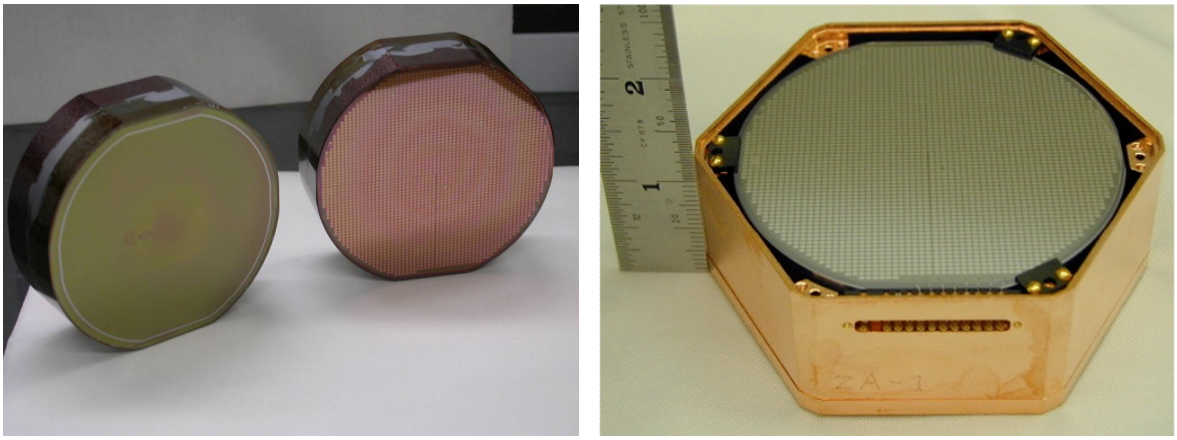

(a) (b)

Figure 7.32: (a) Photo of two 1 inch detectors showing both the ionization and phonon detector faces. (b) Photo of a 1 inch detector, with phonon detector face up, after packaging.

The second detector modification was to the phonon collection. A new mask optimized the coverage area of aluminum phonon collecting fins for maximum phonon coverage and collection efficiency (Figure 7.33). Furthermore the thin film fabrication process was changed to allow full detector patterning. This decreased the amount of passive aluminum on the phonon surface that was needed for wire bonding to connect all of the sensors together. Through these two changes, improvements were made to the phonon signal to noise by decreasing the passive aluminum and surface event discrimination by optimizing the phonon collection area and efficiency.

Finally, better radial position reconstruction has been achieved by changing the phonon sensor geometry from the quadrant design to a radial phonon sensor surrounding three internal sensors (Figure 7.34). With this improved event reconstruction, position dependent timing quantities become more powerful discrimination tools.

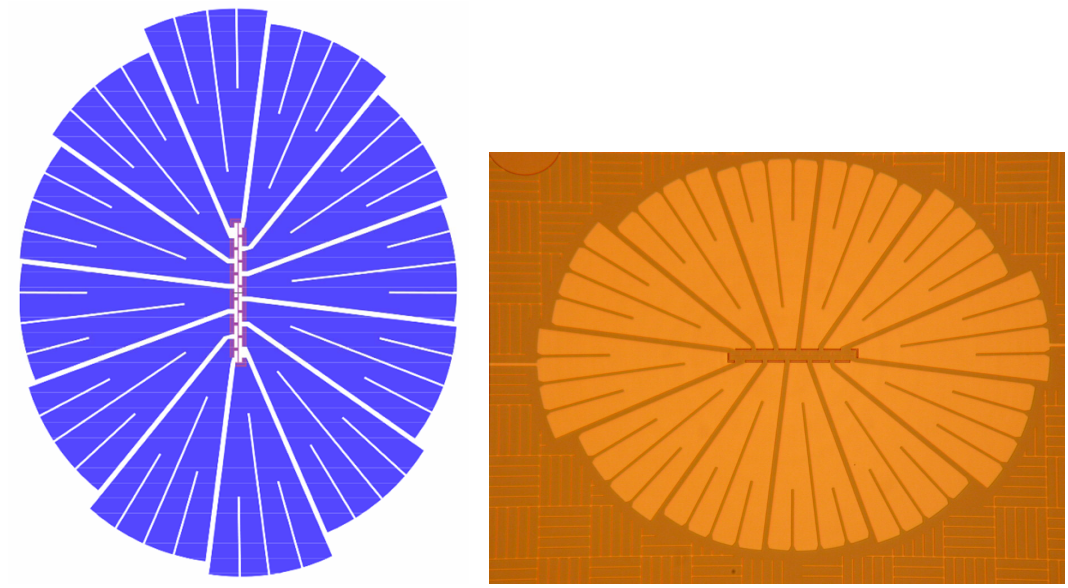

(a) (b)

Figure 7.33: (a) Drawing of the mask for the new QET design with the same amount of tungsten and greater aluminum coverage. (b) Photo of a single QET during fabrication.

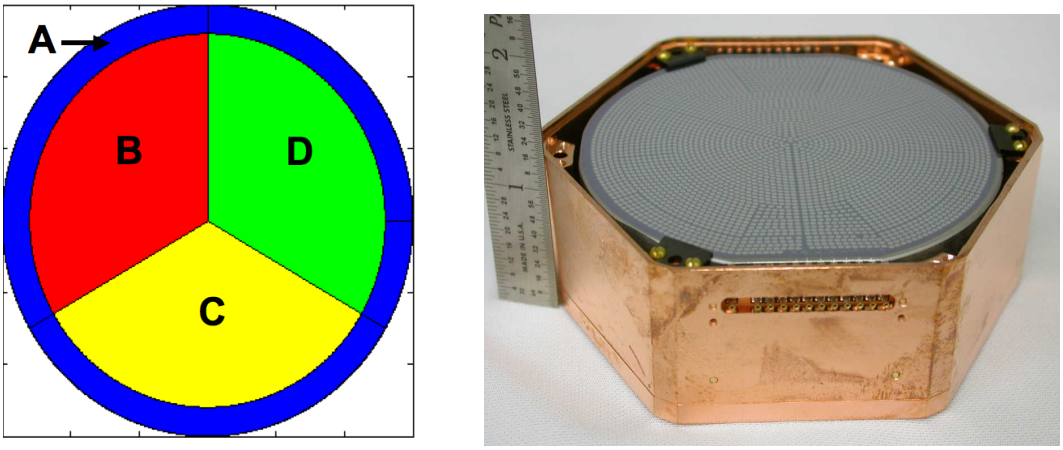

(a) (b)

Figure 7.34: (a) Schematic showing the new geometry for the four phonon sensors which allows for better radial event position reconstruction. (b) Photo of a 1 inch detector with this new phonon sensor geometry.

In April 2009 the first SuperTower was built (Figure 7.35a). It consists of five 1 inch detectors with the new QET design and phonon geometry. In addition to the 1 inch detectors, two 1 cm detectors were also included in the tower, one at the top and one at the bottom, as veto detectors. Incorporating these veto detectors in the tower causes all 1 inch detector surfaces to be "interior" surfaces (facing another detector) which have high sensitivity to low-energy multiple scatter events arising from particle interactions at the surfaces of adjacent detectors. This first SuperTower was installed in the Soudan icebox in May 2009 alongside the three newest CDMS-II towers used throughout the Soudan 5-tower runs (Figure 7.35b).

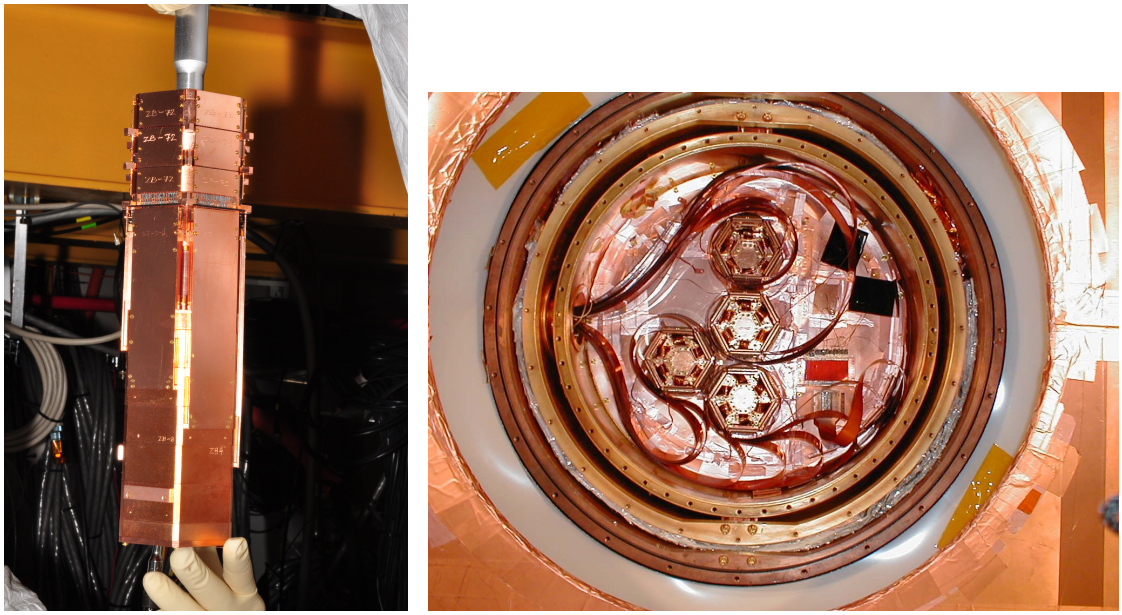

(a) (b)

Figure 7.35: (a) Photo of the first SuperTower prior to installation in the Soudan icebox. (b) Photo of the Soudan icebox with three towers of CDMS-II detectors along with the new SuperTower.

As SuperCDMS continues increasing the total target mass, additional detector modifications to streamline the fabrication and improve background discrimination are likely. Near term detector adaptations will use the results of the analysis discussed in Section 7.3 and incorporate the use of a mask during iron ion implantation to reduce damage in the germanium crystals and the ionization yield discrimination

asymmetry between the ionization and phonon side surface events. Possible detector changes that may occur in the longer term such as the interleaved ZIP design, even larger size detector crystals, and more are currently under development and testing.

Chapter 8

Conclusion

The analysis of the first two 5-tower data runs from the CDMS-II experiment has resulted in the world leading WIMP-nucleon spin-independent cross section limit for WIMP masses above $44\,\mathrm{GeV/c^2}$. This result is $\sim$3 times stronger than the previous Soudan 2-tower results. Since the completion of the first two 5-tower data runs CDMS has continued taking data with those 30 detectors at the Soudan Underground Laboratory. The total 5-tower CDMS-II data now exceeds the exposure of the first two runs by of factor of $\sim$4. Analysis of this new data is currently underway and expected to reach a sensitivity of $\sim 2\times10^{-44}\,\mathrm{cm^2}$ for WIMP masses near $60\,\mathrm{GeV/c^2}$.

The next few years will be an exciting time for the field of dark matter detection. As illustrated in Figure 5.15, direct detection is becoming a highly competitive field with many experiments using different technological approaches. The XENON10 experiment has proven the power of using liquified noble gases as the target material for WIMP interactions. Currently several noble liquid experiments are being commissioned, or under construction, which have expected sensitivities at or below $10^{-45}\,\mathrm{cm^2}$. As discussed in Section 7.5, CDMS has modified their detectors so that a single ZIP has 2.5 times more mass as well as improved phonon collection and discrimination power. The first superTower has been installed in the cryostat at the Soudan Underground Laboratory and was commissioned in June 2009. An additional two su-

perTowers are scheduled to be installed within the next year to achieve an expected sensitivity of $\sim 5\times 10^{-45}\,\mathrm{cm}^2$ by 2012.

Besides implementing the simple modifications to the CDMS-II ZIP detectors, the CDMS collaboration is engaged in research and development projects to further increase their WIMP sensitivity. Some of these projects include creating even larger radius detectors and using an interleaved ZIP design. Other areas of study include further understanding detector processes which create background events, especially electron recoil events with poor ionization collection. This dissertation focused on further understanding ionization collection in the CDMS ZIP detectors. By improving our knowledge of the fundamental physics involved with charge trapping, changes can be made to detector operation, analysis, and future designs to reduce poor ionization collection.

Finding a quantitative figure-of-merit tracing detector neutralization has already been shown to improve data quality through real-time monitoring and analysis cuts. Using this technique has led to optimizing the detector neutralization process and achieving the best possible neutralization. Understanding what affects detector neutralization (i.e., temperature, event rate, charge bias, and the level of crystal impurities or doping type) impacts operational detector settings and possibly future crystal selection.

In addition to improved understanding of detector neutralization and bulk charge trapping, examining how fabrication changes affect surface trapping can lead to improved surface event rejection. Surface event studies that compared the detector dead layers in detectors with standard processing, the addition of a hydrogenated amorphous silicon layer, and iron ion implantation indicates the best ionization yield discrimination of surface events occurs for standard processing without iron ion implantation. Based on these results, future iron ion implantation, to lower detector transition temperatures, will be done using a mask to prevent the ions from penetrating into the bare amorphous silicon and germanium layers. To understand the

improvement in ionization yield discrimination (and decreased dead layer), surface event studies will need to be completed with detectors implanted with this mask.

Regardless of which experiment 'wins the race' to become the first to detect WIMP interactions, confirmation of that signal by multiple technologies will create a more compelling case in support of the WIMP hypothesis. In addition, a direct detection signal alone will not independently measure all of the WIMP particle properties. Understanding WIMPs will be greatly enhanced by complementary signals from direction detection, indirection detection, and collider techniques, all of which have experiments on the brink of probing promising regions of parameter space.

Appendices

Appendix A

LED Neutralization Details

A.1 Introduction

As discussed in Section 6.2.1, LEDs mounted on the detector housing are able to reduce bulk trapping in the crystal by freeing charge carriers and allowing them to undergo Coulomb attraction with ionized impurity sites, thereby neutralizing the detector. This section addresses some of the details about these LEDs and how they work.

A.2 LEDs

The CDMS-II LEDs are from Photonic Detectors, Inc (SMT Type PDI-E940SM). These LEDs are made of Galium Arsenide (GaAs), have a peak wavelength of 940 nm, and a 140 degree radiating pattern out of the cathode face. They are mounted, facing upwards, on the phonon side of the detector housing (Figure 6.1). There are two separate positions with 2 LEDs installed, however only 1 of the LEDs in each position is wired; the other acts as a spare. In the 1 inch detector housings, the LEDs are again mounted facing upwards in two LED positions, one each the phonon and ionization side of the detector housing.

A.3 LED Circuit

Each LED is connected to the Front End Board (FEB) warm electronics board through the tower wiring, SQUET, and stripline traces. In addition, each LED is grounded to the chassis so that one stripline per LED is sufficient to create a complete circuit. The CDMS-II LED forward voltage drop ranges between 10 and 13 V for each LED at 30 mK and is 1 V at room temperature.

The LED is driven by a current source located on the FEB. This source is able to supply currents between -5 mA and +5 mA is 2.5 μA steps. It is able to supply this current in a DC or burst mode for a given time. Pulses can vary between 10 μs and 2.56 ms in 10 μs steps.

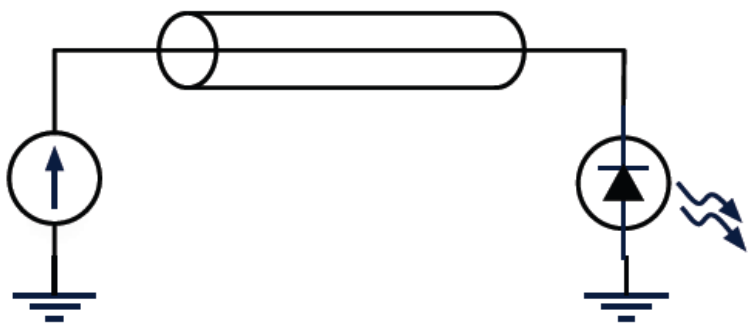

Figure A.1: Schematic of the LED drive circuit with the current source, stripline, and LED diode.

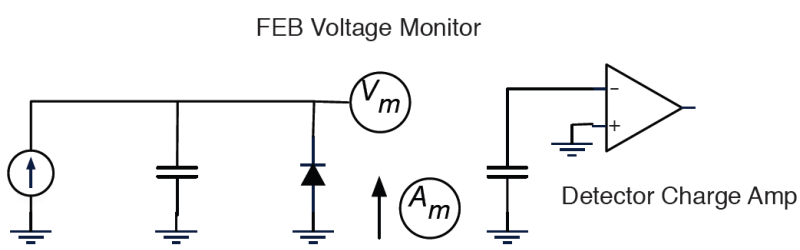

Figure A.2: Schematic of the LED drive equivalent circuit showing the current source, stripline capacitance, and LED diode in parallel.

Due to the LED drive circuit (Figures A.1 and A.2), the current supplied by the source initially charges the stripline capacitance until the voltage reaches the forward

drop of the LED [148]. Therefore, the time it takes to charge the stripline capacitance to the forward drop of the LED can be calculated using the following formula:

$$\tau = C \times V/I \tag{A.1}$$

where τ is the stripline charging time constant, C the stripline capacitance, V the LED's forward voltage drop, and I the applied bias current.

The stripline capacitance was measured at the UC Berkeley test facility to be 700 pF. Assuming a LED bias current of 800 μA and a forward drop of 10 V, the stripline charging time should be approximately 9 μs.

The FEB warm electronics board has a test point on its front panel which can be used to measure the voltage across the LED. A sample of this FEB front panel voltage monitor trace, taken at the Case Western test facility with a LED bias current of 950 μA, can be seen in Figure 6.3.

This FEB front panel voltage monitor trace plots the voltage across the LED as a function of time. The drive current source first turns on at "T_{on}" when the voltage changes from zero. Between "T_{on}" and "T_{max}," the time when the voltage is at its maximum amplitude, the change in voltage is approximately linear. This is when the drive source is charging the stripline capacitance until it equals the forward drop of the LED. Near "T_{max}," the LED is able to "turn-on" and begin emitting photons. Shortly after "T_{max}," the voltage decreases in amplitude and then nearly plateaus. The plateau occurs at a lower absolute voltage than maximum because as the LED emits photons it warms up and the LED I-V characteristics change with temperature. The change in voltage occurs as the LED switches to a different I-V curve (Figure A.3) [148].

By measuring the FEB front panel voltage monitor trace, the stripline charging time can be determined and compared with the calculation. Looking at the above trace, the stripline charging time, the time difference between "T_{on}" and "T_{max}" is approximately 3 times the calculated time [122]. After further tests and capacitance

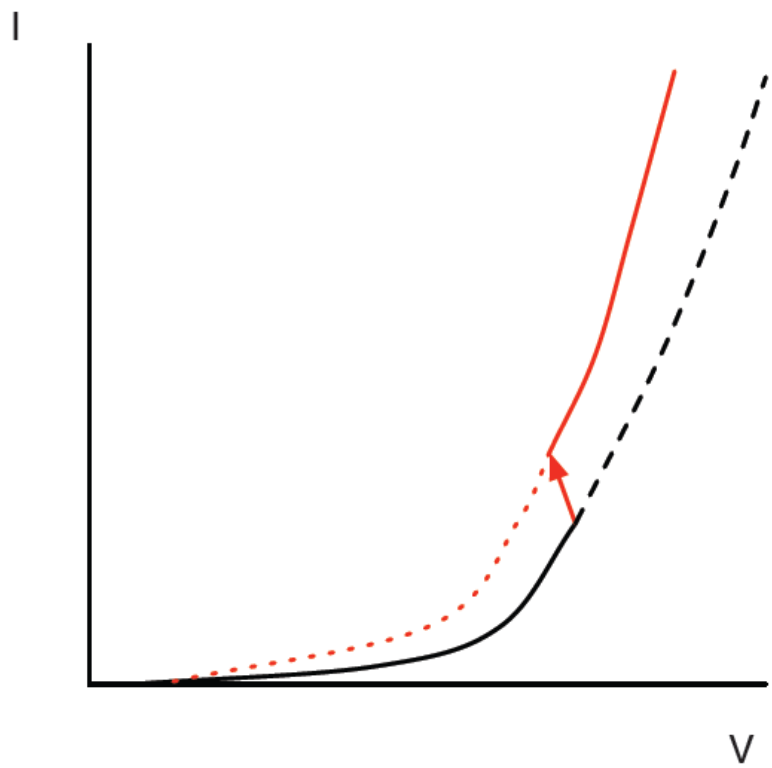

Figure A.3: Illustration of a LED's current vs. voltage curve. The black and red curves represent profiles for different temperatures. As the LED emits photons and warms it changes between these two curves.

measurements, it was discovered at the UC Berkeley test facility that there is an additional source of capacitance, between 1.5 - 2.4 nF, in parallel with the 700 pF stripline capacitance, due to one of the operational amplifiers in the FEB current source circuit [149]. Taking this additional capacitance into account, the capacitance charging time is then calculated to be approximately 28 μs, for a 800 μA LED bias current, which is consistent with the measurements using the FEB font panel voltage monitor.

Note that the forward voltage drops of the LEDs can vary by a few volts. This changes the time to turn on the LEDs by as much as about 30%. In order to minimize the heat load, especially on the Soudan fridge, it is important to characterize each individual LED prior to determining the settings appropriate for it. Studies done with the Soudan detectors prior to Run 127 (discussed in Appendix B and summarized in

Section 6.4.1) show that by the time the LED voltage monitor trace is at its maximum amplitude the LEDs are causing detector neutralization.

A.4 Non-working LEDs

Besides providing a means to determine appropriate LED settings for detector neutralization, the FEB front panel voltage monitor trace can also be used to identify LEDs that are not working or which are being biased with the wrong polarity. The signature of a LED that is not working is that the voltage monitor trace shows a linear slope as the stripline capacitance charges and then flat lines at a voltage that is usually significantly lower than 10 V before returning to 0 V when the LED bias current turns off (Figure A.4).

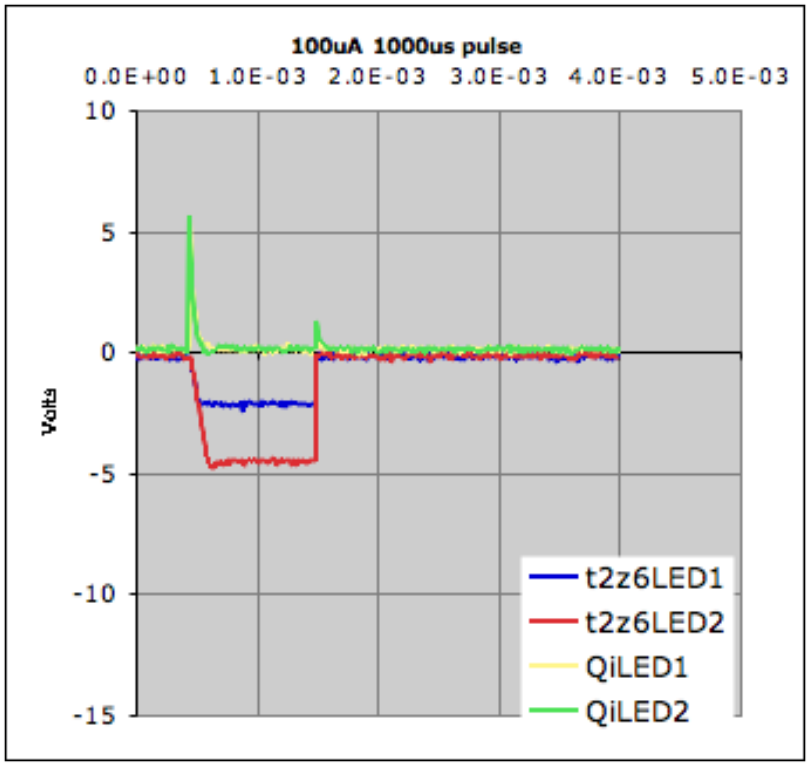

Figure A.4: Oscilloscope trace showing voltage as a function of time for the FEB front panel voltage monitor trace showing the voltage through the LEDs (blue and red) and the charge pulse due to the LED pulses (yellow and green) for two non-working LEDs.

Note that if a LED is not being biased long enough to produce photons the voltage

monitor traces will show a linear slope as the stripline capacitance charges and then abruptly drop back to 0 V when the LED bias current turns off (Figure A.5). There will be no plateau or flat line in the voltage trace.

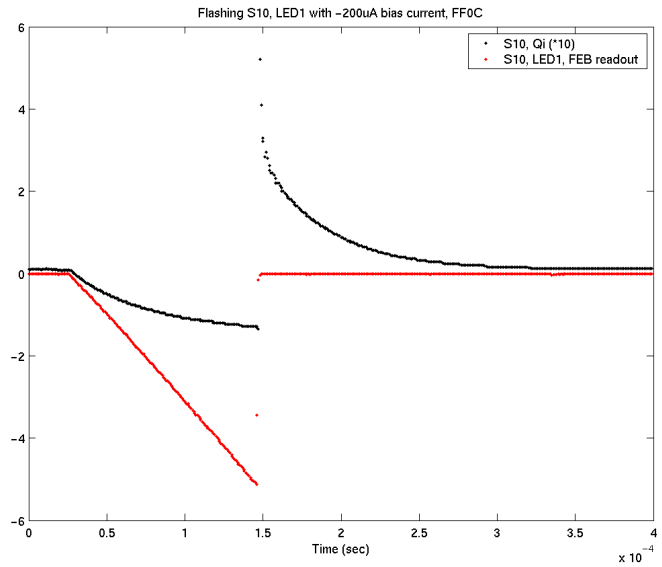

Figure A.5: Oscilloscope trace showing voltage as a function of time for the FEB front panel voltage monitor trace showing the voltage through a LED (red) and the charge pulse due to the LED pulse (black) for a working LED with a pulse that was not sufficiently long to produce photons.

Appendix B

Soudan LED Tests

B.1 Introduction

At the beginning of many of the Soudan 5-tower runs, the initial detector neutralization was performed very systematically in order to study the effectiveness of different neutralization techniques. One of the more intensive of these studies was performed at the beginning of Run 127 [125] in order to determine which LED properties provide effective neutralization. Specifically, studies determined what feature in the FEB front panel voltage monitor trace corresponds to effective neutralization so that the LED heat load can be minimized and if LEDs neutralize adjacent detectors. This section discusses the details of how the test was performed. Test results are discussed in Section 6.4.1.

B.2 Run 127 LED tests

In order to achieve these goals, only six detectors were used, one in each tower except for Tower 4 where two detectors were used, so that there would be greater control throughout the study and so that adjacent detector neutralization could be studied without confusion as to which LED was responsible for neutralization. These six

detectors underwent a series of 6 LED bakes, each with the same bias current, 400 μA, but with varying LED pulse on times. The times were chosen after looking at the FEB front panel voltage traces for each of the LEDs and determining the time so that the pulse would be turned off at (Table B.1).

LEDbake #	location on FEB front panel voltage trace
1	80% of the maximum amplitude
2	90% of the maximum amplitude
3	maximum amplitude
4	maximum amplitude + 5 μs (LED settings used for all Soudan 5-tower runs, starting with Run 124)
5	maximum amplitude + 10 μs
6	equivalent to Run 123 settings (120 μs)

Table B.1: Individual LED bakes taken during the Soudan 5-tower study

The LED test bake procedure followed was:

- Use only six detectors (Table B.2)

Detector	detector above	detector below
T1Z2	Ge	Ge
T2Z4	Si	Ge
T3Z3	Si	Ge
T4Z2	Ge	Si
T4Z5	Ge	Ge
T5Z5	Ge	Ge

Table B.2: Detectors used during the Soudan 5-tower study

- LED bias current = -400 μA (400 μA in Soudan guis, the same as the settings used since Run 124)
- LED on times to use (for each successive LED bake) can be seen in Table B.3
- Each LED bake lasts 20-30 minutes
- Use nominal LED pulse on/off times (0.8 min on, 1.2 min off)

- Each (weak) barium dataset (with all 30 detectors) should last 300k events, 1 hr (with LED baking after barium disabled)

LED bake #	T1Z2 LED2	T2Z4 LED2	T3Z3 LED1	T4Z2 LED2	T4Z5 LED2	T5Z5 LED2
1	60 μs on 2550 μs off	60 μs on 2550 μs off	50 μs on 2550 μs off	60 μs on 2550 μs off	60 μs on 2550 μs off	70 μs on 2550 μs off
2	70 μs on 2550 μs off	70 μs on 2550 μs off	60 μs on 2550 μs off	70 μs on 2550 μs off	70 μs on 2550 μs off	80 μs on 2550 μs off
3	100 μs on 2550 μs off	90 μs on 2550 μs off	80 μs on 2550 μs off	90 μs on 2550 μs off	90 μs on 2550 μs off	100 μs on 2550 μs off
4	100 μs on 2550 μs off	100 μs on 2550 μs off	90 μs on 2550 μs off	100 μs on 2550 μs off	100 μs on 2550 μs off	100 μs on 2550 μs off
5	110 μs on 2550 μs off	100 μs on 2550 μs off	90 μs on 2550 μs off	100 μs on 2550 μs off	100 μs on 2550 μs off	110 μs on 2550 μs off
6	120 μs on 2550 μs off	120 μs on 2550 μs off	120 μs on 2550 μs off	120 μs on 2550 μs off	120 μs on 2550 μs off	120 μs on 2550 μs off

Table B.3: LED on times used for each bake (note that the LED pulse step size is 10 μA)

The maximum fridge temperatures were recorded for each of the LED bakes and are documented in Table B.4. Note that these temperatures are measured by a LR700 resistance bridge which cycles through several different thermometers, reading each for 1 minute. Therefore the temperature measurements were made coarsely in time. In addition, during the LED bake, the LEDs are pulsed in a 2 minute cycle. Due to both the LED pulse and LR700 measurement cycles, it is possible for the LR700 temperature measurements to read an artificially low maximum temperature.

LED bake #	MC peak temp	T5 10 mK peak temp
1	no change	no change
2	not measured	0.05 K
3	not measured	0.20 K
4	0.06 K	0.20 K
5	0.03 K	0.16 K
6	0.08 K	0.35 K

Table B.4: Maximum mixing chamber and Tower 5 temperature during each LED bake

Appendix C

Neutralization Methods

C.1 Introduction

There are several methods that can be used to neutralize the CDMS detectors. These different methods often are particularly well suited for a specific location and circumstance. This section explains the implementations of the various neutralization methods.

C.2 Soudan Neutralization Methods

During the Soudan 5-tower runs (Runs 123 through 129), detector neutralization was achieved through a combination of LED and strong source bakes and maintained through LED flashes. Below describes when each of these bakes and flashes were used and how they were implemented.

C.2.1 Strong Source Bake

During the Soudan 5-tower runs, strong source bakes were used only at the beginning of a run in order to achieve initial detector neutralization. The first time this technique was used during CDMS-II at Soudan was at the end of Run 124 and beginning

of Run 125.

At Soudan, a strong source bake typically lasted overnight and consisted of the following procedure:

- Initialize detector settings and ground the charge channels
- Insert the strong Cesium and Cobalt sources into the two source tubes
- Leave the sources shining on the detectors overnight
- Remove the sources from the source tubes

As discussed in Section 6.2.2, it was found that the neutralization states of detectors from the Germanium B Boule worsened after a strong source bake. For this reason, it is important to perform an LED bake immediately following a strong source bake. This causes the neutralization states of the Boule B Germanium detectors to become good again.

C.2.2 LED bake

During the Soudan 5-tower runs, LED bakes were typically performed at the beginning of a run in order to achieve initial detector neutralization or after an anomalous event that might affect the detector neutralization states.

During a LED bake, there is one LED used for each detector (except for detectors which have no working LEDs and then no LEDs are used). The LEDs for all the detectors in a single tower are pulsed together and each tower is baked sequentially. The total amount of time each tower is baked has varied slightly, but typically it lasts for 45 minutes each.

For the first Soudan 5-tower run (Run 123), the important LED parameters were:

- LED bias current (amplitude) = 800 μA

- LED pulse train duration = 0.8 minutes with a 1.2 minute pause between pulse trains
- LED pulse duty cycles = 60 μs ON, 2550 μs OFF

Between Run 123 and 124 there was an evaluation of all 60 LEDs mounted on the detectors. After this evaluation, the LED parameters were modified, for Run 124 and all the subsequent Soudan 5-tower runs, to:

- LED bias current (amplitude) = 400 μA
- LED pulse train duration = 0.8 minutes with a 1.2 minute pause between pulse trains
- LED pulse duty cycles ON times vary per LED (usually between 90 - 110 μs so that the LED is on for 5 μs past the peak of the FEB front panel voltage monitor trace), with 2550 μs OFF times

During an LED bake, the Tower 5 base temperature does not exceed 200 mK. After pulsing all the LEDs, there is a cool down period of approximately 15 minutes for the detectors to return to base temperature. This entire process lasts a little more than 5 hours.

C.2.3 LED flash

During the Soudan 5-tower runs, LED flashes were typically performed during the daily cryogen transfers, after approximately 11 hours of WIMP search data taking, and after every barium calibration dataset lasting more than 30 minutes.

A LED flash is very similar to a LED bake, except for the total time for which the LEDs are pulsed in each tower. The Tower 1 LEDs are pulsed for a total duration of 10 seconds, Tower 2 for 4 seconds, Tower 3 for 6 seconds, Tower 4 for 4 seconds, and Tower 5 for 4 seconds. As in the LED bake, the LEDs for each detector in a

single tower are pulsed together and each tower is flashed sequentially. The LED flash parameters are the same as documented above for the LED bakes, including the difference between Run 123 and Run 124. However, the main item to note is that the LED pulse train is not used because the total time of the LED flash is shorter than the pulse train.

During an LED flash, the Tower 5 base temperature does not exceed 200 mK. After pulsing all the LEDs, there is a cool down period of approximately 15 minutes for the detectors to return to base temperature. This entire process lasts about 25 minutes.

C.3 Test Facility Neutralization Methods

The neutralization methods used at test facilities have been varied. Part of this is due to the fact that neutralization is much easier to achieve at a surface facility than underground. Appendix F outlines the basic procedure that should be used to ensure good detector neutralization. This section describes some of the techniques that have been used and the Case Western Reserve University and University of California - Berkeley surface test facilities.

As is the case for detectors underground at Soudan, it is important to ensure detectors at the surface test facilities are effectively neutralized prior to taking data and maintain stable neutralization during data taking. Since the surface environment and test facility set-up is much different than that underground owing to the different ambient background rates, the techniques used can be slightly different. At test facilities, both initial detector neutralization and detector neutralization stability are usually achieved through a combination of ambient background radiation and LED baking.

The ambient background radiation at the surface is able to neutralize a grounded detector. While this makes some neutralization studies at surface test facilities very difficult, it makes detector neutralization easier. If a detector's charge channels are

grounded while cooling down from room temperature, the ambient background radiation begins the neutralization process. The main item to think about to ensure this early detector neutralization is how the detector is grounded. In order to ground a detector through the Front End Board (FEB) electronics board, the detector I/O cable must be connected and the FEB power must be one. At a test facility, the detector can be grounded in this standard way, however there are times when this may be impossible or inconvenient, especially during cool-down. Fortunately, the detector can be grounded through other methods. One such method, used at the Case Western test facility, is to modify a spare connector with two jumpers connecting the inner and outer charge biases to phonon returns. This modified connector is then connected to the end of the detector I/O cable maintaining zero electric field across the detector and allowing the ambient background radiation to neutralize it. Another method of grounding a detector is used at the Berkeley test facility. There the detector I/O cable is pulled into the breakout box and the charge channels are then grounded through there.

LEDs are also used in order to neutralize a detector once it reaches base temperature. Since, at a test facility, there is usually one detector to neutralize at a time, the LED heat load on the fridge is not nearly as big a concern as at Soudan. For this reason the LED parameters and bake times are different, and much longer, than those used underground. A typical LED bake at the Case Western test facility would use one of the two LEDs with a LED bias current (amplitude) = 800 μA and LED pulse duty cycle of between 90 - 250 μs ON, 2550 μs OFF, for a total time of approximately 10 hours. Typically two or three of these LED bakes would occur, if possible at least one with each LED, prior to data taking.

Since test facility data taking always has a higher event rate than underground WIMP search data due to the ambient background and calibration sources, data collection must be interrupted much more frequently than underground. Typically, in order to ensure stable neutralization during data collection, data taking is paused

approximately every 4 minutes for neutralization. Note that this time can be different depending on the detector as well as the type and location of the calibration sources. In order to ensure stable neutralization, one could take a long dataset without stopping to neutralize in order to see how long the detector maintains stable charge collection and then use that dataset to determine the optimal interval for data collection.

When maintaining neutralization during a run at a test facility, the data collection is paused, not stopped, for a neutralization period. During datasets, the detector can maintain neutralization either by the ambient background radiation or through a brief LED flash. The Case Western test facility typically uses the ambient background radiation while the Berkeley test facility typically uses the LEDs. A typical dataset taken at the Case Western test facility will bias the detector for between 4 and 12 minutes, ground the detector for 3 minutes to allow neutralization by the ambient background radiation, and then repeat the cycle for several hours (depending on the statistics required from the dataset). A typical dataset taken at the Berkeley test facility will bias the detector for 4 minutes, ground the detector for 3 minutes and do a short LED flash, and then repeat the cycle for several hours (again depending on the required statistics).

Appendix D

Five-Tower Run Neutralization Summary

D.1 Introduction

During the seven 5-tower runs that took place at Soudan between mid 2006 and early 2009 (Runs 123 - 129), the initial detector neutralization was accomplished using a variety of techniques. Many times a particular neutralization procedure was used in order to learn about the effectiveness of a neutralization method or setting and to learn about how neutralization changes. This section summarizes the neutralization strategy used at the beginning of each run. In addition, information about the maximum temperature reached between runs is included to help understand differences in detector neutralization states for different runs and motivate some of the neutralization studies that were performed.

D.2 Run 123

At the beginning of Run 123, the first 5-tower Soudan run, the detectors were cooled down from room temperature and all neutralization was done at base temperature

with LED baking.

Run 123 ended due to increased circulation pressures. In order to remove the circulation blockage, located in the dilution refrigerator's snow trap (internal helium cold trap), the fridge was warmed to a maximum Tower 5 base stage temperature of approximately 9.5 K (on March 30, 2007). The blockage was then removed by back flushing the circulation loop.

D.3 Run 124

At the beginning of Run 124, the detectors were cooled from a maximum Tower 5 base stage temperature of approximately 9.5 K and all neutralization was done at base temperature with LED baking.

Between Runs 123 and 124 there was a survey done documenting the FEB front panel voltage monitor trace (Figure 6.3) for every LED. This led to changing the LED parameters prior to Run 124. Section C.2.2 details the LED settings used in Run 123 as well as in Run 124 and the rest of the Soudan 5-tower runs. The LED tests detailed in Appendix B and whose results are described in Section 6.4.1 showed that the new LED settings effectively neutralize the detectors.

At the end of Run 124, detector neutralization using strong sources was first used during CDMS-II at Soudan. The effectiveness of strong source neutralization, especially on detectors with non-working LEDs, caused this method to be used alongside LED baking to neutralize detectors at the beginning of many of the Soudan 5-tower runs after these initial tests.

Run 124 ended due to increased circulation pressures. The circulation blockage, located in the snow trap, was once again removed by back flushing the circulation loop. During this warm-up, the fridge warmed to a maximum Tower 5 base stage temperature of approximately 8 K (on July 16, 2007).

D.4 Run 125

At the beginning of Run 125, the detectors were cooled from a maximum Tower 5 base stage temperature of approximately 8 K and neutralization was done through a combination of strong source and LED bakes beginning during the cool down and continuing after reaching base temperature.

Run 125 ended due to degraded detector performance. The degraded detector performance was initially identified by an increased phonon trigger rate. In addition, affected detectors had a large number of events with zero ionization collection and degraded phonon amplitudes. The cause of this degraded performance was hypothesized to be due to helium films on the detectors where the helium was introduced into the system via the e-box leak. In order to improve detector performance, the fridge was warmed up to a maximum Tower 5 base stage temperature of approximately 43 K (on January 10, 2008), while the e-box was pumped on in order to remove any built up gas.

D.5 Run 126

At the beginning of Run 126, the detectors were cooled from a maximum Tower 5 base stage temperature of approximately 43 K and all neutralization was done at base temperature with a combination of strong source and LED baking.

Run 126 ended due to increased circulation pressures. The circulation blockage, located in the snow trap, was once again removed by back flushing the circulation loop. During this warm-up, the fridge warmed to a maximum Tower 5 base stage temperature of approximately 72 K (on May 1, 2008). In addition to removing the circulation blockage, the e-box was also pumped on in order to remove any gas that may have built up.

D.6 Run 127

At the beginning of Run 127, the detectors were cooled from a maximum Tower 5 base stage temperature of approximately 72 K and all neutralization was done at base temperature with a combination of strong source and LED baking.

Run 127 ended due to degraded detector performance. Similar to the end of Run 125, the degraded detector performance was initially identified by an increased phonon trigger rate. Once again, affected detectors had a large number of events with zero ionization collection. However, degraded phonon amplitudes were not seen this time. Although, once a detector exhibited signs of degraded performance, its phonon trigger was turned off, so there may not have been data taken with the detectors for a long enough period of time in order to see the phonon amplitudes affected. The cause of this degraded performance was once again hypothesized to be due to helium films on the detectors where the helium was introduced into the system via the e-box leak. In order to improve detector performance, the fridge was warmed up to a maximum Tower 5 base stage temperature of approximately 67 K (on January 10, 2008), while the e-box was pumped on in order to remove any built up gas. In addition, there was a back flush of the circulation loop to remove any excess gas built up in the snow trap.

D.7 Run 128

At the beginning of Run 128, the detectors were cooled from a maximum Tower 5 base stage temperature of approximately 67 K. Neutralization began during the cool down with a combination of strong source and LED baking and continued after reaching base temperature.

Run 128 ended in order to warm to room temperature to perform cryocooler maintenance and install the new e-box.

D.8 Run 129

At the beginning of Run 129, the detectors were cooled down from room temperature and all neutralization was done at base temperature with a combination of strong source and LED baking.

Run 129 ended in order to warm to room temperature to remove Towers 1 and 2 and install SuperTower 1.

Appendix E

Soudan Neutralization Procedure

At Soudan, because it is an underground facility, the recommended neutralization procedure based on work performed for this thesis is:

1. Keep detectors grounded while cooling down the fridge. This requires the detector I/O cables to be connected from the electronics box, e-box, to the front end boards, FEBs, and the FEB power to be ON

2. Insert strong sources in the source tubes. (Optional, especially if there are special test datasets that are to be taken once at base temperature looking at the detector states prior to any neutralization)

3. Once at base temperature, take a barium or gamma calibration dataset in order to evaluate the neutralization states of the detectors

4. Do an LED bake for all detectors, subsequently baking one tower of detectors at a time. (This should be sufficient to neutralize most germanium detectors)

5. Take a barium or gamma calibration dataset in order to evaluate the neutralization states of the detectors

6. Overnight, perform a strong source bake of the detectors by grounding all ionization channels and inserting strong sources in the source tubes

7. In the morning, remove the strong sources from the source tubes and do an LED bake for all detectors. (This improves the neutralization state for detectors the strong source bake worsens)

8. Take a barium or gamma calibration dataset in order to evaluate the neutralization states of the detectors

9. During the day, target detectors that are difficult to neutralize, particularly silicon detectors, and do longer LED bakes using only the LEDs on the problem detectors. (this can be done using the LED bake gui)

10. Take a barium or gamma calibration dataset in order to evaluate the neutralization states of the detectors

11. Repeat steps 4 through 10 as needed until acceptable levels of neutralization are achieved in the detectors

Appendix F

Test Facility Neutralization Procedure

The ideal test facility neutralization procedure is similar to that for an underground site in that they should both use a combination of neutralization methods. However, the test facility and underground site procedures differ for several reasons. At a test facility the ambient background is orders of magnitude higher than underground owing to cosmic rays, shielding, and the use of low background materials. When a detector is grounded, this ambient background acts to neutralize the detector, much as the strong sources do underground. While the ambient background helps neutralize detectors, it also makes it difficult to do some neutralization studies, especially those looking at the on-set of and subtle changes in neutralization. In addition to having a high ambient background, test facilities often only take data with one or two detectors at a time. This means that there are fewer total detectors to neutralize at a given time and a lower heat load on the fridge due to individual LEDs during baking. LED bakes at test facilities fridges can typically run at a higher duty cycle and for longer periods of time than at the Soudan fridge.

At surface test facilities the recommended neutralization procedure is:

1. Keep detectors grounded while cooling down the fridge. This requires the detector I/O cables to be connected from the fridge bulkhead to the front end

boards, FEBs, and the FEB power to be ON. If the detector is not connected a powered on FEB, it can be grounded by creating jumpers between the charge biases and QET returns.

2. Once at base temperature, evaluate all LEDs to ensure proper functionality and determine appropriate LED bias currents and on times. To ensure proper functionality, first look at the electrical check-outs. Next, take oscilloscope traces of the FEB front panel LED voltage monitor output for each LED and several bias current / on times. These traces and appropriate bias conditions were discussed above. During a bake, the tower temperature should not need to exceed 400 - 500 mK.

3. When not taking data, make sure to keep the detector grounded.

4. Prior to data taking with a particular detector, do an overnight, 8-12 hour, LED bake of that detector.

5. When not taking data, make sure to keep the detector grounded.

6. Repeat steps 4 and 5 with both LEDs, especially for the 1 inch detectors which have LED1 on the phonon side and LED2 on the ionization side.

Appendix G

Calculating the Detector Dead Layer

G.1 Introduction

This section outlines the procedure used to calculate the detector dead layer for the analyses discussed in Section 7.3.1. A similar analysis was used previously to calculate the dead layer for sample devices [69, 70] and early CDMS-II detectors.

G.2 Procedure

The analysis procedure to calculate the detector dead layer is as follows:

1. Start with the ionization spectrum collected from ^{241}Am 60 keV gamma rays (or another line with a given energy). Apply all data quality cuts and identify events from each individual source. Select the 60 keV events by phonon energy. Figure 7.22a shows an example of the data this analysis begins with. This data will be used as the example throughout and is from the 1 inch Germanium detector G3D. The data was taken with -3 V charge bias and four ^{241}Am sources, two on the ionization side (channels A, cyan, and C, magenta) and two on the phonon detector face (channels B, blue, and D, green). Recall that half of G3D's ionization face was iron ion implanted (under channels C, magenta,

and D, green) in order to test if that affected the ionization yield asymmetry (Section 7.3.2).

2. Fit the 60 keV photo peak with a gaussian distribution.

3. Calculate the residuals (the gaussian fit subtracted from the data) and replace the counts from the gaussian fit as a step function at the mean value (as determined from the fit). Figure G.1 shows the residuals for the G3D -3 V charge bias data.

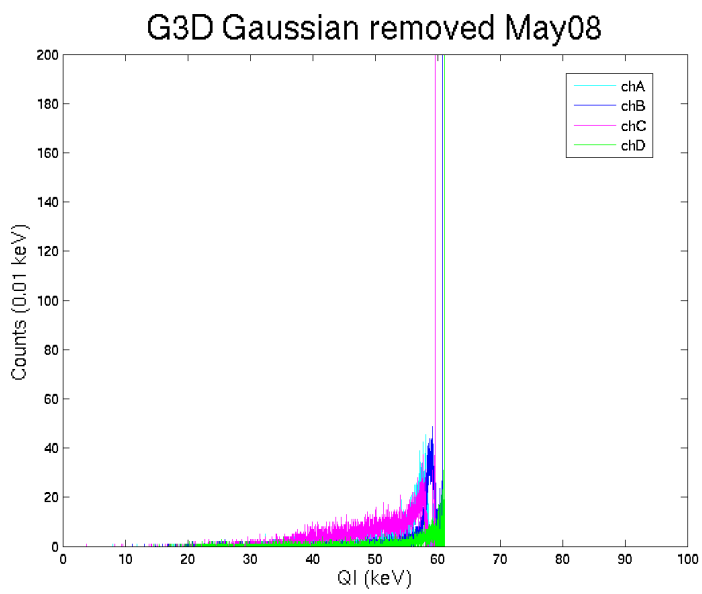

Figure G.1: G3D -3 V residuals between the data and gaussian fit of the ^{241}Am 60 keV line.

4. Create a Cumulative Distribution Function (CDF) of the residual + step function plot.

5. Determine the event number distribution as a function of depth in the detector as calculated by theory based on the 60 keV 909 μm penetration depth into Germanium.

6. Assuming that events with poorly collected ionization energy are due to surface trapping and are related to the number distribution as a function of depth in

the detector, do a one-to-one mapping between the CDF created by the data (in step 4) and the CDF created by the theory (discussed in step 5) in order to plot the fractional ionization collection as a function of depth. Figure G.2 plots the partial ionization collection of 60 keV ^{241}Am gamma rays as a function of depth into the Germanium crystal, or the dead layer distribution, for the G3D -3 V charge bias data.

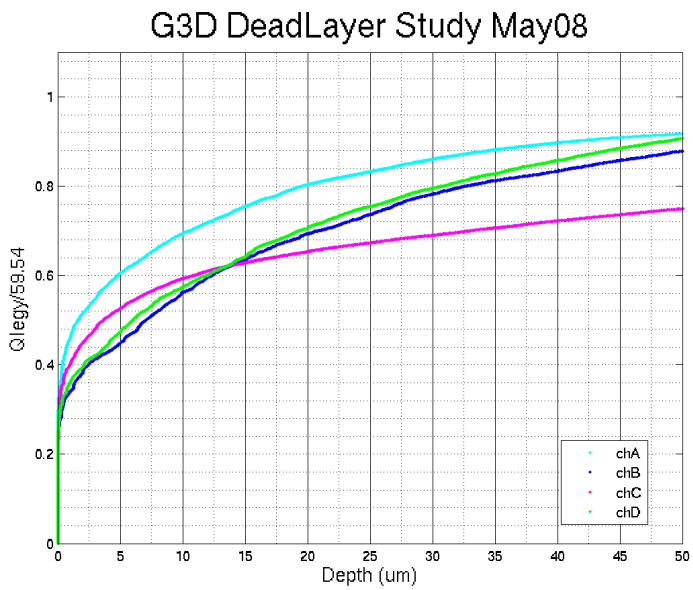

Figure G.2: Dead layer distribution for G3D -3 V charge bias data. This plot shows the partial ionization collection of 60 keV ^{241}Am gamma rays as a function of depth into the Germanium crystal.

7. Determine the dead layer, defined to be the depth at which the partial ionization collection is 63%. Table G.1 gives the ionization and phonon side dead layer for G3D with -3 V charge bias based on this analysis.

Phonon Channel Source is Over	Source Side	Dead Layer
ch A	ionization side	6.3 μm
ch B	phonon side	14 μm
ch C	ionization side (ion-implanted)	15 μm
ch D	phonon side	14 μm

Table G.1: G3D -3 V data dead layer based on the 60 keV gamma-rays for each ^{241}Am source, measured at the 63% level of the dead layer distribution.

Bibliography

[1] K.G. Begeman, A.H. Broeils, and R.H. Sanders. Extended rotation curves of spiral galaxies: dark haloes and modified dynamics. *Monthly Notices of the Royal Astronomical Society*, 249(523), 1991. [cited at p. vi, 3, 4]

[2] D. Clowe et al. A direct empirical proof of the existence of dark matter. *The Astrophysical Journal*, 648:L109–L113, 2006. [cited at p. vi, 7]

[3] M.R. Nolta et al. Five-year wilkinson microwave anisotropy probe (wmap) observations: Angular power spectra. *Astrophysical Journal Supplement Series*, 180:296–305, 2009. [cited at p. vi, 9]

[4] M. Colless et al. The 2df galaxy redshift survey: spectra and redshifts. *Monthly Notices of the Royal Astronomical Society*, 328:1039–1063, 2001. [cited at p. vi, 11]

[5] D. Tytler et al. Review of big bang nucleosynthesis and primordial abundance. *Physica Scripta*, T85(12), 2000. [cited at p. vi, 12]

[6] C. Amsler et al. Review of particle physics. *Physics Letters B*, 667, 2008. [cited at p. vi, vii, 13, 14, 16]

[7] E.W. Kolb and M. Turner. *The Early Universe*. Westview Press, 1990. [cited at p. vii, 1, 19]

[8] R.W. Ogburn. *A search for particle dark matter using cryogenic germanium and silicon detectors in the one- and two-tower runs of CDMS-II at Soudan*. PhD thesis, Stanford University, 2008. [cited at p. vii, 22, 92, 115]

[9] T. Saab. *Search for Weakly Interacting Massive Particles with the Cryogenic Dark Matter Search Experiment*. PhD thesis, Stanford University, 2002. [cited at p. vii, 22]

[10] E. Behnke et al. Spin-dependent wimp limits from a bubble chamber. *Science*, 319(933), 2008. [cited at p. vii, 26, 117]

[11] R. Bernabei et al. First results from dama/libra and the combined results with dama/nai. *European Physics Journal*, C56:333–355, 2008. [cited at p. vii, 27, 28]

[12] T. Shutt. *A dark matter detector based on the simultaneous measurement of phonons and ionization at 20 mK*. PhD thesis, University of California, Berkeley, 1993. [cited at p. viii, 38, 39, 40, 120, 152, 184]

[13] D.S. Akerib et al. Design and performance of a modular low-radioactivity readout system for cryogenic detectors in the cdms experiment. *Nuclear Instruments and Methods in Physics Research A*, 591:476–489, 2008. [cited at p. viii, 39, 54, 68, 197]

[14] R. Clarke. *An Athermal Phonon Mediated Dark Matter Detector with Surface Event Discrimination*. PhD thesis, Stanford University, 1999. [cited at p. viii, 39, 40, 184]

[15] J.P. Filippini. *A Search for WIMP Dark Matter Using the First Five-Tower Run of the Cryogenic Dark Matter Search*. PhD thesis, University of California, Berkeley, 2008. [cited at p. viii, x, 42, 65, 66, 92, 94, 109, 111, 112]

[16] P. Luke. Low energy x-ray response of ge detectors with amorphous ge entrance contacts. *IEEE Transactions on Nuclear Science*, 41(4), August 1994. [cited at p. viii, 43]

[17] Z. Ahmed et al. Search for weakly interacting massive particles with the first five-tower data from the cryogenic dark matter search at the soudan underground laboratory. *Physical Review Letters*, 102(011301), 2009. [cited at p. ix, xiii, 47, 110, 114]

[18] D.S. Akerib et al. Exclusion limits on the wimp-nucleon cross section from the first run of the cryogenic dark matter search in the soudan underground laboratory. *Physical Review D*, 72(052009), 2005. [cited at p. ix, 23, 53, 62, 106]

[19] R.W. Ogburn. Bad yield in 140616_1450. CDMS Internal R119 Analysis Note 229, April 2005. [cited at p. xi, 95, 96]

[20] J. Filippini. Neutralization stability in run 123 and 124 barium data. CDMS Internal R123 Analysis Note 124, November 2007. [cited at p. xi, 95, 97]

[21] R. Hennings-Yeomans. Veto cut for r123: cvtstrict_123. CDMS Internal R123 Analysis Note 94, August 2007. [cited at p. xii, 101, 102]

[22] X. Qiu and L. Duong. R123 charge threshold cut. CDMS Internal R123 Analysis Note 95, August 2007. [cited at p. xii, 102, 103]

[23] J. Filippini. Run-by-run fits to r123 noise blobs. CDMS Internal R123 Analysis Note 153, December 2007. [cited at p. xii, 102, 103, 104, 105]

[24] M. Pyle. Timing outlier creation due to miscorrection and potential ameliorating cuts. CDMS Internal R123 Analysis Note 163, November 2007. [cited at p. xii, 106, 107]

[25] J. Filippini. Third pass at r123 bands. CDMS Internal R123 Analysis Note 111, October 2007. [cited at p. xii, 107, 108]

[26] X. Qiu. r123 pminrtc + pdelc timing parameter surface event cut. CDMS Internal R123 Analysis Note 118, November 2007. [cited at p. xiii, 108, 109]

[27] J. Filippini. Unblinding the r123/4 si data. CDMS Internal R123 Analysis Note 248, November 2008. [cited at p. xiii, 110]

[28] J. Filippini. Assorted r123/4 limit plots. CDMS Internal R123 Analysis Note 259, January 2009. [cited at p. xiii, 115, 116, 117]

[29] X. Qiu. Neutralization: Is 12 hour flashing cycle optimal? CDMS Internal Soudan Offsite Shift Note 13, January 2007. [cited at p. xv, 138, 139]

[30] K.M. Sundqvist. The simple model of impurity ionization and carrier trapping. CDMS Internal Note, January 2008. [cited at p. xvi, 141, 142]

[31] D.K. Schroder. *Semiconductor Material and Device Characterization.* John Wiley & Sons, Inc., 2006. [cited at p. xvi, 152]

[32] P.L. Brink et al. First test runs of a dark-matter detector with interleaved ionization electrodes and phonon sensors for surface-event rejection. *Nuclear Instruments and Methods in Physics Research A*, 559:414–416, 2006. [cited at p. xvii, xviii, 163, 167]

[33] K.M. Sundqvist. A hypothesis for impact ionization due to holes. CDMS Internal Note, January 2008. [cited at p. xix, 179, 180]

[34] P. Peebles. *Principles of Physical Cosmology.* Princeton University Press, 1993. [cited at p. 1]

[35] J.A. Peacock. *Cosmological Physics.* Cambridge University Press, 1999. [cited at p. 1]

[36] M. Milgrom. A modification of the newtonian dynamics as a possible alternative to the hidden mass hypothesis. *Astrophysical Journal*, 270:365–370, 1983. [cited at p. 2]

[37] J.D. Bekenstein. Relativistic gravitation theory for the mond paradigm. *Physical Review D*, 70(083509), 2004. [cited at p. 2]

[38] F. Zwicky. Spectral displacement of extra galactic nebulae. *Helvetica Physica Acta.*, 6:110–127, 1933. [cited at p. 2, 5]

[39] F. Zwicky. On the masses of nebulae and of clusters of nebulae. *Astrophysical Journal*, 86:217–246, 1937. [cited at p. 2, 5]

[40] Y. Sofue and V. Rubin. Rotation curves of spiral galaxies. *Annual Review of Astronomy and Astrophysics*, 39:137–174, 2001. [cited at p. 3]

[41] D. Clowe, A. Gonzalez, and M. Markevitch. Weak-lensing mass reconstruction of the interacting cluster 1e 0657-558: Direct evidence for the existence of dark matter. *The Astrophysical Journal*, 604:596–603, 2004. [cited at p. 7]

[42] E. Komatsu et al. Five-year wilkinson microwave anisotropy probe (wmap) observations: Cosmological interpretations. *Astrophysical Journal Supplement Series*, 180:330–376, 2009. [cited at p. 10, 14]

[43] D. Tytler, X. Fan, and S. Burles. Cosmological baryon density derived from the deuterium abundance at redshift z = 3.57. *Nature*, 381:207–209, 1996. [cited at p. 12]

[44] S. Burles and D. Tytler. On the measurements of d/h in qso absorption systems. *Space Science Reviews*, 84:65–75, 1998. [cited at p. 12]

[45] R.D. Peccei and H.R. Quinn. Cp conservation in the presence of pseudoparticles. *Physical Review Letters*, 38(25):1440–1443, 1977. [cited at p. 15]

[46] R. Bradley et al. Microwave cavity searches for dark-matter axions. *Reviews of Modern Physics*, 75, 2003. [cited at p. 17]

[47] J.D. Lewin and P.F. Smith. Review of mathematics, numerical factors, and corrections for dark matter experiments based on elastic nuclear recoil. *Astroparticle Physics*, 6:87–112, 1996. [cited at p. 21]

[48] V. Sanglard et al. Final results of the edelweiss-i dark matter search with cryogenic heat-and-ionization ge detectors. *Physical Review D*, 71(122002), 2005. [cited at p. 23, 116]

[49] G. Angloher et al. Limits on wimp dark matter using scintillating $cawo_4$ cryogenic detectors with active background suppression. *Astroparticle Physics*, 23:324–339, 2005. [cited at p. 24]

[50] P Sorensen et al. Determination of the scintillation and ionization yield of liquid xe from the xenon10 experiment. *Nuclear Instruments and Methods in Physics Research A*, 601(3):339–346, 2009. [cited at p. 24, 116]

[51] V. Lebedenko et al. Result from the first science run of the zeplin-iii dark matter search experiment. *arXiv*, (0812.1150), 2008. [cited at p. 24, 116]

[52] P. Benetti et al. First results from a dark matter search with liquid argon at 87 k in the gran sasso underground laboratory. *Astroparticle Physics*, 28(6):495–507, 2008. [cited at p. 24, 116]

[53] A. Rubia. Ardm: a ton-scale liquid argon experiment for direct detection of dark matter in the universe. *Journal of Physics: Conference Series*, 39:129–132, 2006. [cited at p. 24]

[54] M.G. Boulay and A. Hime. Technique for direct detection of weakly interacting massive particles using scintillation time discrimination in liquid argon. *Astroparticle Physics*, 25:179–182, 2006. [cited at p. 25]

[55] D.N. McKinsey and K.J. Coakley. Neutrino detection with clean. *Astroparticle Physics*, 22:355–368, 2005. [cited at p. 25]

[56] M. Barnabé-Heider et al. Improved spin dependent limits from the picasso dark matter search experiment. *Physics Letters B*, 624:186–194, 2005. [cited at p. 26]

[57] T.A. Girard et al. Simple dark matter search results. *Physics Letters B*, 621:233–238, 2005. [cited at p. 26]

[58] R. Bernabei et al. The dama/libra apparatus. *Nuclear Instruments and Methods in Physics Research A*, 592:297–315, 2008. [cited at p. 27, 116, 117]

[59] P.L. Brink, B.A. Young, and R. Schnee. Detector technical review. Detector SubSystem Internal Note 0201003, August 2001. [cited at p. 30, 62]

[60] R. Hennings-Yeomans. *First 5 Tower WIMP-Search Results from the Cryogenic Dark Matter Search with Improved Understanding of Neutron Backgrounds and Benchmarking.* PhD thesis, Case Western Reserve University, 2009. [cited at p. 32, 111]

[61] H. Maris. Phonon propagation with isotope scattering and spontaneous anharmonic decay. *Physical Review B*, 41(9736), 1990. [cited at p. 33]

[62] H. Maris and S. Tamura. Anharmonic decay and the propagation of phonons in an isotopically pure crystal at low temperatures: Application to dark-matter detection. *Physical Review B*, 47(727), 1993. [cited at p. 33]

[63] B. Cabrera. Notes on electron-phonon scattering. CDMS Internal Note, 1993. [cited at p. 34]

[64] B.S. Neganov and V.N. Trofimov. Possibility of producing a bulky supersensitive thermal detector at a temperature close to absolute zero. *Journal of Experimental and Theoretical Physics*, 28(328), 1978. [cited at p. 34]

[65] P.N. Luke. Voltage-assisted calorimetric ionization detector. *Journal of Applied Physics*, 64(12):6858–6860, 1988. [cited at p. 34]

[66] N.E. Booth. Quasiparticle trapping and the quasiparticle multiplier. *Applied Physics Letters*, 50(5):293–295, 1987. [cited at p. 34]

[67] K.D. Irwin. An application of electrothermal feedback for high resolution cryogenic particle detection. *Applied Physics Letters*, 66(15):1998–2000, 1995. [cited at p. 35]

[68] T. Saab et al. Design of qet phonon sensors for the cdms zip detectors. *Nuclear Instruments and Methods in Physics Research A*, 444:300–303, 2000. [cited at p. 38]

[69] T. Shutt et al. A solution to the dead-layer problem in ionization and phonon-based dark matter detectors. *Nuclear Instruments and Methods in Physics Research A*, 444:340–344, 2000. [cited at p. 44, 168, 174, 236]

[70] T. Shutt et al. Charge collection and electrode structures in ionization and phonon based dark matter detectors. *Low Temperature Detectors*, 2002. [cited at p. 44, 168, 174, 236]

[71] K.M. Sundqvist. How ion implantation can degrade charge collection. CDMS Internal Note, February 2009. [cited at p. 47, 179]

[72] K.M. Sundqvist and B. Sadoulet. Detectors of the cryogenic dark matter search: Charge transport and phonon emission in ge <100 >crystals at 40 mk. *Journal of Low Temperature Physics*, 151:443–447, 2008. [cited at p. 47, 161]

[73] J.R. Weber, A. Janotti, P. Rinke, and C.G. Van de Walle. Dangling-bond defects and hydrogen passivation in germanium. *Applied Physics Letters*, 91(142101), 2007. [cited at p. 47, 174]

[74] C.G. Van de Walle and J. Neugebauer. Universal alignment of hydrogen levels in semiconductors, insulators and solutions. *Nature*, 423, June 2003. [cited at p. 47]

[75] J. Sander. *Results from the Cryogenic Dark Matter Search Using a Chi Squared Analysis*. PhD thesis, University of California at Santa Barbara, 2007. [cited at p. 61]

[76] D.S. Akerib et al. Limits on spin-independent interactions of weakly interacting massive particles with nucleons from the two-tower run of the cryogenic dark matter search. *Physical Review Letters*, 96(011302), 2006. [cited at p. 62, 95]

[77] D.S. Akerib et al. Limits on spin-dependent wimp-nucleon interactions from the cryogenic dark matter search. *Physical Review D*, 73(011102(R)), 2006. [cited at p. 62]

[78] N. Mirabolfathi et al. Detector commissioning for the cdms-ii final run at the soudan underground laboratory. *Nuclear Instruments and Methods in Physics Research A*, 559:417–419, 2006. [cited at p. 62]

[79] V. Mandic. *First Results from the Cryogenic Dark Matter Search Experiment at the Deep Site*. PhD thesis, University of California, Berkeley, 2004. [cited at p. 62, 63]

[80] D.D. Driscoll. *Development and Performance of Detectors for the Cryogenic Dark Matter Search Experiment with an Increased Sensitivity Based on a Maximum Likelihood Analysis of Beta Contamination*. PhD thesis, Case Western Reserve University, 2004. [cited at p. 63]

[81] B.A. Young et al. T_c tuning of tungsten transition edge sensors using iron implantation. *Nuclear Instruments and Methods in Physics Research A*, 444:296–299, 2000. [cited at p. 63, 179]

[82] B.A. Young et al. Measurement of t_c suppression in tungsten using magentic impurities. *Journal of Applied Physics*, 86(12), December 1999. [cited at p. 63, 179]

[83] V. Mandic et al. Study of the dead layer in germanium for the cdms detectors. *Nuclear Instruments and Methods in Physics Research A*, 520:171–174, 2004. [cited at p. 63, 167]

[84] N. Mirabolfathi. Thoughts about qet biasing procedure at soudan. CDMS Internal Note, April 2005. [cited at p. 67]

[85] C.N. Bailey. Run 123 qet tuning. CDMS Internal Soudan Detector Log entry 3920, September 2006. [cited at p. 70]

[86] D.R. Grant. Run 122 blinding proposal. CDMS Internal Note, January 2006. [cited at p. 87]

[87] R. Mahapatra. Steps to unblinding. CDMS Internal Note, February 2007. [cited at p. 88]

[88] R. Mahapatra. Unblinding decisions. CDMS Internal Note, February 2007. [cited at p. 88]

[89] C.N. Bailey. Preliminary r123 blinding cut. CDMS Internal R123 Analysis Note 7, September 2006. [cited at p. 89]

[90] C.N. Bailey. R123 blinding cut. CDMS Internal R123 Analysis Note 24, January 2007. [cited at p. 89, 90]

[91] C.N. Bailey. R123 noise blobs. CDMS Internal R123 Analysis Note 19, January 2007. [cited at p. 90]

[92] C.N. Bailey. R123 recoil bands. CDMS Internal R123 Analysis Note 21, January 2007. [cited at p. 90]

[93] J. Cooley. R124 blinding cut check #1. CDMS Internal R124 Analysis Note 32, December 2007. [cited at p. 90]

[94] J. Cooley. R124 blinding cut check #2. CDMS Internal R124 Analysis Note 33, December 2007. [cited at p. 90]

[95] R.W. Ogburn. Islands in r119. CDMS Internal R119 Analysis Note 85, January 2005. [cited at p. 92]

[96] J. Filippini. Anomalous yields in t3z2. CDMS Internal R123 Analysis Note 115, October 2007. [cited at p. 92]

[97] W. Rau. Data series with insufficient flashing - run 123, wimp search data. CDMS Internal R123 Analysis Note 156, December 2007. [cited at p. 95]

[98] W. Rau. Data series with insufficient flashing - run 124, wimp search data. CDMS Internal R124 Analysis Note 34, December 2007. [cited at p. 95]

[99] C.N. Bailey. Quantitative neutralization evaluation: R123/r124 neutralization stability in wimp search datasets. CDMS Internal R123 Analysis Note 159, December 2007. [cited at p. 95]

[100] C.N. Bailey. Update to the r123/r124 low background neutralization cut. CDMS Internal R123 Analysis Note 174, January 2008. [cited at p. 95]

[101] C.N. Bailey. Neutralization cut comparisons. CDMS Internal R123 Analysis Note 170, December 2007. [cited at p. 97]

[102] C.N. Bailey. Effect of the r123 and r124 neutralization cuts. CDMS Internal R123 Analysis Note 234, July 2008. [cited at p. 97, 98]

[103] C.N. Bailey. Applying r123/r124 neutralization cut method to r119 t2z5. CDMS Internal R123 Analysis Note 241, August 2008. [cited at p. 98]

[104] C.N. Bailey. A look at the r123 fraction of low yield event distribution. CDMS Internal R123 Analysis Note 226, July 2008. [cited at p. 99]

[105] J. Filippini. Preliminary r123 efficiencies. CDMS Internal R123 Analysis Note 160, December 2007. [cited at p. 103]

[106] X. Qiu. Run 123 singles cut. CDMS Internal R123 Analysis Note 85, June 2007. [cited at p. 104]

[107] J. Filippini. R123 singles efficiencies. CDMS Internal R123 Analysis Note 145, December 2007. [cited at p. 104]

[108] J. Filippini. Revised r123 singles cut and efficiency. CDMS Internal R123 Analysis Note 154, December 2007. [cited at p. 104]

[109] M. Pyle and B. Serfass. Run 123: Preliminary qinner cut. CDMS Internal R123 Analysis Note 60, May 2007. [cited at p. 105]

[110] A.J. Reisetter. *Results from the Two-Tower Run of the Cryogenic Dark Matter Search.* PhD thesis, University of Minnesota, 2005. [cited at p. 108, 111]

[111] S. Kamat. *Extending the Sensitivity to the Detection of WIMP Dark Matter with an Improved Understanding of the Limiting Neutron Backgrounds.* PhD thesis, Case Western Reserve University, 2005. [cited at p. 111]

[112] L. Baudis. Gamma background from u/th/k in the icebox cans. CDMS Internal R118 Analysis Note 233, June 2004. [cited at p. 112]

[113] X. Qiu. Monte carlo of 7 tower fission neutron inner veto in the current soudan geometry. CDMS Internal Note, August 2006. [cited at p. 112]

[114] M. Tarka. Expected neutron background from (α-n) reactions and spontaneous fission in soudan as determined by monte carlo simulations. CDMS Internal Note, September. [cited at p. 112]

[115] J. Angle et al. First results from the xenon10 dark matter experiment at gran sasso national laboratory. *Physical Review Letters*, 100(021303), 2008. [cited at p. 116]

[116] E. Aprile et al. New measurement of the relative scintillation efficiency of xenon nuclear recoils below 10 kev. *arXiv*, (0810.0274), 2008. [cited at p. 116]

[117] J.R. Ellis, K.A. Olive, Y. Santoso, and V.C. Spanos. Update on the direct detection of supersymmetry dark matter. *Physical Review D*, 71(095007), 2005. [cited at p. 116]

[118] L. Roszkowski, R. Ruiz de Austri, and R. Trotta. Implications for the constrained mssm from a new prediction for b-sγ. *Journal of High Energy Physics*, 07(075), 2007. [cited at p. 116, 117]

[119] C. Savage, G. Gelmini, P. Gondolo, and K. Freese. Compatibility of dama/libra dark matter detection with other searches. *arXiv*, (0808.3607), 2008. [cited at p. 116, 117]

[120] J. Angle et al. Limits on spin-dependent wimp-nucleon cross-sections from the xenon10 experiment. *Physical Review Letters*, 101(091301), 2008. [cited at p. 117]

[121] S. Desai et al. Search for dark matter wimps using upward through-going muons in super-kamiokande. *Physical Review D*, 70(083523), 2004. [cited at p. 117]

[122] G. Wang. *The Cryogenic Dark Matter Search and Background Rejection with Event Position Information*. PhD thesis, Case Western Reserve University, 2005. [cited at p. 120, 214]

[123] T. Shutt et al. Measurement of ionization and phonon production by nuclear recoils in a 60 g crystal of germanium at 25 mk. *Physical Review Letters*, 69(24), December 1992. [cited at p. 120]

[124] C.N. Bailey. Quantitative comparison between run 123 through 128 neutralization. CDMS Internal Soudan Offsite Shift Note 61, August 2008. [cited at p. 127, 140]

[125] C.N. Bailey. Evaluating beginning of r127 led tests. CDMS Internal Soudan Offsite Shift Note 52, May 2008. [cited at p. 132, 134, 218]

[126] C.N. Bailey. Monitoring r123 wimp search neutralization stability with time. CDMS Internal R123 Analysis Note 227, July 2008. [cited at p. 138]

[127] C.N. Bailey. R125 neutralization: Is 11hr flashing interval sufficient? CDMS Internal Soudan Offsite Shift Note 31, November 2007. [cited at p. 138]

[128] C.N. Bailey. Monitoring r127 wimp search neutralization stability with time. CDMS Internal Soudan Offsite Shift Note 55, July 2008. [cited at p. 138]

[129] C.N. Bailey. Quantitative evaluation of neutralization states during long (weak) barium datasets in r124. CDMS Internal R124 Analysis Note 30, November 2007. [cited at p. 138]

[130] C.N. Bailey. Monitoring r127 long barium neutralization stability. CDMS Internal Soudan Offsite Shift Note 56, July 2008. [cited at p. 138]

[131] C.N. Bailey. Comparing detector neutralization state as a function of temperature. CDMS Internal Soudan Offsite Shift Note 65, November 2008. [cited at p. 143]

[132] K.M. Sundqvist. Where is the fermi level at zero kelvin? CDMS Internal Note, March 2008. [cited at p. 152]

[133] B.G. Streetman. *Solid State Electronic Devices*. Prentice-Hall, Inc., 1980. [cited at p. 152]

[134] P. Luke. Single-polarity charge sensing in ionization detectors using coplanar electrodes. *Applied Physics Letters*, 65(2884), November 1994. [cited at p. 163]

[135] J. Ruderman. Capacitance and electric field computations for interdigitated sensor design. CDMS Internal Note, August 2003. [cited at p. 164]

[136] A. Broniatowski. A new high-background-rejection dark matter ge cryogenic detector. submitted to Physical Review Letters, pre-print reference arXiv:0905.0753. [cited at p. 165]

[137] V. Mandic. Comparison of g31 bands. CDMS Internal G31 Analysis Note 52, January 2004. [cited at p. 167]

[138] K.M. Sundqvist. A quick summary of deadlayer pathology. CDMS Internal Note, November 2008. [cited at p. 167, 178]

[139] R. Mahapatra. Phonon/charge side disparity in yield-based ejectron rejection. CDMS Internal R119 Analysis Note 347, June 2006. [cited at p. 167]

[140] C.N. Bailey. Comparing phonon/charge side yield based ejectron rejection for n- and p-type germanium. CDMS Internal R123 Analysis Note 264, May 2009. [cited at p. 167, 201, 203]

[141] R. Mahapatra. Yield distribution of βs on phonon and charge sides and differences in ge and si detectors. CDMS Internal R119 Analysis Note 351, October 2006. [cited at p. 167]

[142] A. Stesmans. Passivation of p_{b0} and p_{b1} interface defects in thermal (100) si/sio_2 with molecular hydrogen. *Applied Physics Letters*, 68(15), April 1996. [cited at p. 169]

[143] C.G. Van de Walle and R.A. Street. Structure, energetics, and dissociation of si-h bonds at dangling bonds in silicon. *Physical Review B*, 49(20), May 1994. [cited at p. 169]

[144] D. Yvon et al. Low noise voltage and charge preamplifiers for phonon and ionization detectors at very low temperature. *Nuclear Instruments and Methods in Physics Research A*, 368:778–788, 1996. [cited at p. 197]

[145] C.N. Bailey. Comparing numbers of phonon and charge side betas for n- and p-type germanium. CDMS Internal R123 Analysis Note 266, May 2009. [cited at p. 201, 202]

[146] L. Novak. Previous ge boule quotes. Detector SubSystem Internal Note 0707002, July 2007. [cited at p. 201]

[147] D.S. Akerib et al. Present status of the supercdms program. *Journal of Low Temperature Physics*, 151:818–823, 2008. [cited at p. 203]

[148] K.M. Sundqvist and C.N. Bailey. Illustrative notes for led discussion. CDMS Internal Note, January 2007. [cited at p. 214]

[149] D. Seitz. Feb led drive slew rate. CDMS Internal DCRC elog Note 67, November 2007. [cited at p. 215]